5-2018

Molten Core Fabrication of Intrinsically Low Nonlinearity Glass Optical Fibers

Maxime Cavillon
Clemson University, mcavill@clemson.edu

MOLTEN CORE FABRICATION OF INTRINSICALLY LOW NONLINEARITY GLASS OPTICAL FIBERS

A Dissertation
Presented to
the Graduate School of
Clemson University

In Partial Fulfillment
of the Requirements for the Degree
Doctor of Philosophy
Materials Science and Engineering

---

by
Maxime Cavillon
May 2018

Accepted by:
Dr. John Ballato, Committee Chair
Dr. Peter Dragic
Dr. Liang Dong
Dr. Stephen Foulger
Dr. Philip Brown

ABSTRACT

Optical nonlinearities limit scaling to higher output powers in modern fiber-based laser systems. Paramount amongst these parasitic phenomena are stimulated Brillouin scattering (SBS), stimulated Raman scattering (SRS), and nonlinear refractive index (n_2)-related wave-mixing phenomena (e.g., self-phase modulation, SPM, four-wave mixing, FWM). In order to mitigate these effects, the fiber community has largely focused on the development of micro-structured large mode area (LMA) fibers whereby the fiber geometry is engineered to spread the optical power over a larger effective area. In addition to increasing the resultant complexity and cost of these fibers, such LMA designs introduce new parasitic phenomena, such as transverse mode instability (TMI), which presently serves as the dominant limitation in power-scaling.

This dissertation explores a different approach for mitigating these nonlinearities in optical fiber lasers; namely attacking the aforementioned effects at their fundamental origin, i.e., the material through which the light propagates. Indeed, the Brillouin gain coefficient (BGC), the Raman gain coefficient (RGC), the thermo-optic coefficient (TOC) and the nonlinear refractive index (n_2) are all intrinsic material properties that respectively drive SBS, SRS, TMI and wave-mixing phenomena. Though less well studied within the fiber laser community, such a materials approach offers a powerful yet simpler way to address nonlinearities.

Chapter I investigates the thermodynamic origins of light scattering and provides insight into the prime material properties that drive optical nonlinearities. Chapters II and III offer an overview of how these (and other) properties can be measured and modeled in multicomponent glass systems, considering both bulk or fiber geometries. In Chapter IV, a materials road map for binary and ternary glass material systems is provided to identify which compositions should be of specific focus for the development of intrinsically low optical nonlinearity optical fibers. These four Chapters have been adapted from a series of published journal articles[1] entitled "A unified materials approach to mitigating optical nonlinearities in optical fiber" [1]–[4].

In Chapter V, the fabrication of oxyfluoride-core silica-cladding optical fibers using the molten core method is described and their core glass compositions and structures investigated. The thermodynamics and kinetics of fluoride-oxide reactions are also studied, and insights on the dominant mechanisms that drive the fluoride-oxide reactions during fiber processing are discussed. In Chapter VI, optical properties that drive optical nonlinearities are studied, and their relationships with glass compositions investigated. Oxyfluoride fibers exhibiting concomitant reductions of 6-9 dB in BGC, 0.5-1.5 dB in RGC, and 1.2-3.2 dB in TOC, relative to conventional silica fibers, as well as reduced linear and nonlinear refractive indices, are reported. Spectroscopic properties of active Yb-doped fibers are also considered, and suggest enhanced laser performance and higher lasing efficiencies for these systems compared to conventional silica fibers. Finally, Chapter VII

[1] This series of journal articles is the fruit of a collaborative effort and has been suitably modified in this dissertation. Co-authors are greatly acknowledged for their respective contributions.

portrays the current challenges and the future perspectives of these oxyfluoride-core silica-cladding glass optical fibers, along with approaches to overcome them.

[1] J. Ballato, M. Cavillon, and P. Dragic, "A Unified Materials Approach to Mitigating Optical Nonlinearities in Optical Fiber. I. Thermodynamics of Optical Scattering," *Int. J. Appl. Glas. Sci.*, vol. 9, no. 2 pp. 263–277, 2018.

[2] P. D. Dragic, M. Cavillon, A. Ballato, and J. Ballato, "A unified materials approach to mitigating optical nonlinearities in optical fiber. II. A. Material additivity models and basic glass properties," *Int. J. Appl. Glas. Sci.*, vol. 9, no. 2 pp. 278–287, 2018.

[3] P. D. Dragic, M. Cavillon, A. Ballato, and J. Ballato, "A unified materials approach to mitigating optical nonlinearities in optical fiber. II. B. The optical fiber, material additivity and the nonlinear coefficients," *Int. J. Appl. Glas. Sci.*, DOI:10.1111/ijag.12329, 2018.

[4] M. Cavillon, C. Kucera, T. Hawkins, J. Dawson, P. D. Dragic, and J. Ballato, "A Unified Materials Approach to Mitigating Optical Nonlinearities in Optical Fiber. III. Canonical Examples and Materials Roadmap," *Int. J. Appl. Glas. Sci.*, DOI: 10.1111/ijag.12336, 2018.

DEDICATION

I dedicate this work to my beloved parents.

ACKNOWLEDGMENTS

First and foremost, let me thank my advisor, Dr. John Ballato, for giving me the opportunity to be a part of his group at Clemson University. *I am very grateful for your support over these years, and I really enjoyed the enthusiasm you shared with me about my project! You succeeded in making this experience very valuable to me; you gave me the space I needed to express myself, but were always around to give me thoughtful advice. Thank you very much for this fantastic adventure!*

I would also like to thank Dr. Peter Dragic, who performed many of the measurements on the fibers described herein and served very much as a co-advisor. *Thank you for your time, your cheerfulness and the endurance you put into replying to my all my emails over these years! I have learnt so much from you and enjoyed every bit of it.*

I am grateful as well to my other committee members, Dr. P. Brown, Dr. S. Foulger, and Dr. L. Dong, for the time and effort their put into my research work.

Thank you also to Dr. F. Smektala who first presented me to Dr. J. Ballato and for making me discover and like glass science for the very first time!

Let me also thank my office mates, Courtney, Benoit, Matt, Amber, Josh, Colin and Baris, as well as the summer students, Lauren, Thomas, Megan and Cameron. I also want to thank my friends, Jake and his family, Brad, Colton, Bob and his family, Benoît, Jérôme, Hervé, the other VIE people, Jaime, Ashley, the pick-up soccer group people, Andreas, Ted, Andrew, AP, Ryan, Garry & Deborah, the MS&E department people, and all the others I haven't mentioned. *You all contributed to make my Clemson experience very unique to me!*

Special thanks to Courtney, *for being always supportive and around when needed, for caring so much about me (and the group!) and for making sure I will never run out of coffee!* I also want to give a round of applause to Benoît Faugas, for being my molten core mate and friend: *thank you for everything you have done for me, and also for the infinite number of discussion about our respective works. We can safely say that we have raised more questions that we could ever answered, but it was all worth it.*

I am also very grateful to the draw tower guys, Wade Hawkins, Max, Josh, and Ken for their incredible help and assistance over the years. *Thank you Wade for this hard work and your experienced skills on the tower!*

I should also thank the Clemson staff, faculty members, and all the people who contributed to this work: Donald for his precious help at the EM lab, Jianan and Dr. Xiao for their assistance with the Raman spectroscopy, Ying and Dr. Urban for their help with IR spectroscopy, Dr. Sanders for his helps with DSC-TGA measurements, Dr. Peacock and Dr. Runge for their collaboration in n_2 measurements, and Dr. Yablon for the characterization of fibers' RIP. Thank you to Dr. Riman for his thoughtful comments on thermodynamics of oxyfluoride systems, and to Dr. Stolen for his always interesting remarks about optics and for letting me use his lab.

Thank you also to my family, my parents, and my sisters, Marine et Maëlle, for their flawless support during my time in Clemson.

At last, I would like to thank Andrea. *You have always encouraged me in this adventure and I am very glad you were a part of it. Thank you for your incredible support and for being so special to me.*

TABLE OF CONTENTS

LIST OF TABLES

LIST OF FIGURES

CHAPTER I.

THERMODYNAMICS OF OPTICAL SCATTERING

I. A. Introduction

In this Chapter, the material origins from which optical nonlinearities arise are described and their impact discussed. The origins and limitations associated with Brillouin, Raman, and (classical) Rayleigh scattering, as well as n_2-related phenomena, in optical fibers have all been well-established for decades [1], [2]. Significant efforts to understand and minimize their influence were undertaken in the early days of low loss optical fibers for telecommunications. Of particular note are the contributions of *Schroeder* [3], [4], *Lines* [5]–[7], and *Pinnow* [8], whose works are synthesized and recast here through the lenses of current and future needs. By this means, this Chapter provides an understanding of which fundamental material properties drive optical nonlinearities that currently plague power scaling in fiber-based laser systems. Additionally, the influence of materials on these phenomena is discussed.

Irrevocability, key properties that factor into nonlinear effects described herein need to be tailored in order to mitigate these phenomena. Consequently, Chapters II and III treat the materials modeling and measurement of the optical, acoustic, Brillouin, and thermo-optic properties of the glass systems and fibers fabricated and discussed, along with canonical glass systems investigated in Chapter IV.

I. B. Thermodynamics of Optical Scattering and Impact on Optical Nonlinearities

Light scattering results from any process that manifests fluctuations in the dielectric constant. At the most fundamental level, in an otherwise pure material at thermal equilibrium, dielectric fluctuations are a function of conjugate thermodynamic variables: pressure / volume and temperature / entropy [4], [5]. In a multicomponent system, dielectric perturbations also arise from fluctuations in composition (c_i) / chemical potential (μ_i) of component *i*. Further, ionic / molecular rotational and vibration momenta and displacements (Q_i) also contribute. Choosing pressure (P), entropy (S), composition (c) and displacement (Q) as independent variables, as also employed in [4], [5] for consistency, the collective dielectric perturbation, $\Delta\epsilon$, is

$$\Delta\epsilon = \left(\frac{\partial\varepsilon}{\partial P}\right)\Delta P + \left(\frac{\partial\varepsilon}{\partial S}\right)\Delta S + \sum_{i\neq j}\left(\frac{\partial\varepsilon}{\partial c_i} - \frac{\partial\varepsilon}{\partial c_j}\right)\Delta c_i + \sum_k\left(\frac{\partial\varepsilon}{\partial Q_k}\right)\Delta Q_k. \quad (1.1)$$

From a practical perspective, the total power of light scattered, P_s, by such perturbations in permittivity goes as $P_s \propto I_o\langle\Delta\epsilon^2\rangle$, where I_o is the incident light intensity and $\langle\Delta\epsilon^2\rangle$ is the ensemble average of the mean square dielectric fluctuation, $\Delta\epsilon$. Assuming the statistical independence of each term [4], [9], one then arrives at the following relationship, which is linearly proportional to the aforementioned total scattered optical power:

$$P_S \propto \langle\Delta\epsilon^2\rangle = \left(\frac{\partial\varepsilon}{\partial P}\right)^2\langle(\Delta\mathrm{P})^2\rangle v_P + \left(\frac{\partial\varepsilon}{\partial S}\right)^2\langle(\Delta\mathrm{S})^2\rangle v_S + \sum_{i\neq j}\left(\frac{\partial\varepsilon}{\partial c_i} - \frac{\partial\varepsilon}{\partial c_j}\right)^2\langle(\Delta c_i)^2\rangle v_{c_i} +$$

$$\sum_k\left(\frac{\partial\varepsilon}{\partial Q_k}\right)^2\langle(\Delta Q_k)^2\rangle v_{Q_k} \quad (1.2)$$

Here $\nu_{P,S,c,Q}$ are the correlation volumes for each variable as defined in [5]. The first term, relating to P, originates Brillouin scattering. The second and third terms, relating to S and c_i originate Rayleigh scattering. The fourth term, relating to Q_i, originates Raman scattering; all in their spontaneous forms.

The previous treatments of these thermodynamic terms [3]–[5], [8] focus on the origin of the dielectric perturbation (e.g., density and concentration scattering). The section that follows, though largely didactic, represents a departure from this description by focusing instead on the nonlinear phenomena arising from the scattering and materials for their mitigation as these are the more critical considerations when viewed through a modern lens.

I. B. 1. Brillouin scattering

Spontaneous Brillouin scattering (SpBS) [10] is an inelastic interaction between acoustic phonons of the material and the optical signal. This interaction, as noted with respect to Eqn. 1.2, is manifest as pressure fluctuations which perturb the dielectric constant. While the change in dielectric constant (or refractive index, n) with pressure is known in some systems, the influence of density on these properties is more commonly measured. Accordingly, when temperature is reasonably constant such that $(\partial\epsilon/\partial T)_P \ll (\partial\epsilon/\partial P)_T$, then the thermodynamic Maxwell relations [11] yield

$$P_S^{SpBS} \propto \left(\frac{\partial\varepsilon}{\partial P}\right)^2 \langle(\Delta \mathrm{P})^2\rangle v_P = \rho^2 \left(\frac{\partial\epsilon}{\partial\rho}\right)_T^2 kTK_S. \qquad (1.3)$$

Here ρ is the density, k is Boltzmann's constant, T is the absolute temperature, and K_S is the adiabatic compressibility defined as $-(\partial V/\partial P)_S/V$ [12]. As it will turn out, Brillouin scattering is one of the two contributions (Rayleigh being the other, as to be discussed later) from density perturbations that lead to dielectric fluctuations. For greater ease in developing material solutions to these scattering phenomena, it is convenient to recast $\partial\epsilon/\partial\rho$ in terms of the photoelastic coefficient, p, as $\rho(\partial\epsilon/\partial\rho)_T = \mathrm{n}^4\mathrm{p}$ [5]. It can be shown [13] that for a linearly polarized (transverse to the propagation direction) optical fiber mode interacting with a compressional acoustic wave in an isotropic material, p reduces to p_{12}. From a materials perspective then, SpBS scales with the refractive index as n^8, the p_{12} transverse photoelasticity as p_{12}^2, and linearly with the adiabatic compressibility, K_S. Further, the adiabatic compressibility is, itself, related to the c_{11} and c_{44} elastic stiffness coefficients as $K_s = (c_{11} - 4c_{44}/3)^{-1}$ where $c_{11} = \rho v_L^{\,2}$ and $c_{44} = \rho v_T^2$ with v_L and v_T being the longitudinal and transverse acoustic velocities, respectively. More specifically, materially:

$$P_S^{SpBS} \propto n^8 p_{12}^2 K_S. \qquad (1.4)$$

Interference between the forward-propagating optical signal and back-scattered Brillouin light can, through electrostriction, create a Bragg-matched grating that, with sufficient intensity, acts as a highly-efficient reflector to the optical signal. This grating is a traveling periodic index variation resulting from the density perturbations caused by a traveling hypersonic acoustic (or pressure) wave. The single-pass gain in such *stimulated Brillouin scattering* (SBS), first observed in crystals of quartz and sapphire [14] and then in glass

optical fiber [15], is proportional to the exponential of a gain coefficient, BGC, given by BGC$= 2\pi n^7 p_{12}^2 / \, c\lambda_o^2 \rho V_a \Delta\nu_B$[16]. Here, in addition to the previously defined terms, c is the speed of light, V_a is the acoustic velocity of the material, and $\Delta\nu_B$ is the Brillouin linewidth. More completely, the Brillouin gain is proportional to $e^{g_B P L_{eff}/A_{eff}}$, where P is the signal power, L_{eff} is an effective fiber length accounting for attenuation, and A_{eff} is the effective area of the optical signal (mode). As such, SBS has been investigated for use in amplification in communications systems [17]. This dependence clearly shows the advantages of short L_{eff} and large A_{eff} values, should system requirements allow them, in suppressing the effects of SBS.

SBS is well known to limit the intensity of light per unit bandwidth that can be transmitted through or generated in optical fiber lasers and systems [1], [18]. SBS typically has the lowest threshold of all the nonlinear optical processes in narrow line-width systems (Brillouin linewidths typically in the range of 30 to 100 MHz) and is a leading limitation in the scaling of high energy lasers systems to higher powers. Methods of suppression have largely focused on enhanced mode size and acoustically engineered fiber designs that generally require sophisticated core doping profiles or cladding structures [19], [20].

I. B. 2. Material influences on Brillouin scattering

For a given signal wavelength and fiber properties (core size and numerical aperture, NA), Brillouin scattering is related to the following material properties: refractive

index, photoelasticity, and adiabatic compressibility (hence density and acoustic velocity) and, in the case of SBS, Brillouin linewidth as well. In order to reduce Brillouin scattering as a hindrance to continued power handling capability in optical fibers, it stands to reason that modifications to any of these factors in a manner than lessens the scattering is useful. That said, some of these materials properties are more sensitive than others to changes in composition and glass forming ranges must also be considered. For example, alumina (Al_2O_3) is known to reduce p_{12} and increase density when added to silica (SiO_2) in binary aluminosilicate glasses [21]. However, the glass-forming limit of alumina into silica is only about 8 mole percent when conventional optical fiber fabrication methods are employed [22]. Such a balance between how a given material affects each of these parameters will be discussed in greater detail in Chapter IV. However, it is worth noting that – of the nonlinear optical phenomena – Brillouin scattering is especially interesting because one of the factors determining its magnitude, the Pockels p_{12} coefficient, has the physical potential to take on a value of zero [21], [23]. In such materials, the presence of an acoustic (pressure) wave does not give rise to photoelastic change in refractive index, hence perturbation to the dielectric constant, thereby precluding the interaction from ever happening.

I. B. 3. Raman scattering

Raman scattering is a form of inelastic scattering that originates from an interaction of the incident light wave with optical phonons (as opposed to acoustic phonons in the case of Brillouin scattering) [24]. The simplest classical description of Raman scattering requires that the polarizability be not fixed, but is instead dependent upon the interatomic

spacing of the elements (atoms) comprising a classical harmonic oscillator [25]. As such, a vibrating molecule for example, whose interatomic spacing is changing in time, will therefore have a time-varying polarizablity (and therefore time-varying refractive index) which will modulate the phase of an incoming optical field. This phase modulation gives rise to the wavelength or frequency shift encountered during the Raman process. As noted above, the contribution of Raman scattering to the total scattered power described in Eqn. 1.2 goes as

$$P_S^{Raman} \propto \langle \Delta\epsilon^2 \rangle = \sum_k \left(\frac{\partial \varepsilon}{\partial Q_k}\right)^2 \langle (\Delta Q_k)^2 \rangle v_{Q_k}. \qquad (1.5)$$

Estimations of Raman scattering invoke the approximation that a single vibrational mode dominates, which is usually associated with the stretching mode of the main constituent / glass former, e.g., the Si – O – Si bond, or the most polarizable bond in the system, and is modeled as a simple harmonic oscillator [5], [6]. In such approximations, the generalized coordinate, Q_k, is replaced by the average bond length, l, such that $(\partial\epsilon/\partial Q_k) \rightarrow (\partial\epsilon/\partial l)$. Given the interconnected network of typical inorganic glasses, (optical or mechanical) field-induced changes in bond length yield proportional changes in density such that $\partial\epsilon/\partial l \propto \Lambda$, where Λ is the bond compressibility parameter. Further, under the same estimation as invoked above, the correlation volume, v_{Q_k}, is given by $V_m/N_o z_R$, where V_m is the molar volume and z_R is the number of (equivalent) oscillators per unit cell. Therefore, materially,

$$P_S^{Raman} \propto V_m \cdot \Lambda^2. \qquad (1.6)$$

For the purposes of this dissertation, the dependence of P_S^{Raman} on z_R is left out of Eqn. 1.6 since, as will be seen in Chapter IV, the molar volume, V_m, and bond compressibility parameter, Λ, are more directly calculable.

Above a threshold intensity, the spontaneous scattering process becomes stimulated [26]–[30]. Stimulated Raman scattering (SRS) is used for optical amplification in selected telecommunication systems [31], [32]. However, in wavelength division multiplexed (WDM) communication systems, SRS also can manifests channel cross-talk and excess attenuation [33]. Further, in the high power fiber-based laser focus of this work, SRS leads to wavelength shifts and power instabilities that degrade laser performance. Accordingly, as with SBS, SRS is considered a deleterious parasitic phenomenon. Existing approaches to reduce SRS include spectral filtering fibers and techniques have been utilized to suppress SRS [34].

I. B. 4. Material influences on Raman scattering

As with all optical nonlinearities, fundamentally originated from the interaction of the incident light with the material through which it is propagating, a materials approach to its diminution may also be adopted. Interestingly, though, silica from which conventional fibers are made already has an intrinsically low Raman gain and typical waveguide-related additives to SiO_2 (e.g., GeO_2) increase the cross-section for Raman scattering [35]. Somewhat intuitively, such an intrinsically low Raman gain material can be achieved when one or more of the following conditions are met: (i) the material is highly disordered broadening the Raman gain spectrum and thus reducing the peak value, (ii) high concentrations of materials with low Raman gain coefficients, RGC, are employed, and (iii) materials are utilized whose components have minimal overlap in their respective Raman spectra [36]. More quantitatively, Raman scattering (both spontaneous and, therefore, stimulated forms) is reduced for glasses comprised of compounds possessing low molar volume and small bond compressibility parameters, Λ.

Values for Λ generally range from $-2 < \Lambda < +2$, depending on whether the glass (or crystal) structure is more layered, favoring $\Lambda < 0$, or more fully coordinated, favoring $\Lambda > 0$ [7]. For purposes of comparison, $\Lambda_{SiO_2} \cong \Lambda_{GeO_2} = 0.1$ whereas $\Lambda_{As_2Se_3} = -1.4$ [6]. While a zero-value for Λ should negate any Raman scattering, to the accuracy of the estimations, the general incompatibility between materials with positive and negative Λ values makes this a less likely prospect. Lastly, for a thoughtful history and seminal

bibliography of the pioneering early work on stimulated Raman scattering, including aspects of stimulated Brillouin and Rayleigh scattering, the Reader is referred to the 1967 Review by *Bloembergen* [37].

I. B. 5. (Classical) Rayleigh scattering

Rayleigh scattering is the elastic scattering of light by perturbations in dielectric constant associated with sub-wavelength fluctuations in density or composition [38]. As such, and as noted above, the total scattered power associated with (classical) Rayleigh scattering is described by the ΔS and Δc_i terms of Eqn. 1.2; that is

$$P_S^{Rayleigh} \propto \langle \Delta \epsilon^2 \rangle = \left(\frac{\partial \varepsilon}{\partial S}\right)^2 \langle (\Delta S)^2 \rangle v_S + \sum_{i \neq j} \left(\frac{\partial \varepsilon}{\partial c_i} - \frac{\partial \varepsilon}{\partial c_j}\right)^2 \langle (\Delta c_i)^2 \rangle v_{c_i}. \qquad (1.7)$$

Considerations associated with the magnitude of Rayleigh scattering in glass played a central role in the earliest days of the development of optical fiber for long-haul communications. It was well-appreciated that the minimum loss of optical fiber was dependent on Rayleigh scattering and so compositions that reduced its magnitude were an active topic of study [5], [6], [39]–[42]. However, while multicomponent glasses possessing intrinsically low Rayleigh scattering (i.e., lower Rayleigh scattering than silica) have been synthesized and studied [42]–[52], extrinsic impurities ultimately defined practical attenuation limits of optical fibers. As a result, attention then turned to the optimization of the chemical vapor deposition processes for fabricating low loss, essentially intrinsic, silica-based optical fibers.

That said, in the present context of high power fiber lasers, Rayleigh scattering is of interest; not, though, from the perspective of reducing the minimum loss but, rather, reducing backscattering which can lead to noise [53], [54] and seed stimulated processes. The generalities of these material influences on Rayleigh scattering will now be discussed with greater detail of specific glass systems to be provided in Chapter IV.

I. B. 6. Density-related Rayleigh scattering

Per Eqn. 1.7, the scattering impact of density fluctuations on the dielectric constant is given by $(\partial\varepsilon/\partial S)^2\langle(\Delta S)^2\rangle v_S$. Assuming small enthalpic (H) changes with such fluctuations, Lines [5] showed thermodynamically that $\langle(\Delta S)^2\rangle = kT/(\partial^2 H/\partial S^2)_p = kT/(\partial T/\partial S)_p$. Since the heat capacity per unit volume, c_p, is given by $T(\partial S/\partial T)_p/V$, then $\langle(\Delta S)^2\rangle = kc_p v_S$. Under most practical laser conditions where temperature varies relatively slowly, then Maxwell's relations yield $(\partial\epsilon/\partial S)_p^2 = \rho^2(\partial\epsilon/\partial\rho)_T^2 T K_T\left[\left(c_p - c_T\right)/v_S c_p^2\right]$, where K_T is the isothermal compressibility. This relationship for $(\partial\epsilon/\partial S)_p^2$, taken with that given above for $\langle(\Delta S)^2\rangle$, together with the fact that $c_p/c_v = K_T/K_S$ [25], with K_S being the adiabatic compressibility, one arrives at a proportionality of scattering to $\rho^2(\partial\epsilon/\partial\rho)_T^2 kTK_T$. Given the density derivatives noted above as relates to Brillouin scattering, the total power scattered associated with the density component of Rayleigh scattering goes materially as [5]

$$P_{S,density}^{Rayleigh} \propto n^8 p^2 T_f K_S(T). \quad (1.8)$$

As can be observed by comparison of Eqn. 1.8 with Eqn. 1.4, both Brillouin and density-related Rayleigh scattering share a common dependence on density; hence Pockels strain-optic coefficient, $p = p_{12} + (2/3)p_{44}$, though in the case of SBS in optical fibers, it is the p_{12} value that particularly matters. For completeness, it is noted that the photoelastic coefficients are not only compositionally dependent, but spectrally dependent as well; i.e., $p = p(\lambda)$ [55]. Further, in an analogous manner to Brillouin, the density component of Rayleigh scattering can be negated for a glass with a photoelasticity of zero; i.e., $p = 0$, such that $p_{12} = -(2/3)p_{44}$ or $p_{12} = -(1/2)p_{11}$.

I. B. 7. Concentration-related Rayleigh scattering

Estimations for compositional influences on Rayleigh scattering generally assume a random mixture of the glass components with each species having the same nearest neighbors [5], [6]. While this is not true in practice, such as, for example, alkali clustering about non-bridging oxygen (NBO) ions in alkali silicate glasses [56], [57], the results are sufficiently accurate for the general purposes here of identifying material systems with reduced optical loss mechanisms. The optical fibers of interest herein would inevitably employ a multicomponent glass. The simplest such system obviously is a binary in which case

$$P_{S,composition}^{Rayleigh} \propto \left(\frac{\partial \epsilon}{\partial C}\right)_{P,T}^{2} \frac{kT_f'}{N'} \left(\frac{\partial \mu}{\partial C}\right)_{P,T}^{-1}, \qquad (1.9)$$

where C is the composition, given as the molar ratio of solute (N) to solvent (N'), μ is the chemical potential, and T_f' is the fictive temperature [58]. For completeness, *Schroeder*

notes that $T_f^{'}$ is the temperature where compositional fluctuations of a given wavenumber are "thermally arrested" which is different from the conventional fictive temperature, T_f, where density fluctuations in the melt are kinetically frozen into the glassy state [3].

Lines independently derived a similar expression for concentration-related Rayleigh scattering of a binary glass [5]. In that work, the chemical potential was cast in terms of the free energy of mixing (at constant pressure and temperature) and further approximations based on the temperature, T, proximite to the spinodal temperature, T_s, yields

$$P_{S,composition}^{Rayleigh} \propto \left(\frac{\partial \epsilon}{\partial C}\right)_{P,T}^{2} \frac{C(1-C)T}{(T-T_s)}, \qquad (1.10)$$

where C is the concentration of one component in the binary glass and (1 – C) is the concentration of the other component. For completeness, in terms of materials factors influencing the scattering, *Lines'* approach yields a pre-factor given by (M/ρ), where M and ρ are the average molecular weight and density, respectively, of the binary components [5].

I. B. 8. Stimulated (Classical) Rayleigh scattering

Stimulated Rayleigh scattering is not so frequently observed, nor practically detrimental, as to be regularly treated in the literature. As noted by *Bloembergen*, there is a close physical connection between Stimulated Rayleigh scattering and Stimulated Raman scattering (SRS) [37]. In the case of SRS, the difference between pump and Stokes

frequencies is given by the vibrational (or rotational) energies of the molecules excited. In stimulated Rayleigh scattering, the differences between pump and Stokes frequencies are very small and are equal to the inverse of the relaxation times. It appears that the first paper on stimulated Rayleigh scattering dates from 1965 [59] just as high peak power lasers were sufficiently available to observe such stimulated phenomena of otherwise weak nonlinearities; not unlike the timing of the first observations of SRS in 1962 [26] and SBS in 1964 [14].

I. B. 9. Material influences on Rayleigh scattering

From Eqns. 1.8, 1.9, and 1.10, there are several approaches to materially reducing Rayleigh scattering in optical fibers. The dependence of density-related Rayleigh scattering on fictive temperature, T_f, affords an opportunity to reduce this effect. Indeed, thermal processing has been used to this end with important reductions in Rayleigh scattering observed [51], [60]–[64]. Further, as with Brillouin scattering, the contribution of density fluctuations to Rayleigh scattering can also be directly attacked through the photoelastic coefficients. As discussed in Section I. B. 2, the p_{12} component can be zero in selected binary and ternary glasses comprised of compounds possessing positive and negative p_{12} values [21], [23], [65]. It should be noted, though, that while the $p_{12} = 0$ compositions have been considered for SBS mitigation, the realization of their benefit to Rayleigh reduction has not previously been considered.

Recently noted [66], though not reduced to practice, is the "chemical potential engineering," suggested by Eqn. 1.10. Conceptually, in this case, two glasses of different composition but equal (or nearly so) chemical potential should have no (or negligible) thermodynamic driving force to interact and very unusual fiber compositions might be possible. More generally, reductions to the chemical potential difference should reduce Rayleigh scattering. Lastly, as noted by *Tynes* [67], the $(\partial\epsilon/\partial C)$ term should vanish for glasses where the refractive index and density are largely independent of composition, such as the sodium borosilicate system [68]. In such systems, both density- and composition-related scattering can be reduced. Along these lines, Rayleigh scattering contributions have been attacked synergistically in mixed alkali glasses by tailoring the glass transition and fictive temperatures (relative to the spinodal temperature) as well as isothermal compressibility, resulting in a silicate glass whose relative Rayleigh scattering is only 38 % that of pure silica [52]. Specific compositional approaches to reducing Rayleigh scattering will be discussed in greater detail in Chapter IV.

I. B. 10. Stimulated thermal Rayleigh scattering (STRS)

Classical (spontaneous or stimulated) Rayleigh scattering, as just described, is neither the same as nor a progenitor to *(stimulated) thermal Rayleigh scattering* (STRS). It is for this reason that the preceding section qualifies Rayleigh scattering with the word "classical." "Rayleigh" in this STRS context is a misnomer. Whereas classical Rayleigh scattering arises, as noted above, from static perturbations in dielectric constant associated with local compositional and density fluctuations, stimulated thermal Rayleigh scattering arises from dynamic spatial heat fluctuations. With respect to STRS, "Rayleigh" refers by analogy to the pseudo-elastic nature of the scattering. In other words, unlike Brillouin and Raman scattering where there are clear frequency shifts between the incident (excitation) light and the scattered light, the frequency shifts in both classical Rayleigh and stimulated thermal Rayleigh scattering are very small and, essentially, negligible.

Though known and understood for 50 years [69], [70], STRS is presently receiving considerable attention due to its role manifesting *transverse mode instability* in high power rare-earth doped [70] fiber and Raman [71] lasers. Transverse mode instability (TMI) is a dynamic, thermally driven mode-hopping that arises when a grating is formed that phase-matches propagating modes of the incident and scattered light in a multimode (large mode area) optical fiber that is lasing above a given threshold power [72]–[74]. Following the quasi-closed-form formalism for TMI via STRS by *Dong* [70], the (nonlinear) coupling between modes, $g_{01}\chi_{mn}$, goes as

$$g_{01}\chi_{mn} \propto \frac{(dn/dT)}{\rho \cdot c_p}\left(\frac{\lambda_s}{\lambda_p} - 1\right) f(\Gamma_{ml}^{-1}). \qquad (1.11)$$

Here, χ is the nonlinear coupling coefficient where subscripts m and n are the azimuthal and radial mode numbers, respectively, associated with the linearly polarized (LP) modes in a cylindrical optical fiber; i.e., LP_{mn}, and g_{01} is the gain of the fundamental (lowest order, LP_{01}) mode. The other parameters involved in the first term of Eqn. 1.11 are the thermo-optic coefficient, dn/dT, density, ρ, and specific heat, c_p. The second term, $(\lambda_s/\lambda_p - 1)$, is the "quantum defect," which is proportional to the energetic difference between each pump and signal quantum and represents the amount of energy that can be converted to heat through non-radiative processes. Such "quantum defect heating," is the principal source of heat generated during the operation of lasers, both solid state [75] and optical fiber [76]. The last term in Eqn. 1.11 denotes a function of the damping factor, Γ_{ml}, which is proportional to the thermal diffusivity, D, given by $D = \kappa/\rho c_p$, where κ is the thermal conductivity.

Another parasitic effect in fiber lasers operating at high powers is photodarkening (PD) whereby the transmission of the fiber decreases with time. PD is in its own way a nonlinear effect and unquestionably parasitic in that performance of the fiber (laser) degrades with time and optical power level. Its brief mention here stems from potential correlations between photodarkening and the transverse mode instability (TMI) thresholds [77], [78]. For completeness, though, there is no "photodarkening coefficient" and so it

cannot be managed in a similar manner to the other parasitic nonlinearities treated in this dissertation.

At the near infrared wavelengths employed in the fibers considered herein, multiphoton processes associated with the active rare earth dopant can lead to charge transfer either to the host, causing color centers, or to existing defects. Accordingly, PD has been linked to the concentration of rare earth ions (Yb) in their excited state [79], defects in the silica glass [80], and the charge transfer (CT) absorption bands of the host [81]. As the present work focuses on material influences on parasitic phenomena in optical fibers, it is germane to note that the CT band is quite sensitive to the composition of the host glass [82]. In particular, the CT absorption is shifted to shorter wavelength (higher energies) in phosphosilicate glasses in comparison to aluminosilicates. This shift originates from the higher field strength associated with the P^{5+} ion (relative to the Al^{3+} ion), which results in a lower degree of covalency at the Yb-site, and, concomitantly permits low levels of photodarkening in Yb-doped phosphosilicate fibers excited at 915 nm [83].

Further, dopants into the host glass can also significantly reduce PD tendencies by serving as either a reducing agent to annihilate hole-related color centers or as a redox couple for trapping both holes and electrons. Such dopants include hydrogen [84], cerium [85], and Group II compounds [86]. For more thorough discussions of photodarkening, the Reader is referred to [87], [88].

I. B. 11. Material influences on transverse mode instabilities (TMI)

As noted above, there are a number of possible contributing factors to transverse mode instability (TMI), which is presently the major hurdle to continued scaling to higher output powers at high beam quality ($M^2 < \sim 1.3$) in fiber-based high energy lasers.

Thermally induced modulations of the refractive index associated with STRS seem clearly to be a dominant source of modal instabilities (mode coupling) in 'effectively single mode' fiber lasers. Materially, the thermal nonlinearities associated with the *Dong* formalism expect that the TMI threshold is proportional to $\rho \cdot c_p/(dn/dT)$ [70]. Additionally, the damping factor is proportional to the thermal conductivity and inversely so with heat capacity and density; though the dependencies of threshold and damping factor on heat capacity and density are different and so these factors do not cancel out. Of the factors that influence STRS, the thermo-optic coefficient, dn/dT, seems to be the best to target materially. As one example, then, a material with dn/dT = 0 would obviate STRS. Noted briefly here, but discussed in more detail in Chapter IV, combining materials with positive (SiO_2, GeO_2, Al_2O_3) and negative (P_2O_5, B_2O_3) thermo-optic coefficients can give rise to a significant reduction in dn/dT, and possibly even yield a value of zero. This is analogous to the approach for obtaining $p_{12} = 0$ "Zero Brillouin Activity" (ZeBrA) glasses for mitigating SBS.

Though not related to TMI, per se, the thermo-optic coefficient plays a major role in another parasitic effect at high optical powers: thermal lensing [89]. As the fiber heats

up, the thermal gradient across the fiber can create, through the thermo-optic coefficient, an index gradient that can be competitive with the nominal refractive index profile [90]. At sufficiently high temperatures where thermal lensing becomes problematic, other materials-related thermal effects need also to be taken into account including melting and thermal fracture of the fiber [90][91].

I. B. 12. n_2-related effects

For a given composition, temperature, and pressure, the refractive index is also dependent on the intensity of the light propagating through it. This fundamentally originates from the nonlinear response of the dielectric polarizability, P, and generally is given in the form

$$P = \epsilon_o\left(\chi \mathrm{E} + \chi^{(2)}\mathrm{E}^2 + \chi^{(3)}\mathrm{E}^3 \ldots\right), \qquad (1.12)$$

where ε_o is the permittivity of free space (≈ 8.854 pF/m), $\chi^{(i)}$ is the i^{th} dielectric susceptibility, and E is the (applied) electric field. This is fundamentally different from the previous discussions relating to the thermodynamics of scattering. For the case treated here, the E represents the electric field of the light. Since the refractive index, n, is proportional to P/E, the expansion given in Eqn. 1.12 is generically recast as

$$n = n_o + n_1 E + n_2 \mathrm{E}^2 \ldots, \qquad (1.13)$$

where n_o is the nominal (E = 0 or, for all practical purposes, low field) refractive index, n_1 is the second order nonlinear index ($n_1 \propto \chi^{(2)}$ and is most often referred to as *d*), and n_2 is

the third order nonlinearity ($n_2 \propto \chi^{(3)}$) and is more commonly described for glasses as the nonlinear refractive index. The linear dependence of n on E, through *d*, is called the *linear electro-optic* or *Pockels effect* and is named for Friedrich Pockels (same Pockels whose elasto-optic coefficients were discussed above with respect to Brillouin scattering), who first described the effect [92]. The quadratic dependence of n on E, through n_2, is called the *quadratic electro-optic* or *Kerr effect* and is named for John Kerr [93], [94]. For reasons of symmetry, the isotropy of glass negates the existence of even-order susceptibilities; e.g., $\chi^{(2)} \equiv 0$ [12], [25], though this condition can be relaxed if the optical fiber is stressed. Therefore, second-order susceptibility ($\chi^{(2)}$) vanishes for material systems possessing inversion symmetry, such as in amorphous materials including glasses [25]. Further, terms larger than $\chi^{(3)}$ typically are neglected given their inherently weak magnitudes. Accordingly, for the purposes here, Eqn. 1.13 reduces to $n = n_o + n_{2,E}E^2$, which, given the proportionality between E^2 and for the optical intensity, I, one arrives at $n = n_o + n_{2,I}I$. For completeness, the relationship between n_2 and $\chi^{(3)}$ is given as follows, depending upon whether one is considering electric field strengths ($n_{2,E}$) or intensities ($n_{2,I}$) [16]:

$$\text{Electric Field: } n_{2,E} = \frac{3}{8n_o} Re\left[\chi^{(3)}\right] \quad (1.14a)$$

$$\text{Intensity: } n_{2,I} = \frac{3}{4\epsilon_o c n_o^2} Re\left[\chi^{(3)}\right], \quad (1.14b)$$

where "Re" denotes the real part of the complex susceptibility, $\chi^{(3)}$. While this paper will only discuss those nonlinearities most relevant at high optical powers, it is worth noting that $\chi^{(3)}$-related nonlinear processes typically broaden and modify the optical spectrum, and

are especially undesirable in high peak power (pulsed) laser systems and high bandwidth multiplexed communication systems.

In continuous wave (CW) high power fiber lasers, the nonlinear refractive index manifests several parasitic effects. Four-wave mixing (FWM) is amongst the strongest of the parametric wave-mixing nonlinearities and involves the creation of two (new) photons of frequency ω_1 and ω_2 simultaneously from the annihilation of two pump photons of frequency ω_3 and ω_4. The process is elastic and, as such, the phase matching conditions are met only when $\omega_1 + \omega_2 = \omega_3 + \omega_4$. In the degenerate case where $\omega_1 = \omega_2$, only one pump frequency is required. In the non-generate case where $\omega_1 \neq \omega_2$, FWM requires another signal, such as strong amplified spontaneous emission (ASE) or Raman scattering [95]. FWM also is present in telecommunication systems, particularly those employing high degrees of multiplexing in order to enhance bandwidths [96]. The parametric FWM gain is proportional to n_2.

In pulsed fiber laser systems, nonlinear self-focusing (NSF) can be problematic [97]. In this case, the Kerr effect creates a transverse index gradient that acts as a lens leading to beam collapse and damage. In addition to NSF, self-phase modulation (SPM) can lead to both spectral and temporal modifications to laser pulses at high energies; particularly, then, in mode-locked systems. In SPM, the time-varying intensity profile associated with the laser pulse creates a time varying phase contribution through the optical Kerr effect. This induced phase modulation then generates new frequency components to

the pulse which broadens its spectrum. As the pulses propagate along the fiber undergoing SPM, the output spectrum is then dependent not only then on the initial input spectrum but also on the group velocity dispersion (GVD) of the fibers itself. As with FWM, the strength of the SPM signal is proportional to n_2.

Lastly, while stimulated processes typically have a greater parasitic impact, even light from spontaneous scattering can generate noise and seed other nonlinearities such as Rayleigh scattering seeding an efficient Raman fiber laser [98], [99]. For a more thorough yet concise treatment of nonlinear effects in optical fibers, the Reader is referred to [100].

I. B. 13. Material influences on n_2-related effects

For a given fiber design (e.g., refractive index profile, modal effective area, length), the suppression of these nonlinearities materially all require a reduction in n_2. In practice, though, the n_2 value for silica, which is the dominant glass constituent in telecomm and high power laser fibers, is already relatively very low. Indeed, much of the effort spent on compositional tailoring of n_2 has focused on increasing n_2 values relative to silica; not decreasing them [101], [102]. That said, fluorine- (i.e., F:SiO_2 [103]) and phosphate-doping [104] are known to possess reduced n_2 values relative to silica. In the former case, the lower polarizability of fluorine, in comparison to oxygen, is the expected source of reduced n_2 values [105]. In the latter, the higher formal charge of the phosphorus, relative to the silicon, is thought to promote a more covalent bond to the oxygen thus reducing its

polarizability and yielding n_2 values that are up to about 30% lower than pure SiO_2. Accordingly, fluorophosphates exhibit amongst the lowest n_2 values for laser glasses [104].

As discussed briefly above, and will be in more detail in Chapter IV, silicate compositions modified with alkali- and / or alkali-earth oxides and fluorides will be useful for reductions to scattering (Brillouin, Raman, and Rayleigh) as well as to the thermo-optic response. These species, however, tend to promote non-bridging oxygen formation in silicate glasses, which tend to be more polarizable and increase n_2 values over those of more fully networked structures. That said, for a given system, the specific choice of modifier is important since, for example, Ba^{2+} (from BaO) would possess a weaker bond than Sr^{2+} (from SrO) owing to its larger ionic size. This is indeed seen in a comparison of n_2 values for otherwise identical laser glasses where SrO is replaced by BaO and the n_2 value is found the increase as a result [104]. The replacement of the smaller ions (e.g., Li, Na, and Mg) by the larger potassium ions was similarly found to increase n_2 values in alkali- and alkaline-earth silicate glasses [106]. In these families, however, the specific alkali- or alkaline earth ion did not make substantive changes to n_2 values, relative to silica, as long as it was one of the lighter species.

To be discussed in more detail in the following Chapter, there are a number of models that have been proposed for the estimation of n_2. These often are based either on semi-classical Lorentz-Lorenz / Clausius–Mossotti oscillator models [104], [107]–[109] or quantum mechanical models [110], [111]. Given the focus here on identifying material

trends that lead to reduced optical nonlinearities, the former approach is the more convenient as linear refractive index values are employed to estimate n_2. As a general guide, n_2 increases with increasing linear refractive index, n, and the Abbe number, ν [107]. For the purposes here, this suggests that glasses exhibiting lower index and dispersion values are preferred. Assuming conventional glass composition / property additivity [112], this generalized trend in n_2 with *n* and ν, multicomponent (silicate) glasses with low electronic polarizability compounds, such as alkali- and alkali-earth fluorides [104], [105] could balance out components that otherwise raise n_2 values relative to SiO_2, such as La_2O_3 [113] or GeO_2 [103]. With respect to the most common (dielectric) silica fiber compositions and designs, such as those employed for telecommunication applications, n_2 values range from 2.2×10^{-20} m^2/W for conventional single mode fiber (SMF) to about 2.3 – 2.4×10^{-20} m^2/W for dispersion compensating fiber (DCF) to about 2.4 – 2.7×10^{-20} m^2/W for dispersion shifted fiber (DSF) [114].

Lastly, it is worth noting that the Raman gain coefficient, RGC, is proportional to the non-instantaneous (delayed) part of $\chi^{(3)}$ as [115]

$$RGC = \frac{4\pi\omega_o}{cn_o} Im\left[\chi^{(3)}\right], \qquad (1.15)$$

where "Im" denotes the imaginary part of the complex susceptibility, $\chi^{(3)}$. Accordingly, low n_2 materials should not only reduce FWM and SPM, among other nonlinear wave-mixing phenomena, but they should further aid in SRS mitigation. Conversely, perhaps, the reduced Raman scattering associated with a more disordered glass, facilitated by rapid

quenching during the fiber drawing process for example, may also reduce effective n_2 values.

Table I.1 provides a summary of the phenomena that limit the optical power capacity of optical fibers along with the material properties / coefficients that mediate the interactions. As observed, some effects share properties and trends and, of those properties, some are more heavily dependent (e.g., the Brillouin gain coefficient is proportional to n^7 versus p_{12}^2); though this is not shown in Table I.1 More importantly, however, some properties do not change much with composition and others can take on a value of zero; as noted. The impact of these trends with specific compositions and compositional families is discussed in Chapter IV.

As observed in Table I.1, some effects have material parameters in common. Table I.2, then, condenses Table I.1 down to the most fundamental factors. It is quite remarkable, though perhaps not truly surprising, that all of these parameters are ultimately defined in terms of only a handful of material coefficients and their derivatives with selected extensive variables, e.g., pressure and temperature.

Table I.1. Material origins of optical nonlinearities and property trends to reduce their impact.

Nonlinearity and Mediating Material Property	Trend to Reduce Scattering	Condition to Negate
Brillouin scattering		
Refractive index, n	↓	$p_{12} = 0$
Adiabatic compressibility, K_s	↓	
Density, ρ	↓↑ [b]	
Acoustic wave velocity, v_L and v_T	↑	
Transverse photoelastic coefficient, p_{12}	small	
Brillouin linewidth[a], $\Delta\nu_B$	↑	
Raman scattering		
Molar volume, V_m (molar mass / density)	↓	$\Lambda = 0$[c]
Bond compressibility parameter, Λ	low	
(Classical) Rayleigh scattering		
Density-related Rayleigh scattering		
Refractive index, n	↓	$p = 0$
Photoelastic coefficient, p	↓	
Adiabatic compressibility, K_s	↓	
Fictive temperature, T_f	↓	
Concentration-related Rayleigh scattering		
Spinodal temperature, T_s	$T_s << T_g$	$\partial\mu/\partial c = 0$[c]
Average molecular weight, M	↓	
Density, ρ	↓	
Chemical potential, μ (or change with composition, c; $\partial\mu/\partial c$)	small	
Transverse Mode Instability		
Thermo-optic coefficient, dn/dT	small	$dn/dT = 0$
Density, ρ	↑	
Heat capacity, c_p	↑	
Thermal conductivity, κ	↑	
n_2-related wave mixing		
Refractive index, n	↓	$n_2 = 0$[c]
Nonlinear refractive index, n_2	↓	

[a]: Denotes a parameter specific to the case of stimulated scattering.

[b]: The adiabatic compressibility is proportional to density which, for reduced spontaneous Brillouin scattering (SpBS), one wants to lessen. However, for stimulated Brillouin scattering (SBS), the density is inversely proportional to the Brillouin gain coefficient, BGC, and, accordingly, one desires a higher density.

[c]: Though potential to zero this property theoretically exists its practicality is uncertain. For example, the bond compressibility parameter, Λ, that relates to Raman scattering can take on either positive or negative values suggesting the possibility of a composition where $\Lambda = 0$. However, the nature of the bonding necessary for this condition seems very unlikely to be realized.

Table I.2. Core intrinsic[a] material parameters influencing optical nonlinearities.

Material Parameter	Definition or Determination	Core Intrinsic Material Parameters
Refractive index, n	$n^* = n + n_2 I$	n^* and its pressure and temperature derivatives (along with ρ for p and Λ)
Nonlinear refractive index, n_2		
Thermo-optic coefficient, dn/dT	dn/dT	
Photoelastic coefficient	$p = \rho \cdot \partial / \partial \rho \, (-1/n^2)$	
Bond compressibility parameter, $\boldsymbol{\Lambda}$	$\Lambda \rightarrow \rho \cdot dn/d\rho = (1-\Lambda) \cdot \rho \cdot \partial n / \partial \rho$	
Density, $\boldsymbol{\rho}$	ρ	ρ, M or their quotient
Molecular weight, M	M	
Molar volume, V_m	$V_m = M / \rho$	
Acoustic wave velocity, v_L and v_T	$v = (c/\rho)^{1/2}$	ρ and appropriate elastic stiffnesses, c_{ij}
Adiabatic compressibility, K_s	$K_s = (c_{11} - 4c_{44}/3)^{-1}$	
Heat capacity, c_p	c_p	c_p
Thermal conductivity, κ	$\boldsymbol{\kappa}$	$\boldsymbol{\kappa}$

[a]: Fictive temperature, T_f, Spinodal temperature, T_s, Chemical potential, μ (or change with composition, c; $\partial\mu/\partial c$) are left out as not being intrinsic material parameters, per se. The Brillouin linewidth, $\Delta\nu_B$ is left out because it only factors into stimulated, not spontaneous, Brillouin scattering.

I. C. Conclusion

Described herein has been a partially didactic review of the thermodynamics of optical scattering based on perturbations to the dielectric constant associated with localized fluctuations in pressure, entropy, composition, and displacement. These respectively manifest spontaneous Brillouin (pressure), Raman (displacement), and Rayleigh (entropy and composition) scattering. In addition to these better known scattering phenomena, also considered were the origins of thermally stimulated Rayleigh scattering (STRS), which is thought to be central to transverse mode instabilities (TMI) in "effectively single mode," but intrinsically multimode, large mode area (LMA) optical fibers. Effects arising from the nonlinear refractive index, n_2, also were discussed. Above a threshold optical power, each begets stimulated processes that are parasitic and collectively constitute practical limits to the scaling to higher powers / energies in a variety of optical fiber-based telecommunication and directed energy laser systems.

More importantly, this Chapter identified and discussed the material factors that drive each phenomena based on the belief that the only true approach to mitigating nonlinearities in optical fibers is to attack them at their origin; the material through which the light is propagating and, therefore, with which it is fundamentally interacting. Consequently, the material properties relating to Brillouin scattering, Raman scattering, Rayleigh scattering, thermally-stimulated Rayleigh scattering, and n_2-related effects were

identified along with general trends that would lead to their diminution and, in some cases, potential eradication.

The following Chapters (II, and III) treat macro-scale additivity models that have been developed to compute or predict the material properties and gain coefficients for the nonlinearities discussed herein. With these models in hand, Chapter IV then uses the foundations of this Chapter, along with the models from the Chapters II and III, coupled with existing results from the literature to define a series of practical glass families for use in high power and high energy fiber optic systems.

I. D. References

[1] A. R. Chraplyvy, “Limitations on Lightwave Communications Imposed by Optical-Fiber Nonlinearities,” *J. Light. Technol.*, vol. 8, no. 10, pp. 1548–1557, 1990.

[2] R. H. Stolen, “The early years of fiber nonlinear optics,” *J. Light. Technol.*, vol. 26, no. 9, pp. 1021–1031, 2008.

[3] J. Schroeder, R. Mohr, P. B. Macedo, and C. J. Montrose, “Rayleigh and Brillouin Scattering in K_2O-SiO_2 Glasses,” *J. Am. Ceram. Soc.*, vol. 56, no. 10, pp. 510–514, 1973.

[4] J. Schroeder, “Light scattering of glass,” in *Treatise on Materials Science & Technology, Vol. 12*, M. Tomozawa and M. Doremus, Eds. New York: Academic Press, 1977, pp. 157–222.

[5] M. E. Lines, “Scattering losses in optic fiber materials. I. A new parametrization,” *J. Appl. Phys.*, vol. 55, no. 11, pp. 4052–4057, 1984.

[6] M. E. Lines, “Scattering losses in optic fiber materials. II. Numerical estimates,” *J. Appl. Phys.*, vol. 55, no. 11, pp. 4058–4063, 1984.

[7] M. E. Lines, “A possible non-halide route to ultralow loss glasses,” *J. Non. Cryst. Solids*, vol. 103, no. 2–3, pp. 279–288, 1988.

[8] D. A. Pinnow, T. C. Rich, F. W. Ostermayer, and M. Didomenico, “Fundamental optical attenuation limits in the liquid and glassy state with application to fiber optical waveguide materials,” *Appl. Phys. Lett.*, vol. 22, no. 10, pp. 527–529, 1973.

[9] J. Schroeder, R. Mohr, C. J. Montrose, and P. B. Macedo, “Light scattering in a number of optical grade glasses,” *J. Non. Cryst. Solids*, vol. 13, no. 2, pp. 313–320, 1974.

[10] L. Brillouin, “Diffusion de la lumière et des rayons X par un corps transparent homogène. Influence de l’agitation thermique,” *Ann. Phys. (Paris).*, vol. 9, no. 17, pp. 88–122, 1922.

[11] J. C. Maxwell, *Theory of heat*. London: Longmans, 1871.

[12] J. F. Nye, *Physical Properties of Crystals*. Oxford University Press, 1957.

[13] G. W. Faris, L. E. Jusinski, and a. P. Hickman, “High-resolution stimulated Brillouin gain spectroscopy in glasses and crystals,” *J. Opt. Soc. Am. B*, vol. 10, no. 4, p. 587, 1993.

[14] R. Y. Chiao, C. H. Townes, and B. P. Stoicheff, “Stimulated brillouin scattering and coherent generation of intense hypersonic waves,” *Phys. Rev. Lett.*, vol. 12, no. 21, pp. 592–595, 1964.

[15] E. P. Ippen and R. H. Stolen, “Stimulated Brillouin scattering in optical fibers,” *Appl. Phys. Lett.*, vol. 21, no. 11, pp. 539–541, 1972.

[16] G. P. Agrawal, *Nonlinear Fiber Optics*, 2nd ed. Academic Press, 1995.

[17] N. A. Olsson and J. P. Van Der Ziel, “Cancellation of fiber loss by semiconductor laser pumped Brillouin amplification at 1.5 ??m,” *Appl. Phys. Lett.*, vol. 48, no. 20, pp. 1329–1330, 1986.

[18] R. G. Smith, “Optical Power Handling Capacity of Low Loss Optical Fibers as Determined by Stimulated Raman and Brillouin Scattering,” *Appl. Opt.*, vol. 11,

no. 11, pp. 2489–2494, 1972.

[19] M. D. Mermelstein *et al.*, "11.2 dB SBS gain suppression in a large mode area Yb-doped optical fiber," in *Fiber Lasers V: Technology, Systems, and Applications.*, 2008, p. 68730N.

[20] A. Kobyakov, M. Sauer, and D. Chowdhury, "Stimulated Brillouin scattering in optical fibers," *Adv. Opt. Photon.*, vol. 2, no. 1, pp. 1–59, 2010.

[21] P. Dragic and J. Ballato, "Pockels' coefficients of alumina in aluminosilicate optical fiber," *J. Opt. Soc. Am.*, vol. 30, no. 2, pp. 244–250, 2013.

[22] K. Nassau, J. W. Shiever, and J. T. Krause, "Preparation and Properties of Fused Silica Containing Alumina," *J. Am. Ceram. Soc.*, vol. 58, no. 9–10, pp. 461–461, 1975.

[23] P. Dragic and J. Ballato, "Rethinking Optical Fiber: New Demands, Old Glasses," *J. Am. Ceram. Soc.*, vol. 96, no. 9, pp. 2675–2692, 2013.

[24] C. V. Raman, "A new radiation," *Proc. Indian Acad. Sci. - Sect. A*, vol. 37, no. 3, pp. 333–341, 1953.

[25] R. W. Boyd, *Nonlinear Optics*, 3rd ed. Academic Press, 2008.

[26] E. J. Woodbury and W. K. Ng, "Ruby Laser Operation in the Near IR," in *IRE*, 1962, pp. 2347–2348.

[27] R. Hellwarth, "Theory of Stimulated Raman Scattering," *Physical Review*, vol. 130, no. 5. pp. 1850–1852, 1963.

[28] E. Garmire, F. Pandarese, and C. H. Townes, "Coherently driven molecular vibrations and light modulation," *Phys. Rev. Lett.*, vol. 11, no. 4, pp. 160–163,

1963.

[29] N. Bloembergen and Y. R. Shen, “Coupling between vibrations and light waves in Raman laser media,” *Phys. Rev. Lett.*, vol. 12, no. 18, pp. 504–507, 1964.

[30] Y. R. Shen and N. Bloembergen, “Theory of stimulated brillouin and raman scattering,” *Phys. Rev.*, vol. 137, no. 6A, 1965.

[31] M. N. Islam, “Raman amplifiers for telecommunications,” *IEEE J. Sel. Top. Quantum Electron.*, vol. 8, no. 3, pp. 548–559, 2002.

[32] R. H. Stolen, “Raman Fiber Lasers and Amplifiers,” in *Frontiers in Optics, OSA Technical Digest*, 2015.

[33] X. Zang, B. F. Jorgensen, F. Ebskamp, and R. J. Pedersen, “Input power limits and maximum capacity in long-haul WDM lightwave systems due to stimulated Raman scattering,” *Opt. Commun.*, vol. 107, pp. 358–360, 1994.

[34] J. M. Fini *et al.*, “Distributed suppression of stimulated Raman scattering in an Yb-doped filter-fiber amplifier,” *Opt. Lett.*, vol. 31, no. 17, p. 2550, 2006.

[35] F. L. Galeener, J. C. Mikkelsen, R. H. Geils, and W. J. Mosby, “The relative Raman cross sections of vitreous SiO_2, GeO_2, B_2O_3, and P_2O_5,” *Appl. Phys. Lett.*, vol. 32, no. 1, pp. 34–36, 1978.

[36] P. Dragic and J. Ballato, “Characterization of the Raman gain spectra in Yb:YAG-derived optical fibers,” *Electron. Lett.*, vol. 49, no. 14, pp. 895–897, 2013.

[37] N. Bloembergen, “The Stimulated Raman Effect,” *Am. J. Phys.*, vol. 35, no. 11, pp. 989–1023, 1967.

[38] F. R. S. Rayleigh, “On the transmission of light through an atmosphere containing

small particles in suspension, and on the origin of the blue of the sky," *London, Edinburgh, Dublin Philos. Mag. J. Sci.*, vol. 47, no. 287, 1899.

[39] D. B. Keck and A. R. Tynes, "Spectral response of low-loss optical waveguides," *Appl. Opt.*, vol. 11, no. 7, pp. 1502–1506, 1972.

[40] D. B. Keck, R. D. Maurer, and P. C. Schultz, "On the ultimate lower limit of attenuation in glass optical waveguides," *Appl. Phys. Lett.*, vol. 22, no. 7, pp. 307–309, 1973.

[41] M. Horiguchi and H. Osanai, "Spectral losses of low-OH-content optical fibres," *Electron. Lett.*, vol. 12, no. 12, p. 310, 1976.

[42] N. L. Laberge, P. K. Gupta, V. Vasilescu, and P. B. Macedo, "Scattering losses in binary borate glasses," *J. Non. Cryst. Solids*, vol. 13, pp. 164–172.

[43] N. L. Laberge, V. V. Vasilescu, C. J. Montrose, and P. B. Macedo, "Equilibrium Compressibilities and Density Fluctuations in K_2O-SiO_2 Glasses," *J. Am. Ceram. Soc.*, vol. 56, no. 10, pp. 506–509, 1973.

[44] N. Laberge, P. Gupta, and P. Macedo, "Density fluctuations in silicate glasses," *J. Non. Cryst. Solids*, vol. 17, pp. 61–70, 1975.

[45] D. A. Pinnow, L. G. Van Uitert, T. C. Rich, F. W. Ostermayer, and H. W. Grodkiewicz, "Investigation of the soda aluminosilicate glass system for application to fiber optical waveguides," *Mater. Res. Bull.*, vol. 10, no. 2, pp. 133–146, 1975.

[46] K. Shiraki and M. Ohashi, "Optical properties of sodium aluminosilicate glass," *J. Non. Cryst. Solids*, vol. 149, pp. 243–248, 1992.

[47] S. Todoroki and S. Sakaguchi, “Alkali Magnesium/Zinc Silicate Glasses with Low Rayleigh Scattering,” *J. Am. Ceram. Soc.*, vol. 78, no. 9, pp. 2566–2568, 1995.

[48] S. Sakaguchi and S. Todoroki, “Sodium magnesium silicate oxyfluoride glass with low Rayleigh scattering,” *J. Ceram. Soc. Japan*, vol. 104, no. 9, pp. 808–811, 1996.

[49] S. I. Todoroki and S. Sakaguchi, “Effect of F-doping on optical and thermal properties of soda magnesium silicate glasses for ultralow-loss fibers,” *Japanese J. Appl. Physics, Part 1 Regul. Pap. Short Notes Rev. Pap.*, vol. 35, no. 10, pp. 5374–5378, 1996.

[50] S. Sakaguchi and S. Todoroki, “Optical Properties of Na_2O – MgO – SiO_2 Optical Fiber,” *Opt. Fiber Technol.*, vol. 4, pp. 328–337, 1998.

[51] K. Tsujikawa and M. Ohashi, “Rayleigh Scattering in K_2O–MgO–SiO_2 and Na_2O–B_2O_3–SiO_2 Glasses,” *Opt. Fiber Technol.*, vol. 6, no. 1, pp. 74–82, 2000.

[52] K. Tsujikawa and M. Ohashi, “Mixed-alkali effect on Rayleigh scattering in K_2O–Na_2O–MgO–SiO_2,” *J. Am. Ceram. Soc.*, vol. 83, no. 3, pp. 660–662, 2000.

[53] M. N. Zervas and R. I. Laming, “Rayleigh Scattering Effect on the Gain Efficiency and Noise of Erbium-Doped Fiber Amplifiers,” *IEEE J. Quantum Electron.*, vol. 31, no. 3, pp. 468–471, 1995.

[54] P. B. Hansen *et al.*, “Rayleigh scattering limitations in distributed Raman pre-amplifiers,” *IEEE Photonics Technol. Lett.*, vol. 10, no. 1, pp. 159–161, 1998.

[55] M. Cardona, D. Rönnow, and P. V Santos, “Ellipsometric investigations of piezo-optical effects,” *Thin Solid Films*, vol. 313–314, pp. 10–17, 1998.

[56] C. Huang and A. N. Cormack, “Structural differences and phase separation in alkali silicate glasses,” *J. Chem. Phys.*, vol. 95, no. 5, pp. 3634–3642, 1991.

[57] H. Melman and S. H. Garofalini, “Microstructural evaluation of simulated sodium silicate glasses,” *J. Non. Cryst. Solids*, vol. 134, no. 1–2, pp. 107–115, 1991.

[58] L. D. Landau and E. M. Lifshitz, *Statistical Physics*, 2nd ed. Addison-Wesley Publishing Co, 1969.

[59] D. I. Mash, V. V. Morozov, V. S. Starunov, and I. L. Fabelinskii, “Stimulated Scattering of Light of the Rayleigh-line Wing,” *Sov J Exp Theor Phys Lett.*, vol. 2, pp. 25–27, 1965.

[60] B. Champagnon, C. Chemarin, E. Duval, and R. Le Parc, “Glass structure and light scattering,” *J. Non. Cryst. Solids*, vol. 274, no. 1, pp. 81–86, 2000.

[61] K. Tsujikawa, M. Ohashi, K. Shiraki, and M. Tateda, “Effect of thermal treatment on Rayleigh scattering in silica-based glasses,” *Electron. Lett.*, vol. 31, no. 22, pp. 1940–1941, 1995.

[62] K. Tajima, “Low-loss optical fibers realized by reduction of Rayleigh scattering loss,” *OFC’98 Tech. Dig.*, vol. 4, pp. 305–306, 1998.

[63] S. Sakaguchi and S. Todoroki, “Rayleigh Scattering of Silica Core Optical Fiber After Heat Treatment,” *Appl. Opt.*, vol. 37, no. 33, pp. 7708–7711, 1998.

[64] K. Saito, M. Yamaguchi, H. Kakiuchida, A. J. Ikushima, K. Ohsono, and Y. Kurosawa, “Limit of the Rayleigh scattering loss in silica fiber,” *Appl. Phys. Lett.*, vol. 83, no. 25, pp. 5175–5177, 2003.

[65] P. Dragic, T. Hawkins, P. Foy, S. Morris, and J. Ballato, “Sapphire-derived all-

glass optical fibres," *Nat. Photonics*, vol. 6, no. 9, pp. 629–635, 2012.

[66] J. Ballato and P. Dragic, "On the Clustering of Rare Earth Dopants in Fiber Lasers," *J. Dir. Energy*, vol. 6, pp. 175–181, 2017.

[67] A. R. Tynes, A. D. Pearson, and W. R. Northover, "Rayleigh Scattering Losses in Soda Borosilicate Glasses," *J. Am. Ceram. Soc.*, vol. 62, no. 7–8, pp. 324–326, 1979.

[68] G. W. Morey, *The Properties of Glass*. New York: Reinhold, 1954.

[69] R. M. Herman and M. A. Gray, "Theoretical prediction of the stimulated thermal rayleigh scattering in liquids," *Phys. Rev. Lett.*, vol. 19, no. 15, pp. 824–828, 1967.

[70] L. Dong, "Stimulated thermal Rayleigh scattering in optical fibers," *Opt. Express*, vol. 21, no. 3, pp. 915–918, 2013.

[71] S. Naderi, I. Dajani, J. Grosek, and T. Madden, "Theoretical and numerical treatment of modal instability in high-power core and cladding-pumped Raman fiber amplifiers," in *Proceedings of the SPIE 9344, Fiber Lasers XII: Technology, Systems, and Applications*, 2015, vol. 9344.

[72] C. Jauregui, J. Limpert, and A. Tünnermann, "High-power fibre lasers," *Nat. Photonics*, vol. 7, no. 11, pp. 861–867, 2013.

[73] T. Eidam *et al.*, "Experimental observations of the threshold-like onset of mode instabilities in high power fiber amplifiers," *Opt. Express*, vol. 19, no. 14, p. 13218, 2011.

[74] A. V. Smith and J. J. Smith, "Mode instability in high power fiber amplifiers.," *Opt. Express*, vol. 19, no. 11, pp. 10180–10192, 2011.

[75] T. Y. Fan, “Heat generation in Nd:YAG and Yb:YAG,” *IEEE J. Quantum Electron.*, vol. 29, no. 6, pp. 1457–1459, 1993.

[76] T. Yao, J. Ji, and J. Nilsson, “Ultra-low quantum-defect heating in ytterbium-doped aluminosilicate fibers,” *J. Light. Technol.*, vol. 32, no. 3, pp. 429–433, 2014.

[77] H.-J. Otto, N. Modsching, C. Jauregui, J. Limpert, and A. Tünnermann, “Impact of photodarkening on the mode instability threshold,” *Opt. Express*, vol. 23, no. 12, pp. 15265–15277, 2015.

[78] C. Jauregui, H.-J. Otto, F. Stutzki, J. Limpert, and A. Tünnermann, “Simplified modelling the mode instability threshold of high power fiber amplifiers in the presence of photodarkening,” *Opt. Express*, vol. 23, no. 16, p. 20203, 2015.

[79] J. Koponen, M. Söderlund, H. J. Hoffman, D. Kliner, and J. Koplow, “Photodarkening measurements in large mode area fibers,” *Proc. SPIE*, vol. 6453, p. 64531E–64531E–11, 2007.

[80] P. D. Dragic, C. G. Carlson, and A. Croteau, “Characterization of defect luminescence in Yb doped silica fibers: part I NBOHC.,” *Opt. Express*, vol. 16, no. 7, pp. 4688–4697, 2008.

[81] M. Engholm and L. Norin, “The role of charge transfer processes for the induced optical losses in ytterbium doped fiber lasers,” in *Proc. of SPIE Vol.7195*, 2009, no. February, p. 71950T–1–71950T–8.

[82] R. Tao, P. Ma, X. Wang, P. Zhou, and Z. Liu, “Study of wavelength dependence of mode instability based on a semi-analytical model,” *IEEE J. Quantum Electron.*, vol. 51, no. 8, 2015.

[83] M. Engholm and L. Norin, “Preventing photodarkening in ytterbium-doped high power fiber lasers; correlation to the UV-transparency of the core glass.,” *Opt. Express*, vol. 16, no. 2, pp. 1260–1268, 2008.

[84] M. Engholm and L. Norin, “Reduction of photodarkening in Yb/Al-doped fiber lasers,” *Proceeding SPIE*, vol. 6873, p. 68731E–68731E–8, 2008.

[85] M. Engholm, P. Jelger, F. Laurell, and L. Norin, “Improved photodarkening resistivity in ytterbium-doped fiber lasers by cerium codoping.,” *Opt. Lett.*, vol. 34, no. 8, pp. 1285–1287, 2009.

[86] Y. Sakaguchi, Y. Fujimoto, N. Miyanaga, and H. Nakano, “Laser oscillation in low photo-darkening Yb-doped silica glass fiber by co-doping of group-2 element,” in *CLEO SM3Q*, 2016, pp. 975–976.

[87] S. Taccheo *et al.*, “Photodarkening in Yb-doped Al-silicate fibers: Investigation, modelling and mitigation,” in *International Conference on Transparent Optical Networks*, 2014.

[88] C. Ye, L. Petit, J. J. Koponen, I.-N. Hu, and A. Galvanauskas, “Short-Term and Long-Term Stability in Ytterbium-Doped High-Power Fiber Lasers and Amplifiers,” *IEEE J. Sel. Top. Quantum Electron.*, vol. 20, no. 5, 2014.

[89] L. Dong, “Thermal lensing in optical fibers,” *Opt. Express*, vol. 24, no. 17, pp. 19841–19852, 2016.

[90] J. W. Dawson *et al.*, “Analysis of the scalability of diffraction-limited fiber lasers and amplifiers to high average power.,” *Opt. Express*, vol. 16, no. 17, pp. 13240–13266, 2008.

[91] David C. Brown, “Thermal, Stress, and Thermo-Optic Effects in High Average Power Double-Clad Silica Fiber Lasers,” *IEEE J. Quantum Electron.*, vol. 37, no. 2, pp. 207–217, 2001.

[92] F. C. A. Pockels, *Lehrbuch der kristalloptik*. Leipzig: BG Teubner, 1906.

[93] J. Kerr, “A new relation between electricity and light: Dielectrified media birefringent,” *London, Edinburgh, Dublin Philos. Mag. J. Sci.*, vol. 50, no. 332, pp. 337–348, 1875.

[94] J. Kerr, “A new relation between electricity and light: Dielectrified media birefringent,” *London, Edinburgh, Dublin Philos. Mag. J. Sci.*, vol. 50, no. 332, pp. 446–458, 1875.

[95] X. Zhou, M. Birk, and S. Woodward, “Pump-noise induced FWM effect and its reduction in a distributed Raman fiber amplifier,” *IEEE Photonics Technol. Lett.*, vol. 14, no. 12, pp. 1686–1688, 2002.

[96] B. Goebel, B. Fesl, L. D. Coelho, and N. Hanik, “On the Effect of FWM in Coherent Optical OFDM Systems,” *Opt. Fiber Commun. Fiber Opt. Eng. Conf. 2008. OFC/NFOEC 2008. Conf.*, no. 3, pp. 1–3, 2008.

[97] M.-Y. Cheng, Y.-C. Chang, A. Galvanauskas, P. Mamidipudi, R. Changkakoti, and P. Gatchell, “High-energy and high-peak-power nanosecond pulse generation with beam quality control in 200-um core highly multimode Yb-doped fiber amplifiers,” *Opt. Lett.*, vol. 30, no. 4, p. 358, 2005.

[98] H. Zhang, P. Zhou, H. Xiao, and X. Xu, “Efficient Raman fiber laser based on random Rayleigh distributed feedback with record high power,” *Laser Phys. Lett.*,

vol. 11, p. 75104, 2014.

[99] X. Du *et al.*, “Kilowatt-level fiber amplifier with spectral-broadening-free property, seeded by a random fiber laser,” *Opt. Lett.*, vol. 40, no. 22, p. 5311, 2015.

[100] L. Dong and B. Samson, *Fiber Lasers: Basics, Technology, and Applications*. Boca Raton: CRC Press, 2017.

[101] W. H. Kim *et al.*, “Recent progress in chalcogenide fiber technology at NRL,” *J. Non. Cryst. Solids*, vol. 431, pp. 8–15, 2016.

[102] G. Tao *et al.*, “Infrared Fibers,” *Adv. Opt. Photonics*, vol. 7, pp. 379–458, 2015.

[103] K. Nakajima and M. Ohashi, “Dopant dependence of effective nonlinear refractive index in GeO_2- and F-doped core single-mode fibers,” *IEEE Photonics Technol. Lett.*, vol. 14, no. 4, pp. 492–494, 2002.

[104] R. Adair, L. L. Chase, and S. a. Payne, “Nonlinear refractive-index measurements of glasses using three-wave frequency mixing,” *J. Opt. Soc. Am. B*, vol. 4, no. 6, p. 875, 1987.

[105] J. R. Tessman, A. H. Kahn, and W. Shockley, “Electronic polarizabilities of ions in Crystals,” *Phys. Rev.*, vol. 92, no. 4, pp. 890–895, 1953.

[106] M. Grehn *et al.*, “Nonlinear absorption and refraction of binary and ternary alkaline and alkaline earth silicate glasses,” *Opt. Mater. Express*, vol. 3, no. 12, p. 2132, 2013.

[107] N. Boling, A. Glass, and A. Owyoung, “Empirical relationships for predicting nonlinear refractive index change in optical solids,” *IEEE J. Quantum Electron.*,

vol. 14, no. 8, pp. 601–608, 1978.

[108] M. Weber, D. Milam, and W. Smith, “Nonlinear refractive index of glasses and crystals,” *Opt. Eng.*, vol. 17, no. 5, pp. 463–469, 1978.

[109] C. C. Wang, “Empirical relation between the linear and the third-order nonlinear optical susceptibilities,” *Phys. Rev. B*, vol. 2, no. 6, pp. 2045–2048, 1970.

[110] P. W. Langhoff, S. T. Epstein, and M. Karplus, “Aspects of time-dependent perturbation theory,” *Rev. Mod. Phys.*, vol. 44, no. 3, pp. 602–644, 1972.

[111] J. Fournier and E. Snitzer, “The nonlinear refractive index of glass,” *IEEE J. Quantum Electron.*, vol. 10, no. 5, pp. 473–475, 1974.

[112] P. D. Dragic and J. Ballato, “120 Years of Optical Glass Science: From the law of mixtures to mixing the unmixable,” *Opt. Photonics News*, no. May, pp. 44–51, 2014.

[113] C. Karras, D. Litzkendorf, S. Grimm, K. Schuster, W. Paa, and H. Stafast, “Nonlinear refractive index study on SiO_2-Al_2O_3-La_2O_3 glasses,” *Opt. Mater. Express*, vol. 4, no. 10, pp. 2066–2077, 2014.

[114] A. Boskovic, S. V. Chernikov, J. R. Taylor, L. Gruner-Nielsen, and O. A. Levring, “Direct continuous-wave measurement of n2 in various types of telecommunication fiber at 1.55 μm,” *Opt. Lett.*, vol. 21, no. 24, pp. 1966–1968, 1996.

[115] F. a. Oguama, H. Garcia, and A. M. Johnson, “Simultaneous measurement of the Raman gain coefficient and the nonlinear refractive index of optical fibers: theory and experiment,” *J. Opt. Soc. Am. B*, vol. 22, no. 2, p. 426, 2005.

CHAPTER II.

DETERMINATION OF FIRST-ORDER MATERIALS PROPERTY ADDITIVITY IN MUTICOMPONENT SILICATE GLASSES

II. A. Introduction

Without today's understanding of atomistic and quantum physics and chemistry and the benefits of modern high-performance computing, our scientific ancestors developed continuum models for predicting the behavior of a range of materials. Amongst the original approaches was that of Adolph Winkelmann, who introduced an additivity approach for calculating the specific heat of (oxide) glasses of arbitrary composition based on the physical properties of the individual components [1]. Following this pioneering work, many glass scientists have participated in the development of additive models to predict "classical" glass properties (e.g., density, refractive index, coefficient of thermal expansion). For more insights regarding these contributing works, the book by *M. B. Volf, "Mathematical approach to glass"* [2] is recommended, which is dedicated to the various additive models developed over the past centuries in predicting the aforementioned properties.

That said, one does today have the benefit of high performance computing and numerous atomistic and quantum chemical models and codes with which to simulate the performance of glasses [3]–[5]. As a matter of fact, the simulation of glass properties and

processing has become so effective, that glasses have been brought to commercial markets entirely designed and optimized based on modeling [6]. Accordingly, the Readers are then within their rights to wonder why continuum-level additivity models as described herein are employed. The simple answer is simplicity… and speed and versatility. In the work described in Chapter IV, there are entire binary, ternary, and quaternary glass systems whose properties need to be estimated in order to predict their physical, acoustic, and optical behavior as relates to the nonlinearities described in Chapter I. A macro-scale continuum approach offers a rapid yet sufficiently accurate method for screening large computational spaces.

More specifically, the materials modeling described herein is not intended to provide specific insights into glass structure or chemistry. Its principal purposes are to (i) enable sufficiently accurate extrapolation of data measured on a few fibers to a broader range of compositions in that glass family, (ii) help quickly identify precursor core phases that will yield fibers of the desired properties, (iii) provide a simplified tool to present the enabling materials science to fiber designers (who are, at best, amateur glass scientists), and (iv) after fiber fabrication, provide guidance for further compositional optimization.

II. B. Material property additivity

The additivity models utilized here treat the constituent species comprising the glass as (a) separable and fully independent of each other and (b) individually well-mixed with no heterogeneities, such as phase separation or crystallization; see Fig. II.1 for a representative schematic. Put another way, the models predict ensemble averages. A case in point is that of alumina in an aluminosilicate glass where properties as a general function of alumina content, [Al_2O_3], are deduced even though the aluminum in Al_2O_3 is known to exist in multiple coordination environments [7], [8]. Further, reactive species, such as Al_2O_3 and P_2O_5, which can form $AlPO_4$, an index-lowering compound relative to SiO_2 [9], are treated as the single final reactant.

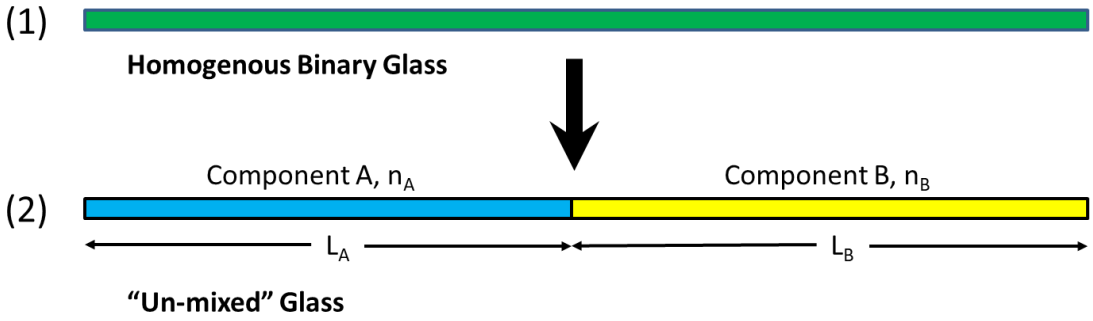

Figure II.1. (1) A schematic representation of a homogeneous multicomponent bulk binary glass. (2) Aggregate glass separated into its two constituents. If the entire starting length ($L_A + L_B$) is a normalized unit length, then each L value represents the fractional volume of that component.

As such, and as noted above, this averaging removes direct physical insight into the glass structure and chemistry, but reflects the power of these additivity models as effective tools for the straight-forward property deduction over large compositional spaces. Therefore, they are useful for the rapid identification of compositions and compositional ranges for designer optical fibers with specific performance attributes, such as the intrinsically low nonlinearities considered in this dissertation.

Beginning with a simple binary system where m is the fractional volume[2] of component A and, therefore, (m – 1) is the fractional volume of component B, one can compute the time-of-flight for light to propagate through this 'un-mixed' glass segment. If said piece of glass is defined as being of unit length and its constituents separated into independent volumes (i.e., lengths in a one-dimensional approximation) that are proportional to their concentrations, then the time, t, taken for the light to traverse the glass is

$$t = \frac{mn_A}{c} + \frac{(1-m)n_B}{c}, \qquad (2.1)$$

where c is the speed of light in vacuum. Given the unit length of this representative binary glass, the time given in Eqn. 2.1 is equivalent to an inverse velocity of light. As such, the numerator in Eqn. 2.1 is the linear refractive index of the aggregate glass, $n_{binary} = mn_A +$

[2] Fractional volume is employed here since it is the refractive index that is being used as an example, which is a volumetric material property. Where additivity in mole fraction is more appropriate, such as in the section on *Debye Temperature and Specific Heat*, this will be specified.

(1-m)n_B. As will be discussed further later, to first order, mixed effects such as thermo-optic, stress-optic, and optical Kerr effect-related nonlinearities can be parametrically included.

The (dimensionless) fractional volume, m, of component A can be determined from the known composition along with the mass density, ρ, and molar mass, M, of the two components (A and B). For a binary system, this is given as [10]

$$m_A = \frac{\frac{M_A}{\rho_A}[C_A]}{\frac{M_A}{\rho_A}[C_A] + \frac{M_B}{\rho_B}[C_B]}, \qquad (2.2)$$

where $[C_A]$ is the concentration of the component A (in mole fraction or percent). The ratio M/ρ is the molar volume, which can depend on the glass thermal history. While the refractive index is the logical place to begin when considering optical materials, the additivity approach may be generalized to other material properties. In its most basic form, the additivity models follow the governing equation

$$G = \sum_{i=1}^{N} g_i x_i. \qquad (2.3)$$

Here, x is the additivity parameter of component i (in this case fractional volume), g_i is the physical property of component i, and G is the aggregate property value of the glass. Provided below are examples for the additivity of the optical, acoustic, and thermal properties required to model the performance of fibers designed to materially mitigate the optical nonlinearities described in Chapter I. Additional details can also be found in [11].

II. C. Basic material properties

II. C. 1. Refractive index

The refractive index is the central optical property of a material and enters into nearly all considerations of its linear and nonlinear performance. As noted in [12], a power of the additivity model can be seen in its remarkable resemblance to the often-used Sellmeier model for a mixed system. The Sellmeier model, which can be directly derived from the physics of the macroscopic refractive index, is given for a unary material by [13], [14]

$$n^2 - 1 = \sum_{i=1}^{N} \frac{A_i \lambda^2}{\lambda^2 - \lambda_i^2}. \qquad (2.4)$$

Here n is the refractive index at (free space) wavelength λ, N is the number of oscillators used to fit the refractive index data (typically 3 as in [13] or 4 as in [14]; this is often referred to as the "term" of the Sellmeier fit; i.e., a 3-term Sellmeier), A_i and λ_i, are the oscillator strength and its resonant wavelength, respectively. The binary form of Eqn. 2.4 can be found in [13] where additivity in the mole fraction is usually employed.

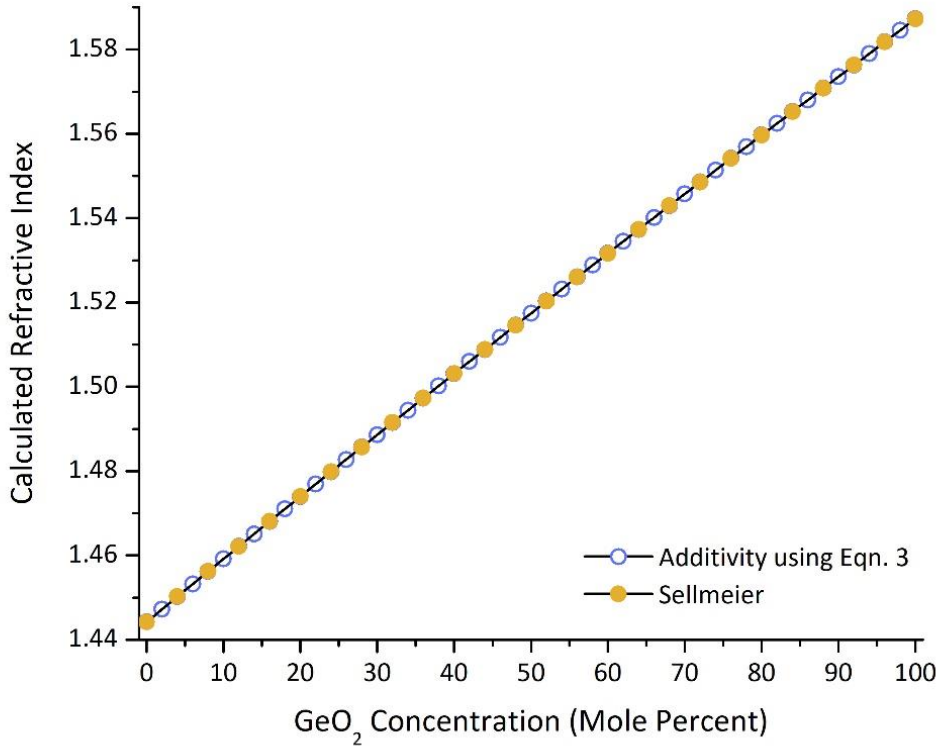

Figure II.2. Comparison of the refractive index for a SiO_2 – GeO_2 binary glass calculated using the conventional Sellmeier model and the additivity model described herein. Data for the Sellmeier model are taken from [13] whereas data for the additivity model are noted in the text.

As an illustrative example of the simplicity and power of the additivity model, consider the comparison provided in Fig. II.2. Plotted there is the refractive index of the SiO_2 – GeO_2 binary system as calculated using the additivity model and the Sellmeier model (data taken from [13]). The data used for the additivity model results are the mass densities (2200 kg/m^3 for SiO_2 and 3650 kg/m^3 for GeO_2), molar masses (60.08 g/mole for

SiO_2 and 104.59 g/mole for GeO_2), and end-member refractive index values (1.4442 for SiO_2 and 1.5873 for GeO_2 taken for a wavelength of 1534 nm). The index values between the two models differ only in the 5th decimal place.

II. C. 2. Thermo-optic coefficient (TOC, dn/dT)

The refractive index as a function of temperature in a linear regime may be expressed simply as $n(T) = n_0 + \frac{dn}{dT}(T - T_0)$ where the subscript '0' refers to some starting temperature (T_0) such as room temperature. This expression may be substituted into Eqn. 2.1 to arrive at the following simple expression for the additivity of the thermo-optic coefficient (TOC) in a binary material:

$$\frac{dn}{dT} = \frac{\mathrm{m}}{\mathrm{c}}\frac{dn_A}{dT} + \frac{(1-\mathrm{m})}{\mathrm{c}}\frac{dn_B}{dT}. \qquad (2.5)$$

Generally, for a multicomponent glass, Eqn. 2.5 may be used with $g_i \rightarrow dn_i/dT$.

II. C. 3. Acoustic velocity

The acoustic velocity can be estimated using a similar time-of-flight consideration for an acoustic phonon as the refractive index was calculated using a photon. In this case, both the aggregate acoustic velocity, V_a, and the total acoustic attenuation, α, through the unit fiber can be deduced [10], [15]. The determination of the acoustic attenuation is of interest to this work since multiplying it by (V_a/π) yields the Brillouin spectral width, $\Delta\nu_B$,

which will be used later to compute the Brillouin gain coefficient, BGC. For an n-component glass, these quantities are given by

$$V_a = \left(\sum_{i=1}^{n} \frac{m_i - m_{i-1}}{V_{a,i}}\right)^{-1} \qquad (2.6)$$

$$\Delta\nu_B = \frac{V_a}{\pi}\sum_{i=1}^{n}(m_i - m_{i-1})\, F_i(\nu). \qquad (2.7)$$

The factor $F_i(\nu)$ in Eqn. 2.7 typically is given by $F_i = (\nu/\nu_{ref})^2\alpha_i$, where α_i are the phonon damping coefficient(s) (m^{-1}) of the oxide constituent(s), which are proportional to the square of the acoustic frequency [16]. For completeness, however, it is worth noting that this relationship generally holds for glasses, such as silica, where the maximum viscoelastic damping occurs far below the glass transition temperature, T_g [17]. For glasses such as those doped with B_2O_3, where the dynamic viscoelastic damping processes peak at temperatures above T_g, the acoustic attenuation is not proportional to ν^2 [18]. Further, since there is dispersion in the acoustic attenuation ($\alpha=\alpha(\nu)$), α_i should be specified at some reference frequency, ν_{ref}. For ease, a convenient reference frequency is 11 GHz, which corresponds to the Brillouin scattering frequency of standard single mode telecommunications fiber, when measured at a wavelength of 1534 nm [10]. In summary, since ν and therefore α (at a fixed optical wavelength) change with composition, $F_i(\nu)$ takes this into consideration by scaling the α_i reference values accordingly.

II. C. 4. Photoelastic coefficients

As shown and discussed in Chapter I, the Pockels photoelastic coefficient, p_{12}, factors into both Brillouin scattering and into the contribution of density fluctuations to Rayleigh scattering. In order to deduce the p_{12} coefficients, consider the axial (z-axis) elongation of a fiber due to an applied strain, ε_z. The transverse electric field components of the propagating (assume x-polarized) optical mode will experience a concomitantly modified refractive index, n_x, given by

$$n_x(\epsilon) = n_{0,x} - \frac{1}{2}\epsilon_z n_{0,x}^3[p_{12} - \nu(p_{11} + p_{12})], \qquad (2.8)$$

where ν is Poisson's ratio and the subscript '0' corresponds to the nominal (unstrained) value [19]. This equation is also valid for strain applied in the transverse (y) direction also perpendicular to the optical polarization. If a transverse strain is applied to the fiber in the direction of polarization (ε_x), Eqn. 2.8 becomes [20]

$$n_x(\epsilon) = n_{0,x} - \frac{1}{2}\epsilon_x n_{0,x}^3[p_{11} - 2\nu p_{12}]. \qquad (2.9)$$

With these in hand, and assuming that the photoelastic constants can be parametrically included into the additivity model through the refractive index, then deduction of the photoelastic coefficients are simplified using the transverse (i.e., strain transverse to polarization direction, ε_z) strain-optic coefficient (εOC), which is defined as $\varepsilon OC = p_{12} - \nu(p_{11} + p_{12})$ and the parallel (i.e., strain parallel to the polarization direction, ε_x) stress-optic coefficient (σOC), which is defined here as $\sigma OC = p_{11} - 2\nu p_{12}$. These definitions are

selected to disambiguate these values from the usual stress optic coefficient, C, which is related to $p_{44} = (p_{11} - p_{12})/2$ for an isotropic material, by $C = -\frac{n^3}{2c_{44}} p_{44}$. [21]

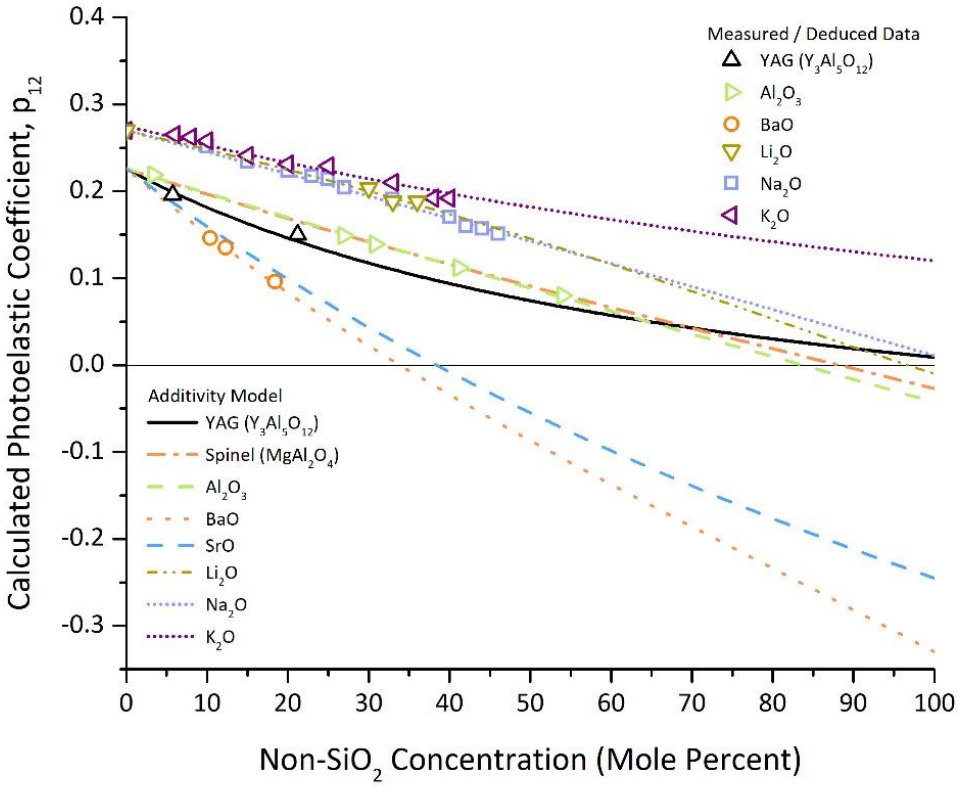

Figure II.3. Comparison of the calculated and measured / deduced Pockels p_{12} photoelastic coefficient as a function of non-silica content for selected fibers deduced using the additivity approach described in the text. Because of the acoustic anti-guiding nature of the spinel-derived optical fiber, the p_{12} photoelasticity for MgO, taken from [22], was employed in the additivity model.

Accordingly, then, for a mixed binary glass of Components A and B, the two effective strain-optic coefficients are

$$\epsilon OC_{eff} = \frac{1}{n_0^3}[mn_A^3(\epsilon OC_A) + (1-m)n_B^3(\epsilon OC_B)], \quad (2.10)$$

$$\sigma OC_{eff} = \frac{1}{n_0^3}[mn_A^3(\sigma OC_A) + (1-m)n_B^3(\sigma OC_B)] \quad (2.11)$$

where n_0 is the zero-strain refractive index of the binary glass and, as above, m is the fractional volume of Component A. Given the transverse and parallel strain-optic components, the p_{12} photoelastic constant for the aggregate glass is [20]

$$p_{12} = \frac{(\epsilon OC_{eff}) + \nu(\sigma OC_{eff})}{(1-2\nu)(1+\nu)}. \quad (2.12)$$

Fig. II.3 provides the calculated p_{12} photoelastic coefficient as a function of additive into silica for a number of crystal-derived all-glass optical fibers [23]–[28], along with corresponding measured data. For the cases of BaO, Al_2O_3, and YAG, the additive model was fit to fiber-based measurements and values of p_{12} for the non-silica additive were subsequently determined. The calculation in Fig. II.3 provides an extrapolation to points beyond compositions available for characterization, which should be taken with caution as any structural changes to the glass outside the available compositional range will cause the fittings to break down. In the available compositional ranges, and in all cases, the fittings are found to be very good. For the alkali metal oxides, the model was fit to bulk data found in [29], which is also reproduced in Fig. II.3. In the case of spinel-derived fiber, its acoustically anti-guiding behavior precluded the determination of p_{12} directly, so the value for MgO found in [22] (p_{12} = -0.07) was instead used in the modeling. Finally, in the case

of SrO, its p_{12} was deduced from a ternary glass (strontium aluminosilicate) and that value was utilized in the modeling of the binary system.

II. C. 5. Coefficient of thermal expansion (CTE)

In general, thermal effects in fiber-based lasers are known to induce a variety of performance-modifying phenomena [30]. While the coefficient of thermal expansion (CTE) does not directly influence the optical nonlinearities that are the focus of this dissertation, it does influence the effective thermo-optic coefficient, as first suggested by Prod'homme [31], which is believed to induce transverse mode instabilities (TMI). Additionally, differential thermal expansion between the core and cladding (or cladding and coating) can lead to polarization effects [32], increased transmission losses [33], and phase shifts, the latter causing jitter in transmission systems and noise in interferometric sensors [34]. It is worth noting that, in addition to differential thermal expansion, thermal stresses also can be generated from differences in core/clad viscosity [35]. Core/clad CTE mismatches can also lead to some novel and useful phenomena not present in bulk glasses, such as temperature independent (athermal) and strain independent (atensic) Brillouin frequency shifts [27], [36], [37].

Many empirical models have been developed regarding the additivity of the coefficient of thermal expansion in glasses [38]–[42]. Recently, using additivity of density in glasses governed by Eqn. 2.3, an additive model for CTE in binary silicate glasses was

developed based on a derivation of the volume expansion in isotropic solids such as glass [43]. The expression of CTE takes the following form

$$CTE = \sum_i \frac{CTE_i \rho_i y_i}{\rho} \qquad (2.13)$$

Here, CTE_i and ρ_i are the coefficient of thermal expansion and the density for each individual constituent of the glass, respectively, whereas y_i is defined as the volume fraction per structural unit for each glass compound. The density of the glass ρ can be calculated from Eqn. 2.3. As shown in Fig. II.4, Eqn. 2.13 fits the data extremely well, not just when considering the addition of ubiquitous glass formers in silica (Fig. II.4a), but also for some other dopants such as the alkaline earth family (Fig II.4.b) [44]–[49]. For completeness, it is noted that a proper additivity relationship needs to be rooted in some physical basis. For example, linear fits to the data in Fig. II.4 would likely lead to acceptably good fits over a certain range, but would have no physical meaning. The time-of-flight approach and volume additivity for the refractive index (Fig. II.2), and this CTE additivity (Fig. II.4) based on the additivity of density both have their origins in the nature of the systems which they are modeling.

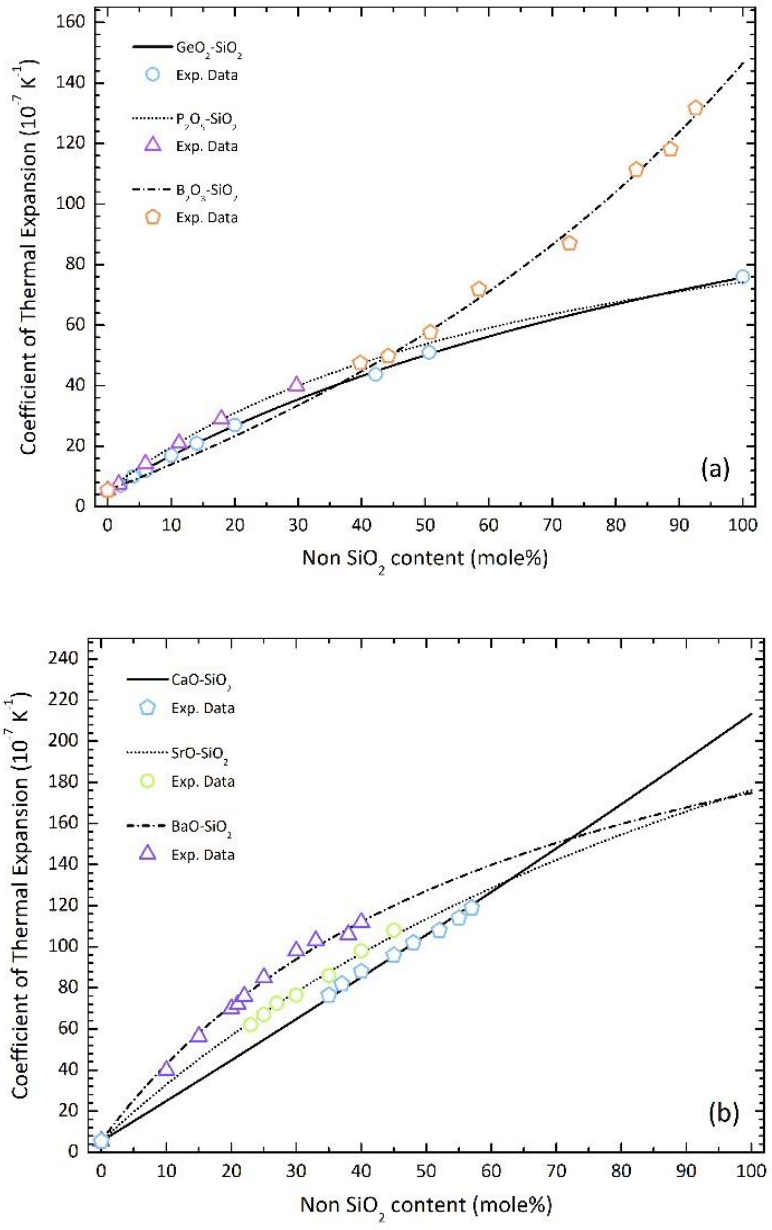

Figure II.4. Evolution of the coefficient of thermal expansion (CTE) for some binary silicate systems using Eqn. 2.13: a) Binary silicate systems with canonical telecom dopants (i.e., GeO_2-SiO_2, P_2O_5-SiO_2, B_2O_3-SiO_2), with data taken from [45]–[49]; b) Binary alkaline earth silicate system (CaO-SiO_2, SrO-SiO_2, BaO-SiO_2), data from [44], [47], [50].

II. C. 6. Specific heat and Debye temperature

The specific heat was shown in Chapter I to factor into both stimulated thermal Rayleigh scattering, which facilitates transverse mode instabilities (TMI), and the density-related component of (classical) Rayleigh scattering. Accordingly, its estimation through simple additivity relationships is of practical value. Consequently, it is convenient first to estimate the Debye temperature, Θ_D [51], which arises in the consideration of the specific heats of elastic solids and provides a quantitative estimate demarcating classical (Dulong-Petit [52]) and quantum regimes. The Debye temperature can also be informative as to the thermal conductivity of a solid [53], which also factors into TMI through STRS per the *Dong* formalism [54]. For a single component, linearly-elastic solid, Θ_D is given by [55]

$$\Theta_D = \left(\frac{h}{k}\right) \cdot V \cdot \sqrt[3]{\frac{3qN\rho}{4\pi M}}, \qquad (2.14)$$

where h is Planck's constant, k is Boltzmann's constant, q is the number of atoms in the molecule, ρ is mass density, N is Avogadro's number, and M is molecular mass. V is the average acoustic wave speed given by $V = \sqrt[2]{C/\rho}$, where C average elastic stiffness. For glasses comprised of a mixture of components, Eqn. 2.14 is modified as follows:

$$\Theta_D = \left(\frac{h}{k}\right) \cdot V \cdot \sqrt[3]{\frac{3\langle q\rangle N\langle\rho\rangle}{4\pi\langle M\rangle}}, \qquad (2.15)$$

where $\langle q\rangle = \Sigma_i f_i^{(mol)} \cdot q_i$, $\langle\rho\rangle = \Sigma_i f_i^{(mol)} \cdot \rho_i$, and $\langle M\rangle = \Sigma_i f_i^{(mol)} \cdot M_i$, $f_i^{(mol)}$ being the mole fraction of the i^{th} component. It is worth noting that this averaging uses the molar fractions, $f_i^{(mol)}$, whereas the previous additivity modeling generally employed volume fractions. The

molar specific heat capacity, c_V, of the glass at a given temperature then can be determined from knowledge of the Debye temperature using the well-known relationship:

$$c_v \approx 9N_A k \left(\frac{T}{\Theta_D}\right)^3 \int_0^{\Theta_D/T} \frac{x^4 \cdot e^x}{(e^x-1)^2} dx. \quad (2.16)$$

The Debye temperature for silica is about 365 K in the range from 70 K to 370 K [56]. Accordingly, one is neither in the $c_v \propto (T/\Theta_D)^3$ quantum nor $C_v/(3 \cdot N_A \cdot k) \approx 1$ Dulong-Petit regimes. Tabulated values of the Debye integral are, however, readily available.

II. D. Conclusion

Provided herein is a compilation of simple additivity models for the deduction of the material properties of multicomponent silicate glasses, central to optical nonlinearities, from the properties of amorphous or crystalline end-member compounds. More specifically, additivity as relates to the refractive index, density, acoustic velocity, photoelasticity, stress- and strain-optic coefficients, thermal expansion coefficients, and thermo-optic coefficients, Debye temperature, and specific heat are discussed and examples provided. In general, over reasonable glass forming ranges in which the glass is presumed to remain compositionally uniform, homogeneous, and structurally similar, the models are found to be sufficiently accurate in order to guide the materials development of optical fibers that exhibit reduced optical nonlinearities. Use of these material properties to model the nonlinear coefficients will be provided in the following Chapter.

II. E. References

[1] A. Winkelmann, “Ueber die specifischen Warmen verschieden zusammengesetzter Glaser,” *Ann. der Phys. und Chemie*, vol. 49, pp. 401–420, 1893.

[2] M. B. Volf, *Mathematical approach to glass*, vol. Glass Scie. New York: Elsevier Science Ltd, 1989.

[3] A. Pedone, “Properties calculations of silica-based glasses by atomistic simulations techniques: A review,” *Journal of Physical Chemistry C*, vol. 113, no. 49. pp. 20773–20784, 2009.

[4] W. Kob, “Computer simulations of supercooled liquids and glasses,” *J. Phys. Condens. Matter*, vol. 11, no. 10, pp. R85–R115, 1999.

[5] S. H. Garofalini, “Molecular Dynamics Simulations of Silicate Glasses and Glass Surfaces,” *Rev. Mineral. Geochemistry*, vol. 42, no. 1, pp. 131–168, Jan. 2001.

[6] J. C. Mauro, A. Tandia, K. D. Vargheese, Y. Z. Mauro, and M. M. Smedskjaer, “Accelerating the Design of Functional Glasses through Modeling,” *Chem. Mater.*, vol. 28, no. 12, pp. 4267–4277, 2016.

[7] P. McMillan and B. Piriou, “The structures and vibrational spectra of crystals and glasses in the silica-alumina system,” *J. Non. Cryst. Solids*, vol. 53, no. 3, pp. 279–298, 1982.

[8] J. F. Stebbins, S. Kroeker, S. Keun Lee, and T. J. Kiczenski, “Quantification of

five- and six-coordinated aluminum ions in aluminosilicate and fluoride-containing glasses by high-field, high-resolution 27Al NMR," *J. Non. Cryst. Solids*, vol. 275, no. 1, pp. 1–6, 2000.

[9] D. J. DiGiovanni, J. B. MacChesney, and T. Y. Kometani, "Structure and properties of silica containing aluminum and phosphorus near the $AlPO_4$ join," *J. Non. Cryst. Solids*, vol. 113, no. 1, pp. 58–64, 1989.

[10] P. D. Dragic, "Simplified model for effect of Ge doping on silica fibre acoustic properties," *Electron. Lett.*, vol. 45, no. 5, pp. 256–257, 2009.

[11] J. Ballato and P. Dragic, "Materials development for next generation optical fiber," *Materials (Basel).*, vol. 7, no. 6, pp. 4411–4430, 2014.

[12] P. Dragic and J. Ballato, "Rethinking Optical Fiber: New Demands, Old Glasses," *J. Am. Ceram. Soc.*, vol. 96, no. 9, pp. 2675–2692, 2013.

[13] J. W. Fleming, "Dispersion in GeO_2—SiO_2 glasses," *Appl. Opt.*, vol. 23, no. 24, pp. 4486–4493, 1984.

[14] B. Brixner, "Refractive-Index Interpolation for Fused Silica," *J. Opt. Soc. Am.*, vol. 57, no. 5, pp. 674–676, 1967.

[15] P. D. Dragic, "The Acoustic Velocity of Ge-Doped Silica Fibers: A Comparison of Two Models," *Int. J. Appl. Glas. Sci.*, vol. 1, no. 3, pp. 330–337, 2010.

[16] G. P. Agrawal, *Nonlinear Fiber Optics*, 2nd ed. Academic Press, 1995.

[17] A. S. Pine, "Brillouin Scattering Study of Acoustic Attenuation in Fused Quartz,"

Phys. Rev., vol. 185, no. 1967, p. 1187-, 1969.

[18] P.-C. Law and P. D. Dragic, "Wavelength dependence of the Brillouin spectral width of boron doped germanosilicate optical fibers.," *Opt. Express*, vol. 18, no. 18, pp. 18852–65, 2010.

[19] M. Huang, "Stress effects on the performance of optical waveguides," *Int. J. Solids Struct.*, vol. 40, no. 7, pp. 1615–1632, 2003.

[20] C. Ryan, P. Dragic, J. Furtick, C. J. Kucera, R. Stolen, and J. Ballato, "Pockels Coefficients in Multicomponent Oxide Glasses," *Int. J. Appl. Glas. Sci.*, vol. 6, no. 4, pp. 387–396, 2015.

[21] K. Matusika, C. Ihara, T. Komatsu, and R. Yokota, "Photoelastic Effects in Silicate Glasses," *J. Am. Ceram. Soc.*, vol. 67, no. 10, pp. 700–704, Oct. 1984.

[22] K. V. K. Rao and V. G. K. Murty, "Photoelastic constants of magnesium oxide," *Acta Cryst.*, vol. 17, p. 788, 1964.

[23] P. Dragic, T. Hawkins, P. Foy, S. Morris, and J. Ballato, "Sapphire-derived all-glass optical fibres," *Nat. Photonics*, vol. 6, no. 9, pp. 629–635, 2012.

[24] P. Dragic, P.-C. Law, J. Ballato, T. Hawkins, and P. Foy, "Brillouin spectroscopy of YAG-derived optical fibers.," *Opt. Express*, vol. 18, no. 10, pp. 10055–67, 2010.

[25] P. Dragic and J. Ballato, "Pockels' coefficients of alumina in aluminosilicate optical fiber," *J. Opt. Soc. Am.*, vol. 30, no. 2, pp. 244–250, 2013.

[26] A. Mangognia *et al.*, “Spinel-derived single mode optical fiber,” *Opt. Mater. Express*, vol. 3, no. 4, p. 511, 2013.

[27] P. Dragic, C. Kucera, J. Furtick, J. Guerrier, T. Hawkins, and J. Ballato, “Brillouin spectroscopy of a novel baria-doped silica glass optical fiber,” *Opt. Express*, vol. 21, no. 9, pp. 10924–10941, 2013.

[28] M. Cavillon *et al.*, “Brillouin Properties of a Novel Strontium Aluminosilicate Glass Optical Fiber,” vol. 34, no. 6, pp. 1435–1441, 2016.

[29] J. Schroeder, “Brillouin scattering and pockels coefficients in silicate glasses,” *J. Non. Cryst. Solids*, vol. 40, no. 1–3, pp. 549–566, 1980.

[30] D. C. Brown and H. J. Hoffman, “Thermal, stress, and thermo-optic effects in high average power double-clad silica fiber lasers,” *IEEE J. Quantum Electron.*, vol. 37, no. 2, pp. 207–217, 2001.

[31] L. Prod’homme, “A new approach to the thermal change in the refractive index of glasses,” *Phys. Chem. Glas.*, vol. 1, no. 4, pp. 119–122, 1960.

[32] I. P. Kaminow, “Polarization in Optical Fibers,” *IEEE J. Quantum Electron.*, vol. C, pp. 15–22, 1981.

[33] H.-L. Lee, “Transient microbending loss induced by thermal loading in double-coated optical fibers,” *Opt. Eng.*, vol. 42, no. 4, pp. 969–976, 2003.

[34] N. Lagakos, J. a Bucaro, and J. Jarzynski, “Temperature-induced optical phase shifts in fibers,” *Appl. Opt.*, vol. 20, no. 13, p. 2305, 1981.

[35] U. C. Paek and C. R. Kurkjian, “Calculation of Cooling Rate and Induced Stresses in Drawing of Optical Fibers,” *J. Am. Ceram. Soc.*, vol. 58, no. 7–8, pp. 330–335, 1975.

[36] P. D. Dragic *et al.*, “Single- and few-moded lithium aluminosilicate optical fiber for athermal Brillouin strain sensing.,” *Opt. Lett.*, vol. 40, no. 21, pp. 5030–3, 2015.

[37] P. D. Dragic *et al.*, “Athermal distributed Brillouin sensors utilizing all-glass optical fibers fabricated from rare earth garnets : LuAG,” *New J. Phys.*, vol. 18, no. 1, p. 15004, 2015.

[38] A. Winkelmann and O. Schott, “Ueber thermische Widerstandscoefficienten verschiedener Glaser in ihrer Abhangigkeit von der chemischen Zusammensetzung,” *Ann. der Phys. und Chemie*, vol. 51, pp. 730–746, 1894.

[39] S. English and W. E. S. Turner, “Relationship between chemical composition and the thermal expansion of glasses,” *J. Am. Ceram. Soc.*, vol. 10, no. 8, pp. 551–560, 1927.

[40] F. P. Hall, “The influence of chemical composition on the physical properties of glazes,” *J. Am. Ceram. Soc.*, vol. 13, no. 3, pp. 182–199, 1930.

[41] P. Gilard and L. Dubrul, “Le calcul du coefficient de dilatation des verres silicates,” *Verre Silic. Ind.*, vol. 5, pp. 122–125, 1934.

[42] H. Doweidar, “Thermal expansion of silicate glasses: physical basis for the

additivity relations," *Phys. Chem. Glas.*, vol. 42, no. 3, pp. 158–163, 2001.

[43] M. Cavillon, J. Ballato, and P. D. Dragic, "Additivity of the coefficient of thermal expansion in silicate optical fibers," *Opt. Lett.*, vol. 42, no. 18, pp. 3650–3653, 2017.

[44] J. E. Shelby, "Effect of morphology on the properties of alkaline earth silicate glasses," *J. Appl. Phys.*, vol. 50, no. 12, pp. 8010–8015, 1979.

[45] E. F. Riebling, "Structural Similarities Between a Glass and Its Melt," *J. Am. Ceram. Soc.*, vol. 51, no. 3, pp. 143–149, 1968.

[46] Y. Y. Huang, A. Sarkar, and P. C. Schultz, "Relationship between composition, density and refractive index for germania silica glasses," *J. Non. Cryst. Solids*, vol. 27, no. 1, pp. 29–37, 1978.

[47] N. P. Bansal and R. Doremus, *Handbook of Glass Properties*. Londond, England: Academic Press, 1986.

[48] C. A. and T. W. E. S., "Study of the Glasses Boric Oxide-Silica," *J. Soc. Glas. Technol.*, vol. 12, p. 169, 1928.

[49] P. C. Schultz, "Fused P_2O_5 Type glasses," 4042404, 1977.

[50] B. G. Varshal, E. M. Rabinovich, A. V. Levitina, and Vaisfeld N. M., "Steklovbraznye Sistemy i Novye Stekla na ikh Osnove," p. 86, 1971.

[51] P. Debye, "Zur Theorie der Anomalen Dispersion im Gebiet der Langwellen Elektrischen Strahlung," *Ber Der Dt Phys Ges.*, vol. 15, pp. 777–793, 1913.

[52] A.-T. Petit and P.-L. Dulong, “Recherches sur quelques points importants de la Théorie de la Chaleur,” *Ann. Chim. Phys.*, vol. 10, pp. 395–413, 1819.

[53] I. Pomeranchuk, “On the thermal conductivity of dielectrics,” *Phys. Rev.*, vol. 60, no. 11, pp. 820–821, 1941.

[54] L. Dong, “Stimulated thermal Rayleigh scattering in optical fibers,” *Opt. Express*, vol. 21, no. 3, pp. 915–918, 2013.

[55] O. L. Anderson, “A simplified method for calculating the debye temperature from elastic constants,” *J. Phys. Chem. Solids*, vol. 24, no. 7, pp. 909–917, 1963.

[56] M. Fukuhara, A. Sanpei, and K. Shibuki, “Low temperature-elastic moduli , Debye temperature and internal dilational and shear frictions of fused quartz,” *J. Mater. Sci.*, vol. 2, no. 5, pp. 1207–1211, 1997.

CHAPTER III.

GLASS MATERIAL ADDITIVITY OF NONLINEAR PROPERTIES IN FIBER GEOMETRY

III. A. Introduction

Chapter II focused on component additivity modeling and the determination of simple first-order materials properties of multicomponent glass. In some instances, these properties can be used in tandem to calculate more complicated nonlinear gain coefficients. For example, the Brillouin gain coefficient is a function of several of the parameters described in Chapter II. The purpose of this chapter is to review the state-of-the-art in modeling of these parameters in the optical fiber configuration (as opposed to bulk glass), and how these can then be applied to the reduction of several nonlinear gain coefficients (including the nonlinear refractive index n_2). Numerous examples are provided and methodologies to determine nonlinear optical coefficients are presented.

As in the previous Chapter, the materials modeling described herein is not intended to provide specific insights into glass structure or chemistry. Further, for several reasons, the optical fiber geometry itself also must be considered in modeling efforts. Firstly, the optical mode may overlap with regions of the fiber that possess differing compositions. Locally, this means that physical properties, such as the acoustic velocity or refractive index, may be varying across the spatial distribution of the mode. In that sense, the

measured physical properties from a fiber are those corresponding to the optical mode rather than to those of a bulk material. Secondly, the cladded fiber geometry can play a significant role when the fiber system is subject to changes in temperature and a core-cladding thermal expansion coefficient (CTE) mismatch is present. The requisite corrections to the bulk glass calculations performed in Chapter II in the fiber geometry are therefore illustrated in this work. Additionally, the direct measurements of selected properties, e.g., fictive temperature, T_f, also are described and exemplified.

III. B. Property deduction and the optical fiber

III. B. 1. Fiber design modeling

While the previous chapter focuses specifically on material property additivity models, such models are guides for the subsequent design and optimization of high performance optical fibers. The performance of the fiber depends on how the electromagnetic modes interact with the materials comprising the core and cladding. Obviously, for a fiber possessing a high numerical aperture, the modes are more tightly confined to the core and the fiber performance will be predicated more on the properties of the core glass. Accordingly, this section briefly discusses approaches for estimating the impact of the optical fiber design on its overall performance when coupled with the additivity models for material properties.

Given material transport facilitated by the high temperature processing of both the preform and the subsequent optical fiber, it is not unusual that the core possesses a graded composition in the radial direction. In such a case, all parameters deduced through measurements of the fiber necessarily are those associated with the waveguide modes, and not exclusively those of the core glass. In the limit of an acoustic or optical wave being tightly confined to the center of the core, the property values associated with the modes will approximate those of the core center material composition. However, in the weakly guiding limit, modeling of the fiber becomes more complicated because the material parameters vary across the core region, which must be taken into account when solving for mode values that best match the measured values.

Adding to the complexity, conventional fibers possess fairly small core sizes and, consequently, the composition is only known at a few locations across the core. In such cases, the core may be partitioned into sections, corresponding to the available measurements. Each layer possesses a specific composition and, therefore, properties. A schematic representation of this is shown in Fig. III.1 for a 4-layer step-wise approximation to the refractive index profile of a fictitious fiber core. Beyond the outermost core layer resides the cladding, which most often is compositionally uniform (e.g., pure silica). In this particular example, 4 regions are defined and the modes can be calculated by enforcing the appropriate electromagnetic and acoustic boundary conditions [1–3]. In short, the boundary conditions are identified at each layer interface and from them a characteristic matrix for the system is determined. The eigenmodes of this characteristic matrix give the

propagation constants for the system (acoustic and optical mode phase velocities, with the effective modal index derived from the latter). As an example, while the various layers shown in Fig. III.1 all have unique electromagnetic (EM) velocities, they come together to give rise to a single, observable EM velocity corresponding to that of the EM fundamental mode.

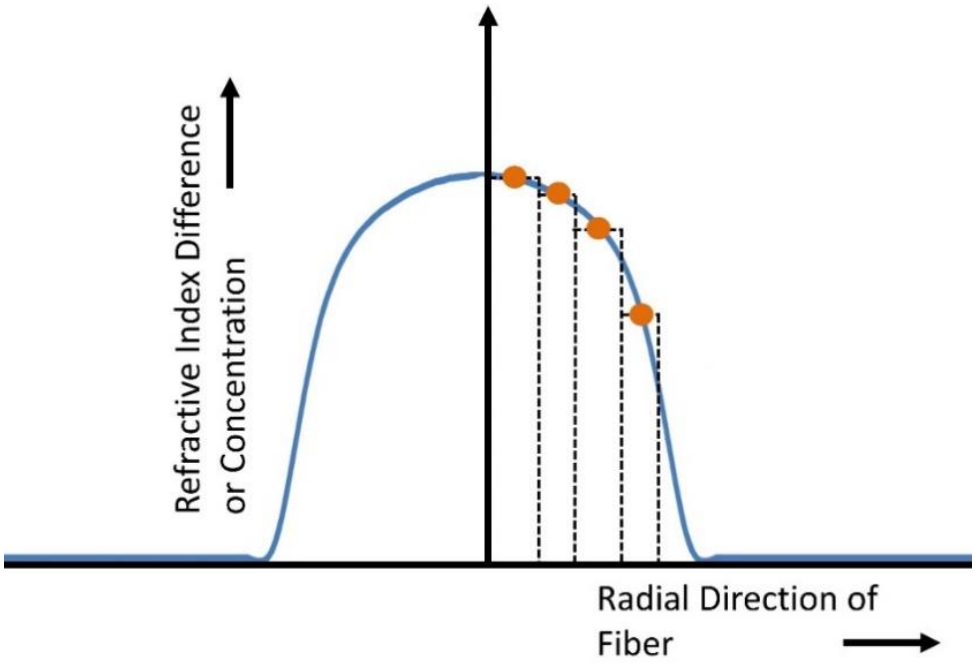

Figure III.1. If a compositional analysis of the fiber core yields only a few data points because, for example, the core size is small compared to the spot size for the elemental analysis (shown representatively as orange), the core may be partitioned into segments in order to approximate the properties of those layers. A fictitious refractive index profile is provided to illustrate a 4-layer (dashed black lines) approximation to the core. Solving for the optical mode then is then a simple boundary condition problem.

III. B. 2. Determination of optical properties (refractive index)

The refractive index of an optical fiber is the most straightforward property to characterize an optical fiber. Numerous commercial systems exist and this can even be performed as a service; e.g., [4]. Given a measurement of the composition (such as via electron probe microanalysis), the refractive index can be plotted as a function of composition. For a binary silicate system, for example, if refractive index and density values for SiO_2 are assumed, then the refractive index and density of the bulk 'dopant' (e.g. BaO) can be used as fit parameters when applying Eqn. 3.3 from Chapter II to the data. Importantly, since each layer of the approximation in Fig. III.1 can be compositionally unique, the refractive index as a function of temperature may also differ for each layer. However, this enables the calculation of the modal thermo-optic coefficient (TOC), and in the reverse direction, the determination of the TOC of said dopant(s), again utilizing the simple additivity model described in Chapter II.

III. B. 3. Determination of acoustic properties

As outlined in other publications, the acoustic properties are determined from measurements of the Brillouin gain spectrum (BGS); e.g., [5]. In short, a heterodyne process is utilized whereby a pump signal is launched into the fiber and a spontaneously Brillouin back-scattered signal is mixed with a portion of the pump signal to produce a Doppler-shifted gain spectrum. Since the acoustic wave involved in the Brillouin scattering process is Bragg-matched to the optical wave, the peak frequency obeys the relationship $\nu_B = 2n_m V_m/\lambda$ where n_m and V_m are the optical mode index and acoustic mode velocity

(P-wave), respectively, and λ is the vacuum optical wavelength. Measurement of ν_B then allows for the determination of V_m, and in a way similar to that of the refractive index and TOC, the acoustic velocity and its dependence on temperature (or strain as described next) for 'dopants' where these values are unknown, can be determined.

III. B. 4. Determination of strain-optic and stress-optic coefficients

The elasto-optic (stress and strain optic) coefficients of bulk glasses can be measured by applying stress to the glass and measuring changes in the refractive index [6–8]. When one is utilizing optical fibers, it is convenient to measure the elasto-optic coefficients on the fiber itself using a fiber ring laser-based strain sensor for the determination of the strain optic coefficient [9] and / or a twisted-fiber method for p_{44} [10,11]. Specific details are provided in [12,13] with brief generalities provided below.

With respect to the determination of the strain-optic coefficient, εOC [14], the fiber is integrated as part of a ring laser cavity which has a free spectral range (FSR) given by $FSR = c/d \cdot n$ where n is the mode refractive index and d is the cavity length. If axial strain is applied to the test fiber, both the cavity length and index will change, thus resulting in a change in the FSR. The elongated length d with the application of strain is easily measured and measurements of the changes in FSR as a function of strain reveals the dependence of the modal index on strain, and hence the fiber εOC [9]. Measurement of the thermo-optic coefficient of a fiber is achieved using the same approach, however in this case, the free-

spectral range (ΔFSR) of a laser cavity is measured by heating (or cooling) the test fiber under controlled conditions.

With respect to the determination of stress-optic coefficient, p_{44}, a mechanical twist is applied to the fiber, which rotates the (linear) polarization state of the light propagating within. Assuming that no linear birefringence is already present or otherwise induced in the twisted fiber, the resultant optical activity, α, is given by $\alpha = g\tau$, where τ is the twist rate (rad/m) and g is [9]

$$g = -\frac{n^2}{2}(p_{11} - p_{12}) = -n^2 p_{44}. \qquad (3.1)$$

Here, n is the mode index of the fiber at the wavelength being employed. Based on a measurement of polarization rotation versus the number of twists per meter, p_{44} is easily determined. Knowing εOC and p_{44} then gives a system of two equations and two unknowns (with the Poisson ratio assumed to follow from simple additivity) whereby p_{12} as seen by the mode can be determined. Once again, methodologies for determining the εOC values of dopants involving the segmented core of Fig. III.1 may be utilized. Measurements of p_{44} using twist requires that the fiber be free of birefringence. Should this condition not be satisfied, an alternative method for the determination of p_{12} requires a direct measurement of the Brillouin gain coefficient, which is proportional to p_{12}^2 (see Chapter I). Both methods were utilized to generate the plots provided in Fig. II.3 of Chapter II.

These measurements can be used to deduce p_{12} values for individual glass constituents, which in turn can be utilized in glass design efforts. As will be discussed in greater detail in the following Chapter, the compositions at which $p_{12} = 0$ are of particular interest as such glasses should exhibit no Brillouin scattering and reduced density-related Rayleigh scattering; the former implying no possibility for parasitic stimulated Brillouin scattering (SBS). Obviously, however, other practical considerations also exist, such as the glass-forming capability for these compositions and their refractive indices, which influence fiber design and fiber laser performance.

III. B. 5. Thermo-optic coefficient (TOC) additivity in the presence of thermal expansion mismatch

When the optical fiber is heated, either externally or through the laser action itself, the core will attempt to expand in accordance with its coefficient of thermal expansion (CTE). However, if the CTE of the cladding is less than that of the core, the core's thermal expansion is restricted and, therefore, the core will experience a compressive force; i.e., a negative stress. This effective compressive force is exerted on the core in all three directions. For silica, most commonly employed in optical fibers, a positive strain (fiber stretch) results in a decrease in the refractive index since the Pockels coefficients are positive. Hence pressure (compressional force) should act to increase the refractive index of SiO_2. Accordingly, if a glass additive contributes a negative thermo-optic coefficient, but also results in an increase in CTE, its negative-valued dn/dT contribution can be partly mitigated.

For a mixed oxide glass, the volume additivity of the refractive index, and of the thermo-optic coefficient, TOC, dn/dT, was described in Eqn. 2.5 of Chapter II. However, that expression must be modified to include the effect of a CTE mismatch between fiber core and cladding as well as resultant strains that are introduced. Given that strain occurs in all three directions (x, y, and z), with two perpendicular (relative to a linear optical polarization) contributions and one parallel contribution [15], the expression for the refractive index of the ith component is

$$n_i(T) = n_{0,i} + \frac{dn}{dT_i}(T - T_0) + \frac{n_{0,i}^3}{2}(\alpha_{core} - \alpha_{clad})(T - T_0)\left[2\left(p_{12,i} - \nu\left(p_{11,i} + p_{12,i}\right)\right) + \left(p_{11,i} - 2\nu_i p_{12,i}\right)\right] \qquad (3.2)$$

where α is again the linear coefficient of thermal expansion. The value for the core can be found utilizing the model present in Chapter II. It is useful to point out that when $\alpha_{core} > \alpha_{clad}$ the refractive index increases as the temperature is increased from T_0 for cases where the Pockels term is positive (such as it is for silica). This effect of differential CTE on TOC is shown in Fig. III.2 for some representative binary silicate systems. In order to convert from the normal strain relationships, the substitution $-\varepsilon_{x,y,z} \rightarrow (\alpha_{core} - \alpha_{clad})(T - T_0)$ has been made [16]. Again, the strain value is considered a stretch, but, for $\alpha_{core} > \alpha_{clad}$, the CTE mismatch results in effective compression, hence the change in sign.

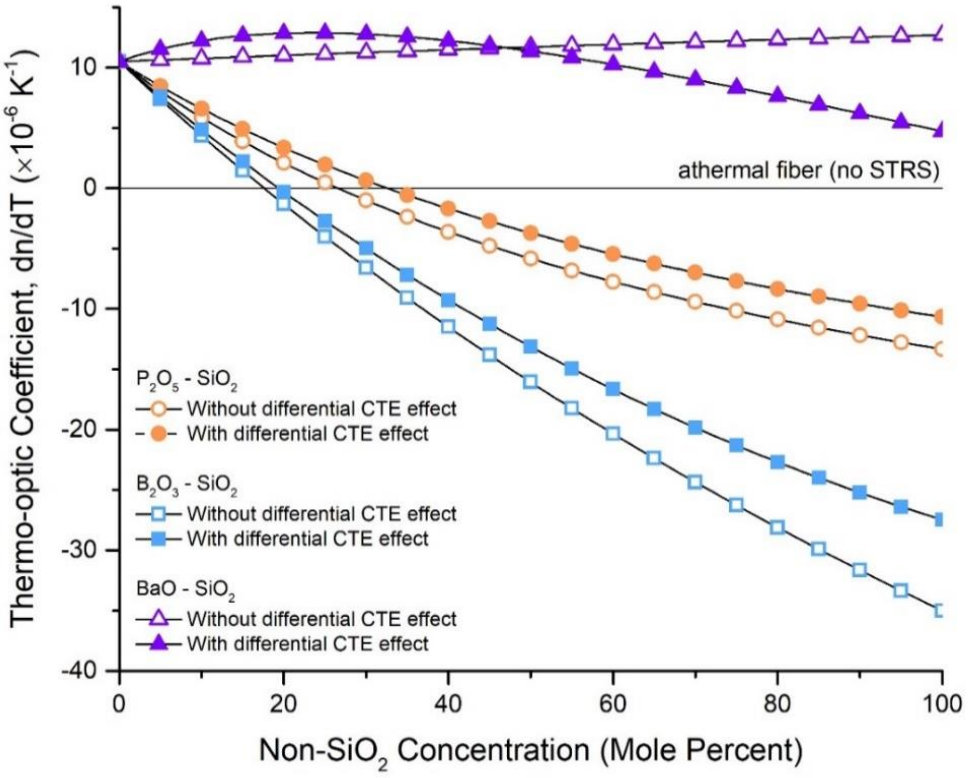

Figure III.2. Thermo-optic coefficient (TOC, dn/dT) as a function of non-SiO_2 content for SiO_2-cladded optical fibers in the P_2O_5 – SiO_2, B_2O_3 – SiO_2, and BaO – SiO_2 systems with and without taking into account differential thermal expansion between core and cladding. The dn/dT = 0 line is provided as a guide and shows those compositions where stimulated thermal Rayleigh scattering (STRS) should be negated.

Finally, the refractive index as a function of temperature can be computed (and an effective dn/dT value determined) over a given range of temperatures. It has clearly been assumed here there is a linear dependence of the refractive index on temperature over the

range of temperatures modeled [17]. A fully analogous corrected equation can be determined for the acoustic velocity [16].

III. B. 6. Fictive temperature

As noted in Chapter I, the fictive temperature, T_f, influences the density-related component of Rayleigh scattering. As such, heat treatments to facilitate relaxation of the as-formed glass have been used to reduce T_f and Rayleigh scattering losses in optical fibers [18]. Most simplistically, T_f is the *temperature* where the structure of an amorphous material is the same as that of the equilibrium liquid (molten) state. In other words, to first order, T_f represents the temperature where the non-equilibrium structure is that of the equilibrium melt. For completeness, it is worth mentioning that care should be taken in how broadly one applies the fictive temperature alone as an indicator of Raleigh scattering and other physical or scattering-related properties. Firstly, T_f is known to influence density with a monotonic proportionality [20,21], which also therefore influences refractive index [22]. Secondly, as noted by *Mauro*, et al. [23], the use of a fictive temperature representation is rigorously valid only for a glass that experienced an infinitely fast quenching from the melt such that the structure of the liquid phase was instantaneously frozen in. Even in the case of the high quench rates (> 2000 K/s) associated with the molten core method [12], used to make the majority of the fibers treated in this dissertation, it is very unlikely that this qualifies as "infinitely fast." Perhaps more importantly is that Mauro also points out that while the macroscopic view of T_f reasonably estimates state properties (e.g., enthalpy and molar volume), it does not at all accurately estimate probability

distributions at lower temperature such as fluctuations in enthalpy and volume (which do influence Rayleigh scattering) or corresponding changes in heat capacity and thermal expansion, which could influence TMI. Readers are directed to Refs. [23,24] if interested in more detailed and thoughtful discussions of the inherent inequalities between glassy and liquid states.

The fictive temperature can be estimated using methods that probe the glass structure, such as Raman [25] and infrared (IR) spectroscopies [26]. More specifically, the micro-Raman approach correlates the fictive temperature to shifts in the Si-O-Si stretching vibration at wavenumbers of about 440 cm^{-1} whereas the IR approach utilizes shifts in the Si-O-Si asymmetric stretch at wavenumbers of about 1120 cm^{-1}. An example of this latter approach is provided in Fig. III.3, which compares the peak position of the Si-O-Si asymmetric stretch in a conventional telecommunications optical fiber to a molten core-derived oxyfluoride core fiber [19]. Based on Eqn. 2 from [26], the computed T_f for the core and clad are between about 1450°C and 1670°C, corresponding to the IR peak positions of 1121 and 1119.5 cm^{-1}, respectively. These values are within the range expected for silica optical fibers [27].

For completeness, it is noted that the slope of the change in Si-O-Si peak position with fictive temperature depends on the glass' dependency of volume with T_f. Indeed, the peak shift for a soda-lime-silicate (SLS) glass was found to be opposite that for pure silica [28], which was justified based on the volume of SLS increasing with increasing T_f

whereas, for pure silica, the opposite trend is known [29]. The fictive temperature profile shown in Fig. III.3 is found to be quite uniform across the fiber cross-section. Thus, it seems reasonable to assume that the fictive temperature of the core material is about the same as the fictive temperature determined for the fused silica cladding; perhaps this is not surprising, given that they both experienced the same thermal history on drawing into fiber and that the core is mainly silica.

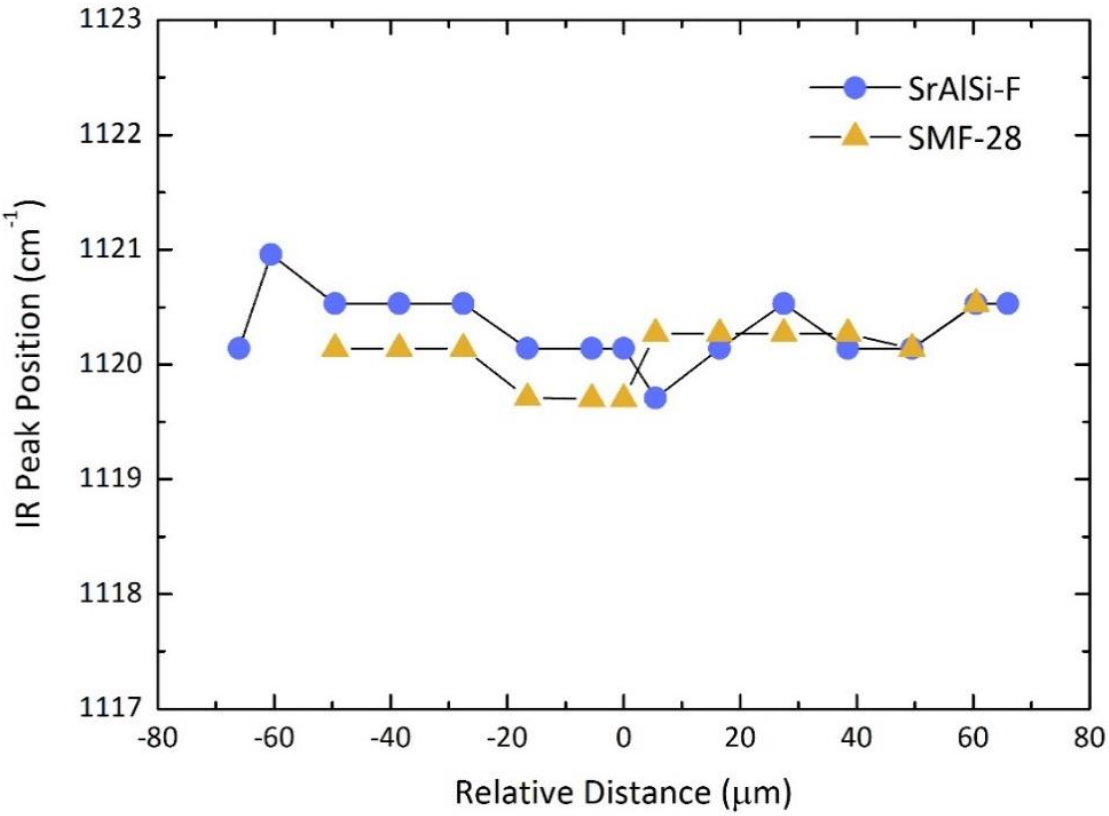

Figure III.3. Wavenumber of the peak of the Si-O-Si asymmetric stretching vibration as a function of position across the optical fiber for a standard single mode telecommunications fiber (SMF-28^{TM}) and a molten-core-derived fiber in the strontium aluminosilicate oxyfluoride system (SrAlSi-F in [19]).

III. C. The nonlinear coefficients

Not all properties of interest in this dissertation are easily modeled using additivity approaches; these include the fictive temperature described above and the Raman gain coefficient. This section describes the approach employed to determine selected quantities directly from measurements on the as-drawn optical fibers.

III. C. 1. Nonlinear refractive index (n_2)

Nonlinear optical effects, such as self-phase modulation (SPM) and four-wave mixing (FWM), can manifest at high optical powers in a fiber-based system [30]. In SPM, both spectral and temporal modifications to optical pulses can arise. In FWM, which is amongst the strongest parametric wave-mixing nonlinearities, new photon frequencies are created from those of the pump. In both cases, the effect is proportional to the nonlinear refractive index, n_2. The Reader is directed to Chapter I for more detail on these effects, their physical origin and material influences.

Similarly to the thermo-optic coefficient, to first order, the nonlinear refractive index can be introduced parametrically into the refractive index additivity model as $n = n_o + n_2 I$, where n_o is the linear refractive index, n_2 is the nonlinear refractive index and I is the light intensity. The simplest and widely employed model for estimating n_2 is the "BGO"

model, (so named for the authors: Boling, Glass, and Owyoung; [31]), reproduced here (in electrostatic units as was standard at the time of its derivation) as

$$n_2(10^{-13}\ \text{esu}) = 391\,\frac{(n_d-1)}{\upsilon_d^{5/4}}, \qquad (3.3)$$

While several empirical relations can be found in [31] for the nonlinear refractive index, the version embodied by Eqn. 3.3 (Eqn. 39 in [31]) seems to offer the best fit to a wide set of n_2 data across compositional ranges, and has gained broad acceptance [32]. An alternative expression, based on a derivation from physical properties (Eqn. 38 in [31]) also is frequently found in the literature [33], but often with modified coefficients to improve data fitting [34]. This alternative formula is given as [31]

$$n_2(10^{-13}\ \text{esu}) = \frac{68(n_d-1)\left(n_d^2+2\right)^2}{\upsilon_d\left[1.517+\frac{\left(n_d^2+2\right)(n_d+1)}{6n_d}\upsilon_d\right]^{1/2}}. \qquad (3.4)$$

The terms in Eqns. 3.3 and 3.4 are the refractive indices (n_F, n_d, n_C) and Abbé number, $\upsilon_d = (n_d - 1)/(n_F - n_c)$, at the historically based wavelengths of the hydrogen F line (486.13 nm), the helium d line (587.56 nm), and the hydrogen C line (656.27 nm). According to Ref. [31], Eqn. 3.3 provides a better fit for materials that possess n_2 values greater than ~2×10^{-13} esu. It should be pointed out, however, that neither equation provides any direct dependence of n_2 (in esu units) on the specific optical wavelength; only on a measure of visible chromatic dispersion.

In order to estimate n_2 for an optical fiber, the refractive index profile (RIP) can be measured at multiple wavelengths. This enables the determination of a set of Sellmeier

coefficients for the fiber from which n_d, n_F, and n_c can be computed. With Eqn. 3.3 these values enable the calculation of n_2. Furthermore, using the additive model enables the determination of the Sellmeier coefficients and effective n_2 of individual glass constituents, allowing for the calculation of n_2 for arbitrary compositions.

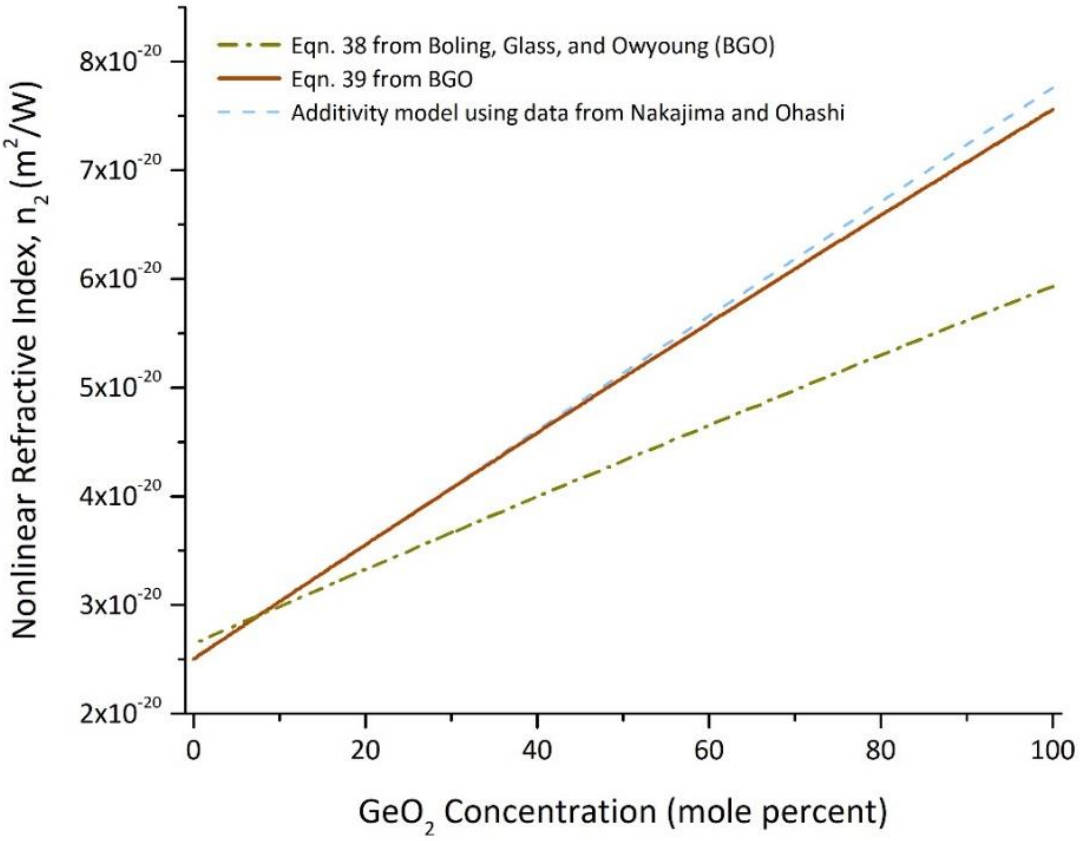

Figure III.4. Calculated nonlinear refractive index, n_2, for the SiO_2 – GeO_2 binary system based on the additivity models discussed herein and compared with findings from [35]. Wavelength is 1550 nm.

With respect to additivity of the nonlinear refractive index, as noted above, $n = n_0 + n_2 I$. Accordingly, the refractive index of a binary glass mixture composed of i and j species is given as

$$n = m(n_i + n_{2,i} I) + (1 - m)(n_j + n_{2,j} I) =$$

$$m n_i + (1 - m) n_j + (m n_{2,i} + (1 - m) n_{2,j}) I. \qquad (3.5a)$$

and, converting [esu] to [m^2/W]:

$$n_2 \left(\frac{m^2}{W}\right) = \frac{40\pi}{c_0}\left(m \frac{n_{2,i}(esu)}{n_i} + (1 - m) \frac{n_{2,j}(esu)}{n_j}\right) \qquad (3.5b)$$

This equation can be rewritten to possess linear and nonlinear components that can be added separately. Therefore, Eqn. 3.5a suggests simple additive modeling of the nonlinear refractive index in a similar fashion to the linear refractive index. When the Sellmeier coefficients of a pure compound are known, it is possible to know the evolution of the linear refractive index as a function of wavelength, and therefore determine the n_2 value for each individual compound using Eqns. 3.5a and 3.5b. Thus, in a binary system, n_2 for each end compound can be determined, and, using Eqn. 3.5a, the n_2 aggregate value of the glass can be computed. Fig. III.4 shows the calculated values of n_2 as a function of GeO_2 content in a SiO_2-GeO_2 binary glass. These results agree with *Nakajima, et al.* [35]. Accordingly, hereafter, when n_2 compound-specific data is not available (which is the case for most compounds), Eqn. 39 from BGO (i.e., Eqn. 3.3 above) will be employed using linear refractive index values. As an example of this, computation of the nonlinear

refractive index for both crystalline and amorphous SrO is performed in Chapter VI using "BGO" empirical model.

III. C. 2. Raman scattering

Although a general description of the material influences on Raman scattering was provided in Chapter I, and approaches to computing absolute Raman intensities have been reported in the literature [36,37], the modeling of Raman gain in multicomponent glasses is beyond the simple additivity models treated here. One important reason for this is that fibers fabricated using the molten core method have been shown to possess more disordered structures than conventionally prepared optical fibers [38]. As a result, the glass structure, and not just the molecular species, plays a considerable role in the resultant Raman properties. That said, as described in more detail below, the Raman spectra of the optical fiber core can be directly measured and meaningful trends with processing conditions and glass constituents can be deduced.

The relative Raman gain (g_R) of the fiber core material can be determined from direct measurement of its spontaneous Raman scattering cross section using micro-Raman spectroscopy. The procedure to correct the spectra is similar to that in [40], which accounts for reflection loss, internal solid angle variation, and the Bose-Einstein correction factor. The corrected spectra are normalized relative to the highest peak intensity of silica (typically around 440 cm^{-1}) since the Raman gain of silica is well known [41,42]. This is especially convenient since pure silica is the cladding material used for the molten core

fabricated fibers often invoked in this dissertation. Thus, a comparative Raman analysis of the intrinsically low nonlinearity core materials can be directly made relative to the cladding of the same fiber, which experienced the exact same thermal history during preform heat-up and fiber draw.

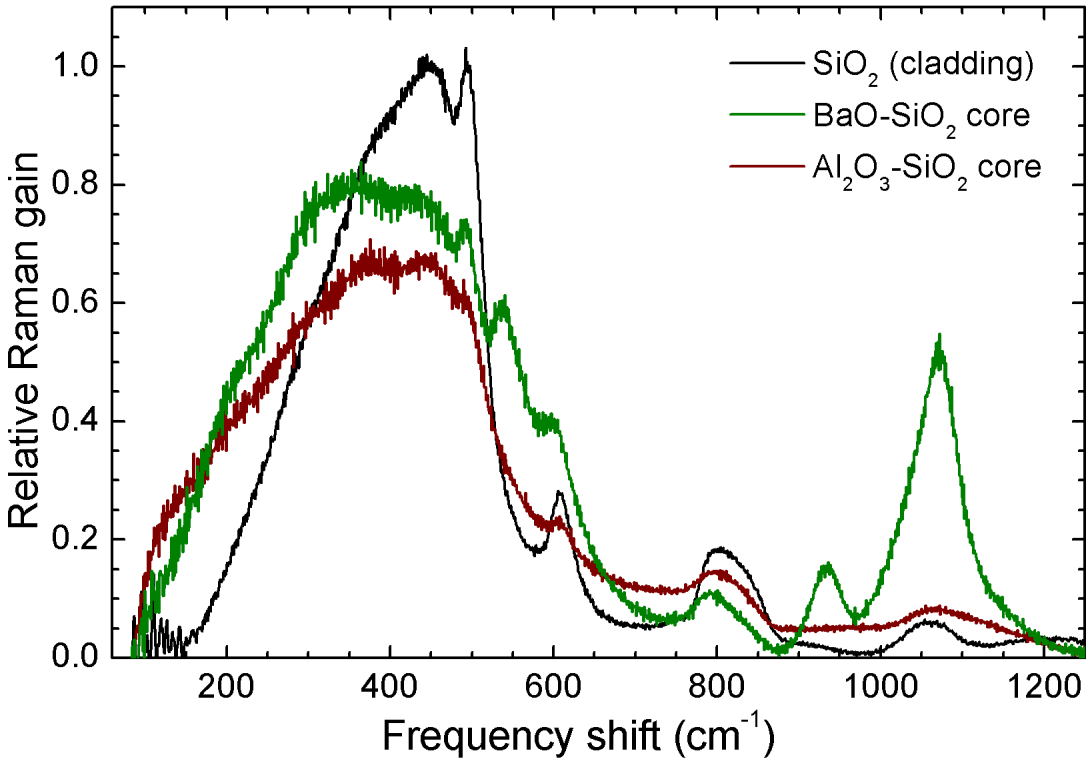

Figure III.5. The relative Raman gain of selected fiber core materials relative to silica. The aluminosilicate ($Al_2O_3 – SiO_2$ core) and bariosilicate ($BaO – SiO_2$ core) fiber core materials are normalized relative to their respective cladding [39].

As an example, corrected and normalized Raman scattering spectra are shown in Fig. III.5 for silica and fibers in the $BaO – SiO_2$ and $Al_2O_3 – SiO_2$ families. The reductions in the magnitude of RGC relative to pure silica are explained by the high cooling rates

associated with the fiber drawing process, which enables the formation of a more highly disordered core glass (as evidenced by the broadened Si – O spectral features) and a reduced overlap of the individual Raman peaks between the differing constituents [39]. A more detailed discussion of the most promising material systems for realizing intrinsically low Raman response is provided in the next Chapter.

III. C. 3. Brillouin scattering

Brillouin scattering was described in some detail in Chapter I. The Brillouin gain coefficient, BGC, is given by $2\pi n^7 p_{12}^2 / c\lambda_o^2 \rho V_a \Delta\nu_B$. Calculating this value is somewhat straightforward. In short, the models presented in Chapter I can be used to calculate the relevant terms and a global BGC can be computed. Measurements of this value can include deducing the individual terms comprising the BGC equation and substituting into the equation. Alternatively, BGC can be measured directly. Most typically, this is done by comparing the strength of the Brillouin back-scattered signal from a fiber to that of a control fiber of known BGC [43].

III. D. Some canonical examples

This section provides specific modeling results, overlaid with measured property values, for selected optical nonlinearities of interest to this work. Chapter IV will delve with greater detail into which glass families warrant further attention for optical fibers that

exhibit simultaneous reductions to all of the parasitic nonlinearities that limit scaling to higher powers in laser and communication systems [44].

III. D. 1. Brillouin scattering

As noted in Chapter I, Brillouin scattering is an inelastic interaction between acoustic phonons of the material and the optical signal. In its spontaneous form, Brillouin scattering materially depends on the refractive index, transverse (p_{12}) photoelastic coefficient, and adiabatic compressibility, which, in turn, are related to density and acoustic wave velocities. In its stimulated form (SBS), the gain is materially dependent upon the Brillouin linewidth in addition to the factors noted above.

As discussed in the previous section, each of the material properties relevant to Brillouin scattering can be calculated utilizing the models discussed in Chapter II. Fig. III.6 provides a comparison of the Brillouin gain, relative to a conventional telecommunications-grade optical fiber, as a function of non-silica concentration for a variety of binary and ternary silicate core glass optical fibers (all employing pure silica cladding glasses) [5,43,45–48].

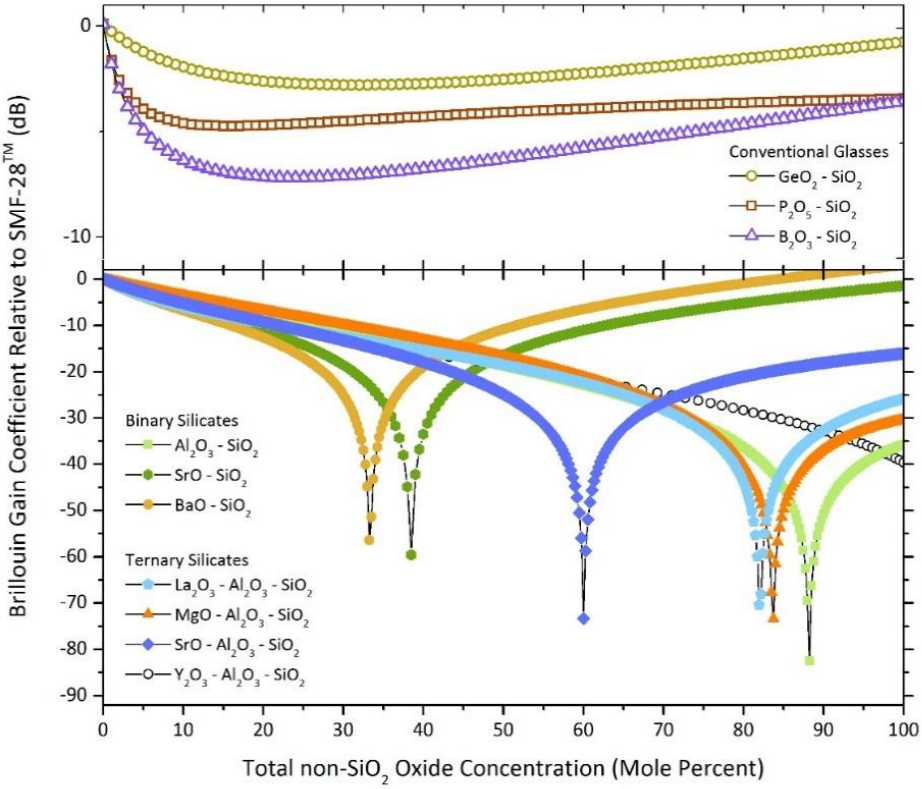

Figure III.6. Relative Brillouin gain (in decibels, dB) relative to conventional, telecommunications single mode fiber (SMF-28^{TM}) as a function of non-silica concentration (in mole percent) for a variety of molten-core-derived optical fibers. The lines are model results based on the additivity approaches described herein.

At first glance, Fig. III.6 shows that conventional dopants into passive and active optical fibers, i.e., GeO_2, P_2O_5, and B_2O_3, all lower the BGC relative to SiO_2. This is due to their acoustic damping terms, which are much larger than that of silica, since their p_{12} values are not especially low [12]. At low silica concentrations, these materials also show an upturn in BGC for the binary systems. This can be attributed to the fact that each of these network formers has an acoustic velocity that is less than that of silica. As the silica

content is decreased, the acoustic velocity decreases, resulting in a concomitant decrease in the Brillouin frequency shift. As discussed in Chapter II, this causes a decrease in $\Delta\nu_B$, mitigating the reduction in gain due to the larger acoustic damping. This is also true of the alkaline earth silicate systems, but BGC is significantly reduced due to reduction in p_{12}. In the case of material systems possessing Al_2O_3, MgO, and Li_2O, they raise the acoustic velocity when added to silica, increasing the Brillouin frequency. This causes further broadening to $\Delta\nu_B$, and thus the BGC graph for these materials appears to drop monotonically (ignoring the zero-gain-coefficient regions) across the compositional range.

Two additional observations are worthy of note with specific material trends to be discussed in greater detail in Chapter IV First is the significant reductions in relative Brillouin gain coefficient at selected compositions. Though the minima as shown in Fig. III.6 attain values of greater than - 60 dB (note the log scale), these zero Brillouin activity ("ZeBrA" [13]) compositions, in theory, should approach - ∞ (dB). Such points are associated with compositions where the effective p_{12} photoelasticity goes to zero, hence, Brillouin scattering is no longer operative. This is achieved through the additive properties of glasses comprised of both $p_{12} > 0$ (e.g., SiO_2) with $p_{12} < 0$ (e.g., BaO) components. The exceptions in Fig. III.6 are the $Y_2O_3 – Al_2O_3 – SiO_2$ fibers whose core properties add as if comprised of SiO_2 and YAG ($Y_3Al_5O_{12}$), both of which exhibit $p_{12} > 0$ (though it is small for the latter), hence no ZeBrA composition exists. The second point of note is that, for all practical purposes, relative Brillouin reductions of greater than 3 dB (preferably 5 dB) are significant to the high power laser community. In this case, even in the YAG-derived fibers,

reductions in relative Brillouin gain of about 6 dB, as has been experimentally validated [45], are useful. The results of Fig.III.6 show that high silica-content optical fibers with only one or two additional components can readily exhibit Brillouin reductions between 5 – 15 dB, all through judicious selection of the enabling materials, rather than the more complex and costly approach of geometric tailoring (e.g., photonic crystal and / or microstructured fibers) of the fiber cross section.

III. D. 2. Transverse mode instability

Transverse mode instability (TMI), also known in the literature as "higher order mode instability" (HOMI), is presently the dominant limitation in scaling fiber-based lasers to higher output powers [49,50]. As noted in Chapter I, TMI occurs in large mode area (LMA) multimode waveguides whereby, above a certain power threshold, the propagating optical modes become random and dynamic [51,52]. It is generally accepted that TMI originates from stimulated thermal Rayleigh scattering (STRS), which is materially dependent on the thermal conductivity, heat capacity, and thermo-optic coefficient (dn/dT) of the glass comprising the core of the optical fiber [53].

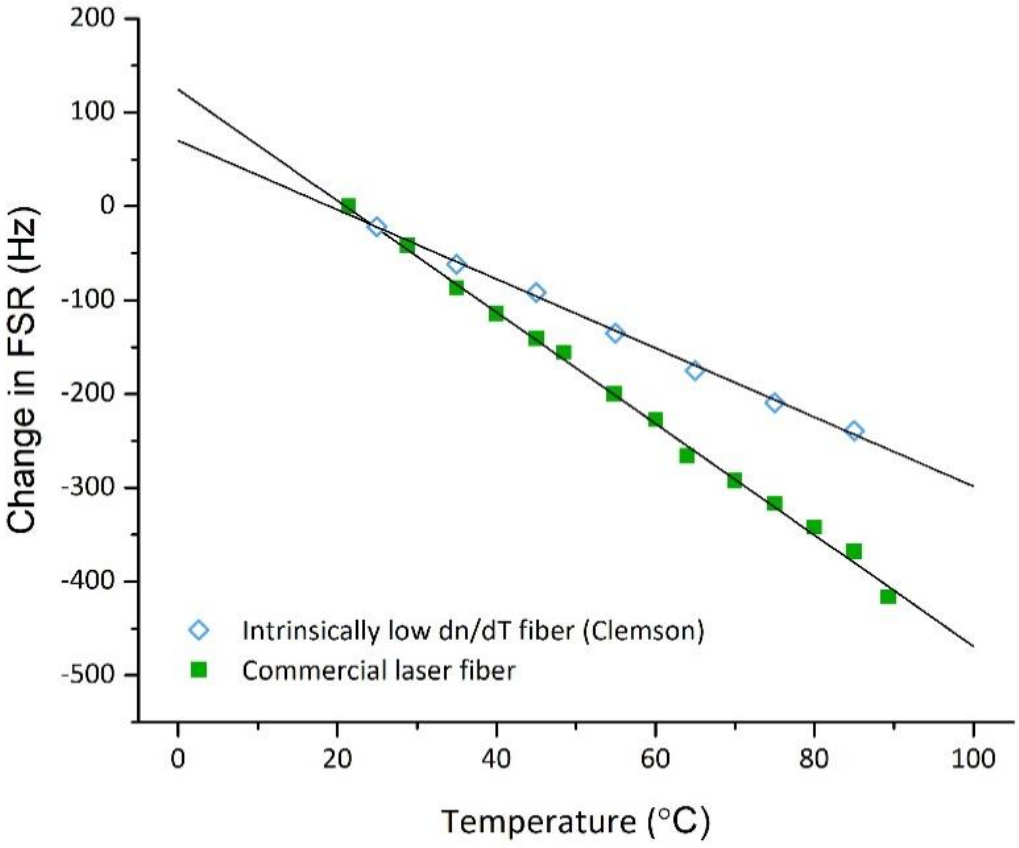

Figure III.7. Change in free spectral range of a ring laser as a function of temperature for a commercially available high power fiber laser compared to that of a fiber whose core material has been tailored with intrinsically low thermo-optic materials. The reduced slope of the latter signifies a reduced dn/dT value, which would increase the threshold for transverse mode instability (TMI) all other fiber design and pump conditions being equal.

While these material dependencies are discussed in greater detail in Chapter IV, suffice it here to note that dn/dT is the one property of these three material influences that is most compositionally tailorable within a given glass family. In an analogous fashion to Brillouin scattering, components exist that possess positive- and negative-valued thermo-optic coefficients such that their additivity yields the potential for dn/dT = 0 compositions where STRS would be mitigated. Canonical examples of this are borosilicate and phosphosilicate binary glasses where both B_2O_3 and P_2O_5 possess dn/dT < 0 values whereas that for SiO_2 is positive-valued. Examples of this additivity were already provided in Fig. III.2. Fig. III.7, on the other hand, shows example data obtained from two Yb-doped fibers using the ring laser measurement apparatus described in Section III. B. 4. The negative slope of the data means that the FSR is decreasing with temperature, implying that the CTE dominates the thermal dependence. Decreasing dn/dT lessens the slope, while a line with zero slope implies that the CTE and dn/dT have fully compensated each other. Interestingly, this suggests a novel way to thermally stabilize single frequency fiber lasers: by making the intracavity fiber system immune to changes in temperature [54].

Also, in a manner analogous to Brillouin scattering, while zero values exist in the operative material parameters, actually obtaining those compositions is not usually critical in practice. Associated trade-offs between given material properties (e.g., dn/dT) and other material properties and fiber design and performance details are discussed further Chapter IV. Indeed, as relates to TMI, the threshold power should scale inversely with dn/dT such

that a 50% reduction in dn/dT should manifest a 3 dB increase in TMI threshold. This would permit multiple kilowatt output powers from a single fiber.

III. D. 3. Self-phase modulation (SPM)

Self-phase modulation (SPM) is a nonlinear effect that leads to both spectral and temporal modifications to laser pulses at high energies, such as in mode-locked ultrafast laser systems. SPM originates from the optical Kerr effect whereby the refractive index is a function of intensity through the nonlinear refractive index, n_2. The time varying intensity associated with the pulse shape gives rise to a time-varying refractive index that modulates the phase of the optical signal. As an illustration, Fig. III.8 provides the idealized spectrum of a 100 ns, 1-kW-peak-power Gaussian pulse propagating through a conventional single mode fiber of different lengths. Here, the n_2 value for a conventional single mode fiber was taken to be $\sim 2 - 3 \times 10^{-20}$ m^2/W [55] and the nonlinear phase change, γ, was computed using $\gamma = 2\pi n_2/\lambda_o A_{eff}$, where λ_o is the free space wavelength (1 μm for the purposes of Fig. III.8), and A_{eff} is the effective area of the waveguide mode [56]. Clearly apparent is the spectral distortion, which translates into a practical threshold value of $\gamma < 2\pi$ to avoid spectral broadening.

While SPM can be tailored geometrically, through enlarging A_{eff} by fabricating a larger fiber, it can also be tailored materially through n (which does also influence A_{eff}), n_2, and the group velocity dispersion of the fiber (through n). As observed conceptually in

Fig. III.8, a reduction in n_2 to ½ of its original value yields a spectral broadening due to SPM that is also reduced by ½ (3 dB), which is quite consequential in practical systems.

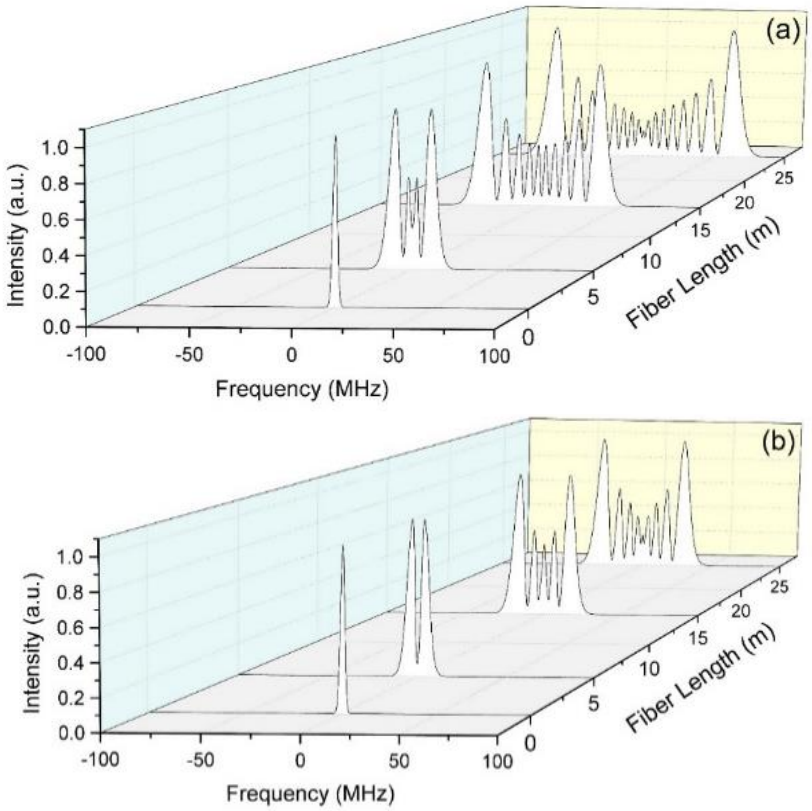

Figure III.8. Modeled effects of self-phase modulation (SPM) on pulse-broadening: Normalized output frequency spectra of a conceptual 100-ns 1-kW-peak-power Gaussian pulse through a single mode fiber at a wavelength of 1 μm for lengths 0.1, 5, 15, and 25 m given (a) conventional nonlinear refractive index, n_2, value for SiO_2 and (b) an n_2 value reduced by 3 dB (50%) based on the use of an intrinsically low nonlinearity glass as conceptualized in this work.

III. E. Compilation of properties for assorted materials studied to date

Table III.1 provides a list of properties, either measured directly or deduced using the models treated above, for a range of materials that have been studied to date. In the case of the deduced values, data on silica were used as known quantities and the properties of the additives to silica were employed as fitting parameters, and adjusted until modeling results matched measured data on actual fibers.

For completeness it is noted that the data obtained for SiO_2, GeO_2, P_2O_5, B_2O_3, and Yb_2O_3 were deduced from fibers that were fabricated utilizing conventional methods for telecommunications grade silica fibers; i.e., modified chemical vapor deposition (MCVD) [9,57,58]. The other fibers were fabricated utilizing the molten core approach [5,12,13,43,45,46,48]. Care should be given in extrapolating property values significantly beyond the compositional ranges and fabrication conditions of the fibers / glasses for which they were deduced since thermal histories, impurities, etc. may influence the resultant glass. As noted above, the continuum additivity approaches employed here are intended principally to provide a rapid and simple compositional guide for the subsequent fabrication of specific optical fiber core properties.

Table III.1. comparison of selected physical, optical, and acoustic properties of interest with respect to optical nonlinearities deduced using the additivity models described herein. Reader should note that while data found in the references were generally obtained at an optical wavelength of 1534 nm, the measurement wavelength can vary.

Compound	n	ρ (kg/m^3)	V_a (m/s)	$\Delta\nu_B$ (MHz)	p_{12}	p_{11}	ν	dn/dT (10^{-6}/K)	References
SiO_2	1.444	2200	5970	17	0.226	0.098	0.16	10.4	[13]
GeO_2	1.571	3650	3510	124	0.288	0.130	0.212	19.4	[58–60]
P_2O_5	1.487	2390	3936	177	0.255	0.132	0.294	-13.3	[9,61]
B_2O_3	1.41	1820	3315	428	0.298	0.25	0.29	-30[a, f]	[57,62,63]
$Y_3Al_5O_{12}$	1.868	3848	7649	253	0.009 @633nm	-0.029[c] @633nm	0.25	9.7[c] @543nm	[45,63,64]
Al_2O_3	1.653	3350	9790	274	-0.027	-0.237	0.25	10.5[f]	[13]
MgO	1.81	3322	8731	[b]	-0.07[c]	-0.31[c]	0.18[c]	13.6[c] @767.9 nm	[46,65,66]
SrO	1.81	4015	3785	187	-0.245	-0.296	0.231	-12.4[f]	[43]
BaO	1.792	4688	3131	178	-0.33	-0.33	0.31	12.7	[5,67]
Yb_2O_3	1.881	8102	4110	1375	-0.123	-0.275	0.28	[d]	[68]
La_2O_3	1.877	5676	3979	181	-0.027	-0.162	0.28	12.7	[48]
Lu_2O_3	1.66	7928	3660	145	-0.043	[d]	[d]	5.8[c]	[69,70]
Li_2O	1.97	3150	6500	[b]	-0.01	0.085	0.086	[d]	[71]

[a]: Ref. [60] gives 30×10^{-6} K^{-1} as dn/dT for B_2O_3, which is much higher that what is found in [62].

[b]: No data.

[c]: Data from crystalline phase.

[d]: Not yet determined.

[e]: At an acoustic frequency of 11 GHz.

[f]: Incladded fiber.

III. F. Conclusion

Provided herein is a discussion of the use of simple additivity models for the deduction of the properties of multicomponent silicate glass fibers (in contrast to bulk glass), central to optical nonlinearities, from the properties of amorphous or crystalline end-member compounds. The clad fiber geometry plays an important role since a core-cladding CTE mismatch can have a significant impact on the observed thermal coefficients. Furthermore, the mode spatial distribution, relative to the compositional profile, is also important to consider when modeling the fiber system and methods used to measure the physical properties of fiber were also outlined. Finally, a brief discussion of the modeling of selected nonlinear coefficients was provided. In general, over reasonable glass forming ranges in which the glass is presumed to remain compositionally uniform, homogeneous, and structurally similar, the models are found to be sufficiently accurate in order to guide the materials development of optical fibers that exhibit reduced optical nonlinearities.

III. G. References

[1] E. Snitzer, “Cylindrical Dielectric Waveguide Modes,” *J. Opt. Soc. Am.*, vol. 51, no. 5, p. 491, May 1961.

[2] R. A. Waldron, “Some Problems in the Theory of Guided Microsonic Waves,” *IEEE Trans. Microw. Theory Tech.*, vol. 17, no. 11, pp. 893–904, 1969.

[3] J. Bures, *Guided Optics: Optical Fibers and All-fiber Components*. Wiley, 2009.

[4] “Interfiber Analysis, LLC (8 Manns Hill Crescent, Saharon, MA 02067); http://www.interfiberanalysis.com/.” .

[5] P. Dragic, C. Kucera, J. Furtick, J. Guerrier, T. Hawkins, and J. Ballato, “Brillouin spectroscopy of a novel baria-doped silica glass optical fiber,” *Opt. Express*, vol. 21, no. 9, pp. 10924–10941, 2013.

[6] M. Guignard, L. Albrecht, and J. W. Zwanziger, “Zero-stress optic glass without lead,” *Chem. Mater.*, vol. 19, no. 2, pp. 286–290, 2007.

[7] J. Galbraith, L. Chapman, J. W. Zwanziger, M. Aldridge, and J. Kieffer, “Elasto-Optic Coefficients of Borate, Phosphate, and Silicate Glasses: Determination by Brillouin Spectroscopy,” *J. Phys. Chem. C*, vol. 120, no. 38, pp. 21802–21810, 2016.

[8] J. Galbraith and J. W. Zwanziger, “Designing glass with non-dispersive stress-optic response,” *J. Non. Cryst. Solids*, vol. 433, pp. 82–86, 2016.

[9] P. Law, A. Croteau, and P. D. Dragic, “Acoustic coefficients of P_2O_5-doped silica fiber : the strain-optic and strain-acoustic coefficients,” *Opt. Mater. Express*, vol. 1, no. 4, pp. 686–699, 2011.

[10] R. Ulrich and A. Simon, “Polarization optics of twisted single-mode fibers,” *Appl. Opt.*, vol. 18, no. 13, p. 2241, 1979.

[11] A. Bertholds and R. Dändliker, “Deterination of the Individual Strain-Optic Coefficients in Single-mode Optical Fibers,” *J. Light. Technol.*, vol. 6, no. 1, pp. 17–20, 1988.

[12] J. Ballato and P. Dragic, “Rethinking Optical Fiber: New Demands, Old Glasses,” *J. Am. Ceram. Soc.*, vol. 96, no. 9, pp. 2675–2692, 2013.

[13] P. Dragic and J. Ballato, “Pockels’ coefficients of alumina in aluminosilicate optical fiber,” *J. Opt. Soc. Am.*, vol. 30, no. 2, pp. 244–250, 2013.

[14] P. Dragic, M. Cavillon, A. Ballato, and J. Ballato, “A Unified Materials Approach to Mitigating Optical Nonlinearities in Optical Fiber. II. A. Material Additivity Models and Basic Glass Properties,” *Int. J. Appl. Glas. Sci.*, 2017.

[15] C. Ryan, P. Dragic, J. Furtick, C. J. Kucera, R. Stolen, and J. Ballato, “Pockels Coefficients in Multicomponent Oxide Glasses,” *Int. J. Appl. Glas. Sci.*, vol. 6, no. 4, pp. 387–396, 2015.

[16] P. D. Dragic, S. W. Martin, A. Ballato, and J. Ballato, “On the Anomalously Strong Dependence of the Acoustic Velocity of Alumina on Temperature in Aluminosilicate Glass Optical Fibers-Part I: Material Modeling and Experimental Validation,” *Int. J. Appl. Glas. Sci.*, vol. 7, no. 1, pp. 3–10, 2016.

[17] S. Chandrasekhar, “The dispersion and thermo-optic behaviour of vitreous silica,” *Proc. Indian Acad. Sci.*, vol. 34, no. 4, pp. 275–282, 1951.

[18] S. Sakaguchi and S. Todoroki, “Rayleigh Scattering of Silica Core Optical Fiber

After Heat Treatment," *Appl. Opt.*, vol. 37, no. 33, pp. 7708–7711, 1998.

[19] R. Douglas and J. Isard, "Density changes in fused silica," *J. Soc. Glas. Technol.*, vol. 35, pp. 206–225, 1951.

[20] J. F. Shackelford, J. S. Masaryk, and R. M. Fulrath, "Water Content, Fictive Temperature, and Density Relations for Fused Silica," *J. Am. Ceram. Soc.*, vol. 53, no. 7, pp. 417–417, Jul. 1970.

[21] U. Haken, O. Humbach, S. Ortner, and H. Fabian, "Refractive index of silica glass: Influence of fictive temperature," *J. Non. Cryst. Solids*, vol. 265, no. 1, pp. 9–18, 2000.

[22] J. C. Mauro, R. J. Loucks, and P. K. Gupta, "Fictive Temperature and the Glassy State," *J. Am. Ceram. Soc.*, vol. 92, no. 1, pp. 75–86, Jan. 2009.

[23] P. K. Gupta and J. C. Mauro, "The laboratory glass transition," *J. Chem. Phys.*, vol. 126, no. 22, pp. 1–9, 2007.

[24] C. Martinet, V. Martinez, C. Coussa, B. Champagnon, and M. Tomozawa, "Radial distribution of the fictive temperature in pure silica optical fibers by micro-Raman spectroscopy," *J. Appl. Phys.*, vol. 103, no. 8, 2008.

[25] D.-L. Kim and M. Tomozawa, "Fictive temperature of silica glass optical fibers-re-examination," *J. Non. Cryst. Solids*, vol. 286, pp. 132–138, 2001.

[26] M. Cavillon *et al.*, "Oxyfluoride core silica-based optical fiber with intrinsically low nonlinearities for high energy laser applications," *J. Light. Technol.*, vol. 36, no. 2, pp. 284–291, 2017.

[27] D. L. Kim, M. Tomozawa, S. Dubois, and G. Orcel, "Fictive temperature

measurement of single-mode optical-fiber core and cladding," *Journal of Lightwave Technology*, vol. 19, no. 8. pp. 1155–1158, 2001.

[28] A. Agarwal and M. Tomozawa, "Determination of Fictive Temperature of Soda-Lime Silicate Glass," *J. Am. Ceram. Soc.*, vol. 78, no. 3, pp. 827–829, Mar. 1995.

[29] R. Brückner, "Metastable equilibrium density of hydroxyl-free synthetic vitreous silica," *J. Non. Cryst. Solids*, vol. 5, no. 4, pp. 281–285, 1971.

[30] R. J. Essiambre and R. W. Tkach, "Capacity trends and limits of optical communication networks," in *Proceedings of the IEEE*, 2012, vol. 100, no. 5, pp. 1035–1055.

[31] N. Boling, A. J. Glass, and A. Owyoung, "Empirical Relationships for Predicting Nonlinear Refractive Index Changes in Optical Solids," *IEEE J. Quantum Electron.*, vol. 14, no. 8, p. 608, 1978.

[32] K. Tanaka, "Optical nonlinearity in photonic glasses," *J. Mater. Sci. Mater. Electron.*, vol. 16, no. 10, pp. 633–643, 2005.

[33] R. Adair, L. L. Chase, and S. a. Payne, "Nonlinear refractive-index measurements of glasses using three-wave frequency mixing," *J. Opt. Soc. Am. B*, vol. 4, no. 6, p. 875, 1987.

[34] L. Chase and E. W. Van Stryland, "Nonlinear Optical Properties," in *Handbook of Laser Science and Technology, Supplement 2: Optical Materials*, M. J. Weber, Ed. Boca Raton: CRC Press, 1995.

[35] K. Nakajima and M. Ohashi, "Dopant dependence of effective nonlinear refractive index in GeO_2- and F-doped core single-mode fibers," *IEEE Photonics Technol.*

Lett., vol. 14, no. 4, pp. 492–494, 2002.

[36] M. E. Lines, "Absolute Raman intensities in glasses. I. Theory," *J. Non. Cryst. Solids*, vol. 89, no. 1–2, pp. 143–162, 1987.

[37] M. E. Lines, A. E. Miller, K. Nassau, and K. B. Lyons, "Absolute raman intensities in glasses. II. Germania-based heavy metal oxides and global criteria," *J. Non. Cryst. Solids*, vol. 89, no. 1–2, pp. 163–180, 1987.

[38] P. Dragic and J. Ballato, "Characterization of the Raman gain spectra in Yb:YAG-derived optical fibers," *Electron. Lett.*, vol. 49, no. 14, pp. 895–897, 2013.

[39] M. D. O'Donnell *et al.*, "Raman gain of selected tellurite glasses for IR fibre lasers calculated from spontaneous scattering spectra," *Opt. Mater. (Amst).*, vol. 30, no. 6, pp. 946–951, 2008.

[40] R. H. Stolen, E. P. Ippen, and A. R. Tynes, "Raman oscillation in glass optical waveguide," *Appl. Phys. Lett.*, vol. 20, no. 2, pp. 62–64, 1972.

[41] R. H. Stolen, W. J. Tomlinson, H. a. Haus, and J. P. Gordon, "Raman response function of silica-core fibers," *J. Opt. Soc. Am. B*, vol. 6, no. 6, p. 1159, 1989.

[42] J. Ballato and P. Dragic, "Materials development for next generation optical fiber," *Materials (Basel).*, vol. 7, no. 6, pp. 4411–4430, 2014.

[43] M. Cavillon *et al.*, "Brillouin Properties of a Novel Strontium Aluminosilicate Glass Optical Fiber," vol. 34, no. 6, pp. 1435–1441, 2016.

[44] M. Cavillon, C. Kucera, T. Hawkins, J. Dawson, P. D. Dragic, and J. Ballato, "A Unified Materials Approach to Mitigating Optical Nonlinearities in Optical Fiber. III. Canonical Examples and Materials Roadmap," *Int. J. Appl. Glas. Sci.*, Dec.

2017.

[45] P. Dragic, P.-C. Law, J. Ballato, T. Hawkins, and P. Foy, “Brillouin spectroscopy of YAG-derived optical fibers.,” *Opt. Express*, vol. 18, no. 10, pp. 10055–67, 2010.

[46] A. Mangognia *et al.*, “Spinel-derived single mode optical fiber,” *Opt. Mater. Express*, vol. 3, no. 4, p. 511, 2013.

[47] P. Dragic, T. Hawkins, P. Foy, S. Morris, and J. Ballato, “Sapphire-derived all-glass optical fibres,” *Nat. Photonics*, vol. 6, no. 9, pp. 629–635, 2012.

[48] P. D. Dragic, C. Kucera, J. Ballato, D. Litzkendorf, J. Dellith, and K. Schuster, “Brillouin scattering properties of lanthano-aluminosilicate optical fiber.,” *Appl. Opt.*, vol. 53, no. 25, pp. 5660–71, 2014.

[49] M. N. Zervas and C. A. Codemard, “High Power Fiber Lasers: A Review,” *IEEE J. Sel. Top. Quantum Electron.*, vol. 20, no. 5, pp. 1–23, 2014.

[50] A. V. Smith and J. J. Smith, “Mode instability in high power fiber amplifiers.,” *Opt. Express*, vol. 19, no. 11, pp. 10180–10192, 2011.

[51] C. Jauregui, J. Limpert, and A. Tünnermann, “High-power fibre lasers,” *Nat. Photonics*, vol. 7, no. 11, pp. 861–867, 2013.

[52] T. Eidam *et al.*, “Experimental observations of the threshold-like onset of mode instabilities in high power fiber amplifiers,” *Opt. Express*, vol. 19, no. 14, p. 13218, 2011.

[53] L. Dong, “Stimulated thermal Rayleigh scattering in optical fibers,” *Opt. Express*, vol. 21, no. 3, pp. 915–918, 2013.

[54] J. Farroni, K. Tankala, A. Carter, and N. Jacobson, “Method of providing an optical fiber having a minimum temperature sensitivity at a selected temperature,” US 6,904,214 B2, 2005.

[55] A. Boskovic, S. V. Chernikov, J. R. Taylor, L. Gruner-Nielsen, and O. A. Levring, “Direct continuous-wave measurement of n2 in various types of telecommunication fiber at 1.55 μm,” *Opt. Lett.*, vol. 21, no. 24, pp. 1966–1968, 1996.

[56] G. P. Agrawal, *Nonlinear Fiber Optics*, 2nd ed. Academic Press, 1995.

[57] P. D. Dragic, “Brillouin Gain Reduction Via B_2O_3 doping,” *Light. Technol. J.*, vol. 29, no. 7, pp. 967–973, 2011.

[58] P. D. Dragic and B. G. Ward, “Accurate modeling of the intrinsic Brillouin linewidth via finite-element analysis,” *IEEE Photonics Technol. Lett.*, vol. 22, no. 22, pp. 1698–1700, 2010.

[59] G. G. Devyatykh *et al.*, “Material dispersion and Rayleigh scattering in glassy germanium dioxide, a substance with promising applications in low-loss optical fiber waveguides,” *Sov. J. Quantum Electron.*, vol. 10, pp. 900–902, 2007.

[60] W. Vogel, *Optical Properties of Oxide Glasses*. American Ceramic Society, 1991.

[61] P. Dragic, M. Cavillon, and J. Ballato, “On the thermo-optic coefficient of P_2O_5 in SiO_2,” *Opt. Mater. Express*, vol. 7, no. 10, pp. 3654–3661, 2017.

[62] J. M. Jewell, “Model for the thermo-optic behavior of sodium borate and sodium aluminosilicate glasses,” *J. Non. Cryst. Solids*, vol. 146, no. C, pp. 145–153, 1992.

[63] M. J. Weber, *Handbook of optical materials*. CRC Press, 2003.

[64] Z. Huang, J. Feng, and W. Pan, “Elastic properties of YAG: First-principles calculation and experimental investigation,” *Solid State Sci.*, vol. 14, no. 9, pp. 1327–1332, 2012.

[65] K. V. K. Rao and V. G. K. Murty, “Photoelastic constants of magnesium oxide,” *Acta Cryst.*, vol. 17, p. 788, 1964.

[66] C.-S. Zha, H. -k. Mao, and R. J. Hemley, “Elasticity of MgO and a primary pressure scale to 55 GPa,” *Proc. Natl. Acad. Sci.*, vol. 97, no. 25, pp. 13494–13499, Dec. 2000.

[67] M. Cavillon, J. Ballato, and P. D. Dragic, “Additivity of the coefficient of thermal expansion in silicate optical fibers,” *Opt. Lett.*, vol. 42, no. 18, pp. 3650–3653, 2017.

[68] P. D. Dragic, J. Ballato, S. Morris, and T. Hawkins, “The Brillouin gain coefficient of Yb-doped aluminosilicate glass optical fibers,” *Opt. Mater. (Amst).*, vol. 35, no. 9, pp. 1627–1632, Jul. 2013.

[69] P. D. Dragic *et al.*, “Athermal distributed Brillouin sensors utilizing all-glass optical fibers fabricated from rare earth garnets: LuAG,” *New J. Phys.*, vol. 18, no. 1, 2016.

[70] P. A. Loiko *et al.*, “Thermo-optic properties of Yb:Lu_2O_3 single crystals,” *Appl. Phys. B*, vol. 120, no. 4, pp. 601–607, 2015.

[71] P. D. Dragic *et al.*, “Single- and few-moded lithium aluminosilicate optical fiber for athermal Brillouin strain sensing.,” *Opt. Lett.*, vol. 40, no. 21, pp. 5030–3, 2015.

CHAPTER IV.

CANONICAL EXAMPLES AND MATERIALS ROAD MAP

IV. A. Introduction

This dissertation focuses on mitigating the optical nonlinearities that arise when high optical powers are propagated through modern optical fibers. These nonlinearities, which include stimulated Brillouin scattering (SBS), stimulated Raman scattering (SRS), transverse mode instability (TMI), and nonlinear refractive index (n_2)-mediated wave mixing phenomena, are parasitic effects in that they limit the achievable output powers from fiber lasers. The intent of this Chapter is to build from the fundamentals described in Chapter I and the additive models from Chapters II and III the properties of specific glass families as they relate to the aforementioned performance-limiting optical nonlinearities.

Ideally, the compositions discussed herein would be realized using conventional chemical vapor deposition (CVD) methods [1]. However, given the high processing temperatures associated with preform consolidation and collapse, which usually exceed 2200 °C (and are often closer to 2400 °C), volatile species such as germania (GeO_2), boria (B_2O_3), and fluorine (F) are difficult to maintain in the necessary concentrations required for marked reduction in parasitic nonlinearities. In this sense, the molten core approach to fiber fabrication [2], [3], employed to make many of the fibers described in this work, can

be considered a “low temperature” method since the highest temperature experienced is approximately the melting point of the core precursor. Chapter V provides complementary details and insights on the benefit in using the molten core method to fabricate optical fibers in the context of this work.

In specific regard to the nonlinearities themselves, this work assumes the following reductions to be both practical and viable. Practical here means that achieving these levels of reduction would be meaningful from a HEL systems perspective: - 15 dB in Brillouin gain coefficient (BGC); - 5 dB in Raman scattering; a thermo-optic coefficient (dn/dT) of – 5 dB; and an n_2 value equivalent to that of pure SiO_2. While the last goal does not sound like an improvement, achieving the other reductions will necessitate reasonably high concentrations of non-SiO_2 compounds. Accordingly, this n_2 goal essentially means that these non-SiO_2 dopants would not have any additional contribution to the nonlinear refractive index beyond that of the SiO_2 component.

IV. B. Trends with glass components and families

The properties of multicomponent glass optical fibers were studied in detail in the 1970s and 1980s while efforts to optimize optical fibers for long haul communications were being undertaken with great enthusiasm. In those days, low optical loss was the principal driver and so compositions that exhibited intrinsically low Rayleigh scattering garnered the most attention. Seminal material examples of such fibers will now be

described as a preamble to the discussions that follow.

Amongst the first studies were those conducted on the classic soda-lime-silica (SLS) system [4]. An analysis similar to that provided in Chapter I was conducted, though focused primarily on losses associated with Rayleigh scattering. Due to the reduced fictive temperature, the density-related Rayleigh scattering was predicted to be lower for the SLS than for fused silica. However, additional scattering due to compositional fluctuations in the multicomponent SLS glass led to a calculated intrinsic loss that was slightly over 3× larger than that for silica across the visible and near infrared spectral range (extrinsic impurities notwithstanding).

The binary potassium silicate system was studied with both Rayleigh and Brillouin scattering being investigated as a function of K_2O concentration [5]. With increasing K_2O, both p_{12} and p_{44} photoelasticity coefficients, shear and longitudinal wave velocities, and fictive temperature were found to decrease. Conversely, the refractive index and isothermal compressibility were shown to increase with increasing K_2O concentration. These trends were shown by *LaBerge, et al.*, to yield density fluctuations, $<\Delta\rho^2>$, that were nearly 50% lower than those for SiO_2 at a concentration of about 20 mole percent K_2O [6]. However, *Schroeder, et al.* [5] found that the immiscibility gap that exists in the K_2O – SiO_2 system, which extends over the range from nominally 0 – 25 mole % of K_2O, led to significant compositional fluctuation-induced scattering. For K_2O concentrations greater than 25 mole %, the scattering losses were found to be roughly 30 % lower than those for fused silica

due primarily to the very small compositional fluctuation term associated with Rayleigh scattering. Taken in total, potassium silicates are intrinsically low Brillouin and Rayleigh glasses for K_2O concentrations in excess of 20 – 25 mole %. Again, it is worth noting that extrinsic losses associated with impurities likely would make this system impractical from the perspective of low loss telecommunication fibers. However, given the differing focus of this dissertation, where ultimate low loss is not as critical, such a simple system with intrinsically low Brillouin and (classical) Rayleigh scattering could be of interest.

Ternary silicate glasses also received considerable attention, particularly those in the sodium borosilicate ($Na_2O – B_2O_3 – SiO_2$) and sodium aluminosilicate ($Na_2O – Al_2O_3 – SiO_2$) systems. As noted by *Tynes, et al.* [7], a glass system that exhibits both refractive index and density values that are roughly independent of composition must then exhibit a $\partial\varepsilon/\partial C$ value of zero (or nearly so), which implies low Rayleigh scattering. Akin to the concept employed here of component additivity to achieve multiple property tailoring, *Tynes, et al.*, further postulated that a ternary borosilicate with low total Rayleigh scattering could be achieved by mixing a binary borosilicate ($B_2O_3 – SiO_2$) having reduced $\partial\varepsilon/\partial\rho$ with a binary alkali-silicate exhibiting a reduced $<\Delta\rho^2>$ value (see Chapter I for more detail on these factors). These conditions occur over a fairly broad compositional range in the sodium borosilicate system, where, for a molar composition of about 50 SiO_2 – 20 B_2O_3 – 30 Na_2O a minimum in Rayleigh scattering occurs due to the aforementioned combined effects of reduced density fluctuations and reduced change in permittivity (hence refractive index) with density. A similar approach was followed in the sodium aluminosilicate

system, where Rayleigh scattering was reduced through reductions in fictive temperature to minimize density fluctuations coupled with components well-matched in dielectric properties to minimize compositional fluctuations [8]. A molar composition of 78 SiO_2 – 6 Al_2O_3 – 16 Na_2O was found to exhibit scattering losses 60 % lower than fused silica.

Quaternary systems also have been studied with the mixed alkali, alkaline earth-silicate system being especially interesting. Specifically, *Tsujikawa and Ohashi* evaluated glasses in the K_2O–Na_2O–MgO–SiO_2 system [9]. They found a marked reduction in Rayleigh scattering for a molar composition of 22 K_2O – 8 Na_2O – 10 MgO - 60 SiO_2 where the scattering losses are only about 38% those for fused silica. For this composition, the combined effects at play are a reduced glass transition temperature (surrogate for fictive temperature), hence reduced density-related scattering, as well as the reduced concentration fluctuations postulated to arise from a maximum at this composition in the difference between the glass transition and spinodal temperatures. This later consideration being thought to occur based on the mixed alkali effect whereby the mobility of the faster diffusing alkali species exhibits a minimum at a ratio of K_2O / (K_2O + Na_2O) of about 0.73 [9].

A more general and systematic consideration of alkali ion effects in silica-based optical fiber glasses was made by *Lines* [10]. Shown there were changes in fictive temperature, T_f, refractive index, n, photoelastic constant p_{12}, and difference between glass transition and spinodal temperatures, (T_g – T_s), with small (< 4 mole percent) alkali addition

into silica. Of the alkali ions, sodium and potassium silicates were found to have the lowest overall scattering loss, relative to the other alkali, due primarily to their having the greatest reduction in T_f, larger $T_g - T_s$ difference (particularly for $K_2O - SiO_2$), and smallest increase in refractive index. A minimum in scattering was found at a concentration of about 2 mole percent alkali with the sodium and potassium silicates exhibiting a calculated Rayleigh scattering that was 15 – 20 percent lower than for fused silica. These dependencies, however, in some part derive from the formation of non-bridging oxygen (NBO) ions upon alkali addition into silica. Such defects will not be helpful at higher intensities in active optical fibers because they are believed to facilitate photodarkening. However, this is set aside for the time being in the present discussion.

For completeness, it is noted that in all of these aforementioned cases, only the cationic species are changed. The influence of fluorine addition was studied by Lines in the alkali silicate system [11]. Fluorine is known to reduce the refractive index and, when added into glass with small alkali concentrations, it was found also to decrease $\partial\varepsilon/\partial C$. For fluorine concentrations up to 2 weight percent (*N.B.*, weight percent; not mole percent as previously employed), the total attenuation of low alkali content (fluoro)silicate was shown to be reduced by 15 – 20 % relative to fused silica. This is instructive since, below, examples will be provided on multicomponent oxyfluoride glass that are used to further tailor Raman scattering and the nonlinear refractive index, n_2.

The point of this section has not been to provide an exhaustive literature survey of

multicomponent glasses for low loss optical fibers. Instead it has been to offer a few examples of how simple, well-known and studied glass systems, offer opportunities for reducing what are today the performance-limiting parasitic effects in some of the most advanced optical fiber laser and communication systems.

Table IV.1 provides the general trends in selected properties of interest to this work with addition of said dopants into SiO_2. As can be seen, in each case, compounds can be found that either increase or decrease a given property and so the consideration here is to identify those compounds that suitably reduce each or, preferably, several nonlinearities, while forming a homogeneous core glass that meets the aforementioned practicality conditions; this is no simple task. Where no trend (arrow) is given, the direction of the change with said compound into silica has not yet been determined.

Table IV.1. general property trends on addition of noted compound into silica.[a]

Compound	Physical [b]			Brillouin [b]			STRS [b]	Raman [b] *	Wave-Mixing [b]
	n	ρ	CTE	V_a	$\Delta\nu_B$	p_{12}	dn/dT	V_m	n_2
SiO_2 [c]	1.444	2200	0.55×10^{-6}	5970	17	0.226	10.4×10^{-6}	27.31	2.5×10^{-20}
GeO_2	↑	↑	↑	↓	↑	↑	↑	↑	↑
F	↓	↓	↑	↓			↓		↓
P_2O_5	↑	↑	↑	↓	↑	↑	↓	↑	
B_2O_3	↓	↓	↑	↓	↑	↑	↓	↑	
Al_2O_3	↑	↑	↑	↑	↑	↓	≈	↑	↑
Yb_2O_3	↑	↑		↓		↓		↑	
La_2O_3	↑	↑		↓		↓		↑	
Lu_2O_3	↑	↑		↓		↓		↑	
MgO	↑	↑	↑	↑				↓	
CaO	↑	↑	↑						
SrO	↑	↑	↑	↓	↑	↓	↓	↓	
BaO	↑	↑	↑	↓	↑	↓	↑	↑	
Li_2O	↑	↑	↑	↑		↓	↓	↓	
Na_2O	↑	↑	↑				↓		
K_2O	↑	↑	↑				↓		
$Y_3Al_5O_{12}$	↑	↑		↑	↑	↓		↑	

[a]: Trend strictly valid over homogeneous glass forming range and for the binary composition with silica. Ternary and n-ary glasses may show equivalent trends but will depend on the relative concentrations of each component. Additionally, trends presume that no new phase or structure is formed such as with the mixed alkali effect [12] or in the Al_2O_3 – P_2O_5 system where both Al_2O_3 and P_2O_5 increase the refractive index, for example, when individually added to silica but decrease it when both Al_2O_3 and P_2O_5 are added in equal proportions to silica due to the formation of $AlPO_4$ [13].

[b]: Property abbreviations and units: n is the linear refractive index [dimensionless], ρ is the density [kg/m], CTE is the coefficient of thermal expansion [K^{-1}], V_A is the acoustic velocity [m/s], $\Delta\nu_B$ is the Brillouin linewidth [MHz], p_{12} is the transverse photoelastic coefficient [dimensionless], dn/dT is the thermo-optic coefficient [K^{-1}], V_m is the molar volume (cm^3/mol), and n_2 is the nonlinear refractive index (m^2/W).

[c]: Values for silica: refractive index, n, measured at a wavelength of 1550 nm. Brillouin linewidth, $\Delta\nu_B$, measured in MHz at a Brillouin frequency of 11 GHz.

IV. C. Compositional effect on individual optical nonlinearities

As noted above, it is infeasible to thoroughly review the impact of each possible compound on all of the material properties that influence the parasitic nonlinearities discussed in this dissertation. Accordingly, this section discusses compositional effects of a few compounds and compound families that have been shown to influence each nonlinearity in the manner desired.

IV. C. 1. Brillouin scattering

As detailed in Chapter I, spontaneous Brillouin scattering materially depends on the refractive index, transverse photoelastic coefficient, and adiabatic compressibility. In its stimulated form (SBS), the Brillouin gain coefficient, BGC, is materially dependent upon the Brillouin linewidth, $\Delta\nu_B$, (which is inversely proportional to the phonon lifetime) in addition to the factors noted above. Accordingly, to determine the magnitude of Brillouin scattering or, for the more specific purposes of this work, the BGC, one needs either to directly measure or accurately deduce the following material properties: refractive index, p_{12} photoelastic coefficient, density, acoustic wave velocities, and Brillouin spectral width.

Considerable literature exists detailing compositional effects on refractive index and density. To a lesser extent, photoelasticity and acoustic wave velocities (hence elastic constants and, therefore, adiabatic compressibility values) are known as are, to an even

lesser extent, Brillouin spectral widths. Further, care should be taken when citing photoelastic coefficients from the literature since many conventional methods for their determination measure magnitude but not sign, the latter being quite critical here.

Fig. IV.1 provides an overlay of the Brillouin gain coefficient, relative to a conventional telecommunications optical fiber, as a function of non-SiO_2 content of the core glass composition. More specifically, it depicts $\mathrm{BCG\,(dB)} = 10\mathrm{Log}_{10}\left(\mathrm{BGC}_{\mathrm{glass\ material}}/\mathrm{BGC}_{\mathrm{SMF-28}}\right)$ where the BGCs in the operand are in units of m/W. Consequently, where the BGC goes to zero, the graph takes on a singularity that extends to -∞ on the vertical scale. This composition is referred to as zero Brillouin activity, or ZeBrA [14]. Fig. IV.1 is equivalent to Fig. III.6 in Chapter III, which employs data from Table III.1 in Chapter III, except that experimental values are overlaid here as the open color-coded circles to show the fit between measurements and modeling.

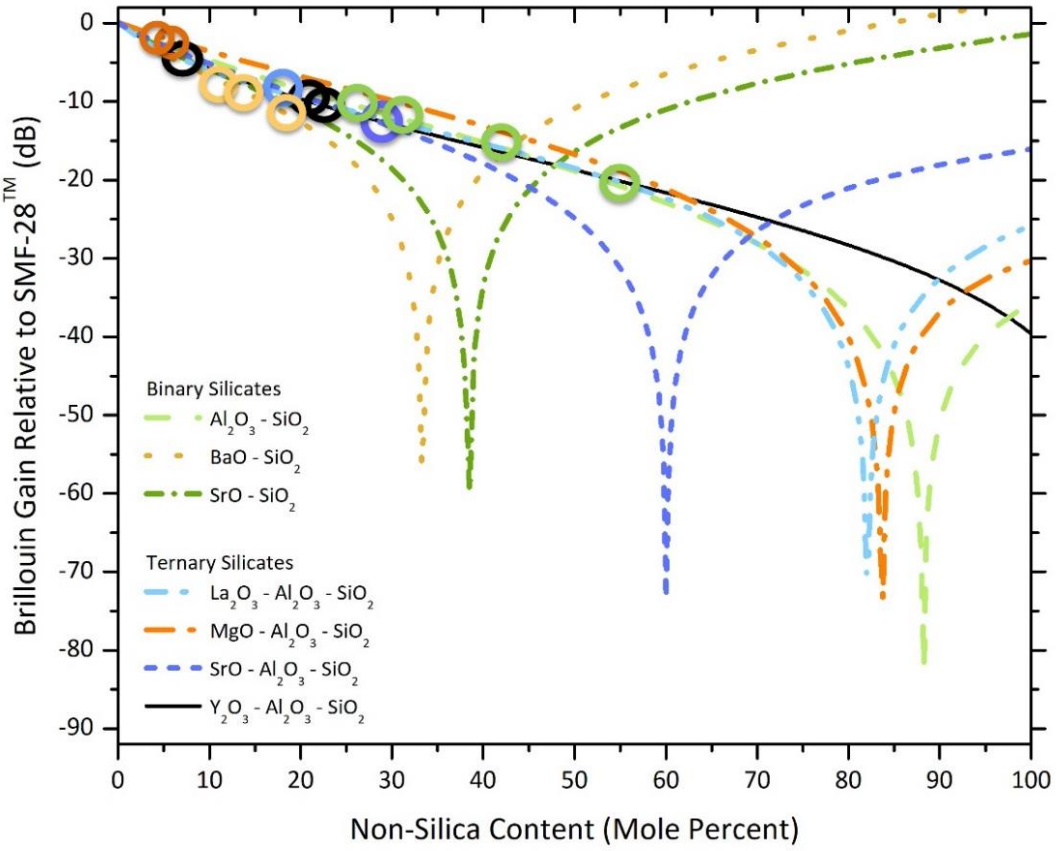

Figure IV.1. Relative Brillouin gain coefficient (in decibels, dB) relative to conventional, telecommunications single mode fiber (SMF-28™) as a function of non-silica concentration (in mole percent) for a variety of molten core-derived optical fibers. The lines are model results based on the additivity approaches described in Chapters II and III and the open circles, color-coded to match the glass systems associated with the model lines, are experimental results. Data on each fiber and specific compositions of the ternaries can be found in [14]–[20].

A second feature is that the (modeled) curve associated with the YAG-derived yttrium aluminosilicate ($Y_2O_3 – Al_2O_3 – SiO_2$) fiber does not show such a $BGC_{log} \rightarrow - \infty$ minima [20] while the (modeled) curve for lanthanum aluminosilicate ($SiO_2 – Al_2O_3 – La_2O_3$; SAL) does [18]. In the yttrium aluminosilicate fiber, single crystalline YAG ($Y_3Al_5O_{12}$) was employed as the core precursor during the molten core fabrication. In the lanthanum aluminosilicate fiber, a homogenous LAS glass rod was first made and then employed as the core phase in a rod-in-tube fiber draw arrangement. In conducting the modeling, per those methods outlined in Chapter III, the measured data fit both systems best when the properties of crystalline YAG were employed in the former case and the properties of a mixture of La_2O_3 and Al_2O_3 were used in the latter. Since homogeneous crystalline YAG possesses a small but positive p_{12} value [20], when mixed with the $p_{12} > 0$ SiO_2 ($p_{12} = 0.226$ at 1550 nm for fused silica), there is no composition where the resultant "YAG-derived" silicate glass would show a BGC (log scale, dB)$\rightarrow - \infty$ feature.

For the SAL fiber, the measured Brillouin gain data fit best when the individual La_2O_3 and Al_2O_3 components, along with SiO_2, were used. Based on the known properties of fused silica, along with previously additivity-deduced properties of the Al_2O_3 component from measurements on aluminosilicate glasses, contributions from the La_2O_3 components also can be deduced and are shown in Table III.1 in Chapter III. Based on the $p_{12} < 0$ values deduced for Al_2O_3 and La_2O_3, the resultant (modeled) curve exhibits the $p_{12} = 0$ minima. This clearly is a point for continued study: other than being the source of the individual components, what other roles might the form (crystal versus glass, homogeneous

versus heterogeneous powder) of the precursor play in the properties of the final glass fiber? For completeness, the compositions achieved are not especially near the ZeBrA compositions for either of these glasses and so perhaps the argument is moot and one simply cannot extrapolate property trends over the entire range of compositions. Over what range of compositions then can property values be extrapolated is another question for continued study.

As a brief aside, it is of direct benefit to amplifier and laser fibers that these sesquioxides lower the Brillouin gain coefficient when added into silica. Sesquioxide Al_2O_3 is added to silica in order to reduce the thermodynamic tendency for rare-earth dopant clustering. Such clustering diminishes the quantum efficiency of the light emission [21]–[23]. Accordingly, the typical dopants employed for making active silica-based optical fibers are intrinsically low Brillouin materials, though, in most applications, their concentrations are fairly low (~ few weight percent) and so the effect is less obvious.

In conclusion with respect to this section, while the conventional dopants into SiO_2 that are employed in communication optical fibers do lower the Brillouin gain coefficient, markedly lower BGC values are possible when compounds possessing negative p_{12} values are incorporated into silica, whose p_{12} is positive. This “mean value theorem” additivity yields $p_{12} = 0$ compositions that could, if realized in practice, negate Brillouin scattering. As will be discussed in more detail below, dopants of choice for reduced Brillouin scattering are the alkaline earth oxides, (AE)O, specifically SrO and BaO. They possess

the most negative p_{12} values deduced to date and have miscibility limits in SiO_2 of 42 and 40 mole percent, respectively [24], though sub-solidus metastable immiscibility is known [25]. The inclusion of 5 – 10 mole percent Al_2O_3 has proven an effective approach to mitigating phase separation at high (AE)O concentrations should glass formation be problematic [17]; see the *(Classical) Rayleigh Scattering* section. However, it is noted that the linear (and presumably nonlinear) refractive index, density, and coefficient of thermal expansion all increase with increasing (AE)O concentration [24]. Accordingly, such dependencies need to be considered with respect to the overall fiber design and property impact on these parasitic nonlinearities.

IV. C. 2. Raman Scattering

In both its spontaneous and stimulated forms, Raman scattering is reduced for glasses comprised of compounds possessing low molar volume, V_m, and small bond compressibility parameters, Λ; specifically, $P_S^{Raman} \propto V_m \cdot \Lambda^2$ (Chapter I). As two points of reference: (a) in the well-studied alkali halide system, Λ decreases with both increasing cationic ($\Lambda_{Li} > \Lambda_{Na} > \Lambda_K > \Lambda_{Rb}$ for a given halide) and anion ($\Lambda_F > \Lambda_{Cl} > \Lambda_{Br} > \Lambda_I$ for a given cation) mass [26]–[28] and (b) of greater relevance here, Λ for SiO_2 is quite small (0.1) and tends to increase with increasing modifier content [10], [29]. Given the few tangible material parameters that directly influence Raman scattering and, for those factors, the scarcity of available data on their magnitude as a function of composition, Fig. IV.2 provides a meager compilation of results from more common glass systems. The data

employed in Fig. IV.2 is either directly provided or computed from [27], [30]–[32][3] and the fractional cationic concentrations were calculated per *Lines* [29].

While the bond compressibility parameter is not as directly measureable as is, for example, the photoelastic coefficient(s), as noted in Chapter I, Λ does take on positive and negative values depending on the molecular structure and polarizability of the compound at hand. Thus, at least in theory, $\Lambda = 0$ ($\Lambda^2 = 0$) glasses could be possible. However, as with all nonlinearities, diminution is of greater practical consequence than eradication.

[3] Two points of caution for the reader planning to use the data from [30]. First, note the typographical error in Table 1, where the refractive index value for the $15Al_2O_3 – 33Na_2O - 52SiO_2$ glass should be 1.51229. Second, as noted by Lines [29], if the reader is interested in computing the hydrostatic photoelasticity, $p = (1/3)[p_{11} + 2p_{12}] \approx p_{12} - (2/3)|p_{44}|$, then the $½(p_{11}-p_{12})$ values provided in Table 1 of should be preceded by a negative sign.

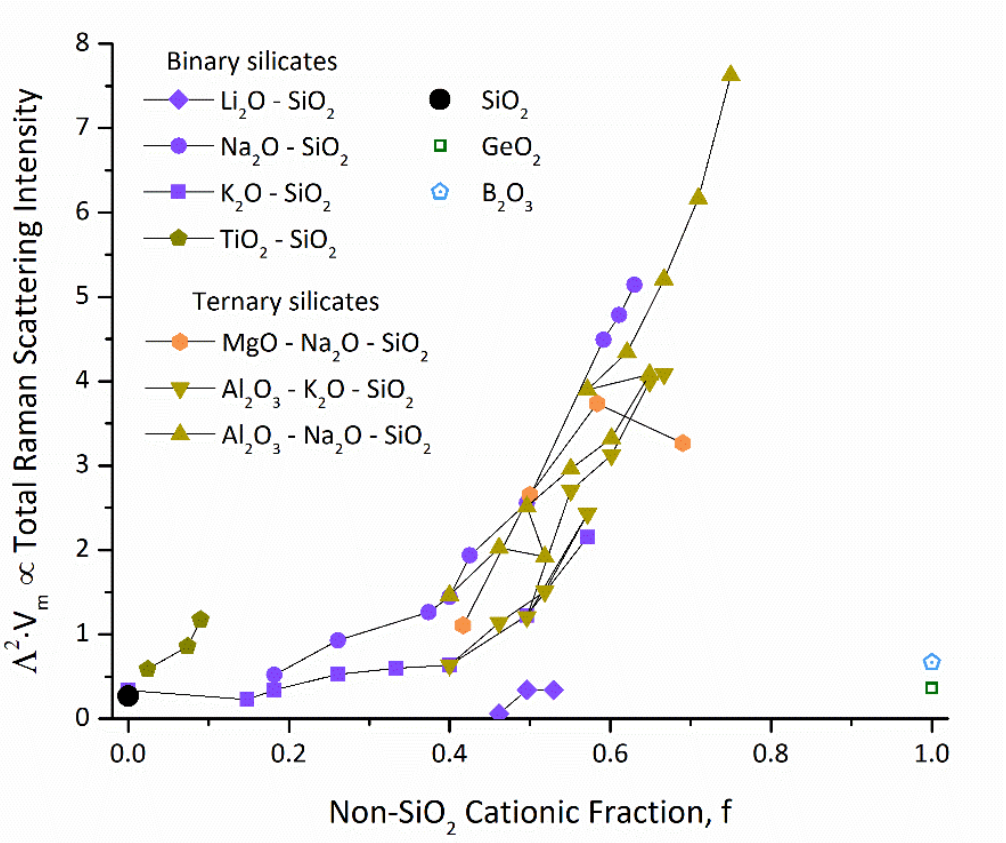

Figure IV.2. The product $V_m \times \Lambda^2$ (molar volume and squared bond compressibility parameter), which is proportional to the total Raman scattering intensity (Chapter I), as a function of non-silica cationic fraction for a series of binary and ternary oxide glasses. Lines connecting data within each glass family are guides-to-the-eye. SiO_2 is included as a point of reference.

Fig. IV.3 provides a compilation of measured relative peak Raman scattering values for a variety of fibers studied for their intrinsically low optical nonlinearities. The Raman scattering data shown in Fig. IV.3 were obtained as discussed in Chapter III using a normalization procedure similar to that in [33].

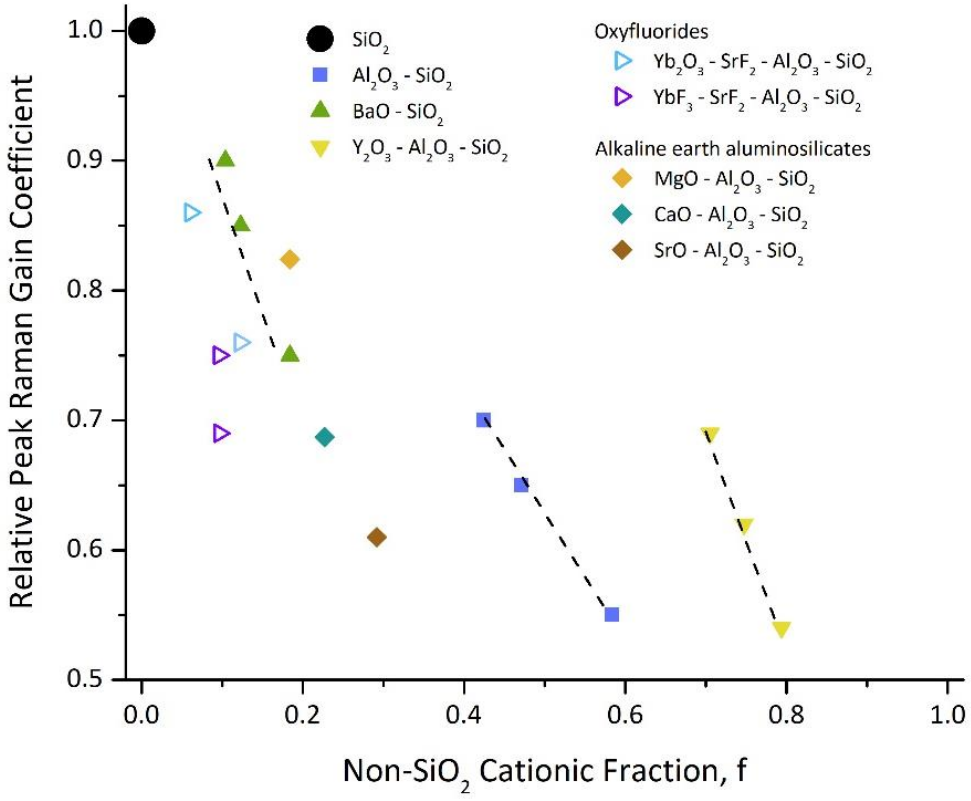

Figure IV.3. Relative peak Raman gain coefficient, relative to that of pure SiO_2, versus cationic fraction for a series of binary and ternary oxide and oxyfluoride core optical fibers reported in the [34], [35], and Chapter VI. Dashed lines connecting data within a specific glass family are guides-to-the-eye. SiO_2 is included as a point of reference. The core compositions represent those of the initial precursor compounds used to fabricate the fibers.

Care should be taken in comparing the results of Figs. IV.2 and IV.3. As noted, Fig. IV.2 is comparing the bond compressibility and molar volume, which are proportional to

the total Raman scattering intensity. Fig. IV.3 is comparing the Raman gain coefficient, which is proportional to the peak Raman intensity suitably normalized. If two molecules scatter with equivalent (spontaneous) Raman strength, but one molecule has twice the spectral bandwidth (or twice as many spectral components), then it will exhibit half the peak Raman gain coefficient.

Additionally, the Raman response is dependent both on the polarizability of the species, the overlap of each species' Raman spectral components, and the degree of disorder in the glass structure. For example, as discussed in [36] relative to yttrium aluminosilicate glasses, the molten-core derived core possessed broader SiO_2-related Raman spectral features than the pure SiO_2 cladding, implying a more random molecular structure. Additionally, there is little overlap between the Raman peaks of the individual components in these multicomponent glasses. As a result, both the peak SiO_2 scattering intensity is reduced by virtue of a lower silica content in the resultant glass, and the broader distribution of Raman spectral features yields a reduced intensity at any given wavenumber. These "structural" factors are not accounted for in the theories that yielded Fig. IV.2 and suggest that the glass structure (and fiber draw processing) may be more deterministic in measured Raman scattering intensity for a given family of glasses.

Interestingly, Λ also factors into laser damage thresholds; a separate but still important factor in the practicality of the high energy laser fibers considered in this dissertation. More specifically, Λ, which formally is defined as $\Lambda = -(\partial\alpha/\alpha)/(\partial\rho/\rho)$

[37], can be evaluated through the relationship: $\rho(dn/d\rho) = (1-\Lambda)\rho(\partial n/\partial\rho)$. As noted by *Waxler*, a material with zero $\rho(\partial n/\partial\rho)$ value (or Λ = 1) would exhibit no electrostrictive effects, including laser damage or (electrostrictive) self-focusing [38], [39]. Perhaps the more important here is that, fundamentally, there are only a handful of materials parameters / coefficients that relate to most (optical) phenomena; e.g., Table I.2 in Chapter I. It is in this simplicity that the sophistication of a unified approach to reducing nonlinearities originates.

Lastly, and for completeness, though not shown in Fig. IV.3, conventional telecommunication dopants, namely GeO_2, B_2O_3, and P_2O_5, all possesses larger Raman scattering cross-sections than SiO_2 [40]. More specifically, the relative Raman cross sections are about 5, 6, and 9 times larger for B_2O_3, P_2O_5, and GeO_2 than for SiO_2, respectively [40]. Further, GeO_2 is well-known to increase the nonlinear refractive index, n_2, of silicate glasses (Chapter III, Fig. III.4). Accordingly, for the purposes of this dissertation, these dopants will not be considered other than to provide baseline comparisons for the intrinsically low nonlinearity glasses discussed later against conventional optical fiber core compositions.

IV. C. 3. (Classical) Rayleigh scattering

As relates to high energy laser fibers, losses are not as critical as in long haul communication fibers since path lengths are markedly shorter than for telecomm fibers. For example, an oceanic fiber cable can extend several thousand kilometers whereas an

amplifier or laser fiber typically is 10 – 20 meters in length. This is not to say that loss is irrelevant, lower losses are always preferred. However, the attenuation of telecommunication fibers is specified as being < 0.2 dB/km whereas for laser fibers, the attenuation is typically < 10 – 20 dB/km.

From Chapter I, it is known that two contributions to Rayleigh scattering exist in optical fibers; those relating to fluctuations in concentration (composition) and in density. Materially, the intensity associated with concentration-related scattering is linearly proportional to the fictive temperature, quadratically proportional to the change in dielectric constant with composition ($(\partial\epsilon/\partial C)^2 = \partial n/\partial C^2$), and inversely proportional to the change in chemical potential with composition. The chemical potential approximately scales inversely with the difference between the fictive and spinodal temperatures (Chapter I). Accordingly, for large ($T_f - T_S$), one prefers then a system with no immiscibility or, for those that do, lower T_S values are better.

From the perspective of specific systems, as noted in Chapter I, a glass system that possesses both refractive index and density values that are roughly independent of composition should exhibit intrinsically low Rayleigh scattering. As an example, binary borosilicates ($B_2O_3 - SiO_2$) possess reduced $\partial\varepsilon/\partial\rho$ values whereas binary alkali-silicates exhibit reduced $<\Delta\rho^2>$ values [7]. Accordingly, the sodium borosilicate system is particularly interesting because it exhibits reduced Rayleigh scattering due to these combined effects.

With respect to increasing ($T_f - T_S$), one approach would be the addition of alumina, which is known to aid in glass formation by shifting the upper consulate point to lower temperatures [22]. In other words, relative to a composition without Al_2O_3, an alumina-containing glass will exhibit phase separation at a larger degree of under-cooling, where kinetics are slower and such instability is therefore less likely. Accordingly, in a system containing Al_2O_3, ($T_f - T_S$) would be larger, which suggests that Rayleigh scattering should be reduced; all other properties being equal. Another approach to increasing ($T_f - T_S$) is to use an isostructural additive that reduces the upper consulate point relative to that compound it is replacing [5].

Contributions to Raleigh scattering associated with density fluctuations are materially dependent on the refractive index, n, the fictive temperature, T_f, the photoelasticity coefficient, p [$p = p_{12} + (2/3)p_{44}$], and the adiabatic compressibility, K_S, through the elastic stiffnesses. Of these dependencies, the trend with refractive index is most pronounced, scaling as n^8, followed by that with photoelasticity, scaling as p^2, and then linearly with T_f and K_S.

From the perspective of specific glass systems, the same compounds discussed above with respect to reduced Brillouin scattering are useful here for reducing the p_{12} contribution to photoelastic influences on Rayleigh scattering. In the limiting case of a $p_{12} = 0$ zero Brillouin Activity "ZeBrA" composition, only the p_{44} contribution would remain

as a photoelastic contributor for Rayleigh scattering. Taken from the other perspective, $p_{44} = 0$ glasses have not only been identified but have been realized [41], [42]. Representative glasses include those in the $SnO – B_2O_3$, $SnO – P_2O_5$, $SnO – SiO_2$, $PbO – B_2O_3$, $PbO – P_2O_5$, and $PbO – SiO_2$ families [42], [43]. Unfortunately, these glasses all exhibit high refractive indices and low melting points making them unlikely candidates for the silica-clad fibers preferred in this work. That said, they do represent excellent systems through which to study the underlying correlations between glass chemistry and structure and optical physics.

Fig. IV.4 provides the photoelastic properties of these glasses, along with those for silica and selected commercial glasses and crystals [5], [26], [27], [31], [42], [44]–[46]. As a general trend, the oxide glasses tend to exhibit larger p_{12} values than do halide crystals. Further, PbO-based glasses, including the SF6 dense flint glass, possess near-zero p_{44} values. Of particular interest is YAG, which has both p_{12} and p_{44} values quite near to the $p = 0$ line. Accordingly, YAG-derived yttrium aluminosilicate glasses, might be of interest for intrinsically low Rayleigh scattering optical fibers.

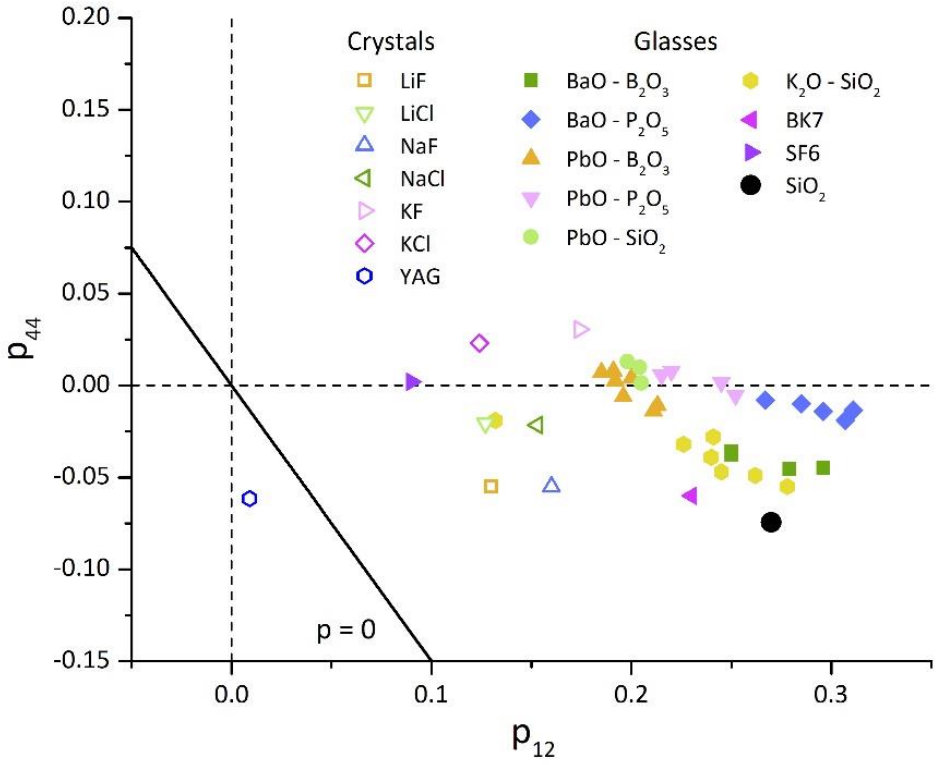

Figure IV.4. Compilation of p_{12} and p_{44} photoelastic coefficients for a variety of glasses, glass families, and crystals (measured at a wavelength of 632 nm). Rayleigh scattering scales quadratically with the Pockels coefficient, $p = p_{12} + (2/3)p_{44}$. Also shown are lines representing a zero Pockels coefficient material, where Rayleigh scattering would be zero. References to data can be found in the text.

As noted in Table I.1 of Chapter I, the density-related component of Rayleigh scattering would go to zero for a glass possessing a zero hydrostatic photoelasticity value, $p = 0$. This is analogous to the $p_{12} = 0$ "ZeBrA" condition for Brillouin scattering previously

mentioned. Accordingly, Fig. IV.4 also displays the $p = p_{12} + (2/3)p_{44} = 0$ line. Assuming equivalent additivity of p to that of p_{12} discussed in Chapter II, the following section discusses potential p = 0 compositions that would negate this contribution to Rayleigh scattering. As noted in Chapter I, while Rayleigh is not a limitation in high power laser systems, any scattering may contribute to other stimulated processes or, more generally, loss. Thus, any diminution in scattering is generally of benefit.

IV. C. 4. Transverse mode instability (TMI)

As noted in Chapter I, transverse mode instability is widely believed to be associated with stimulated thermal Rayleigh scattering (STRS). From a materials perspective, TMI-related mode coupling via STRS is proportional the thermo-optic coefficient (shortened to TOC or dn/dT in the text) and inversely proportional to the product of density with heat capacity [47].

From this, two important considerations arise as relates to this dissertation. First is that, over the range of glass compositions from which practical HEL fibers are made, neither the density nor heat capacity (or thermal conductivity [48]) change very much [49]. The second, and perhaps more important consideration, is that the thermo-optic coefficient has the potential to take on a value of zero; see, for example, Fig. III.2 of Chapter III. In an analogous manner to which $p_{12} = 0$ negates Brillouin scattering, dn/dT = 0 would negate STRS, though, again, negating such physical properties are not always needed in practice as long as sufficient reductions are achieved. Accordingly, for the purposes of this work,

dopants into silica that yield reductions in the thermo-optic coefficient, such as B_2O_3 and P_2O_5, (or, at least, do not dramatically raise dn/dT values, such as the alkaline earth oxides) will be considered further.

Exemplifying this is Fig. IV.5, which represents the dependence of TOC/ρ (heat capacity not considered since it changes very little with composition) for three canonical glass families treated in this dissertation. Values deduced using the additivity models presented in Chapter II and, in the particular case of the TOC, values do not take into account thermal expansion mismatches with the cladding. Of note here, as expected based on the dn/dT = 0 potential in the B_2O_3 – SiO_2 and P_2O_5 – SiO_2 systems, such zero STRS glasses are identified and will be further discussed in the next section.

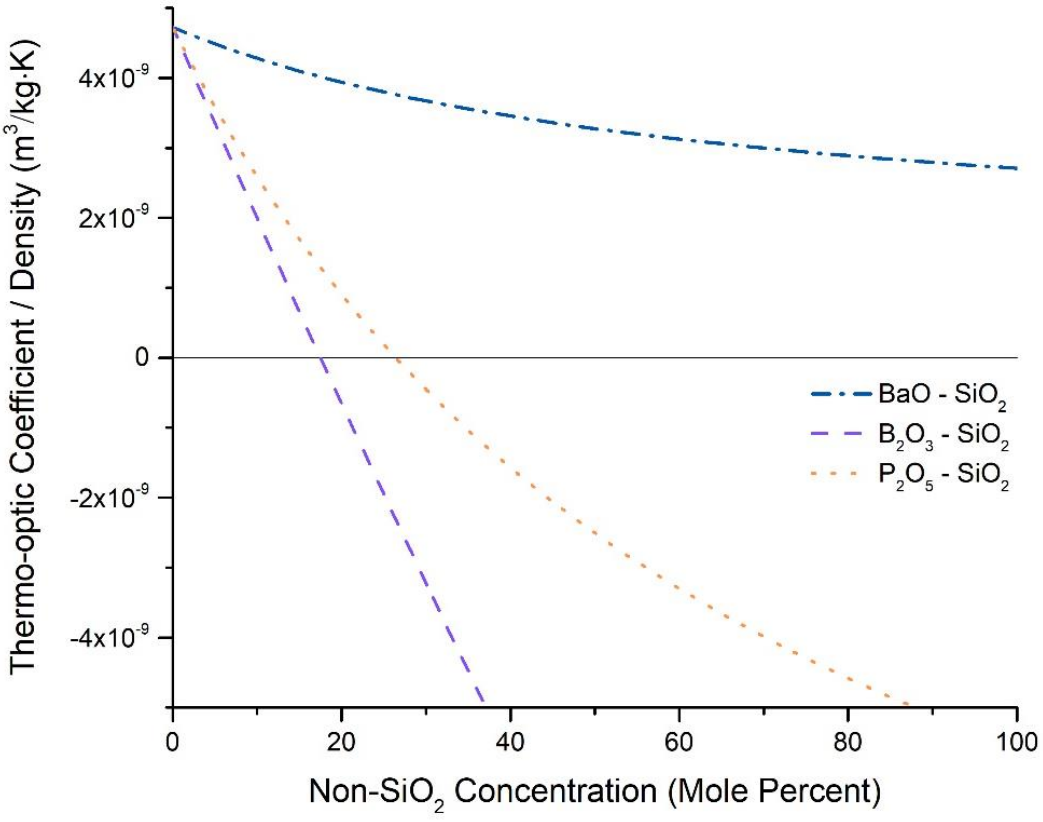

Figure IV.5. Effect of composition on the quotient of thermo-optic coefficient (TOC, dn/dT) and density, which is proportional to the stimulated thermal Rayleigh scattering (STRS) coupling coefficient [47]. STRS is widely held to originate transverse mode instabilities (TMI) in high power fiber lasers.

IV. D. Property value compositional diagrams

The underlying goals of this dissertation are to explicate the fundamental physical origins of performance-limiting nonlinear phenomena in optical fibers, determine or deduce their material dependencies, and identify glass families and compositions that collectively reduce all of the parasitic effects. In other words, to create a path to the "perfect fiber;" i.e., an optical fiber that exhibits intrinsically low nonlinearities based on the materials from which it is made and not through geometric / waveguide microstructuring.

Prior activities investigating the effect of various dopants have largely focused on binary systems for reasons of simplicity in trying to understand the underlying factors at play. Examples of how the nonlinearities scale with composition of single additives into SiO_2 can be found in Fig. IV.1 above, for the Brillouin gain coefficient (BGC), and in Fig. III.2 in Chapter III, for the thermo-optic coefficient that drives TMI. Since no single additive is likely to reduce all of the parasitic nonlinearities to the levels desired, more complex multicomponent systems need to be studied and their influences understood.

Accordingly, this section provides ternary property value diagrams of representative intrinsically low nonlinearity glass systems for continued consideration and development. Such representations are useful for gauging global trends and property dependencies within a given compositional family. These examples are chosen principally because they exhibit the properties that most effectively lead to significant reductions in

optical nonlinearities, such as $p_{12} = 0$, $p = 0$, or $dn/dT = 0$ compositions which would respectively negate Brillouin scattering, density-dependent Rayleigh scattering, and stimulated thermal Rayleigh scattering (STRS). They are believed to represent the glasses having the best potential to achieve the single intrinsically low nonlinearities optical fibers that are the goal of this dissertation. The algorithms used to generate the ternary diagrams found below can be found in Appendix IV.1.

In accordance with Table IV.1, the following compounds are, therefore, more specifically considered:

- SiO_2: Glass formation, thermal and mechanical stability, high laser damage threshold, compatibility with existing fibers and global manufacturing processes. SiO_2 also exhibits a very low Raman cross section and nonlinear refractive index.
  - Needs Attention: Additives to reduce p_{12} and dn/dT (see below).

- Al_2O_3: Facilitates glass formation, hence lowers T_s, which reduces Rayleigh scattering; as has (slightly) negative p_{12} value. Its large longitudinal acoustic velocity can be used to make a fiber acoustically anti-guiding and decrease the phonon lifetime (broaden $\Delta\nu_B$). It is also known to reduce photodarkening, and can allow greater introduction of active rare earth ions relative to silica.
  - Needs Attention: Additive for reduction in dn/dT.

- BaO or SrO: Strongly negative p_{12} value to reduce Brillouin and density-related Rayleigh scattering; though likely would contribute to stronger Raman scattering and wave mixing given the higher molar volume, (likely) bond compressibility, and polarizability of these heavy metal oxides. However, when added to silica in fairly low proportion (up to 10-15 mole percent), it reduces the magnitude of the Raman gain.
  - Needs Attention: Additive(s) to off-set increased n and n_2 values as well as dn/dT of BaO (SrO is found to decrease it relative to silica).

- P_2O_5: Negative dn/dT values, which when incorporated into silica (dn/dT > 0), offer potential to negate STRS, hence greatly reduce TMI. P_2O_5 facilitates reduced photodarkening.

- B_2O_3: Glasses containing B_2O_3 typically exhibit lower density, linear and nonlinear refractive indices, negative dn/dT value; and significantly increases Brillouin linewidth.
  - Needs Attention: Both B_2O_3 and P_2O_5 greatly increase Raman gain relative to silica, but only a small addition may be beneficial such as for alkaline earth oxides. Further, effect of B_2O_3 on photodarkening has not yet been determined.

- Alkali oxides: Lowers T_f and facilitates glass formation, which reduces Rayleigh scattering. Unfortunately, beyond those of Li_2O [50], insufficient data exist from

which to deduce all of the properties of interest here so these glasses, including alkali boro- and aluminosilicates, will not be discussed, but clearly represent areas for further study. That said, there is considerable reason to further investigate their role in reducing parasitic optical nonlinearities given their known potential for reducing Rayleigh scattering at small concentrations [10], [11].

The property value ternary diagrams treated next do not include fluorine or fluorides. This is because, to date, the exact bonding of the fluorine in the multicomponent silicate systems investigated has not been determined. Since, therefore, the exact compound composition cannot be determined, then neither can properties be deduced based on the additivity procedures of Chapters II and III. That said, the following compounds, and related oxyfluoride glasses, are worthy of further consideration.

- F: Reduces linear (n) and nonlinear (n_2) refractive indices; reduces Raman scattering and increases tendency for binary systems to phase separate / devitrify [51].

- Alkaline earth fluorides: Reduces n, n_2, dn/dT [52], [53], and, likely, Raman scattering.

- Rare earth fluorides: Rare earth ions make the glass light emissive while the fluorine contributes to off-setting the index raising qualities of the rare-earth.

IV. D. 1.Caveats

The section that follows begins by providing property value representations for selected ternary and quaternary glass systems based on the compounds noted above. Specifically, compositional trends in the transverse photoelastic coefficient, p_{12}, the hydrostatic photoelastic coefficient, p, and the thermo-optic coefficient (dn/dT, TOC). These coefficients are chosen because they materially influence Brillouin scattering, density-related Rayleigh scattering, and stimulated thermal Rayleigh scattering, which mediates TMI. Further, amongst the material parameters that factor into each parasitic nonlinearity, these are the ones that change most with composition and, most importantly, they have the potential to take on values of zero.

Compositional representations for Raman scattering and nonlinear wave-mixing will not be provided since, at present, there are insufficient data available on the governing material properties (specifically Λ and n_2) to deduce compositional trends. However, as shown in Chapter III, when those properties are known (e.g., GeO_2 [54]), the additivity approaches seem to offer sufficient accuracy for the purposes of this work in identifying glass families and compositional ranges for intrinsically low nonlinearity optical fibers.

SiO_2 is employed as a base constituent in all cases considered in this Section for reasons of practicality; specifically, that silicate core compositions would be most compatible with an SiO_2 cladding that would yield high strength, potentially low loss, and integration with conventional fibers to which these fibers would be spliced; e.g., pump

couplers. That said, as long as attenuation levels were suitably low and strength were to be sufficient, there is no practical reason why a core/clad preform with desired NA and dimensions could not be fashioned and drawn using these multicomponent glasses directly.

Lastly, the diagrams that follow cover the entire ternary compositional regions and are not limited to specific glass-forming regions. The reasoning for this is three-fold: (a) their purpose is to show global compositional trends; (b) the glass-forming "limits" are not well-known for all of these systems; and (c) glass-forming is kinetically enabled and dependent on the glass (or fiber) forming method. It is known that, for example, the molten core approach enables fiber compositions that are not possible using conventional melting / casting or optical fiber chemical vapor depositions methods [2], [55]. Hence, future efforts and approaches may continue to open up the compositional space over which glass optical fibers can be achieved.

Prior to delving into each nonlinearity individually (and then collectively), Fig. IV.6 provides a representative example for the Brillouin gain coefficient, BGC in the SrO – Al_2O_3 – SiO_2 system. The associated Al_2O_3 – SiO_2 and SrO – SiO_2 BGC binaries are overlaid to illustrate the complementary nature of this graphical approach. As expected, whereas Zero Brillouin Activity (ZeBrA) occurs at a single composition in a binary system, it occurs over a range of compositions in a ternary system. In addition to providing a simple graphical representation of compositional dependence on the parasitic nonlinearities, this approach also provides a simple way to visualize wide ranges of compositions that meet

selected criteria, such as a – 30 dB suppression in Brillouin gain coefficient relative to a conventional fiber, which is shown as the dashed lines connecting the binaries to the associated edges of the ternary in Fig. IV.6.

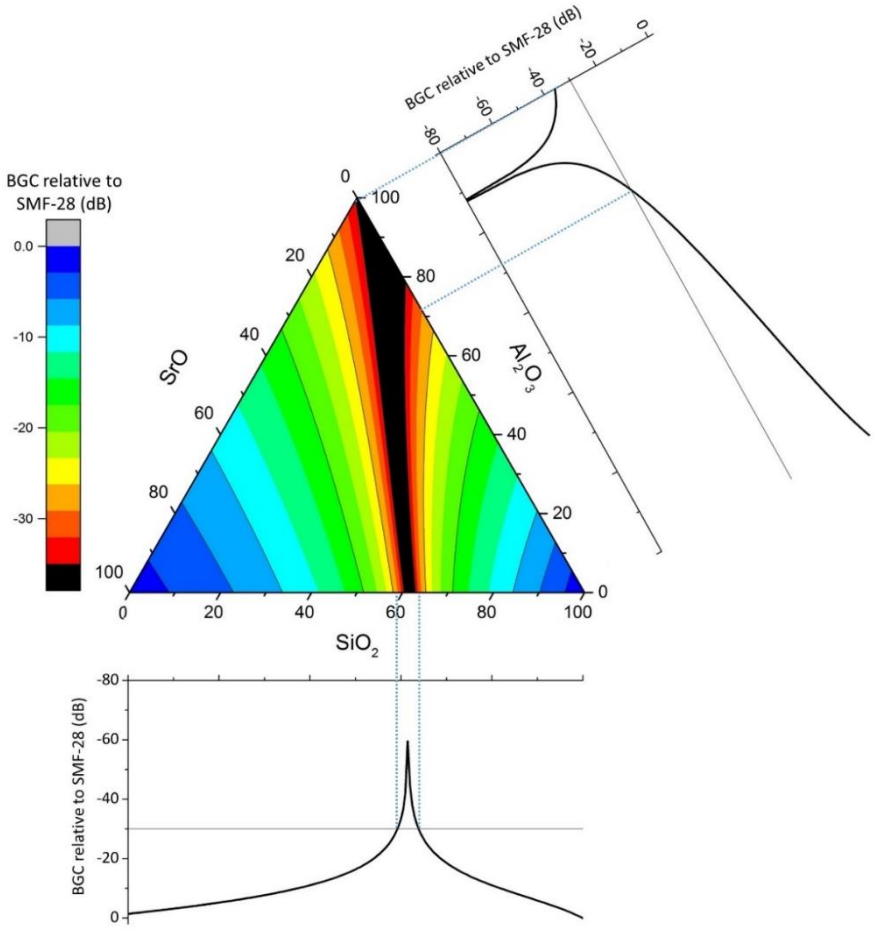

Figure IV.6. Representative ternary property diagram of Brillouin gain coefficient, BGC, in units of dB relative to a conventional single mode telecommunications optical fiber (SMF-28^{TM}), as a function of composition in the SrO – Al_2O_3 – SiO_2 system. The associated binary BGC diagrams for the SrO – SiO_2 and Al_2O_3 – SiO_2 systems also are shown as a guide-to-the-eye regarding trends in the ternary. Values are deduced using the approaches described in Chapters II and III.

IV. D. 2. Intrinsically low (classical) Rayleigh scattering glasses

As a brief reminder, Rayleigh scattering arises from fluctuations in both composition and density. Admittedly, compositional contributions are more difficult to estimate given unknown additivity / deduction of fictive temperatures and chemical potential. As such, just the contributions associated with density will be considered in this Section. That said, while both the refractive index and isothermal compressibility (through the elastic constants) can be estimated, only the photoelasticity (p) will be discussed as it, of the material factors influencing Rayleigh scattering, has the most reasonable potential to take on a value of zero or, at least, be significantly reduced.

Based on deduction of the photoelasticity as described in Chapter II, Fig. IV.7 provides property value diagrams for hydrostatic photoelasticity coefficient, $p = p_{12} + (2/3)p_{44}$, for selected compositional families for the compounds noted above. In the glass systems commonly employed in telecommunication fibers (GeO_2, P_2O_5, and B_2O_3), there are no markedly interesting effects to employ. The inclusion of Al_2O_3, however, begins to drive reductions in aggregate p values due to its low photoelasticity. This is further exemplified with alkaline earth oxide dopants, notably SrO and BaO whereby $p = 0$ compositions can be identified. At these compositions, density contributions to Rayleigh scattering should be zero and marked reductions in the overall Rayleigh scattering should be significant. Again, as noted in Chapter I, while Rayleigh scattering is not, per se, a parasitic nonlinearity as relates to high energy fiber lasers, it can seed other stimulated

processes. Further, it contributes to the fiber's base attenuation. Accordingly, any reduction of Rayleigh scattering is beneficial.

With respect to conventional telecommunication dopants, P_2O_5 and B_2O_3 possess negative dn/dT values whereas GeO_2 and SiO_2 possess positive ones. Accordingly, compositions exhibiting intrinsically low thermo-optic effects can be realized using conventional fiber materials and processes, though compatibility with index profiles and modality may be challenging. Of the additional dopants identified in this dissertation, some alkaline earth oxides with SrO, again show intriguing opportunities for low and possibly zero dn/dT values at high SiO_2 concentrations. For completeness, it is worth noting that one would normally expect SrO and BaO to behave somewhat similarly. The differences in compositional thermo-optic trends shown in Fig. IV.8 between the $SrO – P_2O_5 – SiO_2$ / $BaO – P_2O_5 – SiO_2$ and $SrO – Al_2O_3 – SiO_2$ / $BaO – Al_2O_3 – SiO_2$ ternaries result from the difference in sign between TOC(SrO) and TOC(BaO), which are negative and positive, respectively. If the effect of cladding on TOC shown in Chapter III can partly explain this TOC value difference between both alkaline earth oxide, it is admitted its origin remains indeterminate. It is worth mentioning that TOC(BaO) was determined in a binary BaO-SiO_2 glass system [16]. On the other hand, TOC(SrO) was determined in a ternary SrO-Al_2O_3-SiO_2 glass system [17]. The role of Al_2O_3 on the glass structure and polarizability might play a role on the aggregate TOC value of the fiber, as suggested in sodium aluminosilicate glasses [56].

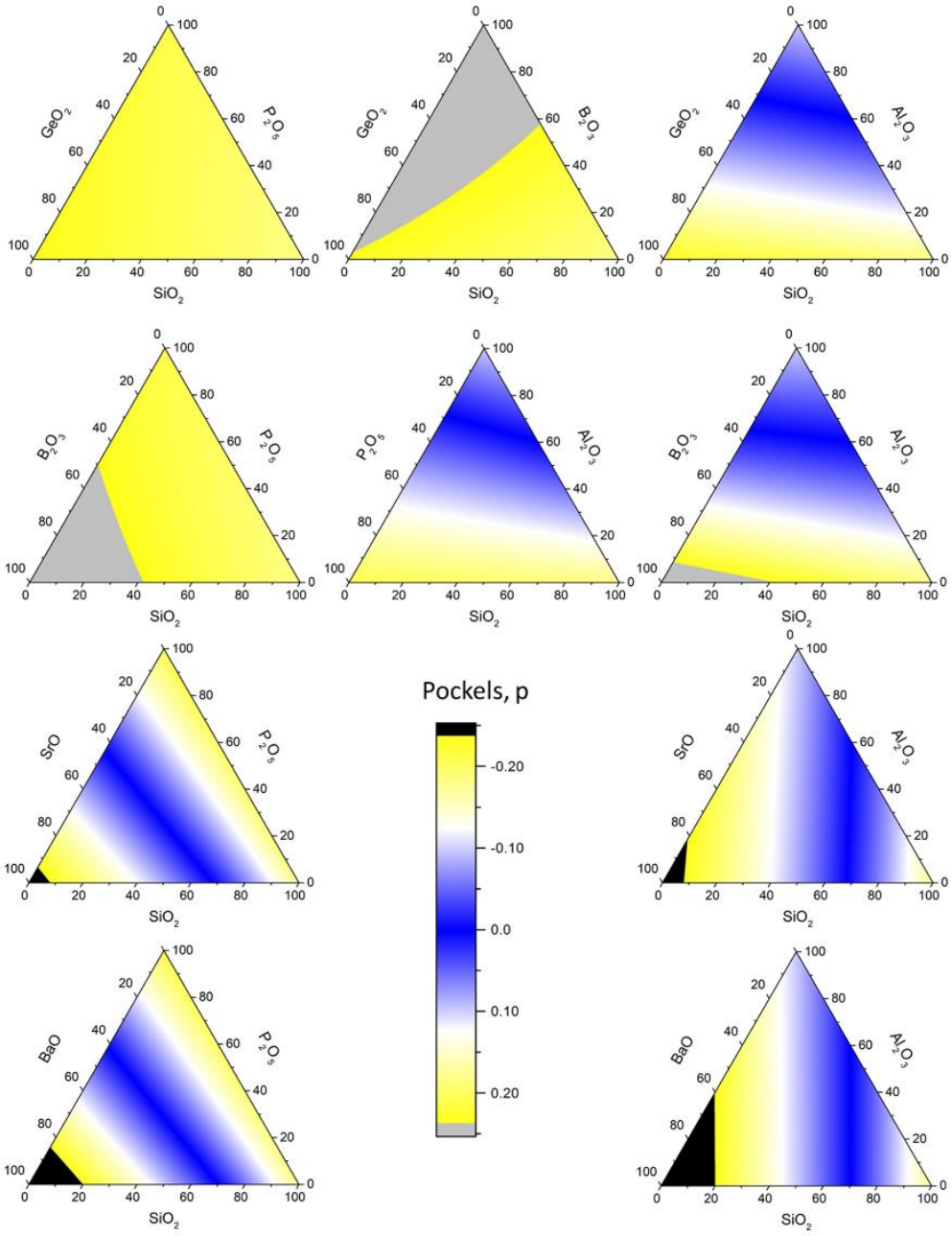

Figure IV.7. Contribution of density-fluctuations to Rayleigh scattering: ternary diagrams of hydrostatic photoelasticity coefficient, $p = p_{12} + (2/3)p_{44}$, for selected compositional families. Values are deduced using the approaches described in Chapters II and III.

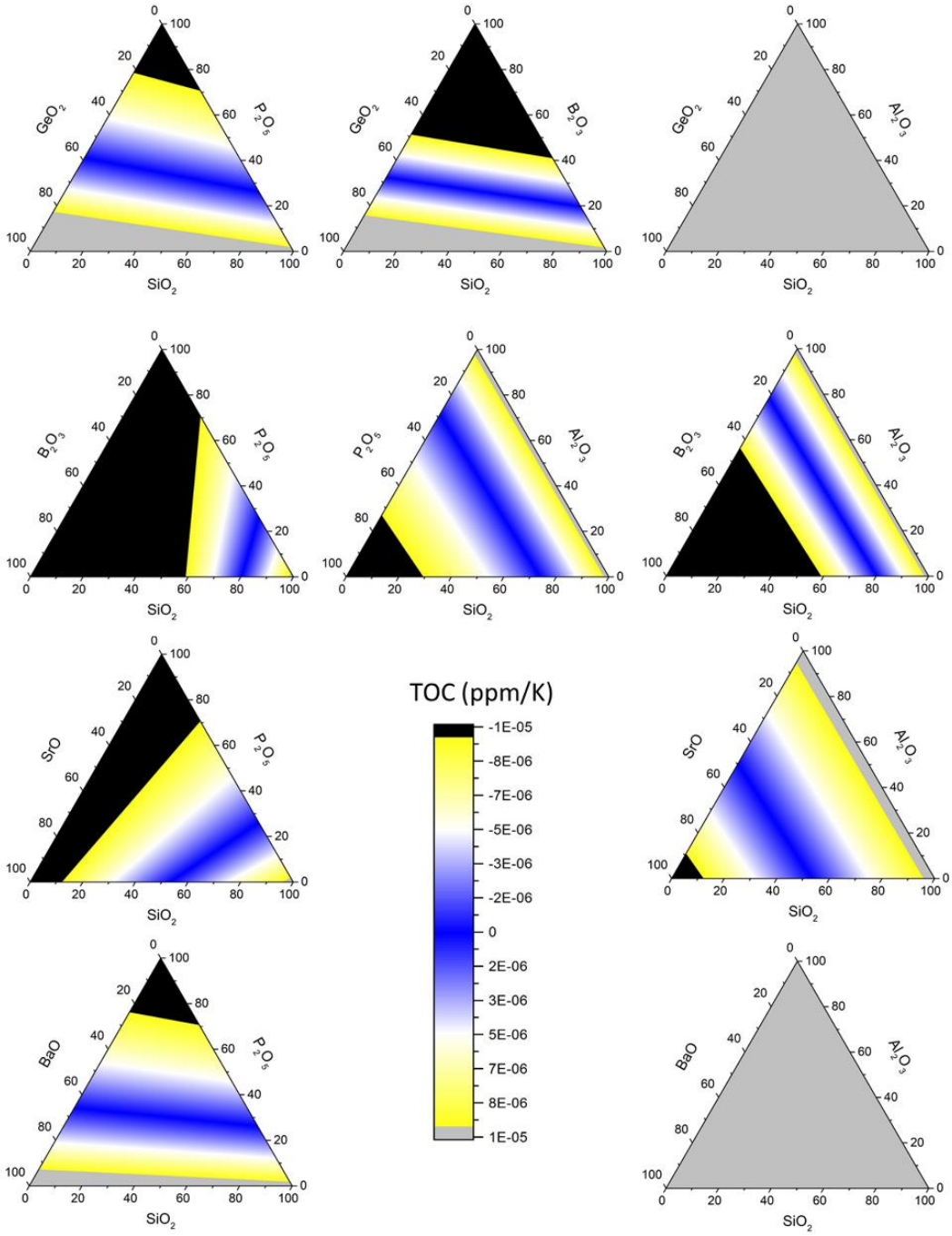

Figure IV.8. Stimulated thermal Rayleigh scattering (STRS): ternary diagrams of thermo-optic coefficient, TOC (dn/dT), for selected compositional families. Values are deduced using the approaches described in Chapters II and III.

IV. D. 3. Intrinsically low Brillouin scattering glasses

In a similar manner, the deduced transverse p_{12} photoelasticity values are shown in Fig. IV.9 for the same glass families. The counter-play between positive and negative p_{12} compounds that was discussed in Chapters I, II, and III, can most clearly be seen in the ternaries possessing Al_2O_3, SrO, and BaO. As expected, given the weak and only slightly negative p_{12} value for Al_2O_3, the zero p_{12} compositions necessarily occur at Al_2O_3 concentrations too high to likely be feasibly made into glass and drawn into fibers. However, both SrO and BaO possess sufficiently large and negative p_{12} values that it is reasonable to expect that bulk glasses could be formed at $p_{12} = 0$ ternary compositions where Brillouin scattering should be negated.

Though mapping out individual material parameters, e.g., p, TOC, and p_{12}, that most influence a given nonlinearity is useful, it is more impactful to understand, where able, all of the underlying factors taken together. Such a complete property value ternary representation is shown in Fig. IV.10 for the Brillouin gain coefficient, BGC, associated with the same systems as described above. Each of the factors used to compute the BGC, as described in Chapter I, were deduced using the approaches described in Chapters II and III.

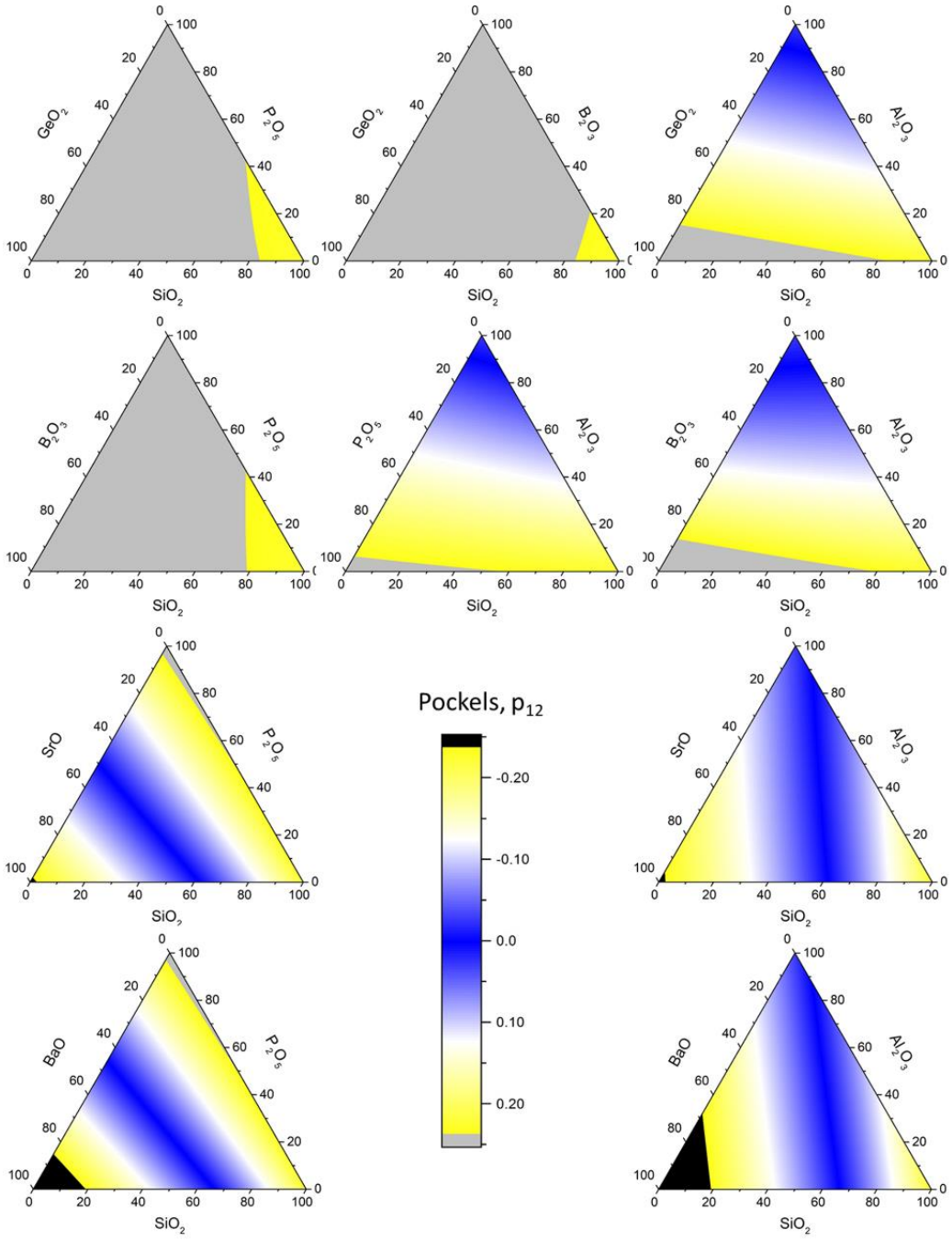

Figure IV.9. Brillouin scattering: ternary diagrams of transverse photoelasticity coefficient, p_{12}, for selected compositional families. Values are deduced using the approaches described in Chapters II and III.

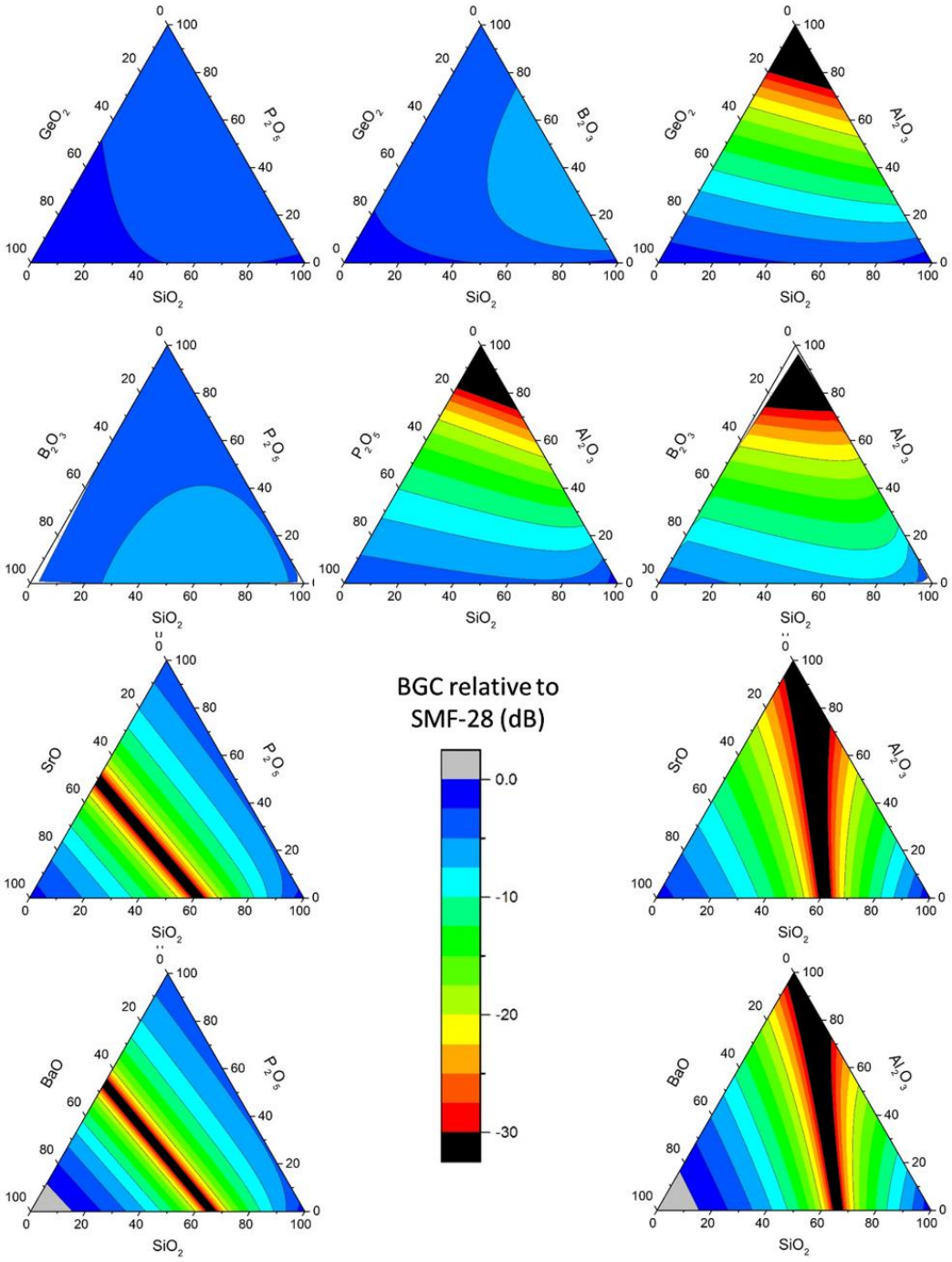

Figure IV.10. Stimulated Brillouin scattering (SBS): ternary diagrams of the Brillouin gain coefficient, BGC, for selected compositional families. Values are deduced using the approaches described in Chapters II and III.

Given the dependence of the BGC on multiple properties (n, p_{12}, ρ, V_a, $\Delta\nu_B$), each one possessing its own compositional trends, the curvature of the contour lines are more complicated than in the single property ternary diagrams; e.g., Figs. IV.7, IV.8, or IV.9. In the ternary diagrams, this manifests interesting and occasionally unexpected compositional trends. The individual BGC binaries that comprise the GeO_2, P_2O_5, B_2O_3-related ternaries with SiO_2 were shown in Fig. III.6 of Chapter III and, not surprisingly, those trends are equally evident in Fig. IV.10. In short, while some reductions (3 – 8 dB) in BGC result from doping SiO_2 with these conventional telecommunication dopants, they do not offer marked mitigations. Important (> 10 dB) reductions are possible with $p_{12} < 0$ dopants, such as Al_2O_3, SrO, and BaO. As noted with respect to Fig. IV.9, it is the large and negative p_{12} values of the alkaline earth oxides that lead to significant (> 15 dB) reductions in BGC even at reasonably high SiO_2 concentrations of about 80 mole percent.

The representations of Fig. IV.10 can be overlaid with similarly important reductions in other parameters, such as in the TOC that drives transverse mode instability (TMI). As a case in point, Fig. IV.11 provides a comparison of compositions that provide significant reductions in both SBS (> 15 dB) and TMI (> 5 dB), relative to conventional single mode fiber, based on the BGC and TOC property value diagrams of Figs. IV.8 and IV.10.

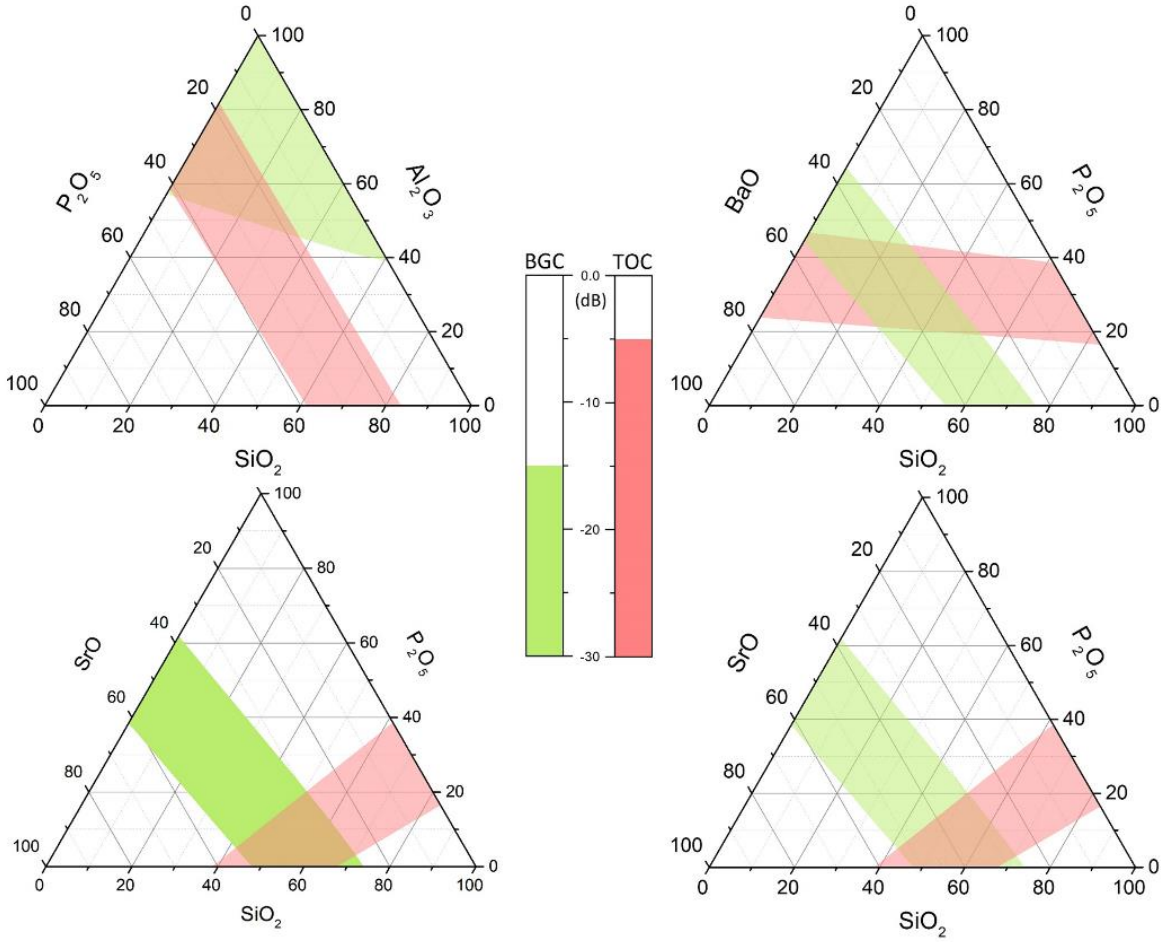

Figure IV.11. Representative ternary compositional diagrams overlaying both Brillouin gain coefficient, BGC, and thermo-optic coefficient, TOC, relative to those for conventional telecommunications single mode fiber, for the reduced magnitudes for these nonlinearities that are the goal of this work.

IV. D. 4. Modeling of the high power / energy performance

The power-scaling potential of the intrinsically low nonlinearity fibers fabricated to-date were modeled using the procedures described in [57]. These results, compared to values for conventional Yb^{3+} doped silica fiber lasers are presented in Fig. IV.12 with the underlying known and estimated material parameters provided in Table IV.2.

As in [57], the simplest fiber geometry is assumed (no advanced waveguide schemes) and for the SBS limited case, single frequency amplification is assumed. Controlled line-broadening is well known to increase the SBS limited output power. However, when this technique is employed [58], one must understand the acceptable line broadening allowed by the application as well as the SBS linewidth of the proposed material. The SBS linewidth is not included in Table IV.2 and is not relevant to Fig. IV.12 due to the assumption of single frequency amplification for the SBS limited case.

It is important to note that Dawson, et al. [57], pre-dates the discovery of transverse modal instability, TMI [47], [59]. Given that a simple predictive model for transverse modal instability is still not fully formed and agreed upon, included here is the better understood effect of thermal lensing as an (imperfect) proxy for transverse modal instability. A study of Table IV.2 will reveal that a number of important material properties are not known for the candidate all-glass fibers treated: YAG-derived yttrium aluminosilicates [20], sapphire-derived aluminosilicates [55], and low silica content

strontium aluminosilicates [17]. Of these, damage threshold and thermal conductivity are the greatest sources of uncertainty in the calculation that produced Fig. IV.12.

The graphs in Fig. IV.12 are generated by the methodology of Dawson, et al. [57]. In this methodology, the physical effects that limit the power scaling of a single fiber laser are expressed as functions of fiber core diameter and fiber length. All parameters except core diameter and fiber length are either state-of-the-art parameters (such as diode laser brightness, which is generally improving with time) or physical constants of the material system, which are varied to greater extent in this dissertation. The main physical effects that are considered are thermal (melting, rupture, lensing), optical nonlinearities (SRS and SBS, note these are typically considered on separate plots depending upon which one dominates based on laser spectral line-width), optical damage and limitations on pump power. Pump power limitations come about from the necessity for a high power laser to be efficient in order to be practical. This requirement means that most of the pump light must be absorbed in the length of the fiber. Thus Dawson, et al. [57] show that if the fiber length is known, then the core diameter, doping concentration and state of the art diode brightness determine the allowed fiber cladding diameter, which in turn limits the total coupled pump power. As the fiber laser efficiency is typically ~ 85%, this, in turn, creates a power-limit based on the amount of pump power that can be efficiently coupled into the fiber laser.

The contour plots in Fig. IV.12 are formed by calculating all the physical limits for each pair of coordinates (core diameter and fiber length) and plotting the lowest limit. What

emerges are regions where different limits dominate. At the smallest core diameters and shortest lengths (lower left hand corner of the graphs), the pump coupling limit typically dominates. For large core diameters and short fiber lengths (lower right side of the plots), the heat load per unit length is high and thermal effects typically are dominant. For small core diameters and long lengths (upper left side of the plots), the light is intense over a long length of fiber and either damage or non-linear optical effects limit the fiber output power. A key finding of Dawson, et al. [57] is that the interaction of thermal and nonlinear effects typically set a hard upper limit on output power from a single optical fiber laser for a given material system that is largely independent of core diameter and fiber length, though there is a specific length associated with each core diameter at which this limit is attained. Below the variations of material parameters considered in this paper are discussed in terms of how they affect the relative size of the regions and ultimate scaling limit of a given material system.

Four main parameters that are assumed to be improved in the three materials: rare-earth doping concentration, TOC (dn/dT), Raman, and Brillouin gain coefficients. The primary impact of increased doping concentration is to reduce the parameter space over which limited pump coupling dominates the fiber laser output power. More specifically:

- YAG-derived yttrium aluminosilicates: A slight increase in the SRS-limited power due to reduced Raman gain coefficient is observed as is an expected reduction in pump-limited parameter space. However, this reduction is offset by the formation of a damage

threshold limited region (again, accurate knowledge of the damage threshold is needed). The SBS limited case shows a > 3 times increase in output power due to a significant reduction in the BGC. Importantly, this is attained at a 40 μm core diameter due to the reduction in the pump limited parameter space.

- Sapphire-derived aluminosilicates: As with the YAG-derived glass, slight improvements are observed in the SRS-limited case other than the reduction in the pump limited zone and appearance of the damage limited zone. However, there is now a dramatic increase in the SBS limited power to > 10 times the conventional silica case. This is a direct result of the 100 times decrease in BGC. Core size remains in the 40 μm region, a relatively practical zone from the standpoint of both fabrication and bending.

- Low silica strontium aluminosilicates: In this case a 2 times increase in power in the SRS limited power is observed due to the reduced Raman gain and reduced TOC. Here the calculation's exclusion of an analysis of TMI is cause for some skepticism of this result. The SBS limited case shows a further increase in the SBS limited power due to the additional reduction in the SBS gain coefficient as well as the reduction in TOC.

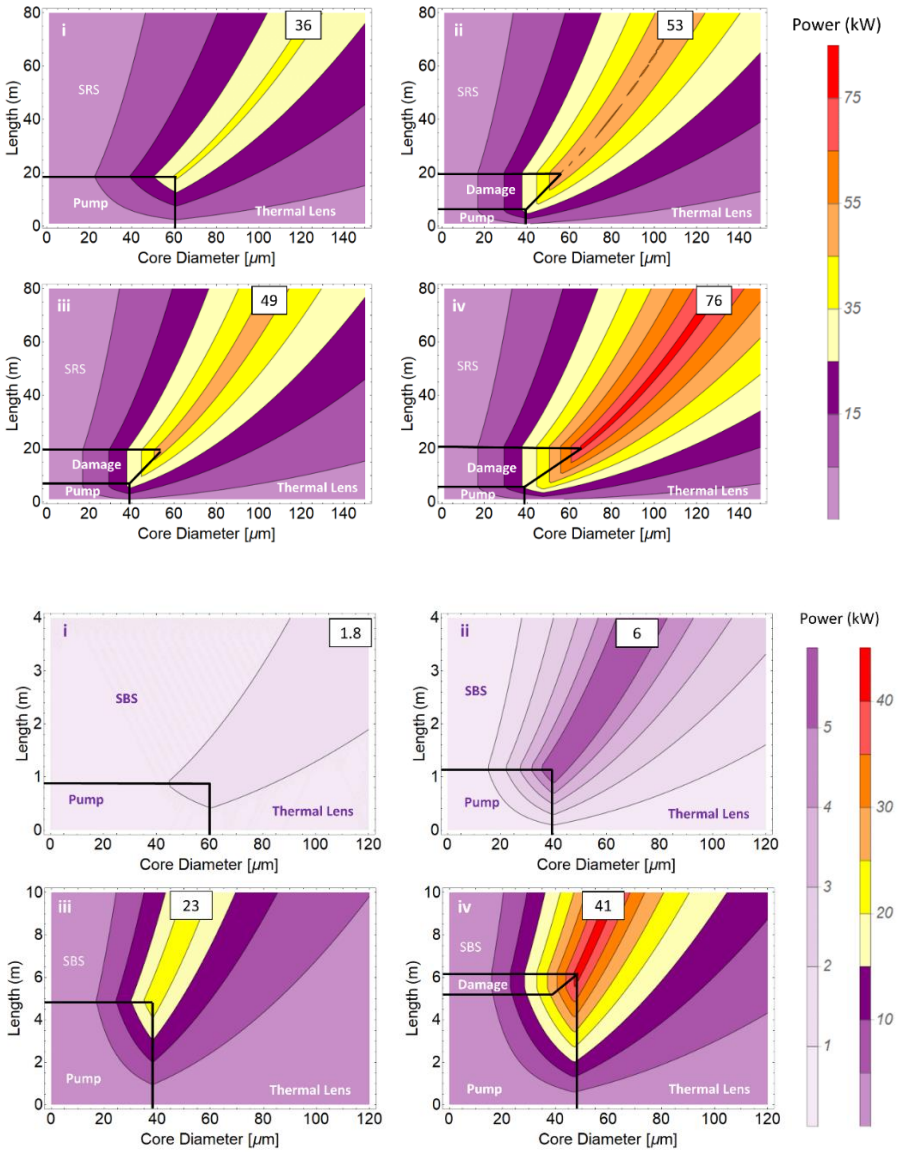

Figure IV.12. Power-scaling diagrams representing the threshold optical power levels where power-scaling is limited by either pump brightness, laser damage, thermal lensing and (a) stimulated Raman scattering (SRS) or (b) stimulated Brillouin scattering (SBS) regimes. In both sets of Figures, the optical fibers modeled are: (i) conventional SiO_2 [57], (ii) YAG-derived [20], (iii) sapphire-derived [55], (iv) strontium aluminosilicates [17].

Table IV.2. Material parameters employed for the calculation of power scaling plots based on [57].

Property (unit)[a]	Conventional value	YAG-derived	Sapphire-derived	Low silica
Non-SiO_2 Content	-	Al_2O_3: 19.9	Al_2O_3: 54.0	SrO: 23.7
Rupture Modulus	4300	4300	4300	4300
Thermal	1.38	1.38	1.38	1.38
Convective film	10000	10000	10000	10000
Melt temperature	1983	1983	1983	1983
dn/dT (K^{-1})	11.8×10^{-6}	10.1×10^{-6}	11.9×10^{-6}	5.3×10^{-6}
g_R (m/W)	1×10^{-13}	0.52×10^{-13}	0.54×10^{-13}	0.5×10^{-13} (est.)
BGC (m/W)	5×10^{-11}	0.5×10^{-11}	3.1×10^{-13}	2.2×10^{-13}
A[c]	20	20	20	20
G[c]	10	10	10	10
Γ[c]	0.8	0.8	0.8	0.8
Damage threshold	35	35	35	35
T_c (K)[c]	300	300	300	300
I_{pump} ($W/\mu m^2/sr$)[c]	0.1	0.1	0.1	0.1
α_{core} (dB/m)[d]	250	1500	1500	1500
η_{laser}[c]	0.85	0.85	0.85	0.85
η_{heat}[c]	0.1	0.1	0.1	0.1
NA[c]	0.45	0.45	0.45	0.45
λ (nm)[c]	1088	1088	1088	1088

[a]: Where not specified, see Ref. [57] for details on a given property.

[b]: Values are unknown for the 3 aluminosilicate systems but, given their relatively high SiO_2 contents, the values for silica are employed as a limit.

[c]: Values reasonably carried over to the 3 aluminosilicate systems.

[d]: Tailorable via precursor Yb concentration.

Overall, these results show promise for improved materials for high energy lasers, particularly narrow bandwidth lasers limited by SBS. The improvements are predominantly due to the increase in doping concentration (reduction in SiO_2 content), which allows the maximum power to be attained at smaller core diameters which reduces thermal effects in general, and is known to be desirable for decreased TMI as the purely single mode waveguide regime is more effectively maintained. Further, dramatically reduced Brillouin gain greatly raises the power threshold for the onset of SBS. Note the maximum power in the SBS case increases as the square root of the reciprocal of the BGC per Equation 27 in [57]. This suggests further development of these classes of materials are a promising approach for scaling power in SBS-limited fiber laser systems with the caveat that a number of the assumed material parameters in Table IV.2 need to be determined and Fig. IV.12 needs to be updated to validate that the true values of these parameters do not affect the conclusions made here.

IV. D. 5. Towards the "perfect" optical fiber

With respect to the best results to date, "best," is somewhat arbitrary as the ideal case is one where all of the nonlinearities are reduced by levels that make the fiber more practical. For example, while ~ 20 dB suppression has been achieved in a sapphire-derived, high alumina-content aluminosilicate glass fibers [55], that fiber was highly multimoded and exhibited a 2.5 dB suppression in Raman gain. Unfortunately, a simple aluminosilicate system does not yield materially reduce parameters such as n, n_2, and dn/dT relative to conventional silica-based fibers. Therefore, and as was discussed throughout this Chapter

and Chapters II and III, the consideration of a more multicomponent system (ternary or greater) is necessary to address each optical nonlinearity materially. In Section IV. D., a variety of multicomponent systems were investigated and their properties modeled. In the realm of the fabrication of a "perfect" fiber as expressed herein, it is necessary to find a material system that can both mitigate all nonlinearities at once but also form a glass material. It is identified here that SrO-Al_2O_3-SiO_2 is a particularly interesting candidate to mitigate SBS, SRS, and TMI. However, considering only this oxide-based system does not provide a solution in reducing n and n_2. As discussed in Chapters II, and III but also noted in Section IV. D., F-containing glasses yield to low n and n_2 materials. As will be discussed in the following Chapter, the substitution of an alkaline earth oxide with an alkaline earth fluoride as a precursor material using the molten core method allows the possibility in introducing fluorine into the glass core. Therefore, alkaline earth fluoro-alumino-silicate systems are considered as promising candidates in the development of intrinsically low optical nonlinearity materials.

As noted in Table I.1 of Chapter I, and described in terms of specific compositions in this paper, each of the parasitic nonlinearities possess the potential to be wholly negated. In some cases, such as with Raman scattering and n_2-related wave-mixing phenomena, the necessary conditions of $\Lambda = 0$ and $n_2 = 0$, respectively, though theoretically possible, seem at present not materially practical. However, the two main phenomena that presently limit power-scaling in high power fibers laser systems, namely SBS and TMI, should be quite reasonably mitigated. In these cases, the $p_{12} = 0$ and $dn/dT = 0$ conditions, respectively, are

well-defined over practically large compositional ranges. Of particular interest are compositional spaces where these zero-points approximately coincide. Examples of these are those shown in Fig. IV.13, which, along with the aforementioned $p_{12} = 0$ and $dn/dT = 0$ compositions, includes $p = 0$ compositions where the density-related contribution to Rayleigh scattering also would be zero.

In Fig. IV.13, it is interesting to note that a BaO - P_2O_5 - SiO_2 system would be of potential interest as in the 40 BaO – 30 P_2O_5 – 30 SiO_2 composition p, p_{12}, and dn/dT could potentially exhibit near to zero value. However, it should be mentioned that there is no evidence to-date that the additivity approaches used to generate these ternaries diagrams would still hold (i.e., not break down) for these low silica materials. It is also worth noting that glass forming regions of these materials remain uncertain. Additionally, the inherent silica incorporation during fiber drawing (Chapter V) is expected to be a difficult obstacle in the formation of such low silica materials. Again, significant reduction (>3-5 dB) of properties that drive optical nonlinearities relative to conventional silicate fibers is of more practical interest that their complete eradication.

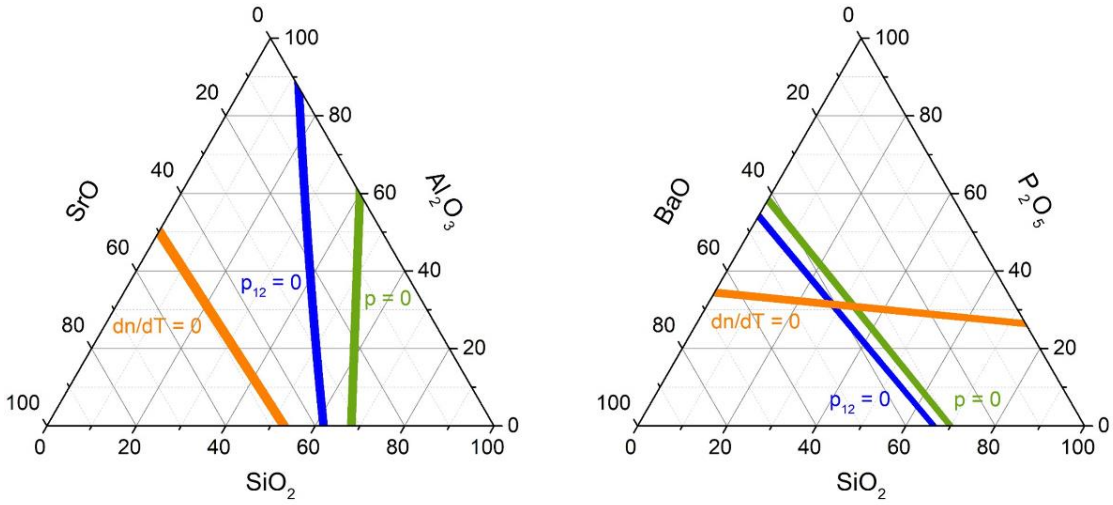

Figure IV.13. Ternary compositional diagrams in the SrO – Al_2O_3 – SiO_2, and BaO – P_2O_5 – SiO_2 systems showing the ranges over which the hydrostatic photoelasticity, p, the transverse photoelasticity, p_{12}, and the thermo-optic coefficient, dn/dT (TOC), are each zero. At compositions where they intersect, the glass should exhibit no Brillouin scattering (p_{12} = 0), density-related Rayleigh scattering (p = 0), and stimulated thermal Rayleigh scattering (TOC = 0); the latter driving transverse mode instabilities in high power fiber lasers.

The compositions identified herein that exhibit markedly reduced collective nonlinearities are beyond the capabilities of industry standard CVD processes used to fabricate conventional (telecom) optical fibers. High-silica-content CVD-derived fibers will remain the industry standard for long-haul communications with evolutionary progress in attenuation being made through process-related thermal history (fictive temperature [60]) and minor dopant engineering [10], [11]. However, to be clear, in order to achieve the power-scaling goals of high power / energy, high beam quality fiber-based lasers,

conventional CVD processes will not be sufficient due to the limited compositional ranges of such processes. Structural / geometric approaches, such as those associated with microstructured and photonic crystal fibers, employing conventional CVD-derived high-silica-content glasses, certainly will continue to make incremental improvements. But revolutionary advances such as > 20 – 30 dB reductions, or even the wholesale negation of Brillouin-related SBS and thermo-optic-related STSR-induced TMI, can only be achieved through a unified materials approach where parasitic nonlinearities are addressed at their fundamental origins.

IV. E. Conclusion

This Chapter provides a road map to glass compositions that would markedly reduce the optical nonlinearities that plague the scaling to higher output powers in present telecommunication and high power fiber lasers. More specifically, based on the theoretical foundations of Chapter I, coupled with the property additivity relations of Chapter II and III, described here are compositional trends to tailor Brillouin-, Raman-, Rayleigh-, thermo-optic-, and $\chi^{(3)}$-related material properties. Examples from existing fibers and bulk glasses are employed where data are available. Further, ternary property value diagrams are employed to more easily represent and identify compositional regions where the greatest opportunities for mitigating nonlinearities are possible. In the specific case of yttrium and strontium aluminosilicate fibers variations in the material could lead to power increases of 2 – 3x or more over current fiber lasers based on classical fused silica compositions. Note this is before other effects such as deliberate linewidth broadening or advanced waveguide design are employed to further scale the output power. It is worth mentioning here that attenuation losses for these fabricated fibers are currently a limit. This point is further developed in Chapter VII where approaches to reduce attenuation losses are proposed.

Further, the impact of higher concentration by itself should not be underestimated as it simplifies the overall requirements on the diode laser portion of the integrated system. Oxyfluoride aluminosilicate glasses containing alkaline earth compounds, potentially with

B_2O_3 and P_2O_5 additions, are especially worthy of further consideration based on their potential to significantly reduce Brillouin, Raman, Rayleigh, and stimulated thermal Rayleigh scattering while possessing a nonlinear refractive index comparable to conventional silica and could potentially lead to much greater power scaling if, for example, the BGC could be reduced beyond that assumed in Table IV.2. In the following Chapter (Chapter V), efforts will be put forward in the fabrication of alkaline earth oxyfluoride glass optical fibers, again due to their specific potential in mitigating optical nonlinearities. Furthermore, an understanding of the glass structure and composition of these oxide-fluoride systems and the role of fiber processing on them will be provided. In Chapter VI, properties that relate to optical nonlinearities are studied and, based of the founding of Chapter V, a comprehensive discussion between properties and composition/structure relationships is given.

IV. F. Appendices

Appendix IV. 1. Matlab code used to generate ternary (and binary) diagrams

```
clear all; close all;
%PART I: DATA

% INFO Parameters: Va (m/s); ? (g/m3); ?vB (MHz); n (15XXnm); p12; M
% (g/mol; m (m/s); lembda (m)
%General parameters
c=3*10^8; lembda=1.534*10^-6;

% PARAMETERS SiO2
VaS=5970; rhoS=2200000; DvBS=17; nS=1.444; p12S=0.226; p11S=0.098; MS=60.08;
muS=0.16; alphaS=8946; TOCS=10.4*10^-6; n2S=2.66*10^-20; %alphaS=8946;
alphaS=(DvBS*10^6*pi)/VaS;

% PARAMETERS Al2O3
VaA=9790; rhoA=3350000; DvBA=274; nA=1.653; p12A=-0.027; p11A=-0.237;
MA=101.96; muA=0.25; alphaA=87926; TOCA=10.5*10^-6; n2A=4.77*10^-20;

 % PARAMETERS "X" compound
%BaO
%VaX=3131; rhoX=4688000; DvBX=178; nX=1.792; p12X=-0.330; p11X=-0.330;
MX=153.33; muX=0.31; alphaX=178600; TOCX=12.7*10^-6;
%SrO
VaX=3785; rhoX=4015000; DvBX=187; nX=1.81; p12X=-0.245; p11X=-
0.296;MX=103.62; muX=0.231; alphaX=155000; TOCX=-12.4*10^-6; n2X=5.06*10^-
20;
%B2O3
```

```
%VaX=3315; rhoX=1820000; DvBX=427.8; nX=1.410; p12X=0.298; p11X=0.25;
MX=69.6182; muX=0.29; alphaX=(DvBX*10^6*pi)/VaX;  TOCX=-30*10^-6;
%P2O5
%VaX=3936; rhoX=2390000; DvBX=176.8; nX=1.487; p12X=0.252; p11X=0.132;
MX=141.94; muX=0.294; alphaX=(DvBX*10^6*pi)/VaX; TOCX=-13.3*10^-6;
%GeO2
%VaX=3752; rhoX=3650000; DvBX=124; nX=1.571; p12X=0.288; p11X=0.13;
MX=104.61; muX=0.212; alphaX=(DvBX*10^6*pi)/VaX; TOCX=19.4*10^-6;

%%%%%%%%%%%%%%%%%%%%%%%%%%%%%%%%%%%

% PART II: ADDITIVE MODEL TERNARY "SiO2-Al2O3-X"
step=0.1;
i=1;

for s=0:step:100;
   W=100-s;
 for a=0:step:W;
    x=W-a;

        %Calculation of volume fractions
        volS=(s*MS/rhoS)/(s*MS/rhoS+a*MA/rhoA+x*MX/rhoX);
        volX=(x*MX/rhoX)/(s*MS/rhoS+a*MA/rhoA+x*MX/rhoX);
        volA=(a*MA/rhoA)/(s*MS/rhoS+a*MA/rhoA+x*MX/rhoX);

        %Additive model aggregate value calculation

        %REFRACTIVE INDEX, DENSITY, ACOUSTIC VELOCITY, POISSON:
        n=volS*nS+volX*nX+volA*nA;
```

```
        Index(i)=n;
        rho=volS*rhoS+volX*rhoX+volA*rhoA;
        RHO(i)=rho/1000;
        Va=(volS/VaS+volX/VaX+volA/VaA)^-1;
        VA(i)=Va;
        mu=volS*muS+volX*muX+volA*muA;
        MU(i)=mu;

        %POCKELS COEFFICIENT P12:
        SigcoS=(p11S-2*muS*p12S); SigcoA=(p11A-2*muA*p12A); SigcoX=(p11X-
2*muX*p12X);

Sigco=(2/n^3)*((((nS^3)/2)*SigcoS*volS)+(((nA^3)/2)*SigcoA*volA)+(((nX^3)/2)*Sig
coX*volX));
        StracoS=p12S-muS*(p11S+p12S); StracoA=p12A-muA*(p11A+p12A);
StracoX=p12X-muX*(p11X+p12X);

Straco=(2/n^3)*((((nS^3)/2)*StracoS*volS)+(((nA^3)/2)*StracoA*volA)+(((nX^3)/2)*St
racoX*volX));
        p12(i)=(Straco+mu*Sigco)/((1-2*mu)*(1+mu));

        %POCKELS COEFFICIENT P11:
        p11(i)=Sigco+2*mu*p12(i);

        %POCKELS COEFFICIENT P44:
        p44(i)=(p11(i)-p12(i))/2;

        %POCKELS COEFFICIENT P for Rayleigh concentration contribution
        p(i)=p12(i)+(2/3)*p44(i);
```

```
p_square(i)=p(i)^2;

%BRILLOUIN BANDWIDTH:
alpha=volS*alphaS+volA*alphaA+volX*alphaX;
frequencylist=Va*2*n/lembda;
alphafixed=((frequencylist/(11*10^9))^2)*alpha;
DvB=(10^-6)*Va*alphafixed/pi;
DVB(i)=DvB;

DvBS=(10^-6)*VaS*((VaS*2*nS/lembda/(11*10^9))^2)*alphaS/pi;
DvBA=(10^-6)*VaA*((VaA*2*nA/lembda/(11*10^9))^2)*alphaA/pi;
DvBX=(10^-6)*VaX*((VaX*2*nX/lembda/(11*10^9))^2)*alphaX/pi;

frequencylistS=VaS*2*n/lembda;
alphafixedS=((frequencylistS/(11*10^9))^2)*alphaS;

%TOC:
TOC(i)=volS*TOCS+volA*TOCA+volX*TOCX;
TOCnormSilica(i)=10*log10(abs(TOC(i)/(TOCS))); %%% gives complex number because log(-x) gives complex results!
TOCnormSilicaMagnitude(i)=10*log10(abs(TOC(i))/(TOCS)); %%% gives magnitude of TOC relative to Silica (absolute values taken!)
% n2:
% n2(i)=volS*n2S+volA*n2A+volX*n2X;

%BRILLOUIN GAIN:
% Silica %
gBS=((((p12S^2)*nS^7)*2*pi)/(c*lembda*lembda*VaS*rhoS*(10^-3)*(DvBS*10^6)));
```

```
        % Aggregate value %
        gB(i)=((((p12(i)^2)*n^7)*2*pi)/(c*lembda*lembda*Va*rho*(10^-
3)*(DvB*10^6)));
        gBnormSMF28(i)= 10*log10(gB(i)/(2.5*10^-11));
        gBnormSilica(i)= 10*log10(gB(i)/(gBS));

        % Axis
        %Silica
        S(i)=s;
        %Alumina
        A(i)=a;
        %Compound X
        X(i)=x;

        % Iteration
        i=i+1;
    end
end
```

IV. G. References

[1] K. Oh and U.-C. Paek, *Silica Optical Fiber Technology for Devices and Components: Design, Fabrication, and International Standards*. New York, NY: John Wiley & Sons, 2012.

[2] P. Dragic and J. Ballato, "Rethinking Optical Fiber: New Demands, Old Glasses," *J. Am. Ceram. Soc.*, vol. 96, no. 9, pp. 2675–2692, 2013.

[3] B. S. Morris and J. Ballato, "Molten-core fabrication of novel optical fibers," *Am. Ceram. Soc. Bull.*, vol. 92, no. 4, pp. 24–29, 2013.

[4] D. A. Pinnow, T. C. Rich, F. W. Ostermayer, and M. Didomenico, "Fundamental optical attenuation limits in the liquid and glassy state with application to fiber optical waveguide materials," *Appl. Phys. Lett.*, vol. 22, no. 10, pp. 527–529, 1973.

[5] J. Schroeder, R. Mohr, P. B. Macedo, and C. J. Montrose, "Rayleigh and Brillouin Scattering in K_2O-SiO_2 Glasses," *J. Am. Ceram. Soc.*, vol. 56, no. 10, pp. 510–514, 1973.

[6] N. L. Laberge, V. V. Vasilescu, C. J. Montrose, and P. B. Macedo, "Equilibrium Compressibilities and Density Fluctuations in K_2O-SiO_2 Glasses," *J. Am. Ceram. Soc.*, vol. 56, no. 10, pp. 506–509, 1973.

[7] A. R. Tynes, A. D. Pearson, and W. R. Northover, "Rayleigh Scattering Losses in Soda Borosilicate Glasses," *J. Am. Ceram. Soc.*, vol. 62, no. 7–8, pp. 324–326, 1979.

[8] D. A. Pinnow, L. G. Van Uitert, T. C. Rich, F. W. Ostermayer, and H. W.

Grodkiewicz, “Investigation of the soda aluminosilicate glass system for application to fiber optical waveguides,” *Mater. Res. Bull.*, vol. 10, no. 2, pp. 133–146, 1975.

[9] K. Tsujikawa and M. Ohashi, “Mixed-alkali effect on Rayleigh scattering in K_2O–Na_2O–MgO–SiO_2,” *J. Am. Ceram. Soc.*, vol. 83, no. 3, pp. 660–662, 2000.

[10] M. E. Lines, “Can the minimum attenuation of fused silica be significantly reduced by small compositional variations? I. Alkali metal dopants,” *J. Non. Cryst. Solids*, vol. 171, no. 3, pp. 209–218, 1994.

[11] M. E. Lines, “Can the Minimum Attenuation of Fused-Silica Be Significantly Reduced By Small Compositional Variations? II. Combined Fluorine and Alkali-Metal Dopants,” *J. Non. Cryst. Solids*, vol. 171, no. 3, pp. 219–227, 1994.

[12] J. O. Isard, “The mixed alkali effect in glass,” *J. Non. Cryst. Solids*, vol. 1, no. 3, pp. 235–261, 1969.

[13] D. J. DiGiovanni, J. B. MacChesney, and T. Y. Kometani, “Structure and properties of silica containing aluminum and phosphorus near the $AlPO_4$ join,” *J. Non. Cryst. Solids*, vol. 113, no. 1, pp. 58–64, 1989.

[14] P. Dragic and J. Ballato, “Pockels’ coefficients of alumina in aluminosilicate optical fiber,” *J. Opt. Soc. Am.*, vol. 30, no. 2, pp. 244–250, 2013.

[15] P. Dragic, T. Hawkins, P. Foy, S. Morris, and J. Ballato, “Sapphire-derived all-glass optical fibres,” *Nat. Photonics*, vol. 6, no. 9, pp. 629–635, 2012.

[16] P. Dragic, C. Kucera, J. Furtick, J. Guerrier, T. Hawkins, and J. Ballato, “Brillouin spectroscopy of a novel baria-doped silica glass optical fiber,” *Opt. Express*, vol.

21, no. 9, pp. 10924–10941, 2013.

[17] M. Cavillon *et al.*, “Brillouin Properties of a Novel Strontium Aluminosilicate Glass Optical Fiber,” vol. 34, no. 6, pp. 1435–1441, 2016.

[18] P. D. Dragic, C. Kucera, J. Ballato, D. Litzkendorf, J. Dellith, and K. Schuster, “Brillouin scattering properties of lanthano-aluminosilicate optical fiber.,” *Appl. Opt.*, vol. 53, no. 25, pp. 5660–71, 2014.

[19] A. Mangognia *et al.*, “Spinel-derived single mode optical fiber,” *Opt. Mater. Express*, vol. 3, no. 4, p. 511, 2013.

[20] P. Dragic, P.-C. Law, J. Ballato, T. Hawkins, and P. Foy, “Brillouin spectroscopy of YAG-derived optical fibers.,” *Opt. Express*, vol. 18, no. 10, pp. 10055–67, 2010.

[21] K. Arai, H. Namikawa, K. Kumata, Y. Ishii, H. Tanaka, and I. Iida, “Fluorescence and its Nd^{3+} Concentration Dependence of Nd-Doped SiO_2 Glasses Prepared by Plasma Torch CVD,” *Jpn. J. Appl. Phys.*, vol. 22, no. Part 2, No. 7, pp. L397--L399, 1983.

[22] B. Hatta and M. Tomozawa, “Effect of Al_2O_3 on phase separation of SiO_2-Nd_2O_3 glasses,” *J. Non. Cryst. Solids*, vol. 354, no. 27, pp. 3184–3193, 2008.

[23] J. Ballato and P. Dragic, “On the Clustering of Rare Earth Dopants in Fiber Lasers,” *J. Dir. Energy*, vol. 6, pp. 175–181, 2017.

[24] J. E. Shelby, “Effect of morphology on the properties of alkaline earth silicate glasses,” *J. Appl. Phys.*, vol. 50, no. 12, pp. 8010–8015, 1979.

[25] T. P. Seward, D. R. Uhlmann, and D. Turnbull, “Phase Separation in the System

BaO-SiO2," *J. Am. Ceram. Soc.*, vol. 51, no. 5, pp. 278–285, May 1968.

[26] H. Coker, "The electronic strain polarizability constants of the alkali halides," *J. Phys. Chem. Solids*, vol. 40, no. 12, pp. 1079–1088, 1979.

[27] W. Kucharczyk, "Photoelastic effect and density derivative of the refractive index in alkali halides," *J. Phys. Chem. Solids*, vol. 50, no. 7, pp. 709–712, 1989.

[28] H. P. Sharma, J. Shanker, and M. P. Verma, "Evaluation of strain polarizability parameter in alkali halides," *J. Phys. Chem. Solids*, vol. 38, no. 3, pp. 255–256, 1977.

[29] M. E. Lines, "A possible non-halide route to ultralow loss glasses," *J. Non. Cryst. Solids*, vol. 103, no. 2–3, pp. 279–288, 1988.

[30] J. Schroeder, "Brillouin scattering and pockels coefficients in silicate glasses," *J. Non. Cryst. Solids*, vol. 40, no. 1–3, pp. 549–566, 1980.

[31] M. E. Lines, "Scattering losses in optic fiber materials. I. A new parametrization," *J. Appl. Phys.*, vol. 55, no. 11, pp. 4052–4057, 1984.

[32] M. E. Lines, J. B. MacChesney, K. B. Lyons, A. J. Bruce, A. E. Miller, and K. Nassau, "Calcium aluminate glasses as potential ultralow-loss optical materials at 1.5-1.9 μm," *J. Non. Cryst. Solids*, vol. 107, pp. 251–260, 1989.

[33] M. D. O'Donnell *et al.*, "Raman gain of selected tellurite glasses for IR fibre lasers calculated from spontaneous scattering spectra," *Opt. Mater. (Amst).*, vol. 30, no. 6, pp. 946–951, 2008.

[34] J. Ballato and P. Dragic, "Materials development for next generation optical fiber," *Materials (Basel).*, vol. 7, no. 6, pp. 4411–4430, 2014.

[35] P. D. Dragic and J. Ballato, “Characterisation of Raman gain spectra in Yb:YAG-derived optical fibres,” *Electron. Lett.*, vol. 49, no. 14, pp. 895–897, 2013.

[36] P. Dragic and J. Ballato, “Characterization of the Raman gain spectra in Yb:YAG-derived optical fibers,” *Electron. Lett.*, vol. 49, no. 14, pp. 895–897, 2013.

[37] H. Mueller, “Theory of photoelasticity in amorphous solids,” *Physics-a J. Gen. Appl. Phys.*, vol. 6, no. 1, pp. 179–184, 1935.

[38] R. Waxler, “Laser glass composition and the possibility of eliminating electrostrictive effects,” *IEEE J. Quantum Electron.*, vol. 7, no. 4, pp. 166–167, Apr. 1971.

[39] A. Feldman, D. Horowitz, and R. M. M. Waxler, “Mechanisms for Self-Focusing in Optical Glasses,” *IEEE J. Quantum Electron.*, vol. 9, no. 11, pp. 1054–1061, 1973.

[40] F. L. Galeener, J. C. Mikkelsen, R. H. Geils, and W. J. Mosby, “The relative Raman cross sections of vitreous SiO_2, GeO_2, B_2O_3, and P_2O_5,” *Appl. Phys. Lett.*, vol. 32, no. 1, pp. 34–36, 1978.

[41] M. Guignard, L. Albrecht, and J. W. Zwanziger, “Zero-stress optic glass without lead,” *Chem. Mater.*, vol. 19, no. 2, pp. 286–290, 2007.

[42] J. Galbraith, “Photoelastic properties of oxide and non-oxide glasses,” Dalhousie University Halifax, 2014.

[43] J. Galbraith, L. Chapman, J. W. Zwanziger, M. Aldridge, and J. Kieffer, “Elasto-Optic Coefficients of Borate, Phosphate, and Silicate Glasses: Determination by Brillouin Spectroscopy,” *J. Phys. Chem. C*, vol. 120, no. 38, pp. 21802–21810,

2016.

[44] R. W. Dixon, “Photoelastic properties of selected materials and their relevance for applications to acoustic light modulators and scanners,” *J. Appl. Phys.*, vol. 38, no. 13, pp. 5149–5153, 1967.

[45] P. Benassi, V. Mazzacurati, G. Ruocco, and G. Signorelli, “Elasto-optic constants in silicate glasses: Experiment and theory,” *Phys. Rev. B*, vol. 48, no. 9, pp. 5987–5996, 1993.

[46] I. C. Chang, “Acoustooptic devices and applications,” *IEEE Trans. sonics Ultrason.*, vol. 23, no. 1, pp. 2–22, 1976.

[47] L. Dong, “Stimulated thermal Rayleigh scattering in optical fibers,” *Opt. Express*, vol. 21, no. 3, pp. 915–918, 2013.

[48] J. J. Freeman and A. C. Anderson, “Thermal conductivity of amorphous solids,” *Phys. Rev. B*, vol. 34, no. 8, pp. 5684–5690, Oct. 1986.

[49] L. G. Van Uitert, “Relations between melting point, glass transition temperature, and thermal expansion for inorganic crystals and glasses,” *J. Appl. Phys.*, vol. 50, no. 12, pp. 8052–8061, 1979.

[50] P. D. Dragic *et al.*, “Single- and few-moded lithium aluminosilicate optical fiber for athermal Brillouin strain sensing.,” *Opt. Lett.*, vol. 40, no. 21, pp. 5030–3, 2015.

[51] J. Markis, K. Clemens, and M. Tomozawa, “Effect of Fluorine on the Phase Separation of Na_2O-SiO_2 Glasses,” *Communications of the American Ceramic Society*, vol. 64, no. 1. p. C-20, 1980.

[52] M. J. Weber, *Handbook of optical materials*. CRC Press, 2003.

[53] G. Ghosh, *Handbook of Thermo-Optic Coefficients of Optical Materials with Applications*, vol. 5. 1998.

[54] K. Nakajima and M. Ohashi, "Dopant dependence of effective nonlinear refractive index in GeO_2- and F-doped core single-mode fibers," *IEEE Photonics Technol. Lett.*, vol. 14, no. 4, pp. 492–494, 2002.

[55] P. Dragic, T. Hawkins, P. Foy, S. Morris, and J. Ballato, "Sapphire-derived all-glass optical fibres," *Nat. Photonics*, vol. 6, no. 9, pp. 629–635, 2012.

[56] J. M. Jewell, "Model for the thermo-optic behavior of sodium borate and sodium aluminosilicate glasses," *J. Non. Cryst. Solids*, vol. 146, no. C, pp. 145–153, 1992.

[57] J. W. Dawson *et al.*, "Analysis of the scalability of diffraction-limited fiber lasers and amplifiers to high average power.," *Opt. Express*, vol. 16, no. 17, pp. 13240–13266, 2008.

[58] J. O. White *et al.*, "Suppression of stimulated Brillouin scattering in optical fibers using a linearly chirped diode laser," *Opt. Express*, vol. 20, no. 14, p. 15872, Jul. 2012.

[59] T. Eidam *et al.*, "Experimental observations of the threshold-like onset of mode instabilities in high power fiber amplifiers," *Opt. Express*, vol. 19, no. 14, p. 13218, 2011.

[60] K. Tajima, "Low-loss optical fibers realized by reduction of Rayleigh scattering loss," *OFC'98 Tech. Dig.*, vol. 4, pp. 305–306, 1998.

CHAPTER V.

COMPOSITIONAL AND STRUCTURAL INVESTIGATION OF ALKALINE EARTH OXYFLUORIDE GLASS OPTICAL FIBERS

V. A. Introduction

In the previous Chapters, material solutions to intrinsically reduced optical nonlinearities were discussed. In Chapter IV, it has been shown that alkaline earth fluoro-alumino-silicate compositions were of specific interest as fiber core materials, as each glass constituent contributes to the reduction of optical nonlinearities.

Thus, in this chapter, the focus will be on the realization and the understanding of alkaline earth fluoride (AEF_2)-containing silicate and aluminosilicate fibers, and the comprehension of the underlying thermodynamic and kinetic mechanisms that govern these systems. This chapter principally investigates the structural and compositional dependence of oxyfluorides in a context of fiber fabrication.

Firstly, the molten core method used in the fiber fabrication is discussed in detail, as the materials investigated herein justify the use of such a technique. Secondly, the role of the dopants and the fiber draw temperatures on glass forming and phase separation are investigated, along with the compositional evolution of each dopants (AE, Al, F) in a variety of oxyfluoride glasses. As insights into the role of fiber processing on the investigated oxyfluoride compositions are gained, complementary thermodynamic and

kinetic studies are performed, with the help of thermogravimetric analysis (TGA) coupled with x-ray diffraction (XRD) studies of pellets in the SrF_2-Al_2O_3-SiO_2, SrF_2-Al_2O_3, and, SrF_2-SiO_2 systems. Finally, a Raman spectroscopy analysis of specific core compositions enables the understanding of the local glass structure.

V. B. Fiber fabrication using the molten core method

Since the initial realization of practical optical fibers, a variety of methods for their fabrication have been developed such as the Modified Chemical Vapor Deposition (MCVD), Plasma-activated Chemical Vapor Deposition (PCVD), Vapor Axial Deposition (VAD) and Outside Vapor Deposition (OVD) [1]. All of these techniques fall into the same category of conventional methods of preform fabrication and they provide excellent material quality and thus extremely low attenuation values (~0.2 dB/km). Despite the success of these methods, the level of dopant concentrations is limited to only a few mole percent [1]. Additionally, the variety of dopants that can be added to the glass system is also limited [1]. As conjectured in Chapter IV, a glass optical fiber exhibiting low nonlinearities will necessitate glass fiber cores in the alkaline earth fluoride/oxide aluminosilicate family. The high melting and boiling temperatures of the alkaline earth fluorides and oxides (AEO, AEF_2), reported in Table V.1, coupled with their tendency to phase separate (which will be discussed later), render the use of conventional methods challenging to fabricate and study these systems.

Table V.1. Melting and boiling temperatures of the alkaline earth fluoride (AEF_2) and oxide (AEO) families.

Component	BaF_2	SrF_2	CaF_2	MgF_2	BaO	SrO	CaO	MgO
Melting Temp (°C)	1368	1477	1418	1263	1923	2531	2570	2800
Boiling Temp (°C)	2260	2460	2533	2260	2000	3200	2850	3600

Instead, a molten core approach is preferred for this work since it enables the development of a larger variety of optical fiber compositions than conventional methods [2]. A variety of very different AEO-derived fibers (BaO-derived [3], SrO-derived [4], MgO-derived [5]) have already been successfully fabricated and characterized using this technique. This technique also allows the investigation over a very wide range of compositions, where, for instance, aluminosilicate fibers containing up to 55 mole % of Al_2O_3 were fabricated [6]. Consequently, this technique is used, as the principal focus of this dissertation is to improve the understanding of the glass structure/composition – optical property relationships in these oxyfluoride systems.

In this approach, the precursors (e.g., powder, crystal, rod, pellets) are first inserted into a fused silica glass capillary preform as shown in Fig. V.1. The choice of silica as the preform cladding material has several advantages: i) it has been manufactured for decades and is a robust material with a wide drawing temperature range (from 1925 °C to 2150 °C), ii) it has very low optical losses at wavelength of interest to telecom and high energy laser applications [7], and, iii) it is an excellent glass former with good chemical durability and thermomechanical stability.

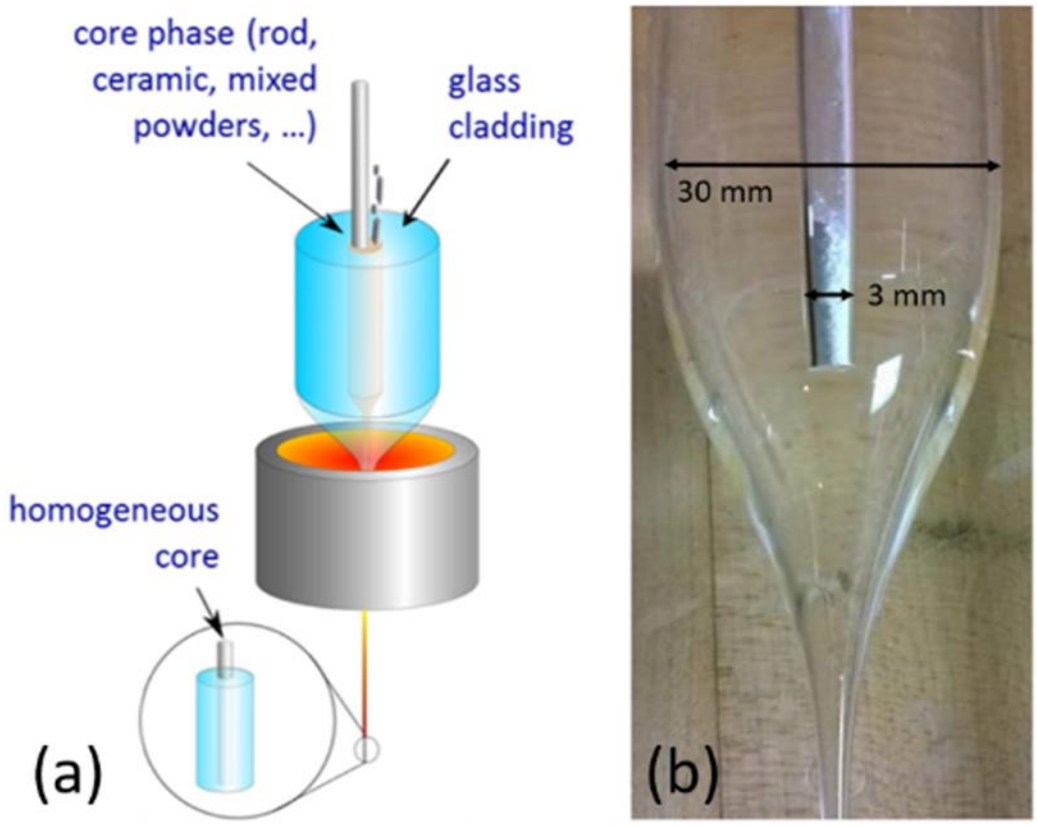

Figure V.1. a) Illustration of the molten core method, taken from [8] . A precursor (e.g., AEF_2-Al_2O_3 mixture) is sleeved inside a silica glass capillary preform. The preform is then heated to high temperature (typically 2000 °C) where the precursor is in a molten state. The silica preform is then drawn into a fiber. b) Example of a precursor mixture (powder packed) inserted in a 3x30 mm silica capillary preform.

The silica preform is placed in a graphite furnace, and heated in order to melt the core phase and draw the fiber. As the fiber is drawn, the silica from the preform is incorporated into the molten core (and the precursor diffuses outward), thus leading to a "X-derived" silicate fiber, where X refers to the nature of the initial precursor, e.g.,

"sapphire-derived fiber" for an aluminosilicate glass fiber made using sapphire as the precursor core. As the fiber cools, the molten core is quenched due to a fast drop in temperature (>2000 °C/s) and thereby is kinetically trapped in its glassy state. In order to protect the fabricated bare fiber from external abrasion, a polymer coating (e.g., UV-cured acrylate, DSM Desotech, Elgin, IL) is deposited on to the external cladding surface before the fiber is spooled. The fiber, once drawn, takes the shape of a circular core/clad geometry

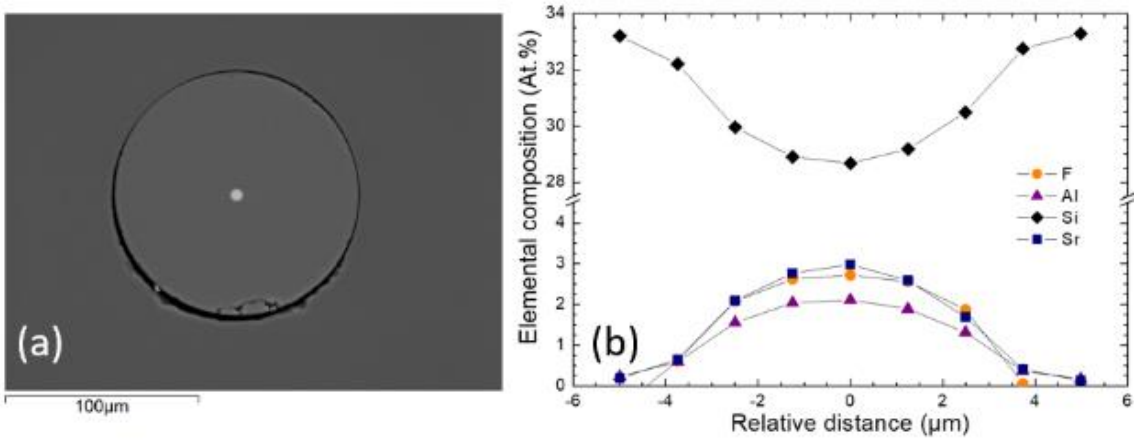

Figure V.2. a) Scanning electron microscope (SEM) micrograph of a silica-cladding, strontium aluminosilicate oxyfluoride core fiber. b) Compositional profile across a strontium fluoro-alumino-silicate fiber core. Not shown for reasons of clarity is the oxygen concentration, %O. However, %O (At. %) = 100 – [%F + %Sr + %Al + %Si]. Data are taken from [9].

(Fig. V.2a), and the glassy core, composed of the aforementioned silica and some remaining precursors, typically gives rise to a transversally graded-index profile as exemplified in Fig. V.2b.

Above was given a general description of the molten core technique, and here more specific information regarding fiber fabrication and sample preparation are provided. In this work, the use silica glass capillary preforms of the same dimensions, i.e., 3 mm inner diameter (ID) and 30 mm outer diameter (OD), are kept identical except if stated otherwise. The method of precursor mixture preparation is also kept the same and is described as follow. First, high purity (99.9% purity minimum) precursors are selected in the appropriate proportion and mixed together with the help of a vortex machine. Then, the powder is grounded in a mortar to ensure a good homogeneity of particle sizes of the mixture. Once the mixture is prepared, it is placed in a desiccator for several days to ensure the powder is reasonably dry. Finally, the powder is loaded into the silica preform (very approximately ~0.5 g gives ~1 km of 125 µm cladding-diameter fiber length). Thereafter, the fiber is drawn as previously described. The targeted dimension of the silica cladding is 125 µm, the targeted feed speed and draw speed are respectively 0.5 mm/min and ~28 m/min. The draw temperature is set depending on the precursor materials. It should be noted that the drawing parameters can be adjusted as the fiber is drawn, since each precursor composition will have a direct impact on the drawing conditions. The collection of fiber samples, for analysis, is typically performed at different positions along the fiber. Characteristic fibers segments are sleeved into ferrules and UV-epoxy cured. Then, the segments are mechanically polished to a mirror finish, and elemental composition analysis is performed using an Energy Dispersive X-ray (EDX) probe coupled with a Scanning Electron Microscope (SEM). The instrument used throughout this entire study is a Hitachi

SU-6600, and accelerating voltage is adjusted as a function of the elements considered for analysis (20 kV being standardly used).

In this section the process of fiber fabrication was detailed. More information regarding other techniques used in the investigation of the systems, such as thermogravimetric analysis or Raman spectroscopy, will be given when appropriate later. In the following section, the influence of the precursor materials composition and the draw temperature on the phase separation of these oxyfluoride fibers is studied.

V. C. Phase separation and glass formation

In order to study the influence of the precursor composition, 3 fibers, with precursor compositions of pure BaF_2, pure SrF_2, and, pure CaF_2, were drawn. An attempt to draw pure MgF_2 was not successful due to its too high reactivity with SiO_2 which caused the preform to blow out, and will not be considered in the following study. The 3 fibers were drawn at the same draw conditions, that is, a draw temperature of 2000 °C, a feed speed of 0.5 mm/min, and a draw speed of ~28 m/min. Additionally, observation of the glass morphology was performed at different positions along of the fiber, and was found to be similar throughout the entire draw length (~800 m for each fiber). Therefore, the SEM images for the three fibers, at the same position (beginning of the fiber draw) are displayed in Fig. V.3.

From Fig. V.3, it is evident that the nature of the alkaline earth fluoride has a direct impact on the glass stability of the core materials. Whereas the BaF_2-derived fiber exhibited no phase separation, both SrF_2- and CaF_2- derived fibers did and were composed of silica rich regions embedded in a AE-rich silicate matrix. At high temperatures, AEF_2 is expected to react with SiO_2 and form its oxide (i.e., AEO) counter-part and the volatile SiF_4 species [10], [11]. More information regarding the mechanisms involved during reactivity of AEF_2 with SiO_2 will be provided later. In the binary AEO-SiO_2 system, there exists a two liquid immiscibility region at high silica concentrations [12], [13]. This immiscibility region becomes less pronounced as one traverses down Group II of the periodic table, which is consistent with the observation in Fig. V.3. In addition, the remaining fluorine post-draw is expected to play a secondary role in the phase separation morphology of the glassy core [14]. It must also be pointed out that the morphologies of the two phase separated fibers in Fig. V.3 are very different. SrF_2-derived fiber core has a very fine phase separated core, where CaF_2-derived fiber contains larger phase separated regions. This difference can be explained based on the liquid-liquid immiscibility in the AEO-SiO_2 system. In this binary system, the critical temperature, defined as the highest temperature of the liquid-liquid immiscibility dome, decreases from MgO to BaO, as does the width of the immiscibility region [13]. Therefore, a Ca-containing glass will be more prone to phase separate than a Sr-containing glass, leading to the appearance of coarser phase separated regions. The limiting case can be described with Ba-containing fiber where the critical temperature is lower than for the others AE-containing binary silicate systems. The draw temperature (2000 °C) is sufficiently high for the glass melt to reach an

equilibrium above the liquid-liquid immiscibility region to yield a homogeneous glass fiber core.

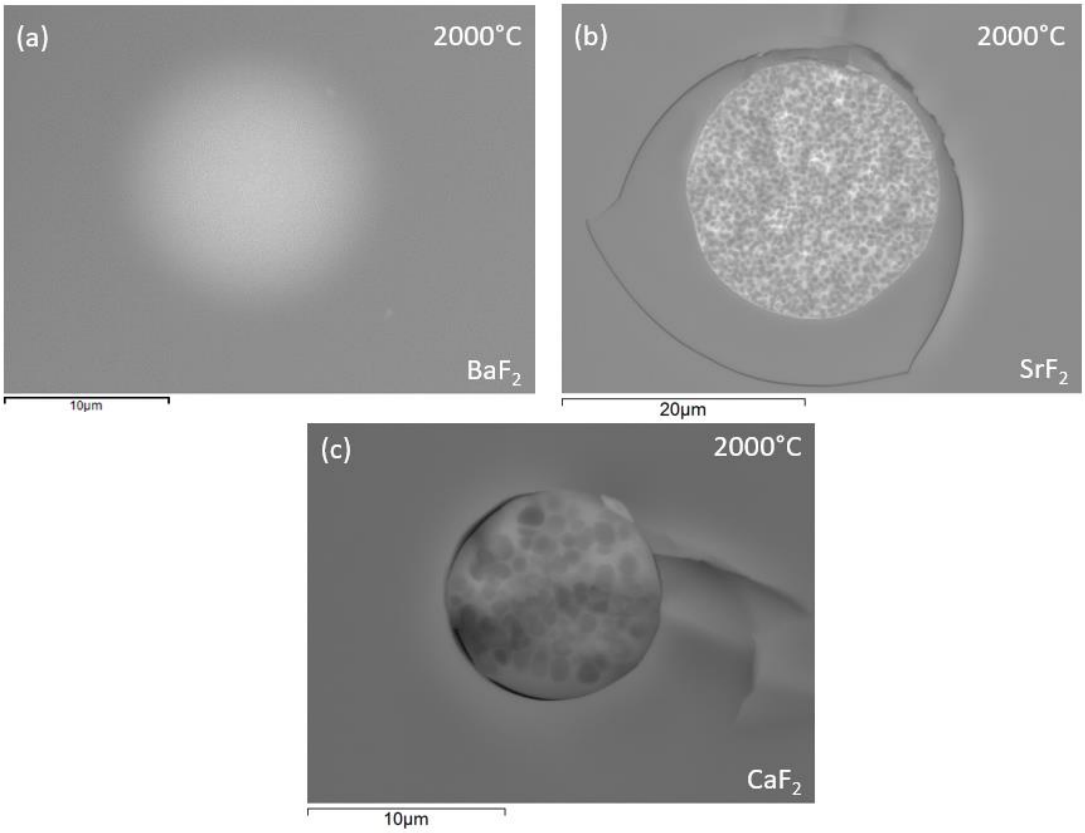

Figure V.3. SEM micrographs of fiber core for different initial precursor compositions (i.e., pure BaF_2, SrF_2, and, CaF_2, respectively, and all with a fused silica cladding and drawn at 2000 °C under the same conditions). BaF_2-derived fiber (a) does not exhibit phase separation, whereas SrF_2- and CaF_2-derived fibers (b, c) do. The phase separated regions in CaF_2-derived fiber appear "darker" because the contrast was enhanced for better observation (Ca being much lighter than Sr or Ba).

Clearly, a phase separated fiber is of no use in the context of this work, since most of the light passing through the fiber core would be scattered away. Therefore, to prevent phase separation, some Al_2O_3 is added to the precursor composition as it is known to prevent this effect in silicate glasses [15].

The substitution of pure AEF_2 powder (in the case of CaF_2 and SrF_2) for a $3AEF_2$ to $1Al_2O_3$ initial mixture ratio, at the same drawing conditions as before, is found to prevent phase separation (Fig. V.4a and Fig. V.4b vs. Fig. V.3b and Fig. V.3c). Furthermore, a decrease of the draw temperature for the $3SrF_2$-$1Al_2O_3$ mixture from 2000 °C to 1925 °C (Fig. V.4b vs. V.4c) did not influence the morphology of the glassy core, in the sense that it remains homogeneous.

However, for a $9SrF_2$-$1Al_2O_3$ ratio drawn at 1925°C, appearance of finely phase separated region is observed (Fig. V.4d). Based on these observations, it can be concluded that the nature of the alkaline earth fluoride, the amount of alumina and the drawing temperature have a direct impact on the phase separation in these oxyfluoride systems. Specifically, a high draw temperature and initial alumina concentration, coupled with a large alkaline earth ion (Ba>Sr>Ca), favors homogenous glass formation.

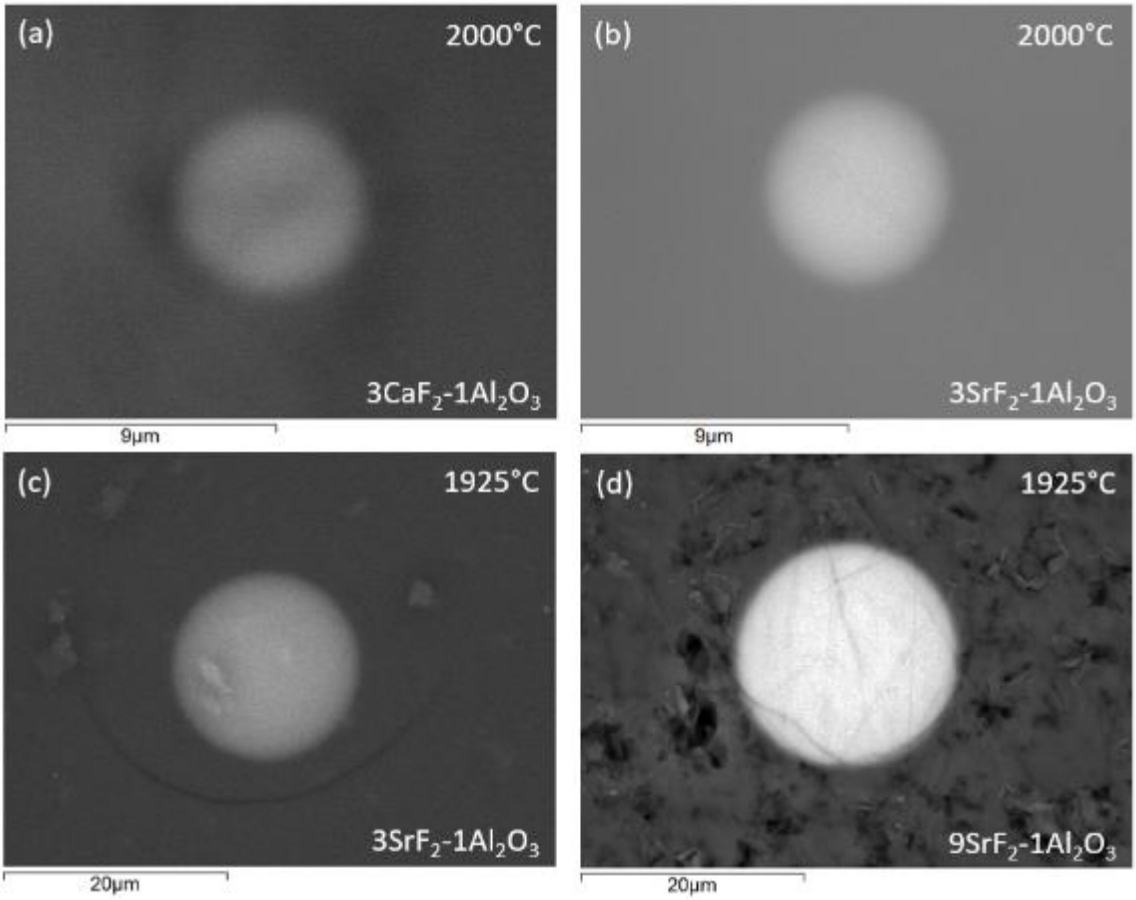

Figure V.4. Role of alumina and drawing temperature on the phase separation of oxyfluoride systems. (a) and (b): The addition of 25 mole % of alumina in the initial composition (instead of pure CaF_2 and SrF_2, see Fig. V.3b and Fig. V.3c) prevents formation of phase separation. (c): The decrease of draw temperature from 2000 °C to 1925 °C for the SrF_2-SiO_2; the core remains free of phase separation. (d): A decrease from 25 % to 10 % of Al_2O_3 at a temperature of 1925 °C results in the apparition of very finely phase separated regions.

If most of the cores appear homogeneous under SEM, in Chapter VI the somewhat high attenuation coefficients for some fabricated Yb-doped strontium oxyfluoride systems suggests some potential nanoscale phase separation that could occur but not be visualized/detected under SEM. Consequently, in Chapter VII a Section (VII. B.) is specifically dedicated to the investigation of nanoscale phase separation in these oxyfluoride glass systems using a transmission electron microscope (TEM). The presence of some nanoscale phase separation for some of the glasses can be explained by invoking similar argument as formulated above with regards to liquid-liquid immiscibility region.

However, if the direction to take in order to prevent phase separation seems straight forward, there are other parameters that also need to be considered. For instance, the remaining concentration of fluorine in the core post fiber fabrication will dictate the reduction of some parameters that drive optical nonlinearities, namely n, n_2 and dn/dT. In this context, it becomes necessary to study the evolution of dopant concentrations during fiber drawing as a function of the initial precursor composition and time, to understand the principal thermodynamic and kinetic mechanisms that govern these oxyfluoride systems during fiber processing.

V. D. Dopant compositional evolution of the oxyfluoride fiber core

In Chapter IV it has been seen that core materials in the AEF_2-Al_2O_3-SiO_2 composition was of interest, and, specifically, the SrF_2-Al_2O_3-SiO_2 system. In order to monitor the evolution of dopant concentrations in the fiber core during the draw, a fiber with $3SrF_2$-$1Al_2O_3$ precursor composition (powder packed) was drawn into fiber (~1000 m) as previously descripted. Then, samples at different positions along the fiber length were collected and analyzed by SEM/EDX. The evolution of the fiber core composition, taken at the core center for each segment, is plotted in Fig. V.5 as a function of draw length. The composition is expressed in atomic percent (At. %) instead of compound mole percent (mole%) since at this point there is no clear evidence if SrF_2 remains as such before and after fiber drawing. A more detailed discussion on this is provided later in this Chapter.

As it can be seen in Fig. V.5, the Si content increases rapidly at the beginning of the draw, then increases at a lower rate above about 200 m of fiber drawn. Counter the Si, concentrations of F, Al, and, Sr, decrease as the fiber is drawn. Interestingly, the F concentration decreases at a higher rate compared to Al and Sr over the first hundred meters. This decrease of fluorine content also scales with an increase of silicon content in the core, which suggest the typical reaction of F mainly into SiF_4 [16], [17]. Because the fiber was drawn at a nearly constant rate of 28-30 m/min, the draw length is directly a function of time, where 1000 m of fiber correlates approximately to 35 min of drawing time. For completeness, a similar fiber was drawn, using the same condition but with the

precursor materials being pellet pressed instead of powder packed into the silica capillary preform. This experiment was performed with the goal of comparing the influence of the initial precursor shape/form in the compound concentration over time. The results, presented in Appendix V.1, show similar trends to what is observed for a powder packed precursor mixture. However, over the first 200-300 hundred meters, the silicon content increases at a slower rate than for a powder packed precursor, and can be expected as the "pellet pressed material" is more compact than the "powder-packed material", which may slow down the rate at which SiO_2 is incorporated into the core.

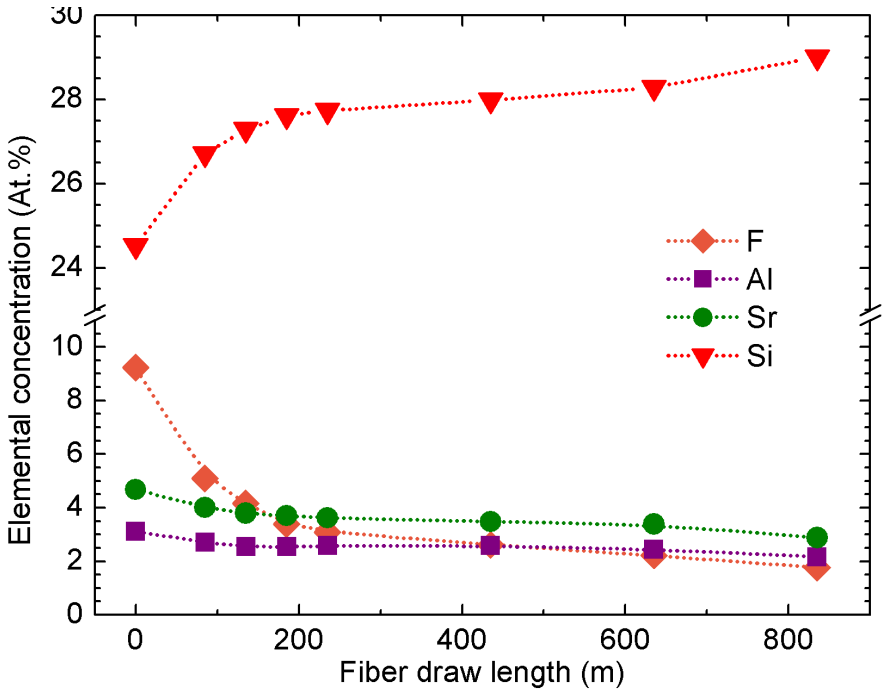

Figure V.5. Elemental concentration (At. %) as a function of draw length (taken at the core center of each segment analyzed for a $3SrF_2$-$1Al_2O_3$ initial precursor system). Not shown, for reasons of clarity, is the oxygen concentration, %O. However, %O (At. %) = 100 – [%F + %Sr + %Al + %Si].

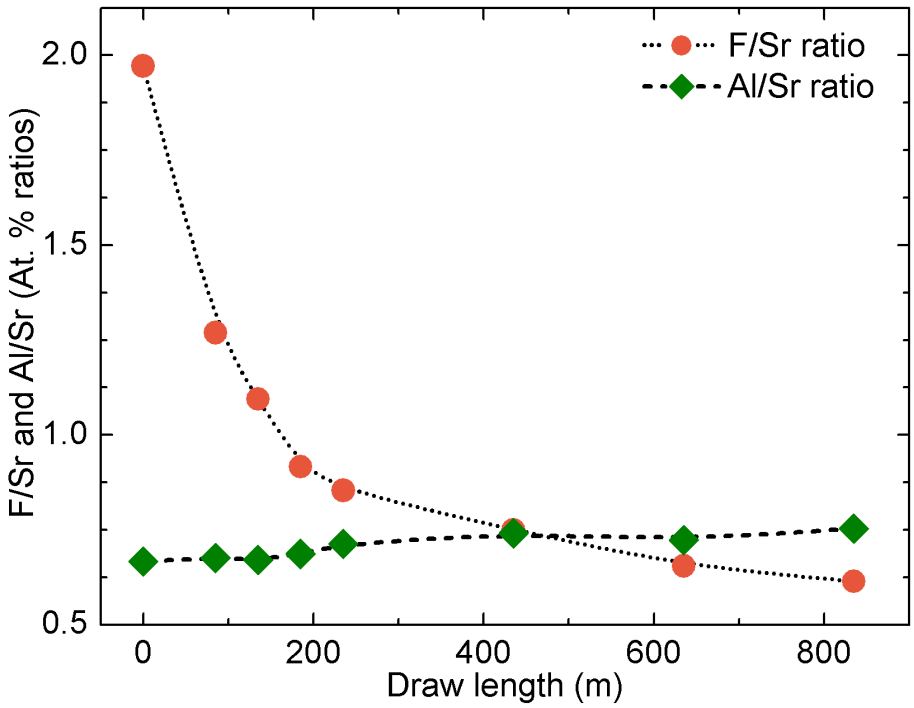

Figure V.6. At. % ratio of F/Sr (orange) and Al/Sr (green) at the core center and at different position of the fiber draw length, for a powder packed $3SrF_2$-$1Al_2O_3$ precursor mixture drawn in a 3x30 mm silica capillary preform at 2000 °C.

It is observed, again from Fig. V.5, that the F content decreases more rapidly than Sr, and this when the starting precursor material is SrF_2, where F is initially bound to Sr with a stoichiometry of 2F for 1Sr. This F/Sr ratio can be monitored as a function of distance and is displayed in Fig. V.6. Interestingly, one can notice that at the beginning of the draw, F/Sr is close to 2, and decreases almost exponentially as the fiber is drawn.

The initial F/Sr ratio of 2 strongly suggests that F remains attached to Sr at least at the beginning of the draw, in the "SrF_2" form. As the fiber is drawn, a decrease of this ratio

suggests that SrF_2 reacts with its aluminosilicate environment to form volatile species (e.g., SiF_4).

Furthermore, in Fig. V.6, the Al/Sr ratio is displayed. It should be noted that this ratio, initially of ~0.67, corresponds exactly to the Al/Sr ratio found in the initial precursor composition. Interestingly, this ratio increases smoothly over draw length, and accordingly time, to reach a value of ~0.75, which is approximately 13 % larger that the initial ratio value. This rise can originate from various reasons speculated below.

- Differences in diffusion coefficients between Al and Sr in vitreous silica:

  Diffusion coefficient data for species into vitreous silica at 1000 °C from [18] clearly suggest that alkaline earth or alkali metal ions, such as Ca, Li, Na, or Ka diffuse more quickly than Al (from 5 to 8 order of magnitude difference), so presumably does Sr, or Ba, though less than the smaller and less charged ions. If at higher temperatures, the diffusion coefficients will be higher in the low viscosity molten core, it is expected that Al will diffuse outward in the cladding at a slower rate than Sr, and therefore could explain the increase in Al/Sr ratio.

- Volatilization of SrF_2:

  It has been reported in silicate slags that, in addition to the formation of SiF_4, the transformation of the alkaline earth fluoride from its molten state into its gaseous state

[19] is one of the many mechanisms leading to fluorine volatilization. That said, a volatilization of SrF_2 could explain why Al/Sr ratio increases with time/draw length.

- Inhomogeneous melting:

  As the precursor is heated and the fiber is drawn, the precursor mixture will melt. However, each constituent that composes the initial precursor mixture has its own individual melting temperature, e.g., 1475 °C and 2050 °C for SrF_2 and Al_2O_3, respectively. Therefore, SrF_2 will melt first, resulting in an inhomogeneous melting, where the SrF_2 liquid flows to the bottom of the capillary under the action of gravity, while Al_2O_3 reacts later. Such phenomenon will result in an increase of the Al/Sr ratio as the precursor melts and the fiber is drawn. However, phase transformations upon heating and the complex dynamics associated with fiber processing also likely play a determinant role. Moreover, the initial Al/Sr ratio is found to be the same as the initial precursor at the beginning of the draw, which supports the idea that the mixture melts "homogenously".

A similar analysis of the F/Sr and Al/Sr ratios as a function of draw length was performed on the "pressed pellets" fiber described above, and is reported in Appendix V.2. For this fiber, the initial F/Sr and Al/Sr ratios start around 1.7 and 0.67, respectively, which are close to that observed for the powder packed fiber, with similar trends. Also, presented in Appendix V.3, is the evolution of the core diameters for both fibers as a function of draw length and Si content. From this analysis, two general trends are observed, i) the core

diameter generally decreases as the fiber is drawn, and ii) the core diameter decreases as Si content increases.

In order to better understand the compositional evolution of the dopants during fiber drawing, compositional analysis using EDX for a series of various oxyfluoride fibers, with different initial precursor compositions and drawing conditions was studied. The fiber initial precursor compositions, along with some draw parameters, are summarized in Table V.2. For each fiber, segments from the beginning and the end of the draw were taken for EDX/SEM analysis.

Table V.2. Fiber systems used to study the evolution of dopants during fiber drawing.

Initial fiber precursor composition (molar ratio)	T_{draw} (°C)	Total length of fiber drawn (m)
$3CaF_2$-$1Al_2O_3$	2000	800
$3SrF_2$-$1Al_2O_3$	2000	800
$3BaF_2$-$1Al_2O_3$	2000	550
$3(1SrF_2$-$1CaF_2)$-$1Al_2O_3$	2000	650
$9SrF_2$-$1Al_2O_3$	2000	800
$3SrF_2$-$1Al_2O_3$	1925	500
$1MgF_2$-$1Al_2O_3$	1925	550
$1CaF_2$-$1Al_2O_3$	1925	550
$1SrF_2$-$1Al_2O_3$	1925	475
$1BaF_2$-$1Al_2O_3$	1925	500

If the evolution of the dopants can be monitored as a function of time or draw length, using time as comparative study is not convenient as each draw chronology varies

from one fiber to another. As an example, in-draw conditions can differ as a function of the core precursor nature, which exhibit dissimilar thermal behavior. It can lead to misinterpretation, where, for instance, silica can be found in large amount in the core, not because of more pronounced thermally activated processes that govern silica incorporation during fiber drawing, but simply due to a longer time spent by the preform in the furnace before the draw starts. However, it should be mentioned that fiber drawing conditions (excepted temperature and precursor compositions, which are voluntarily changed) are being kept as constant as permissible between fibers. It is recalled that the silica capillary preform (3x30 mm), the targeted fiber cladding diameter (125 µm) and draw speed (~28-30 m/min), but also the sample preparation (powder packing), remain identical throughout this work, unless otherwise specified.

That said, the evolution of precursor concentration can be expressed as a function of Si. Indeed, as seen previously, Si is introduced when the silica from the cladding interacts with the precursor core, and is function of "draw length, or time" (Fig. V.5). Additionally, there exists possible reactions between the alkaline earth fluoride and silica, that could lead to the formation of SiF_4 and possibly new compounds during the oxidation of the oxyfluoride melt. Consequently, it is convenient to express the evolution of the At. % of the element as a function of Si (At. %). The evolution of dopant concentration, relative to their initial precursor concentration, and as a function of Si content, is displayed in Fig. V.7. For simplicity and to compare differing fibers, only the composition at the very core centers are reported. Interestingly, the data exhibit trends even when considering the

variety of systems investigated (Table V.2). Fig. V.7a, Fig. V.7b, and Fig. V.7c gives the evolution of the AE, Al, and F as a function of Si concentration. Fig. V.7d is a compilation of these data by grouping species together, in order to better observe general trends in the oxyfluoride system.

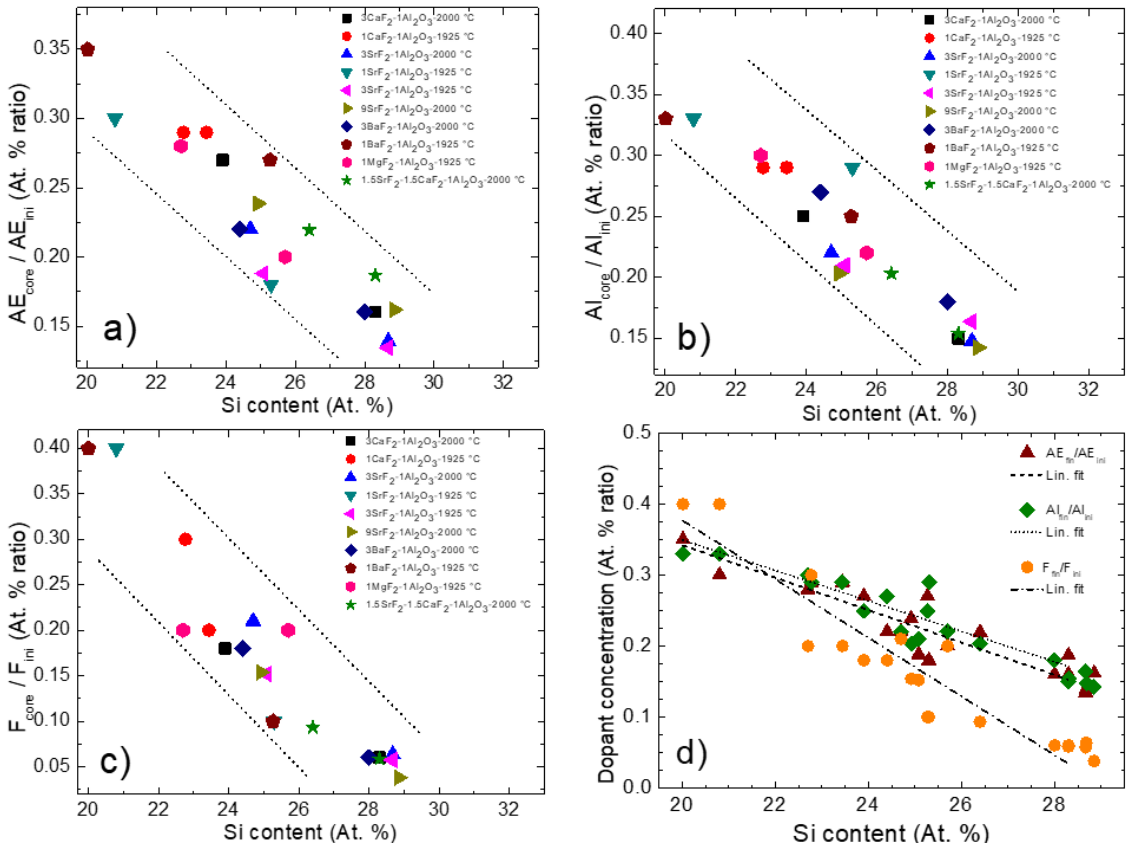

Figure V.7. (a), (b), (c): Dopant concentration, at the core center, relative to its initial content (calculated based on precursor composition) and plotted as a function of Si content. AE stands for alkaline earth, Al for aluminum and F for fluorine. The compositions in the legends correspond to the initial precursor compositions (in molar ratios), and the temperatures are the draw temperatures for each fiber. Each fiber

was drawn using 3x30 mm silica capillary preform and a targeted draw speed of 28-30 m/min. Note that each composition is taken at the core center, and for two positions per fiber: Beginning of the draw (higher Si content) and end of the draw (lower Si content). On graph (d) is a compilation of data from (a), (b), and (c), to better visualize trends across a large number of oxyfluoride fibers drawn using the molten core method. Detailed composition (At. %) for each fiber segment is given in Appendix V.4. Dotted lines in (a), (b), and (c) are guides-to-the-eye.

At first, it should be noted that the ratio of AE, Al, and F all decrease as a function of increasing Si content, with F decreasing at a higher rate than both AE and Al. Interestingly, it also is worth noting that AE and Al content decrease at a somewhat similar rate (best seen in Fig. V.7d), this being consistent with the previous observation made on the $3SrF_2$-$1Al_2O_3$ fiber (Fig. V.5). Again, regarding the plurality of the systems investigated (different AEF_2, initial precursor ratios, or draw temperatures), the compositional evolution of dopants are surprisingly consistent. The fiber cores presenting higher Sr, Al, and, F content are the ones drawn at 1925 °C, and with a higher Al_2O_3 initial concentration (see for example, $1SrF_2$-$1Al_2O_3$ and $1BaF_2$-$1Al_2O_3$ at 1925 °C, from the beginning of the draws). On the other hand, the AE-derived fiber segments exhibiting the lowest F, Sr, Al content and the highest Si content are exclusively found at the end of the draws. For completeness, a series of strontium aluminosilicate fibers, with varying SrO-Al_2O_3 initial precursor ratios, has also been investigated and is reported in Appendix V.5.

It can be observed that the rate at which Al and Sr content decreases as a function of Si content is independent on its initial Al_2O_3 to SrO ratio.

The relative compositional evolution (at beginning and end of the draw) for 3 fibers, $3SrF_2$-$1Al_2O_3$ at 2000 °C, $3SrF_2$-$1Al_2O_3$ at 1925 °C, and, $1SrF_2$-$1Al_2O_3$ at 1925 °C is displayed in Fig. 5.8. This enables to more closely observe the evolution of F concentration as a function of AE (here Sr, Fig. V.8a), Al (Fig. V.8b), and this for different drawing conditions (temperatures and positions).

Firstly, starting with a $1SrF_2$-$1Al_2O_3$ ratio (filled and round symbol) leads to higher Sr, Al, and, F content than starting with a $3SrF_2$-$1Al_2O_3$ ratio (filled triangle and rectangle symbols). Secondly, if the amount of F is proportional to the amount of Sr and appears trivial as F is incorporated along with Sr through SrF_2, the increase of fluorine concentration as a function of Al is surprising. Indeed, it is found that starting with less SrF_2 but more Al_2O_3, as it is the case for the 1 to 1 ratio vs. 3 to 1 ratios, tends to promote higher fluorine concentration in the fiber core. If the differences in concentration are clearly observed at the beginning of the draw, they become less evident toward the end of the draw. It is also noticed that lowering the draw temperature from 2000 °C to 1925 °C may have a little impact on final compound concentration. This is seen when drawing the same initial precursor composition ($3SrF_2$-$1Al_2O_3$) but at a different temperature (2000 °C vs 1925 °C, i.e., solid vs. dot lines in Fig. V.8). The F content appears to be slightly driven toward higher concentrations. Therefore, addition of Al_2O_3 and lower drawing

temperatures have a beneficial effect in retaining more fluorine in the fiber core, at least at the beginning of the draw. However, after long length of drawn fiber, the fluorine level becomes nearly identical. It will be seen later in this Chapter than Al_2O_3 plays a direct role in preventing fluorine loss as it is found to not react with AEF_2 upon heating to form F-containing volatile species, which greatly impact final core composition.

Table V.3 summarizes the fluorine content (in At. %, at core center) at both beginning and end of drawn fiber length for a variety of fiber systems, along with the fluorine loss over that fiber length for each fiber. In the case of pure AEF_2-derived fibers, the fluorine loss for BaF_2-derived fiber is much higher than for the SrF_2- and CaF_2-derived fibers, and this for the shorter distance. It should also be mentioned that this fiber has the lowest fluorine content at the start and at the end of the draw, of about ~50 % and ~20 % that of the others AEF_2-derived fibers, respectively. This can be partially explained by the higher melting and boiling temperatures of SrF_2 and CaF_2 than BaF_2. These compounds, more refractory, will slow down the kinetics of mixing/reaction with the SiO_2-cladding during heating and drawing processes, reducing the rate of volatilization of fluorine through formation of SiF_4.

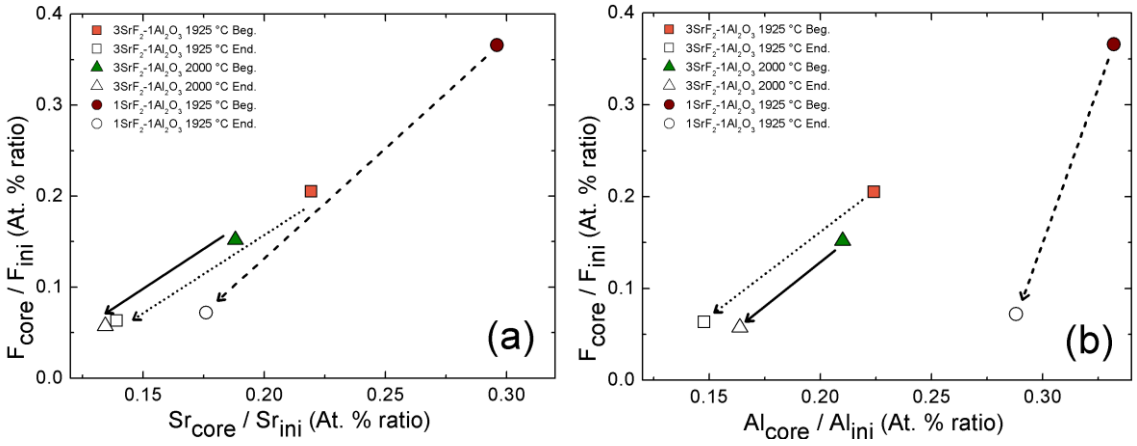

Figure V.8. Evolution of fluorine concentration (relative to its initial precursor amount) as a function of Sr (a) and Al (b), for fibers with different draw temperatures (2000 °C vs. 1925 °C), and initial precursor ratios: $3SrF_2$-$1Al_2O_3$ and $1SrF_2$-$1Al_2O_3$. On the graphs, "Beg." And "End" stand for "Beginning of the draw" and "End of the draw", respectively. The arrows correspond to the evolution s of the ratios from Beginning to End of the draw for the 3 fibers investigated: $3SrF_2$-$1Al_2O_3$ at 2000 °C (dot line), $3SrF_2$-$1Al_2O_3$ at 1925 °C (solid line), and $1SrF_2$-$1Al_2O_3$ at 1925 °C (dash line). Lines are guides-to-the-eye.

Now, in the fluoro-alumino-silicate systems, instead of fluoro-silicates, it is observed that the fluorine concentrations are substantially higher at the beginning and only slightly higher at the end of the draw. This is observed even if the initial starting fluorine content is lower than for pure AEF_2 precursors (75 % AEF_2 instead of 100 % AEF_2 in the $3AEF_2$-$1Al_2O_3$ vs pure AEF_2), which is consistent with observation from Fig. V.8. More interestingly, the BaF_2-Al_2O_3-derived fiber is found to have a much higher fluorine content than its pure BaF_2-derived fiber counter-part. Again, this drastic increase of F content (at

the beginning of the draw only) is attributed to Al_2O_3 being added as an initial precursor constituent.

Table V.3. Evolution of fluorine content (at core center) at different position for some given systems of interest is reported. All the fibers were drawn at 2000 °C. [F_i] and [F_f] correspond to F concentration (in At. % and at the core center) at the beginning and at the end of the draw, respectively.

Fibers	Initial precursors	[F_i]	[F_f]	Fiber length (m)	Relative F loss (%)
Alkaline earth fluoro-silicates	BaF_2	2.5	0.5	700	80
	SrF_2[a]	5.2	2.3	1050	56
	CaF_2[a]	5.6	2.3	800	59
Alkaline earth fluoro-alumino-silicates	$3BaF_2$-$1Al_2O_3$	8.1	2.0	550	75
	$3SrF_2$-$1Al_2O_3$	7.6	2.7	800	64
	$3CaF_2$-$1Al_2O_3$	7.8	2.6	800	67

[a]: SrF_2- and CaF_2-derived fibers were phase separated (see Fig. V.3), but the fluorine content was found to be maximal at the core center, and therefore this value is reported to provide more comparative data points.

To summarize this section, compositional analysis on a variety of different oxyfluoride systems showed general trends that appear valid for a wide range of composition, such as:

- Concentrations of precursor compounds decrease as the fiber is drawn, while Si content increases as inherent to the molten core method with the incorporation of SiO_2 in the molten precursor-containing core.

- F decreases at a much higher rate than AE and Al, and is attributed to the formation of volatile species (SiF_4).

- Al_2O_3 plays a significant role in retaining more F inside the fiber core. This effect will be further developed later.

- A lower draw temperature also has a beneficial impact on retaining fluorine in the core, although less pronounced than the impact of Al_2O_3 under the studied conditions.

V. E. Role of optical basicity on the volatilization of fluorine

Optical basicity is a property that describes the ability of an oxygen to give its negative charge to the surrounding cations [20]. It is found to potentially impact the effect of fluorine volatilization [21], and, therefore, its role on two systems, BaF_2-BaO-Al_2O_3 and MgF_2-MgO-Al_2O_3, is now investigated. In order to study this effect, 6 fibers of different initial precursor compositions (Table V.4), and, consequently, with different initial optical basicity, were drawn, with a targeted draw temperature of 1925 °C. The optical basicity values for the initial compositions are calculated using data from [22] and reported in Table V.4. BaF_2-BaO-Al_2O_3 initial precursors are more basic than MgF_2-MgO-Al_2O_3 and, therefore, these last ones are expected to retain less fluorine during the draw, everything

else being equal. The comparative study between BaF_2-BaO and MgF_2-MgO was preferred as they provide the largest optical basicity difference among the AEF_2 family (including only Mg, Ca, Sr, and, Ba, as relevant for this work) [22]. During the draw, the Ba-containing fibers drew well at the targeted draw temperature of 1925 °C. Although the fiber containing the highest MgO content was successfully drawn at 1925 °C, an empty (i.e., with air) core was found throughout the fiber length (~1 km), and therefore no data analysis could be performed on this fiber. Additionally, the MgF_2-MgO containing fibers did not draw at 1925 °C, but an increase of temperature from 1925 °C to 1975 °C allowed the two compositions (see Table V.4) to be drawn. These two fibers had core materials and therefore could be characterized.

Table V.4. Optical fiber systems used to study the effect of optical basicity in oxyfluoride systems.

Fiber (initial molar ratio)	Initially targeted T_{draw} (°C)	T_{draw} (°C)	Optical basicity
$0.8MgO-0.2MgF_2-1Al_2O_3$	1925	1925[a]	0.43
$0.5MgO-0.5MgF_2-1Al_2O_3$	1925	1975[b]	0.40
$0.2MgO-0.8MgF_2-1Al_2O_3$	1925	1975[b]	0.37
$0.8BaO-0.2BaF_2-1Al_2O_3$	1925	1925	0.60
$0.5BaO-0.5BaF_2-1Al_2O_3$	1925	1925	0.56
$0.2BaO-0.8BaF_2-1Al_2O_3$	1925	1925	0.53

[a]: No core was found throughout the fiber (precursor did not melt); no analysis performed on this fiber.

[b]: These precursors could be drawn by increasing the initial T_{draw}=1925 °C to 1975 °C.

The evolution of the dopant concentrations (F, AE, Al), relative to their initial concentration and as a function of Si content, are displayed in Fig. V.9 (a, b, and, c). First, the evolution of F (Fig. V.9a) shows that the BaF_2-BaO containing fibers have similar fluorine loss relative to their initial concentration. Second, the F content for MgF_2-MgO containing fibers are substantially higher. At first, this is contradictory with respect to the optical basicity argument enunciated above, where melts with higher optical basicity (i.e., Ba-containing fibers) should have a higher remaining fluorine concentration. However, for the Mg-containing fibers, the difficulty of drawing these fibers should be recalled. This is attributed to the presence of MgO, which has a much higher melting temperature than BaO (~2850 °C vs. 1925 °C). This higher melting temperature prevents the precursor from melting and, consequently, silica to be rapidly incorporated into the fiber core. As a consequence of this "limited" interaction, the reaction between MgF_2 and SiO_2 to form SiF_4 is somewhat slowed down, which favors higher F content.

Now, looking at Fig. V.9b, one can observe that Mg is present in a higher quantity than Ba, which correlates with the highest F content found for the Mg-containing fibers, and supports the argument that the MgF_2-MgO-Al_2O_3 compositions did melt with difficulty (retaining AE and, therefore, F). In the Ba-containing series, the Ba is found in higher quantity for the composition containing the most "oxide" precursor, and in lowest quantity for the composition containing the most "fluoride" precursor. It should be noted that this behavior is also observed for Mg-containing fibers. These observations are consistent with the higher melting temperature argument enunciated above: the addition of fluorides tends

to favor the melting (they possess a much lower melting temperature than their oxide analogs and decrease viscosity of the melt [23]). Interestingly, it is found that a higher fluorine content is accompanied with a higher AE concentration (Appendix V.6). This again suggests that fluorine preferentially remains attached to the AE during the fiber draw.

The evolution of Al (Fig. V.9c) is interesting as it does not follow the trend observed by the AEs (Fig. V.9b). The relative content of Al for the various systems is much less dispersed for the two families compared to the AE content. This can be explained by Al originating from a single precursor compound, namely Al_2O_3, whereas the AE precursors are incorporated as a mixture of AEF_2 and AEO species. Moreover, Mg-containing fibers are found to contain lower amount of Al relative to Ba-containing fibers, where the opposite trend is observed for the AEs (where AE content is higher for Mg-containing fibers). Again, Mg-containing fibers were drawn at a higher temperature, caused by the difficulty in melting MgO, and could result in a lower Al content simply due to higher drawing temperatures.

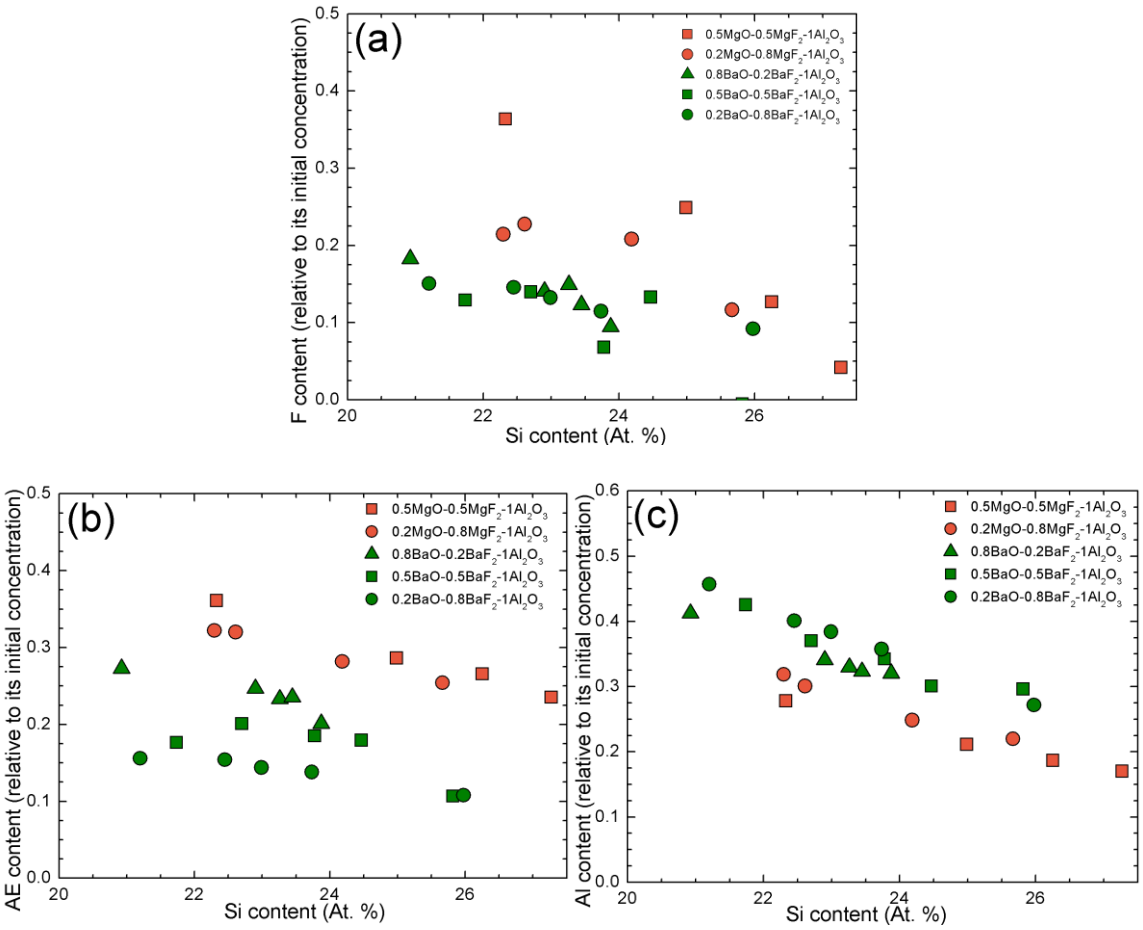

Figure V.9. Evolution of the elemental composition for some AEF_2-AEO-Al_2O_3-derived silicate optical fibers. The compositions, taken at the core center of the fibers, are given relative to the initial precursor composition (initial precursor molar ratio given in legend).

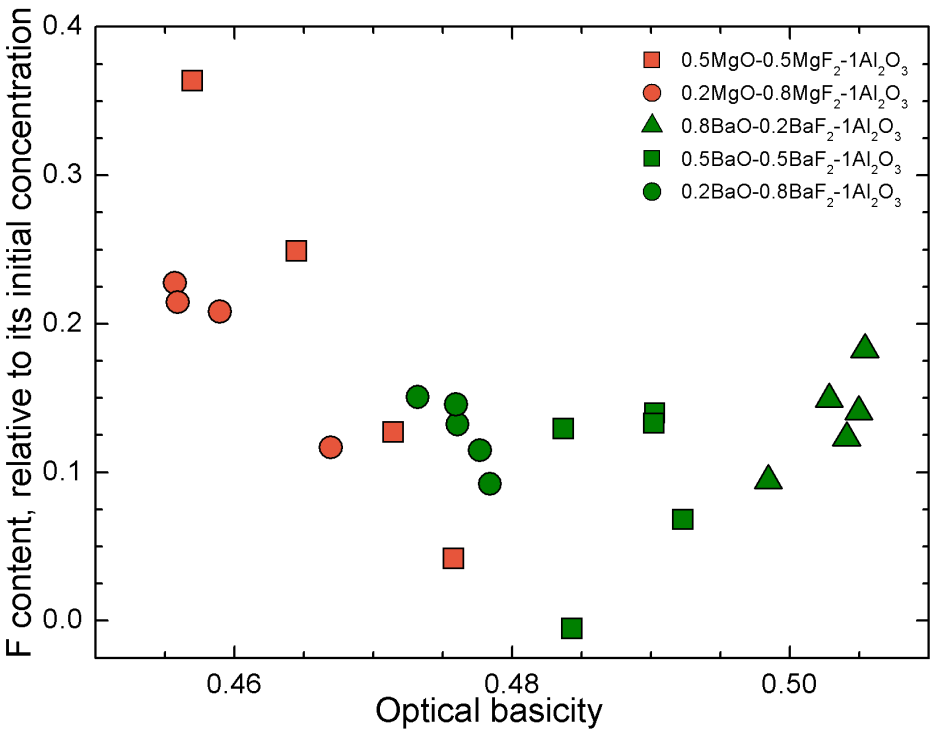

Figure V.10. Fluorine concentration (relative to its initial concentration) at the core center and as a function of optical basicity for a series of BaO-BaF_2-Al_2O_3 and MgO-MgF_2-Al_2O_3 initial precursor compositions. The optical basicity is calculated assuming the remaining fluorine stays attached as AEF_2 in the fiber core and the remaining AE forms AEO species. The calculations are performed using data from [22]. Note the convergence toward a value of 0.476, which is the optical basicity of SiO_2.

Thus, in Fig. V.10 is plotted the fluorine concentration, relative to its initial content (At. % ratio) as a function of optical basicity. The optical basicity is calculated assuming the remaining fluorine is bound as AEF_2 in the fiber core and the remaining AEs form AEO species (composition and optical basicity values can be found in Appendix V.7). This

Fluoride → Oxide transformation will be discussed in greater details in the following Section. As mentioned earlier, a higher fluorine content should remain in the fiber core under the effect of an increased optical basicity value. However, no such correlation is found here. Instead, the data converge toward the value of 0.467, which was taken as the optical basicity value for SiO_2. Furthermore, the Mg-containing fibers, which are supposedly exhibiting lower optical basicity (and subsequently lower F content) are found to have the highest F content. Therefore, it is concluded that optical basicity does not play a determinant, if any, role in these systems with respect to volatilization of fluorine. It is worth mentioning that the trends observed in Fig. V.10 within data points of a same fiber are the result of the variation of SiO_2 concentration at different fiber length position, but are not a direct consequence of optical basicity. On the other hand, it has been shown that the melting temperature of the precursor composition essentially drive the compositional evolution of F, and AE, and Al.

Parameters/properties that could influence the compositional evolution of the different constituent of the silicate core were investigated. Nevertheless, additional information need to be gained regarding the mechanisms that drive fluorine volatilization. Alumina, coupled with the melting temperature of the precursors, fiber drawing temperatures and draw time, have a determinant role in fluorine volatilization. Consequently, it becomes crucial to study the thermodynamics and kinetics of oxyfluoride systems in order to better understand the underlying mechanisms that drive F volatilization

and fluoride to oxide phase transformations, but also to gain insight into the structure of the fabricated fiber glass cores.

V. F. Thermodynamics and kinetics investigation of the oxyfluoride system

The importance of understanding the mechanisms that drive fluoride-to-oxide transformations is many fold. First, understanding the underlying thermodynamics that drive fluoride-oxide reactions allow one to better comprehend the structure of the glass and the nature of the bonds/interactions within the glass network. This is necessary when it comes to relate structure versus properties, as it will be the principal effort in the following chapter. Secondly, as fluorine plays a principal role in the magnitude of some nonlinear optical effects (n, n_2, dn/dT), controlling its rate of volatilization during fiber fabrication is critical. In the interest of this dissertation the SrF_2-Al_2O_3-SiO_2 system will be particularly investigated, as it has been shown to be one of the most promising system in mitigating optical nonlinearities. This Section is organized as follow. First, a mixture in the aforementioned system is analyzed by thermogravimetric analysis (TGA), coupled with a Fourier Transform Infrared (FTIR) spectrometer, in order to provide insight into the kinetics of reactions in these systems upon heating. Based on this first effort, heat treatment of powder mixtures in the same compositional family are performed, and the weight loss after heat treatment is monitored, and the samples are then interrogated using X-Ray Diffraction (XRD).

Thermogravimetric analysis (TGA) was carried out on a $3SrF_2$-$1Al_2O_3$ and a $3SrF_2$-$1Al_2O_3$-$4SiO_2$ powder mixture to determine the influence of Al_2O_3 and SiO_2 on the reactivity of SrF_2. The measurements were performed using a NETZSCH STA 449 C instrument, with a heating rate of 10 K/min from room temperature to 1325 °C, in a controlled atmosphere of $1N_2$-$1O_2$. The results are presented in Fig V.11a. It is shown that the non-silica containing powder exhibit an almost null mass loss over the temperature range investigated, whereas addition of some SiO_2 for the second powder mixture correlates with a drastic mass loss above ~1175°C, which also corresponds to the formation of SiF_4 that was monitored by an FTIR coupled with the TGA instrument (Fig. V.11b). Unfortunately, it was found impossible to monitor the mass and SiF_4 content over a larger temperature region due to the powder fusing with the alumina pan at these temperatures, which could also potentially damage the instrument. For completeness, 2 other powders, BaF_2-Al_2O_3 and BaF_2-Al_2O_3-SiO_2, also were studied by TGA and the results can be found in Appendix V.8. A similar behavior to the presently studied powder was observed, but the reaction onset was determined to be at ~1075°C, that is, 100 °C lower.

Based on these results, some interesting features regarding these strontium oxyfluoride systems can be stated. Primarily, Al_2O_3 does not react with SrF_2, or at least, does not form volatile species. Therefore, the principal source of fluorine loss in the systems investigated is due to the formation of SiF_4 that occurs when SrF_2 encounters SiO_2. Furthermore, this sudden reaction has a characteristic onset, where going from absence of volatilization to ~10 wt% loss within ~200 °C (and ~20 min as a reason of a 10 K/min

heating rate) for the SrF_2-Al_2O_3-SiO_2 powder. Additionally, for both SrF_2-containing (Fig V.11a) and BaF_2-containing systems (Appendix V.8), the mass loss as a function of temperature (in % per °C) can be approximate to be nearly linear as SiF_4 starts to be formed. That said, the rate for SrF_2 and BaF_2 containing powders would be of ~0.27 and ~0.43 wt.% loss per °C, respectively (or ~0.027 and ~0.043 wt.% loss per min). In other words, the SiF_4 volatilization rate is found to be ~60 % higher for BaF_2 containing mixture than for SrF_2 containing mixture. The higher reactivity of BaF_2 powder correlates with the previously discussed observation that a lower F content is found in BaF_2-derived, as opposed to SrF_2-derived, silicate systems.

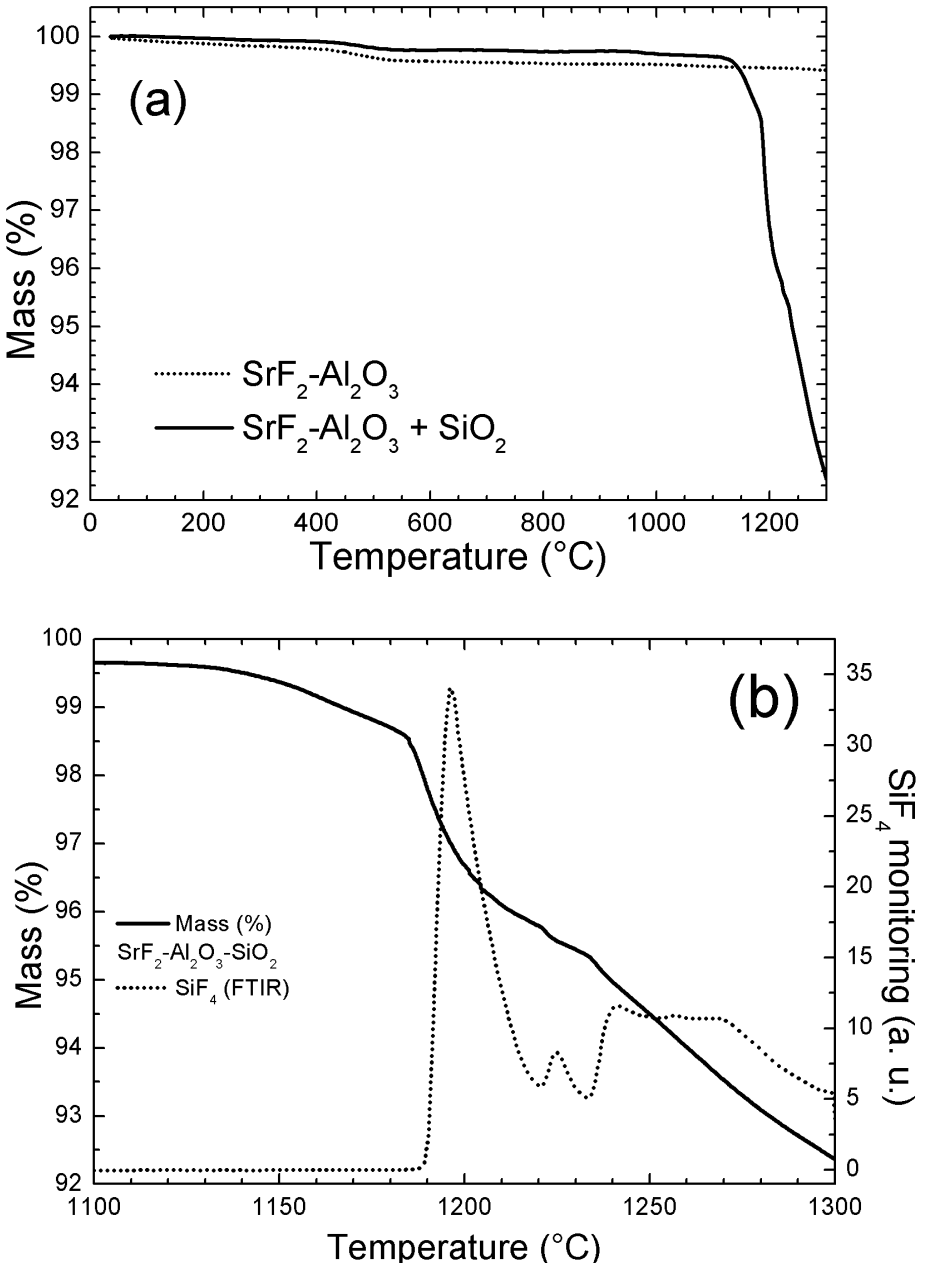

Figure V.11. a) Thermogravimetric analysis of two powder mixtures: $3SrF_2$-$1Al_2O_3$ and $1(3SrF_2$-$1Al_2O_3)$-$1SiO_2$. b) SiF_4 volatilization is monitored by FTIR in the SiO_2 containing mixture and is corresponding to the onset of the mass loss.

One should note that the temperature used in the fabrication of oxyfluoride fibers, typically 1925-2000 °C, is much higher than the range of temperature investigated by TGA. However, it is fair to assume that continuing to increase the temperature would lead to the formation of more SiF_4, although formation of other byproducts cannot be ruled out [24], [25]. To further investigate which components are formed upon heating in this SrF_2-Al_2O_3-SiO_2 system, as series of pellets in the $2SrF_2$-$1Al_2O_3$-$1SiO_2$ molar composition were fabricated (10 mm diameter and 2 mm thickness, ~0.3 g per pellet) with the help of a uniaxial floor press. These fabricated pellets were then heat-treated for one hour at different temperatures (1300 °C, 1400 °C, 1500 °C) in a tube furnace, and in air atmosphere (as it will be done during the draw process where the core materials are not in a close environment, see Fig. V.1b). A higher temperature would cause the pellets to fuse with the Pt foil substrate on which they are deposited in the furnace, and therefore no trial at higher temperature than 1500 °C was attempted. The pellet masses (in wt%) as a function of heat-treatment temperature is displayed in Fig. V.12. As the pellet is heated and the temperature increased, a decrease in the sample masses is observed, and this up until 1400 °C above which it stabilizes. This decrease in mass is expected due to the formation of SiF_4 species, as observed with TGA data.

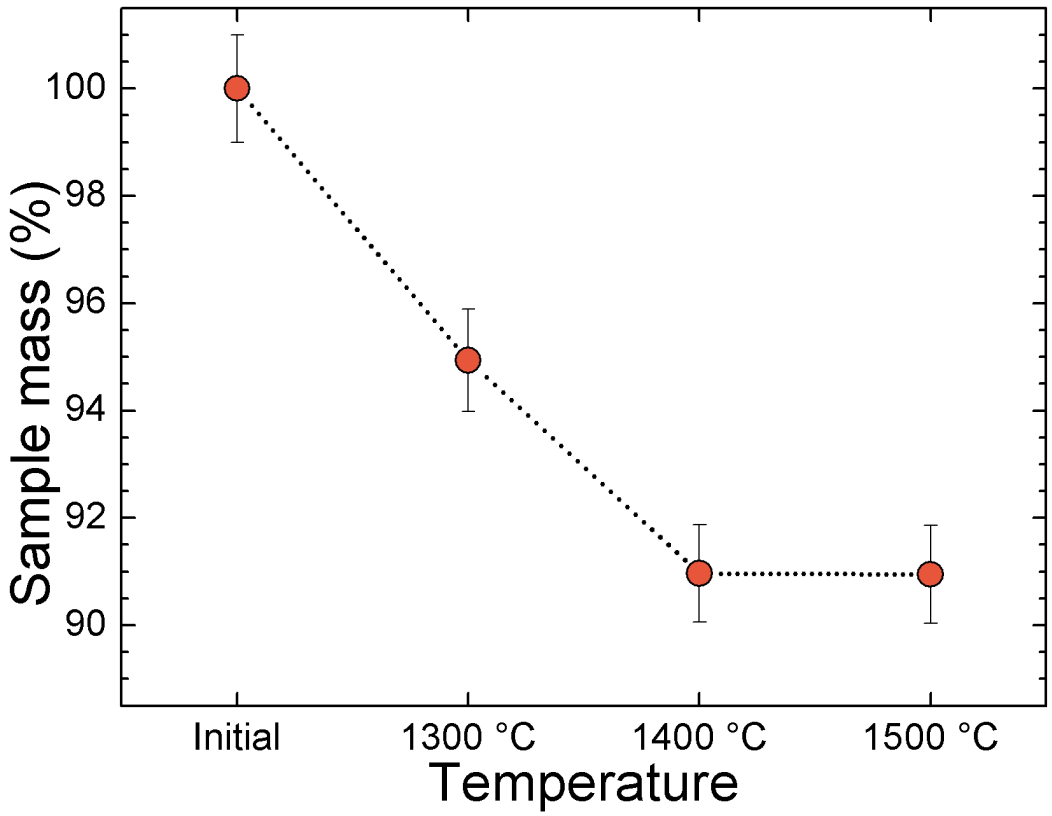

Figure V.12. Evolution of pellet mass (mixture of $2SrF_2$-$1Al_2O_3$-$1SiO_2$) as a function of temperature. A pellet is heated at different temperatures for an hour. « Initial » corresponds to the non-heated pellet.

Each heat-treated pellet is then studied by XRD using a Rigaku Ultima IV x-ray diffractometer, with Cu K_α radiation (λ=1.5408Å) as the x-ray source. The scan speed was set to 0.7 deg/min and the 2-theta scan range was from 10 to 80 deg. The objective of this XRD analysis is to determine the formation of new phases upon heat treatment, and, therefore, to best understand the chemical reactions that lead to SiF_4 volatilization. It is worth mentioning that for this study, a SiO_2-quartz precursor material was used instead of SiO_2-glass, in the goal of determining phases more easily with XRD. In Fig. V.13, the XRD

patterns are reported. First, the XRD pattern for the "initial" sample, that is, the standard sample, is a combination of SrF_2, Al_2O_3 (corundum) and low α-quartz (SiO_2). More information regarding the attribution to the peaks can be found in Appendix V.9. For the benefit of the reader, it is worth mentioning that the principal peaks at 26.57°, 44.12°, and 52.27° are attributed to SrF_2.

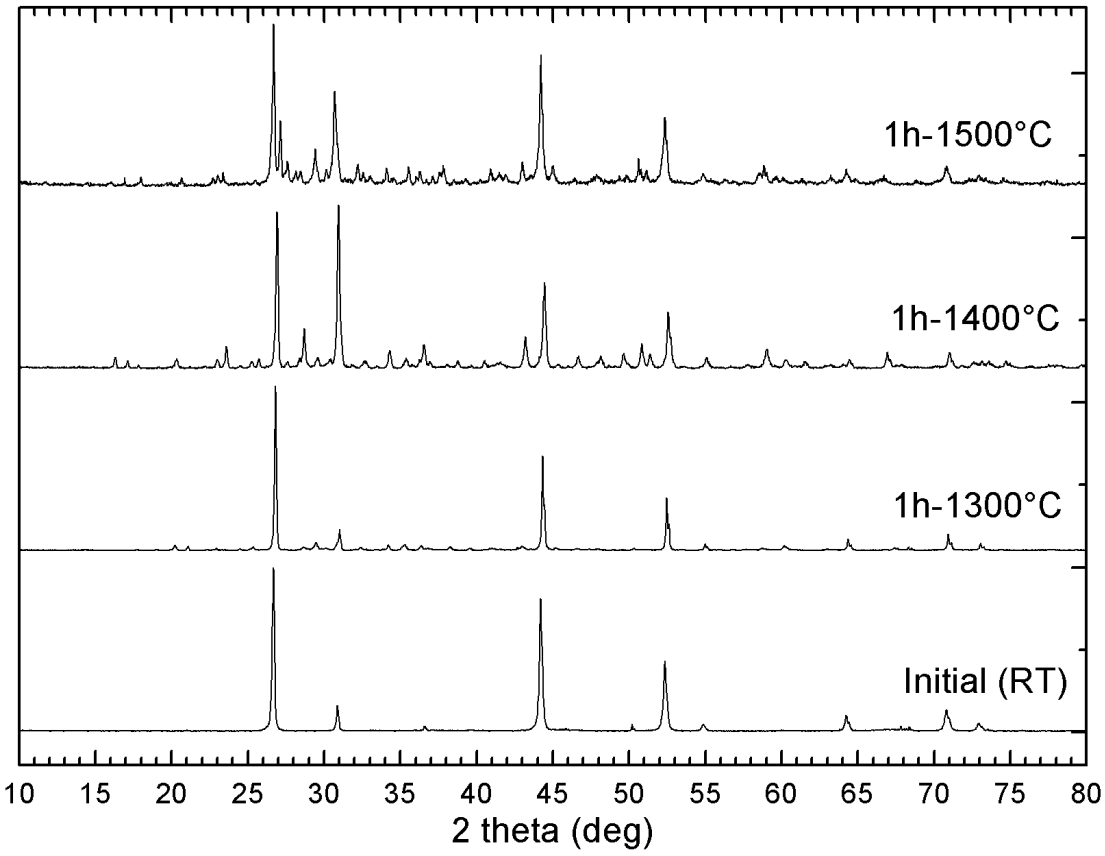

Figure V.13. XRD pattern for $2SrF_2$-$1Al_2O_3$-$1SiO_2$ heat-treated pellets at different temperatures and for 1h. The reader is referred to Appendix V.9 for more details concerning peak attribution.

Table V.5 summarizes the phases detected for each characterized pellet. Interestingly, it is found that the formation of strontium fluoro-alumino-silicate phases predominates ($Sr_6Al_{18}Si_2O_{37}$, $Sr_2SiAl_2O_7$, $SrSi_2Al_2O_8$) with some remaining SrF_2 (and, less obviously, Al_2O_3 and SiO_2).

Table V.5. Phases detected with XRD analyses for $2SrF_2$-$1Al_2O_3$-$1SiO_2$ (molar ratio) pellets heat treated at different temperatures for 1h.

Pellets	Phases detected[a, c]	Potential additional phases[b, c]
Initial (non heat-treated)	SrF_2 - Al_2O_3 - SiO_2	-
1300 °C	SrF_2 - $Sr_6Al_{18}Si_2O_{37}$ - $Sr_2SiAl_2O_7$	$SrSi_2Al_2O_8$ - SiO_2 - Al_2O_3
1400 °C	SrF_2 - $Sr_2SiAl_2O_7$ - $Sr_6Al_{18}Si_2O_{37}$	$SrSi_2Al_2O_8$ - SiO_2 - Al_2O_3 α-$Sr_4Al_2O_7$ - $Sr_3Al_2O_6$ - $SrAl_2O_4$
1500 °C	SrF_2 - $Sr_2SiAl_2O_7$ - $Sr_6Al_{18}Si_2O_{37}$ - $SrSi_2Al_2O_8$	α-$Sr_4Al_2O_7$ - $Sr_3Al_2O_6$ - $SrAl_2O_4$

[a]: Phases clearly observable in the XRD pattern.

[b]: Some of these phases may be present, but the complexity of the XRD pattern does not allow for a definitive answer.

[c]: SrF_2 (PDF card No. 00-006-0262), SiO_2 quartz low (PDF Card No. 00-005-0490), Al_2O_3 Corundum, synthetic (PCPDF 46-1212), $Sr_6Al_{18}Si_2O_{37}$ (PCPDF 10-0025), $Sr_2Al_2SiO_7$ (PDF Card No. 00-038-1333), $SrAl_2Si_2O_8$ (PDF Card No. 01-070-7145). Potential other phases are α-$Sr_4Al_2O_7$ (PCPDF 28-1204), $Sr_3Al_2O_6$ (PCPDF 24-1187), and $SrAl_2O_4$ (PDF Card No. 00-034-0379).

Interestingly, at higher temperature, many potential strontium aluminate phases are detected. It should be remembered that, as the mixture is heated, formation of SiF_4 (associated with the weight loss) depletes the mixture from its initial SiO_2, and consequently favoring the formation of aluminates at the expense of aluminosilicates. Moreover, no strontium fluoro-silicate ($Sr_wSi_xF_yO_z$) nor strontium fluoro-aluminate

($Sr_wAl_xF_yO_z$) phases were detected. SrF_2 is found to be oxidized in contact with SiO_2 and Al_2O_3, forming a strontium aluminosilicate ($Sr_wAl_xSi_yO_z$), and the remaining fluorine is found as SrF_2. If the draw temperatures used in the previous studies were in the 1925 °C - 2000 °C range and the composition ratio different, it was previously suggested than F remains attached to Sr during the draw. The XRD experiments also favor this hypothesis.

As has been observed, the initial oxyfluoride composition of the studied mixture ($2SrF_2$ – $1Al_2O_3$ – $1SiO_2$ in molar ratio) is progressively transformed into an oxide composition. The principal phases formed during heat-treatment, reported in Table V.5, are shown on a ternary SiO_2-SrO-Al_2O_3 phase diagram, taken from [26]. This diagram is reported in Fig. V.14. The arrows in Fig. V.14 are guide-to-the-eyes and show the paths taken during heat-treatment and the formation of new phases, as previously discussed, at higher temperatures and as the system evolves over time. If some weak signal for $SrSi_2Al_2O_8$ were detected for the pellets heat-treated at 1500 °C for 1 hour, the main phases formed were principally $Sr_6Al_{18}Si_2O_{37}$ at 1300 °C, and progressively shifting toward $Sr_2SiAl_2O_7$ at 1400 °C and 1500 °C. Finally, although less apparent in the XRD diffractograms, the presence of some strontium aluminates at 1400 and 1500 °C is likely. Again, these phase transformations are consistent with a decrease in SiO_2 content over time.

From the many phases formed and identified above, some potential equations that drive the SrF_2 transformation mechanisms can be determined (and assuming only SiF_4 is formed):

$$2\ Al_2O_3 + 5\ SiO_2 + 2\ SrF_2 = SrAl_2Si_2O_8 + SiF_4 \qquad (5.1)$$

$$9\ Al_2O_3 + 5\ SiO_2 + 6\ SrF_2 = Sr_6Al_{18}Si_2O_{37} + 3\ SiF_4 \qquad (5.2)$$

$$Al_2O_3 + 2\ SiO_2 + 2\ SrF_2 = Sr_2Al_2SiO_7 + SiF_4 \qquad (5.3)$$

By knowing the initial SrF_2-Al_2O_3-SiO_2 ratio and considering each reaction to be complete, it is possible to calculate the theoretical weight loss resulting from formation of SiF_4. Hence, theoretical losses for Eqns. 5.1, 5.2, and 5.3 are 6.0 wt. %, 9.0 wt. % and, 12.6 wt. %, respectively. From Fig. V.12, the weight loss plateaus around 9 wt. %, which is consistent with Eqn. 5.2 (and corresponds to the phase primarily form at 1300 °C).

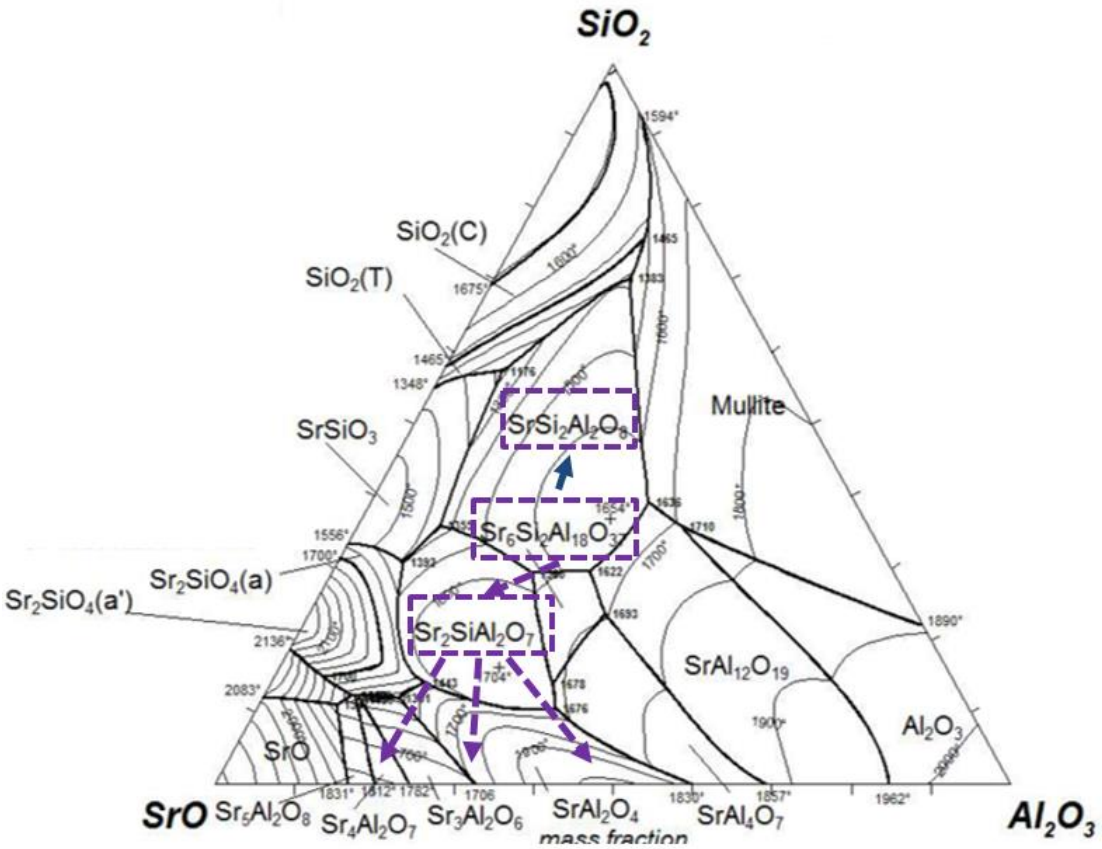

Figure V.14. SrO-Al_2O_3-SiO_2 ternary diagram taken from [26] (and given in wt%). The phases detected by XRD (Table V.5), which are in the strontium aluminosilicate system, are reported here. The arrows are guide-to-the-eye to show the phase transformations that occur upon heating as the SrF_2-Al_2O_3-SiO_2 system is progressively transformed into a SrO-Al_2O_3-SiO_2 system.

Additionally, from the initial composition and assuming complete reaction through Eqn. 5.2, the final composition (in mole %) is 33.33 % SrF_2 - 11.11 % SiO_2 - 2.78 % $Sr_6Al_{18}Si_2O_{37}$ - 8.33 % SiF_4. The remaining SrF_2 is easily detectable with XRD. An attempt was made to analyze the pellets pre- and post- heat treatment with EDX. Unfortunately,

compositional analysis on the pellets was found challenging. The silica, and to a lesser extent, alumina powders, are difficult to shape (i.e., pressed into pellets). Thus, when crushing the powder mixture (necessary to provide good homogeneity) in a mortar and then pressing it into pellets, the SiO_2 and Al_2O_3 particles tend to be embedded/encapsulated by the softer SrF_2 powder. Therefore, an EDX compositional analysis is strongly affected, which, in turn, prevents a trustworthy analysis.

Based on previous observations, one may expect the fluorine to be entirely removed from the system in a fiber core system, as the precursor materials typically spend between 30 to 60 mins at 2000 °C, which is contradictory to the observations, since in each fiber drawn, there exists some remaining fluorine in the core. However, the initial mixture inserted in the capillary does not contain any silica, and, as seen before, Al_2O_3 does not lead to fluorine volatilization when in contact with SrF_2. Therefore, it is easy to imagine the fluorine at the core center not to be physically in contact with any silica during the heating process (at least for some time), preventing the fluorine from volatilizing. Based on this simple argument, surrounding SrF_2 by an "inert material" (i.e., which does not react with it) such as alumina, hinders the reaction between SrF_2 and SiO_2 as SrF_2 is surrounded by this "non-reacting" material. Another possible reason that can impact the prevention of fluorine volatilization during fiber drawing when alumina is added into the core composition is its ability to increase the melt viscosity [23], and could, in turn, decrease the rate at which silica gets incorporated from the cladding into the core.

Another study was performed by analyzing a heat-treated pellet in the binary SiO_2-SrF_2 system, in order to provide further information on the reactivity of SrF_2 with SiO_2 only, without any Al_2O_3. An initial molar ratio of $2SrF_2$-$1SiO_2$ was originally chosen, as the widely-accepted reaction between SiO_2 and AEF_2 (and specifically recast here for SrF_2, as it is typically given for CaF_2) that governs SiF_4 volatilization is given as follow [11], [16], [17], [27]:

$$SiO_2 + 2\ SrF_2 = 2\ SrO + SiF_4, \qquad (5.4)$$

where SrO is in a "molten state or slag". Therefore, the initial ratio is chosen to maximize weight loss (33.3 wt.%) based on initial ratio and assuming reaction is complete. From previous TGA experiments, it is known that the reaction between SrF_2 and SiO_2 starts at ~1175 °C.

Therefore, a pellet is heated to 1300 °C for 120 min and analyzed under XRD (and compared to a non-heat-treated powder for reference). The XRD patterns are displayed in Fig. V.15. For the non-heat-treated sample, SrF_2 and SiO_2 are detected as they are initial precursor materials. Post-heat treatment, $SrSiO_3$ is formed, and possibly some β-Sr_2SiO_4 (not shown here for clarity but peak positions can be found in Appendix V.9). Note also that some SrF_2 and SiO_2 remains, and no SrO, nor strontium fluoro-silicates ($Sr_wSi_xO_yF_z$) were detected post heat-treatment.

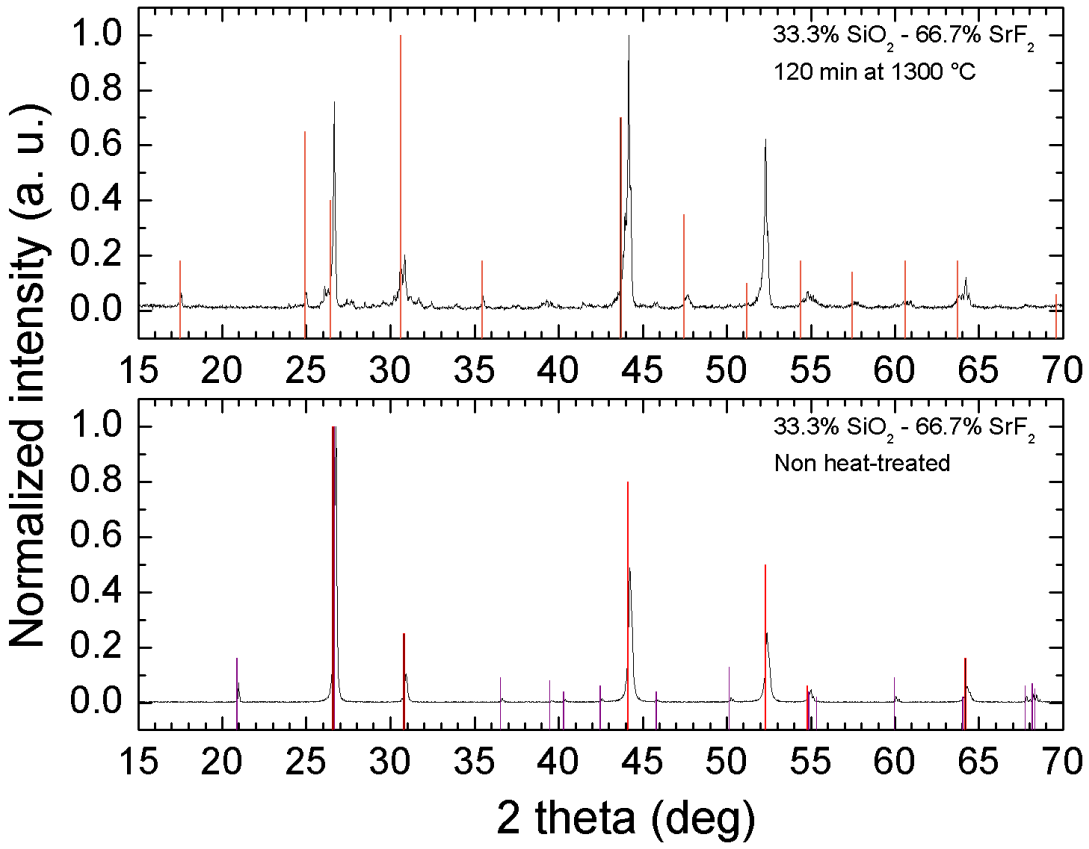

Figure V.15. XRD patterns for two $2SrF_2$-$1SiO_2$ powder mixtures: One is a non-heat-treated mixture (bottom), the other is heat-treated at 1300 °C for 120 min. Peak attribution: In red is SrF_2 (PDF card No. 00-006-0262), in purple is SiO_2 quartz, low (PDF Card No. 00-005-0490), and in orange is $SrSiO_3$ (PDF card No. 00-006-0415). Another secondary phase, β-Sr_2SiO_4, may potentially be present (Appendix V.9).

Additionally, weight loss for the heat treated SrF_2-SiO_2 sample gave ~6.0 wt% loss, which is very far off the 33.3 wt% loss expected based on the reaction stoichiometry typically described in literature. Now, considering the reaction between SrF_2 and SiO_2 to

be complete and forming exclusively $SrSiO_3$ (as it is the principal phase detected), the following reaction is obtained:

$$3\ SiO_2 + 2\ SrF_2 = 2\ SrSiO_3 + SiF_4 \qquad (5.5)$$

The calculated theoretical weight loss due to SiF_4 volatilization would be of 11.1 wt.%, which is a significantly lower than the 33.3 wt.% expected from Eqn. 5.4. Additionally, if Eqn. 5.5 was taken to completion, there should be no SiO_2 left, as all of it should have reacted to form SiF_4. However, some remaining SiO_2 post heat treatment is detected, which suggests the reaction was not complete. This can also explain the lower mass loss observed relative to the expected theoretical value (6.0 wt.% instead of 11.1 wt.%). Furthermore, a pellet of the same composition and heat treated with identical condition as before (2 hours at 1300 °C) was made, but the SiO_2 quartz used previously was substituted by pristine silica glass that was crushed into powder. The weight loss post heat treatment was of ~8.3 wt%. This value, slightly higher than in the case of SiO_2 quartz being used, stays within the same range and therefore the observations made using SiO_2 quartz powder are also valid to SiO_2 glass. The differences in wt. % loss can arise from different thermal behavior between glass and crystal. Complementarily, due to the pellet progressively fusing against the Pt crucible foil as time is increased, no further attempt at higher temperature and longer time was tried. XRD experiments have shown that SrF_2 will progressively react with SiO_2 to form either aluminosilicates or silicates depending on the system considered, with F remaining attached to Sr as in "SrF_2". Moreover, as SiF_4 is the principal gaseous species formed as the fluoride-oxide mixture reacts, its partial pressure can be estimated at a given temperature and pressure and for a given system. Hence, the

evolution of partial pressure for the SrF_2-SiO_2 system is investigated as a function of temperature, due to its simplicity, compared to SrF_2-Al_2O_3-SiO_2 system, which can be driven by numerous reactions. The thermodynamic systems are considered open in air (as it is inside the silica capillary preform) and at atmospheric pressure (1 bar). From thermodynamics database (JANAF tables and [28]), the standard Gibbs free energy of formation for Eqn. 5.4 and Eqn. 5.5 are calculated for different temperatures and reported in Table V.6.

Table V.6. Gibbs free energy of formation (kJ/mole), at 3 different temperatures for two possible reactions involving SiO_2 and SrF_2.

Reactions	300 K		900 K		1300 K	
	ΔG_f[a]	$p(SiF_4)$[b]	ΔG_f[a]	$p(SiF_4)$[b]	ΔG_f[a]	$p(SiF_4)$[b]
$SiO_2 + 2\ SrF_2 = 2\ SrO + SiF_4$	489.681	5.44×10^{-86}	385.886	4.01×10^{-23}	324.067	9.51×10^{-14}
$2\ SrF_2 + 3\ SiO_2 = 2\ SrSiO_3 + SiF_4$	227.841	2.13×10^{-40}	123.79	6.53×10^{-8}	63.447	2.82×10^{-3}

[a]: In kJ/mol

[b]: In bar

ΔG_f evolution as a function of temperature is found to be linear over the 300K-1300K for both reactions. Therefore, ΔG_f (kJ.mol^{-1}) for reactions 1 and 2 as a function of temperature (in K) can be estimated such as

$$\Delta G_f\ (SrO + SiF_4)\ =\ -0.1662 \times T\ +\ 538.38 \text{ kJ/mol} \qquad (5.6)$$

$$\Delta G_f\ (SrSiO_3 + SiF_4)\ =\ -0.1651 \times T\ +\ 275.95 \text{ kJ/mol} \quad (5.7)$$

and the partial pressure of SiF_4, for each system, is given as:

$$p(SiF_4) = K = exp(\frac{-\Delta G_f}{RT}), \quad (5.8)$$

as reported in Table V.6. Using Eqn. 5.8 the p(SiF_4) is determined for the two reactions and its evolution as a function of temperature (in °C for convenience) is reported in Fig. V.16. Here the activities of the species are assumed to be equal to 1. Interestingly, performing the calculation for Eqn. 5.4 results in very low values of partial pressure, and is not satisfactory to explain the volatilization of fluorine in these systems. On the other hand, the second reaction (formation of $SrSiO_3$) shows a drastic increase of p(SiF_4) as temperature exceeds ~1100°C, which correlates very well with the characteristic onset for the weight loss previously observed by TGA (Fig. V.16).

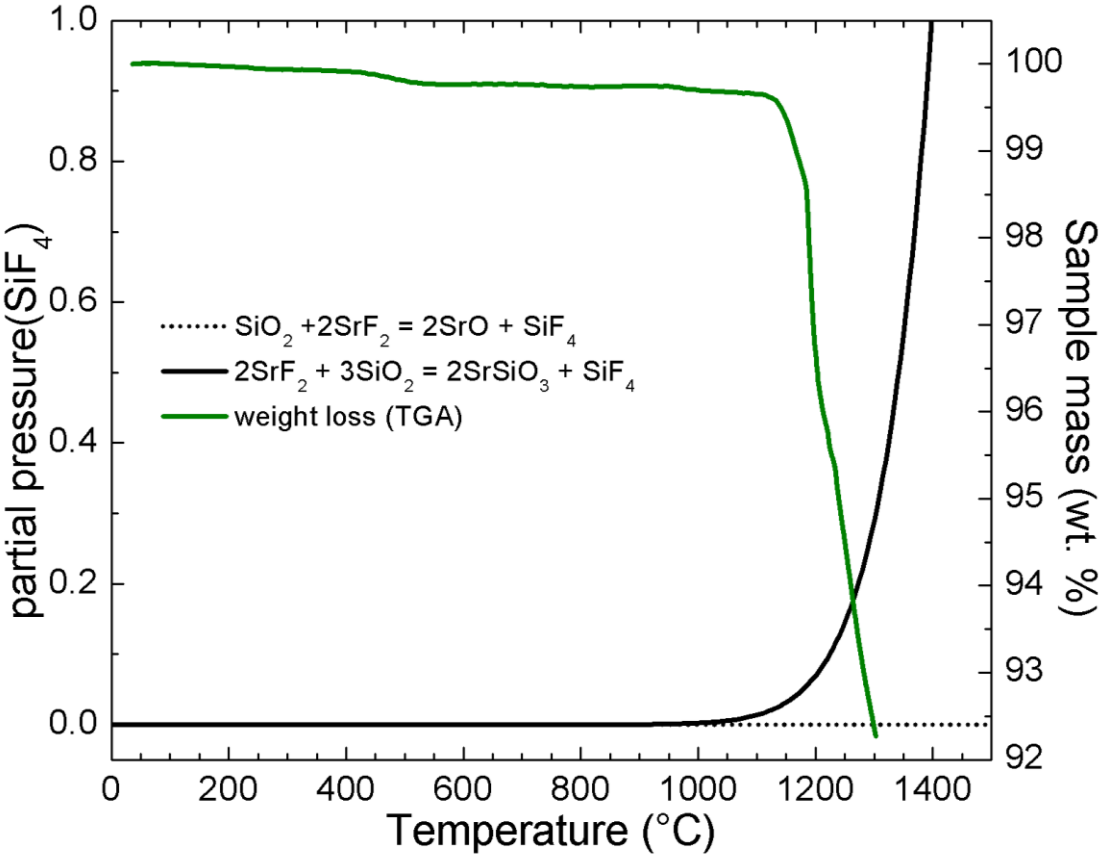

Figure V.16. Evolution of the partial pressure of silicon tetrafluoride (SiF_4) as a function of temperature (°C) for two reactions (Eqn. 5.4 and Eqn. 5.5) involving SrF_2 and SiO_2. The weight loss for SrF_2-Al_2O_3-SiO_2 from previous TGA experiment is also displayed; note the correspondence between the increase of p(SiF_4) for Eqn. 5.4 and the sample mass decrease observed by TGA.

This simple, yet informative, thermodynamic study provides some insights into the nature of the reactions encountered by the precursors in contact with the silica during the fiber draw. Interestingly, the stoichiometric reaction commonly utilized to described SiF_4 volatilization (Eqn. 5.4) is contradictory to herein observations from weight loss

measurements, XRD analysis and thermodynamics investigation. The formation of silicates as in Eqn. 5.5 better describes the mechanisms of fluoride-oxides interactions. This has also been reported for LaF_3 interaction with SiO_2 glass to form $La_2Si_2O_7$ [29], [30], and suggests these conclusions can be valid for a multitude of oxyfluoride systems. This is of considerable importance as the transformation Fluoride → Oxide reactions found to drive the systems investigated in this dissertation show drastically different stoichiometry and byproducts.

However, the kinetics and thermodynamics of oxyfluoride melts are function of their compositions or their temperatures, but are also influenced by the drawing process, as it has been shown that core compositions evolve over time. A good illustration of the complexity of multicomponent oxyfluoride systems is their local structure; fluorine can bond with almost all glass constituents and in different proportions, forming Al-F, Si-F, and AE-F bonds [31]–[35] or more complicated complexes as described in [36]. Also, it is worth mentioning that the structure of the glass is a function of its fictive temperature [37]. Therefore, in an effort of better comprehend the local structure environment and get further insights on the nature of the oxyfluoride glass fiber cores fabricated, a Raman spectroscopy study is carried out and reported in the next Section.

V. G. Structural investigation by Raman spectroscopy.

Details regarding the local arrangement of the glass structure in the various oxyfluoride fiber systems can be investigated using Raman Spectroscopy. Unpolarized Raman spectra of the fiber core materials were obtained using a commercial Raman microscope (alpha300, WItech) in a backscattering geometry, utilizing a 532 nm pump source with a focused beam diameter of about 1 μm and a photon collection time of 120 s per datum. Each Raman spectrum was taken at the core center for each fiber, and direct observation of some typical features in these oxyfluoride systems can be made.

First, the influence of alumina on the scattering bandwidth is studied, with the help of fibers in the SrF_2-Al_2O_3 initial precursor composition system, but with various SrF_2 to Al_2O_3 ratios (1:1, 3:1, 9:1, see Table V.7). Second, the effect of the AE (Ca vs. Sr vs. Ba) in the glass structure is investigated, by comparing three fiber segments of very close compositions, but with different AEF_2 initial precursor compounds ($3AEF_2$-$1Al_2O_3$ series in Table V.7). Third, an oxyfluoride vs. all-oxide fiber segment ($1SrF_2$-$1Al_2O_3$ vs. $0.625SrO$-$1Al_2O_3$) is studied to better comprehend how oxyfluorides glass systems differentiate from their oxide analogs. Finally, Yb-doped strontium oxyfluoride glass cores developed to study their optical properties in Chapter VI are investigated here to determine the relationship between fractional nonbridging oxygens (NBOs) that exist in the molten core fabricated glasses and their corresponding characteristic Raman peak intensity strength.

Table V.7. Compositional analysis (at core center, EDX) of different fibers used to study Raman spectroscopic features of the oxyfluoride systems.

Fiber segment	T_{draw}(°C)	[AE]	[Al]	[Si]	[O]	[F]	[AE]/[Al]
$1SrF_2$-$1Al_2O_3$	2000	2.2	7.2	25.3	63.6	1.8	0.31
$3SrF_2$-$1Al_2O_3$	2000	3.0	2.1	28.7	63.5	2.7	1.43
$9SrF_2$-$1Al_2O_3$	2000	4.5	0.9	28.8	63.4	2.5	5.00
$3BaF_2$-$1Al_2O_3$	2000	3.5	2.6	28.0	63.4	2.4	1.35
$3CaF_2$-$1Al_2O_3$	2000	3.5	2.2	28.3	63.4	2.6	1.59
$0.625SrO$-$1Al_2O_3$	1925	3.0	10.5	22.5	63.9	-	0.29

The Raman spectra, for a series of SrF_2-Al_2O_3 initial precursor materials, with a varying SrF_2 to Al_2O_3 ratio, are displayed in Fig. V.17, this along with the Raman spectrum of fused silica, which is taken in the cladding of $1SrF_2$-$1Al_2O_3$ fiber segment.

Typical features have long been identified for fused silica [38]–[40]. The main peak at ~440 cm^{-1} is attributed to Si-O-Si stretching modes. Peaks at ~490 cm^{-1} and ~600 cm^{-1} correspond to the so-called defect lines, and other features, at ~800 cm^{-1} (bending modes of Si-O bonds), 1060 cm^{-1} and 1200 cm^{-1} (associated with some asymmetric and symmetric stretching vibrations) are also present. In the systems investigated, there is a decrease in the magnitude of the typical features of the silica network (such as ~440 cm^{-1} and ~800 cm^{-1}). This result is expected as the amount of SiO_2 is lower in the fiber core than in the cladding, and therefore its characteristic features are less pronounced.

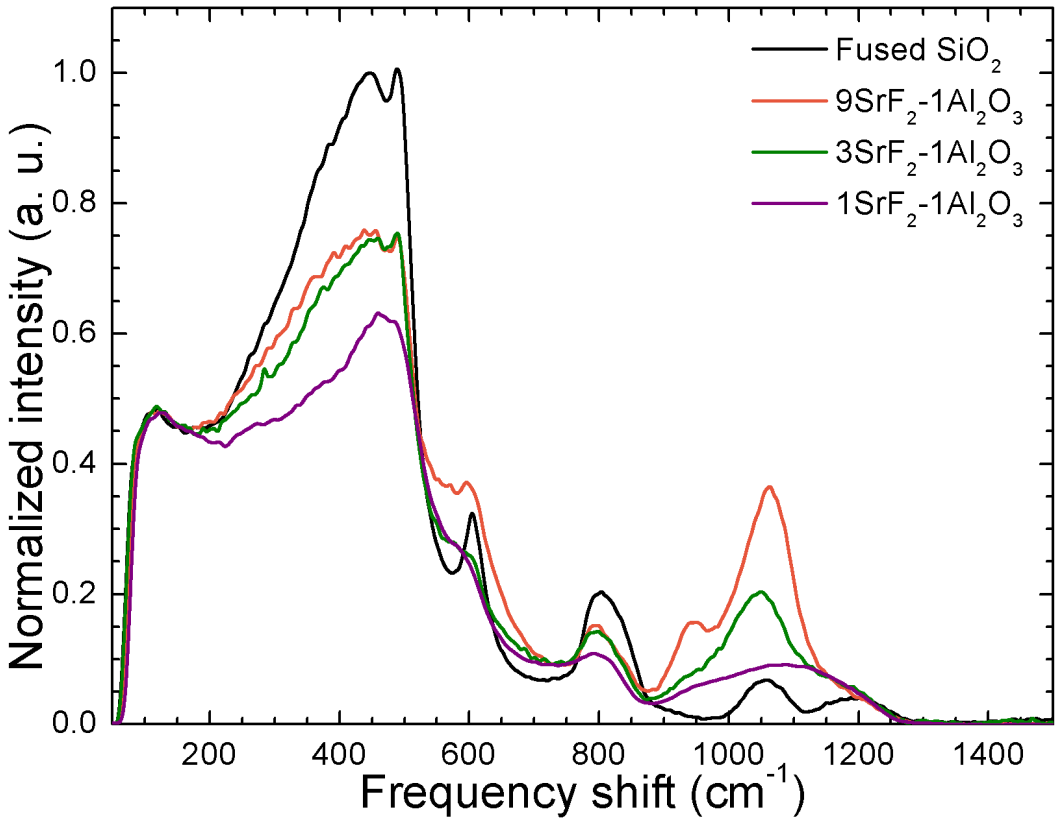

Figure V.17. Raman spectra for a series of strontium fluoro-alumino-silicate core materials with different initial precursor composition ratio of SrF_2 and Al_2O_3. The fused SiO_2 spectrum taken from the cladding of one fiber ($1SrF_2$-$1Al_2O_3$ fiber segment), as a reference.

For each fiber, one can observe the appearance of peaks in the 850-1250 cm^{-1} region (high frequency region). In silicate glasses, the characteristic features at ~1200 cm^{-1}, ~1100 cm^{-1}, ~950 cm^{-1}, ~900 cm^{-1} and ~850 cm^{-1}, are associated with the formation of 0,1,2,3, and 4 nonbridging oxygens (NBOs) per unit silica tetrahedron, respectively [38]. The high frequency features, again from ~850 cm^{-1} to 1250 cm^{-1} are very different for each

fiber and are a strong function of the Sr/Al ratio (see last column of Table V.7). A high Sr/Al ratio gives rise to very pronounced and resolved peaks. These features are very similar to those found in [41] for binary SrO-SiO_2. When the ratio is decreased, these scattering bands are also strongly decreased, as they correlate to a lower AE content and a higher Al content.

Typical features found in aluminosilicate systems are reported such as, i) "smoothening" of the peaks when alumina gets incorporated into the glass system[42]–[44], ii) the peak centered at ~800 cm^{-1} for fused silica is reduced and shifted to lower frequencies, and scales, as expected, with the amount of SiO_2 in the glass system [38], [45], and iii) the line defect at ~600 cm^{-1} is found to disappear with the addition of alumina (3-1 and 1-1 ratios) and is coupled with the appearance of a shoulder around ~550 cm^{-1} [46]. However, in the 9-1 ratio fiber, this peak is still observable and there is an increase of the scattering intensity at ~550 cm^{-1}. This shoulder cannot be attributed to Al_2O_3 as its content is substantially lower than from the 3-1 and 1-1 ratios, but is similar to what is observed in binary BaO-SiO_2 [43]. It should be mentioned that the features in the high frequency regions for binary BaO-SiO_2 systems in [43] resemble to the ones of the 9-1 ratio fiber segment, with a main peak around 1075 cm^{-1} and another one at 950 cm^{-1}, which are characteristic of silica tetrahedral units with one and two NBOs, respectively. These observations are direct evidence that the oxyfluoride systems considered are dominated by an "oxide like" structure. This is somewhat expected as [O]>>[F] (see Table V.7).

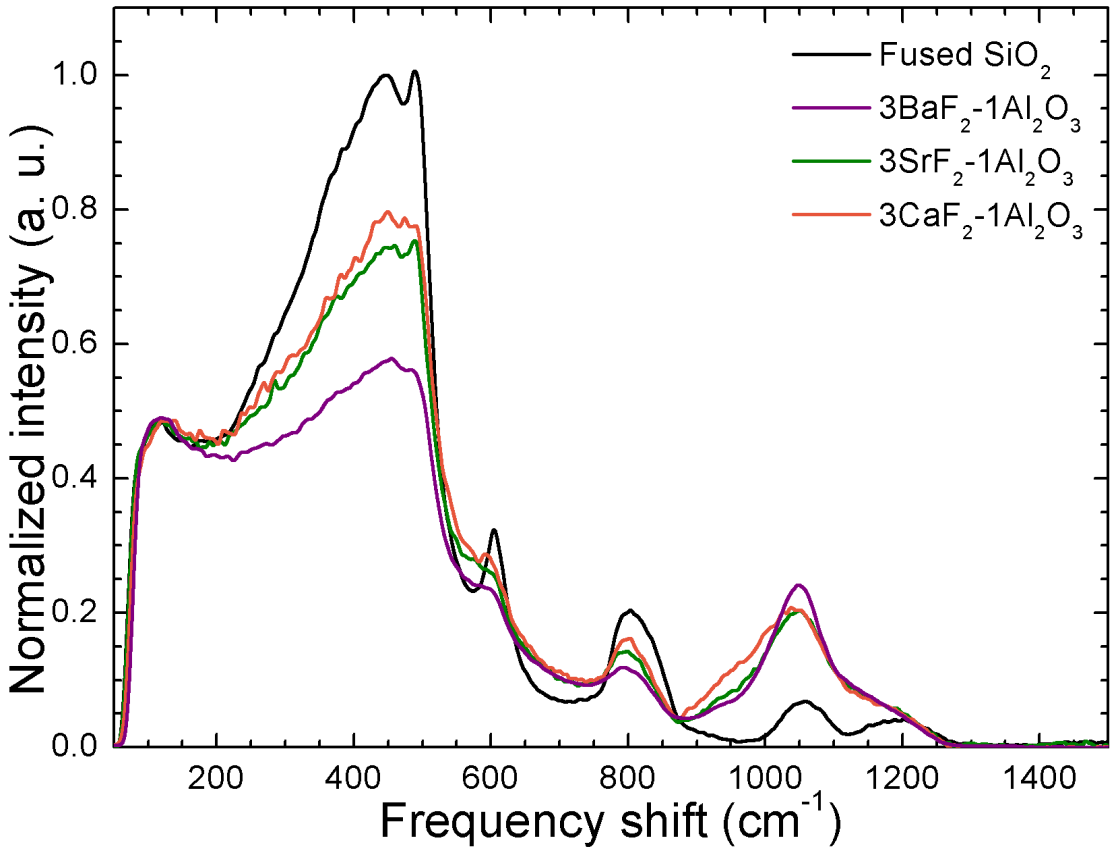

Figure V.18. Raman spectra for a series of alkaline earth (Ba, Sr, Ca) fluoro-alumino-silicate core materials, along with a fused SiO_2 spectrum taken from the cladding of one fiber ($1SrF_2$-$1Al_2O_3$ fiber segment, Fig. V.17), as a reference.

In order to study the influence of the alkaline earth cation on the glass structure, 3 fibers were considered, drawn in the same conditions (2000 °C, in a 3x30 mm silica preform, powder packed) with the same $3AEF_2$ to $1Al_2O_3$ ratio but with different AEF_2 species (i.e., BaF_2, SrF_2, and, CaF_2). Each Raman spectrum, taken at the core center of the fiber segments investigated, is presented in Fig. V.18, with again, the spectrum of fused

silica as a reference. The elemental composition at the core center for each fiber can be found in Table V.7.

First, the features described in Fig. V.18 for SrF_2-derived fibers are generally valid for the two other AEF_2 (i.e., CaF_2, and BaF_2) species studied here. In the high frequency region, the peaks, characteristic of the formation of NBOs, are similar to $3SrF_2$-$1Al_2O_3$ fiber segment, with some minor variations primarily attributed to the small concentration variations, which is discussed below. These observations are in agreement with [41] for BaO-SiO_2, SrO-SiO_2 and CaO-SiO_2 systems.

Nevertheless, some interesting differences arise from comparing AEF_2 species. The features attributed to silica for the BaF_2-derived aluminosilicate segment (e.g., the main peak centered at 440 cm^{-1} in Fig. V.18) are reduced compare to the others, and this with a similar AE, Al, and, F content. This is consistent with observation made in binary alkali silicate systems [47] where addition of heavier cations tend to favor this effect. In the same paper, it is noticed that the main silica peaks are broader for small alkali cations, and this is also observed for the alkaline earth family. Moreover, the convoluted peaks in the high frequency region, again attributed to NBOs, become broader and shifted to lower frequency as the cation field strength (CFS) increases (going up the Group II on the Periodic Table). This observation is consistent with [48] (Fig. V.19, Chapter V), and is attributed to the formation of silicon tetrahedral with 0 and 2 NBOs, instead of 1.

It is clear, based on the Raman spectroscopic data, that the features correlate very well with all-oxide systems. However, the core materials investigated have a non-neglectable amount of F, and some characteristic features should arise from this containing F. To further study and identify the effect of F on the Raman scattering bandwidth, 2 fiber segments are compared to each other: the $1SrF_2$-$1Al_2O_3$ fiber segment from above, and a $0.625SrO$-$1Al_2O_3$ fiber segment (with elemental composition reported in Table V.7), from [4]. Their Raman spectra are reported in Fig. V.19a. First, it should be noted the similar features exhibited by the two systems. The lower magnitude of the main silica peak at ~440 cm^{-1} in the SrO-derived fiber is due to its lower Si content, and its relatively higher alumina content also dictates the evolution of the other peaks as already detailed above. Note that for both fiber segments, Sr/Al content is somewhat close (0.31 vs. 0.29), which also explain generally similar features. In Fig. V.19b, a magnification on the low frequency region (up to 600 cm^{-1}) for these two core materials is displayed, along with the spectra of the crystalline powders SrF_2, SrO, and, SiO_2 quartz. It is worth mentioning that peak intensities for the crystalline powders are not normalized. Interestingly, one should note each powder exhibits a multitude of different peaks which may explain the fine variations in intensity in the 100-500 cm^{-1} region. Additionally, the small increase in the peak intensity centered at ~275 cm^{-1} for the SrF_2-derived fiber, not present in the SrO-derived one, may be the signature of Sr-F bonds. The peak intensity attributed to Sr-F bonds is shifted to lower frequency with respect to the peak of the SrF_2 powder sample; this is expected as an increase of temperature results in a shift of this peak as observed in [49]. Note that the peak

bandwidth also increases as temperature rises [49], which renders observation of Sr-F bond characteristic peak even more challenging.

Complementarily, in [50], the substitution of CaO with CaF_2 in SiO_2 is found to increase the scattering intensities of the peaks centered at 1075 cm^{-1} and 600 cm^{-1}, and to decrease to one around 900 cm^{-1}. In [51], the investigation of, again, a CaO-CaF_2-SiO_2 system, shows only slight modifications in the features. Specifically, in Fig. 2 of [51], the changes that follow substitution of CaO for CaF_2 are not a strong function of CaF_2 concentration. Therefore, it is difficult to attribute any other contribution to the scattering bandwidth to AEF_2, this added to the multicomponent nature of the glass systems investigated. Finally, if F was bonded to Si to form Si-F bonds, a peak should appear around 945 cm^{-1} [52]. If here there is no direct observation of this peak, the strong overlap with other peaks does not allow to draw definitive conclusion regarding this possibility. For completeness, in [53], a study on oxyfluoride aluminosilicates shows that addition of SrO into a LaF_3 containing aluminosilicate melt would lead to the formation of some Sr-F bonds. In [54], the same authors also concluded that fluorine was preferentially bonded to the alkaline earth (i.e., Sr).

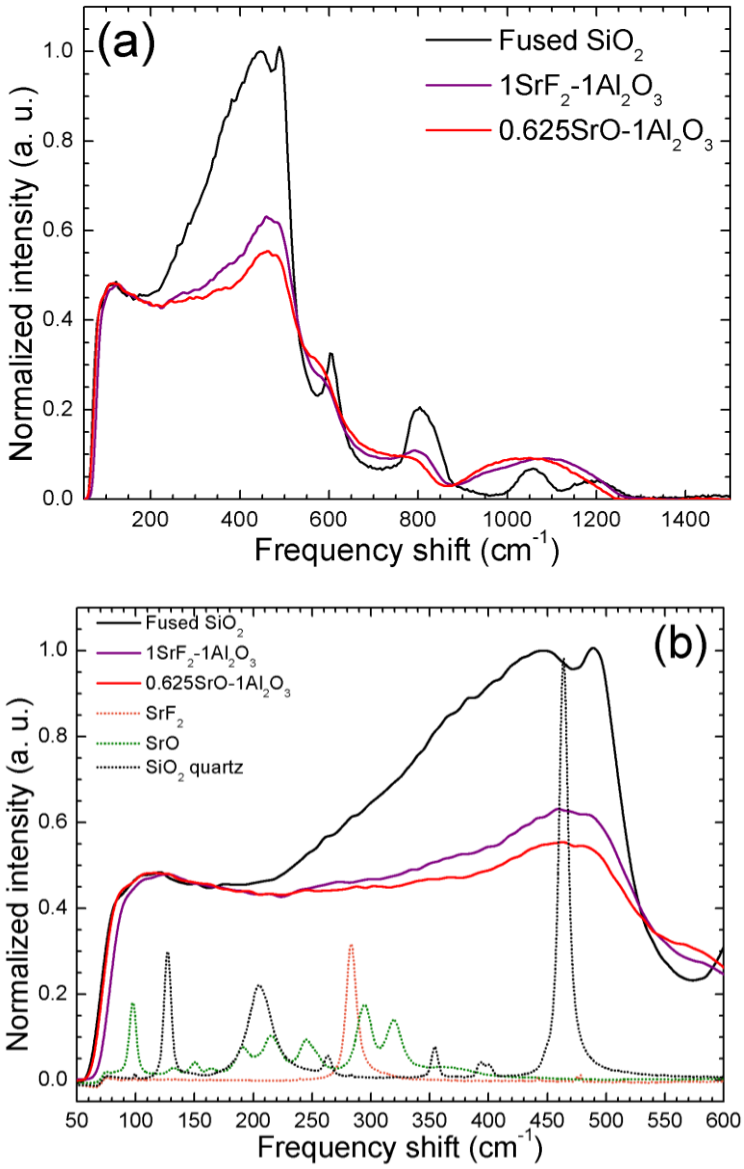

Figure V.19. a) Raman spectra for 2 fiber segments: One is a $1SrF_2$-$1Al_2O_3$-derived fiber, the other is a 0.625SrO-$1Al_2O_3$-derived fiber, taken from [4]. The spectrum of SiO_2 is given here as a reference. b) Magnification on the 50 to 600 cm^{-1} frequency range. Additionally, added are the Raman spectra for 3 crystalline powders: SrF_2, SrO, and SiO_2 quartz.

Raman spectra of a series of Yb-doped strontium aluminosilicate fibers, fabricated in order to study their optical properties (following Chapter), is reported in Fig. V.20a. In Fig. V.20b, the Raman intensity of the peak characteristics of NBOs, centered at ~1050 cm^{-1}, is plotted as a function of the theoretical fraction of NBOs, f(NBOs) in the glass core. f(NBOs) is calculated with the assumption that only the SrO contributes to the formation of NBOs. Both Yb_2O_3 and Al_2O_3 are considered as intermediates and consequently participate to the glass network [55]–[57] in these silica rich glasses. As discussed previously, formation of Sr-F bonds is expected to contribute to the scattering cross section at a frequency of ~275 cm^{-1}. Therefore, it does not contribute to an increase of the ~1050 cm^{-1} peak intensity.

Calculation of f(NBOs) for the aforementioned fiber core glass compositions is performed with two differing assumptions:

1) F is exclusively bound to Sr as in SrF_2, and the remaining Sr is bound to O, as in SrO. The glass results in an admixture of SrF_2 + SrO, additionally to SiO_2, Al_2O_3 and, Yb_2O_3.
2) Sr is considered exclusively bound to the oxygen, therefore forming "SrO" compound only (i.e., no SrF_2). This postulate is equivalent to estimate that core compositions are fluorine-free, and would contain SrO, SiO_2, Al_2O_3 and, Yb_2O_3.

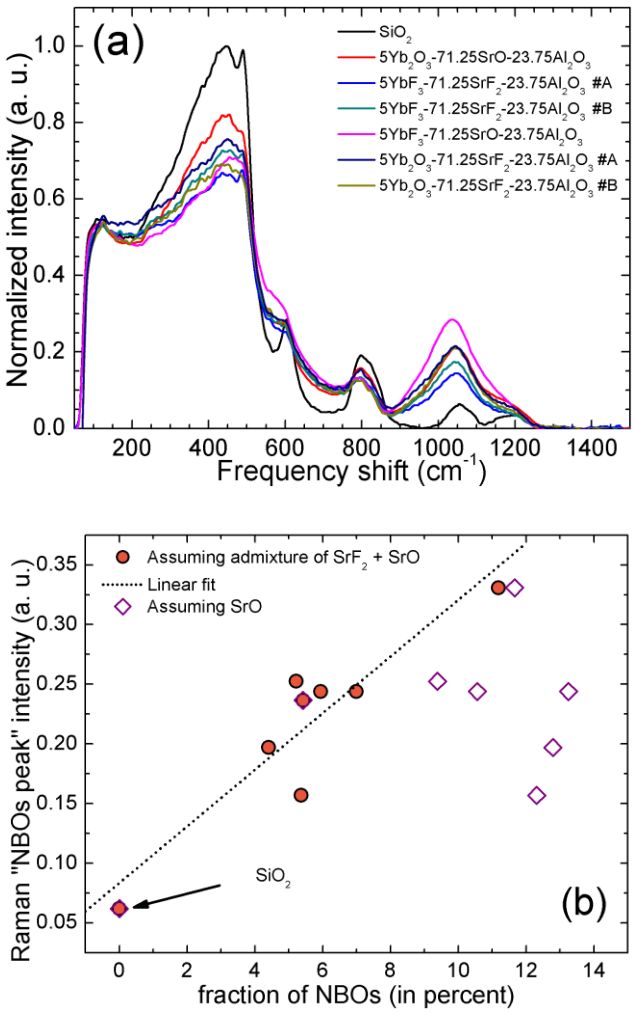

Figure V.20. a) Raman spectra for a series of Yb-doped fluoro-alumino-silicate glass optical fibers. b) Intensity of the Raman peak associated to the formation of NBOs (centered around 1050 cm^{-1}) as the theoretical fraction of the fraction of NBOs in the glass core (at the core center), for 2 different assumptions; i) assuming F is bound to Sr, forming SrF_2, and the remaining Sr is attached to O, forming SrO (in orange) and ii) assuming all the Sr is bound to O, forming only SrO (in purple) and considering the glass contains no fluorine.

The calculated f(NBOs) vs. characteristic Raman peak intensity of the ~1050 cm^{-1} peak is reported in Fig. V.20b. A correlation between the increase of the ~1050 cm^{-1} peak intensity and f(NBOs) when an admixture of SrF_2 + SrO (i.e., firt assumption) is clearly observable. However, assuming only SrO (i.e., no SrF_2) in the glass leads to uncorrelated data. As the trend expected is an increase of the Raman peak intensity as NBOs content increases, considering an admixture of Sr-F and Sr-O bonds in the glass is satisfactory. The results are consistent with the previous findings of this Chapter which suggests F to preferentially bond with Sr in the glass.

Finally, based on the previous findings, the incorporation of SrF_2 into the silicate glass network is expected to be similar to what is proposed for CaF_2 incorporation in [58] (Fig. 6), which is reported here (Fig. V.21) for the benefit of the reader.

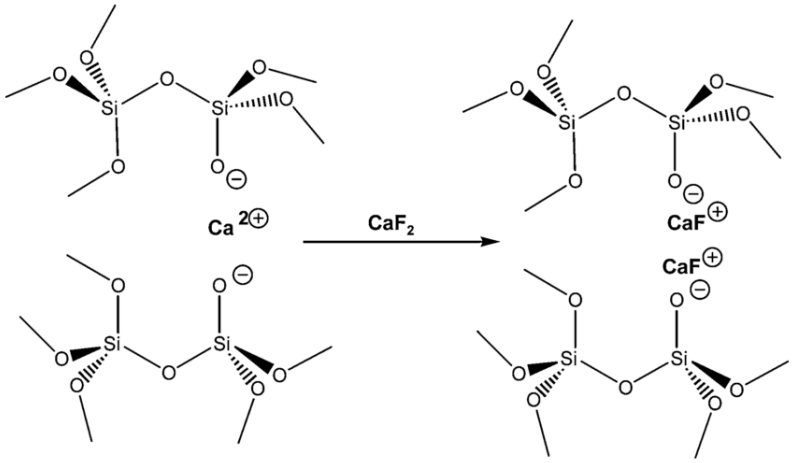

Figure V.21. Illustration (taken from [58]) of the effect of CaF_2 incorporation into the silica network, and how it is expected to modify the structure. SrF_2 is believed to modify the network similarly.

V. H. Conclusion

In this Chapter, the fabrication of oxyfluoride core and silica cladding glass optical fibers, using the molten core method, has been described. AEF_2-derived silicate and aluminosilicate fibers have been fabricated, and the role of alumina and drawing temperature on the glass stability, along with the compositional evolution of dopants during fiber drawing, was discussed. It has been shown that the principal mechanism of fluorine loss was through the formation of the volatile SiF_4 species, and that multiple factors could play a role in its rate of volatilization, e.g., initial amount of alumina in the precursor composition, the nature of the AEF_2 compound, but also the drawing conditions. On the other hand, optical basicity was found not to be a key property as it comes to retain more fluorine into the fiber glass core. In addition to a better understanding of the dynamics of fluoride-oxide reactions in the context of fiber processing, it has been suggested that the AEF_2 partially transforms into an oxide (aluminosilicate and/or silicate), but the remaining fluorine in the core glass remains dominantly bound with AE, as in AEF_2. If it is found valid for SrF_2 containing initial precursors in the range of temperatures and compositions investigated, the complexity of multicomponent systems should be kept in mind and the nature of fluorine bonding in oxyfluorides is a topic of continuous study.

In the next Chapter, optical properties of AEF_2-derived aluminosilicate systems are investigated, with a specific focus on SrF_2-containing systems.

V. I. Appendices

Appendix V. 1. Evolution of dopant concentrations over draw length

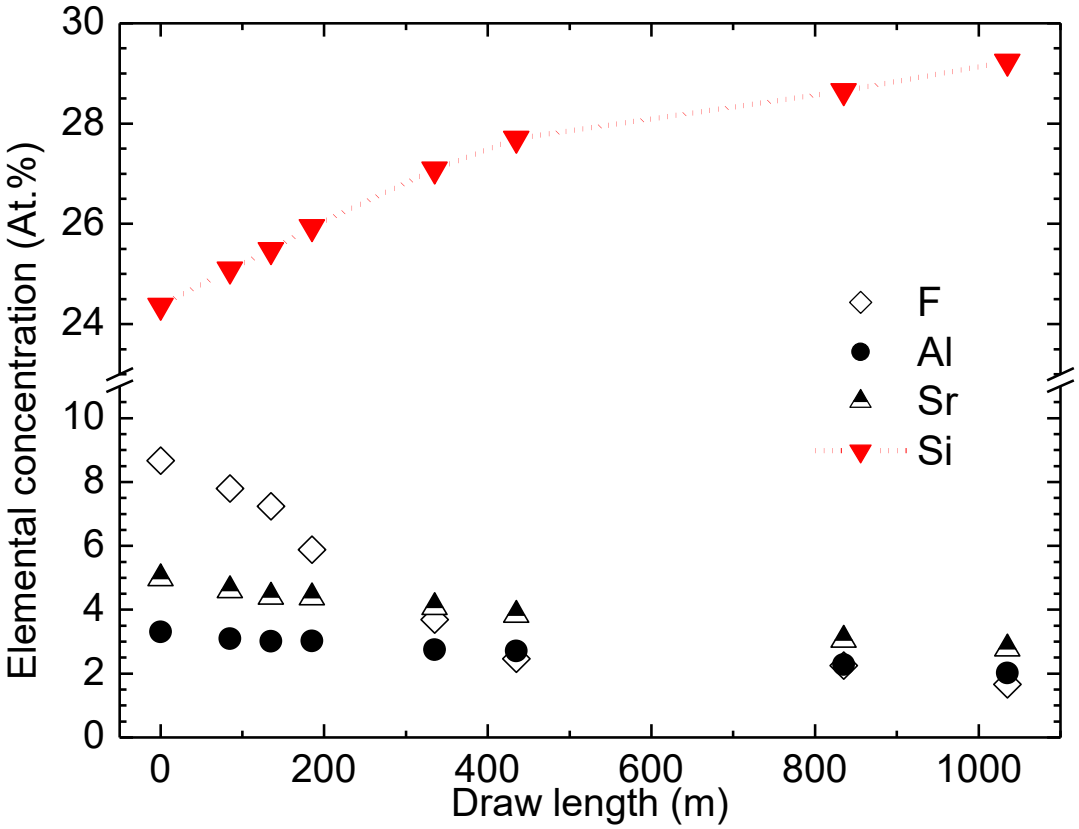

Elemental concentration (At. %) as a function of draw length (taken at the core center of each segment analyzed). Not shown for reasons of clarity is the oxygen concentration, %O. However, %O (At. %) = 100 – [%F + %Sr + %Al + %Si].

Appendix V. 2. Evolution as F/Sr and Al/Sr ratios over draw length

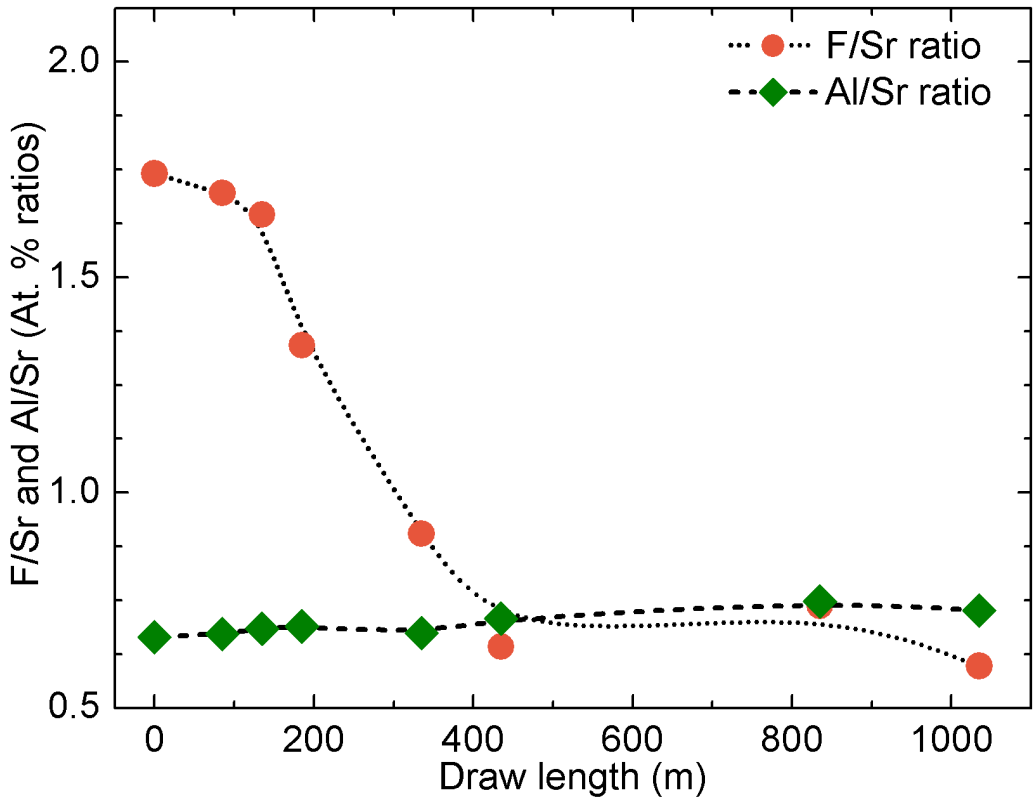

At. % ratio F/Sr (orange) and Al/Sr (green) content at the core center for a pressed pellets $3SrF_2$-$1Al_2O_3$ initial precursor composition mixture drawn in a 3x30 mm silica capillary preform at 2000 °C.

Appendix V. 3. Evolution core diameter as a function of draw length and Si content

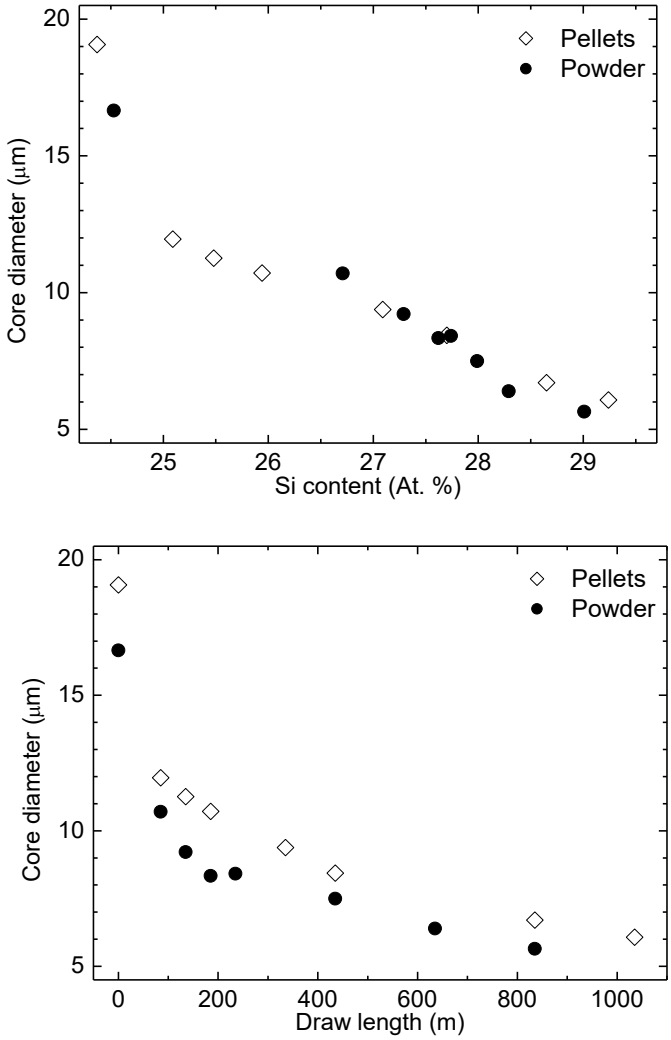

Core diameter (μm) as a function of draw length (m) and Si content (At. %) for two fibers having the same initial precursor composition ($3SrF_2$-$1Al_2O_3$) and drawn into 3x30 mm silica capillary preforms at 2000 °C, but with one precursor being powder packed ("Powder") and the other being pellet pressed ("Pellets").

Appendix V. 4. Drawing temperatures, fiber positions, and elemental compositions of various oxyfluoride fibers

Initial precursor composition	T_{draw} (°C)	Segment position	Elemental composition (in At. %)					At. % ratio (relative to initial precursor)			
			[AE]	[Al]	[F]	[O]	[Si]	[AE]	[Al]	[F]	[O]
$1Al_2O_3$-$3CaF_2$	2000	Beginning	5.70	3.60	7.80	59.00	23.90	0.266	0.25	0.18	2.75
$1Al_2O_3$-$3CaF_2$	2000	End	3.50	2.20	2.60	63.40	28.30	0.16	0.15	0.06	2.96
$1Al_2O_3$-$3SrF_2$	2000	Beginning	4.70	3.20	8.80	58.60	24.70	0.22	0.22	0.20	2.73
$1Al_2O_3$-$3SrF_2$	2000	End	2.98	2.11	2.72	63.51	28.68	0.14	0.15	0.06	2.96
$1Al_2O_3$-$3BaF_2$	2000	Beginning	4.80	3.80	7.60	59.40	24.40	0.22	0.27	0.18	2.78
$1Al_2O_3$-$3BaF_2$	2000	End	3.50	2.60	2.40	63.50	28.00	0.16	0.18	0.05	2.96
$1Al_2O_3$-$1.5SrF_2$-$1.5CaF_2$	2000	Beginning	4.7	2.9	4.0	62.0	26.40	0.22	0.20	0.09	2.9
$1Al_2O_3$-$1.5SrF_2$-$1.5CaF_2$	2000	End	4.0	2.2	2.5	63.0	28.30	0.19	0.15	0.06	2.9
$1Al_2O_3$-$3SrF_2$	1925	Beginning	4.03	3	6.51	60.48	25.08	0.19	0.21	0.15	2.82
$1Al_2O_3$-$3SrF_2$	1925	End	2.88	2.34	2.46	63.68	27.22	0.15	0.17	0.13	2.87
$1Al_2O_3$-$1MgF_2$	1925	Beginning	3.5	7.6	5.7	60.5	22.70	0.28	0.30	0.23	1.61
$1Al_2O_3$-$1MgF_2$	1925	End	2.5	5.5	4.3	62.0	25.70	0.20	0.22	0.17	1.65
$1Al_2O_3$-$1CaF_2$	1925	Beginning	3.68	7.21	6.3	60.04	22.77	0.29	0.29	0.25	0.29
$1Al_2O_3$-$1CaF_2$	1925	End	3.64	7.28	4.2	61.44	23.44	0.29	0.29	0.17	1.64
$1Al_2O_3$-$1SrF_2$	1925	Beginning	3.7	8.3	9.15	58.05	20.80	0.30	0.33	0.37	1.55
$1Al_2O_3$-$1SrF_2$	1925	End	2.2	7.2	1.8	63.5	25.30	0.18	0.29	0.07	1.69
$1Al_2O_3$-$1BaF_2$	1925	Beginning	4.42	8.25	10.52	56.8	20.01	0.35	0.33	0.42	1.51
$1Al_2O_3$-$1BaF_2$	1925	End	3.43	6.27	1.65	63.38	25.27	0.27	0.25	0.07	1.69

Appendix V. 5. Evolution core diameter as a function of draw length and Si content

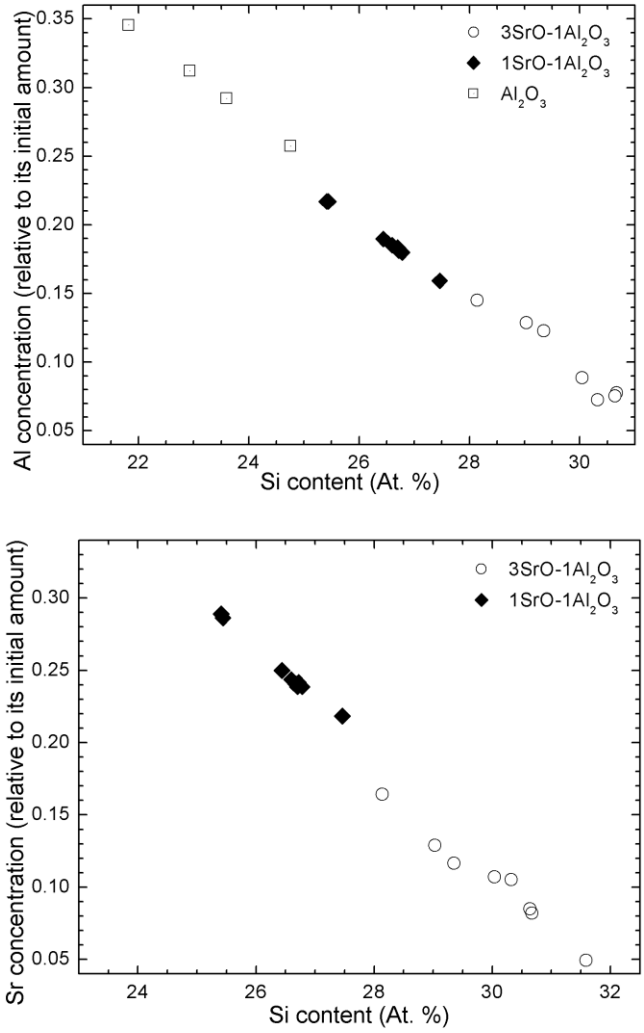

Evolution of Al and Sr (relative to their initial concentration) for different aluminosilicate fibers, drawn in the same conditions and at 2000 °C. The three different fibers have the following initial precursor compositions (molar ratio): 3SrO-1Al_2O_3, 1SrO-1Al_2O_3, and, Al_2O_3.

Appendix V. 6. Relative alkaline earth content as a function of relative fluorine content

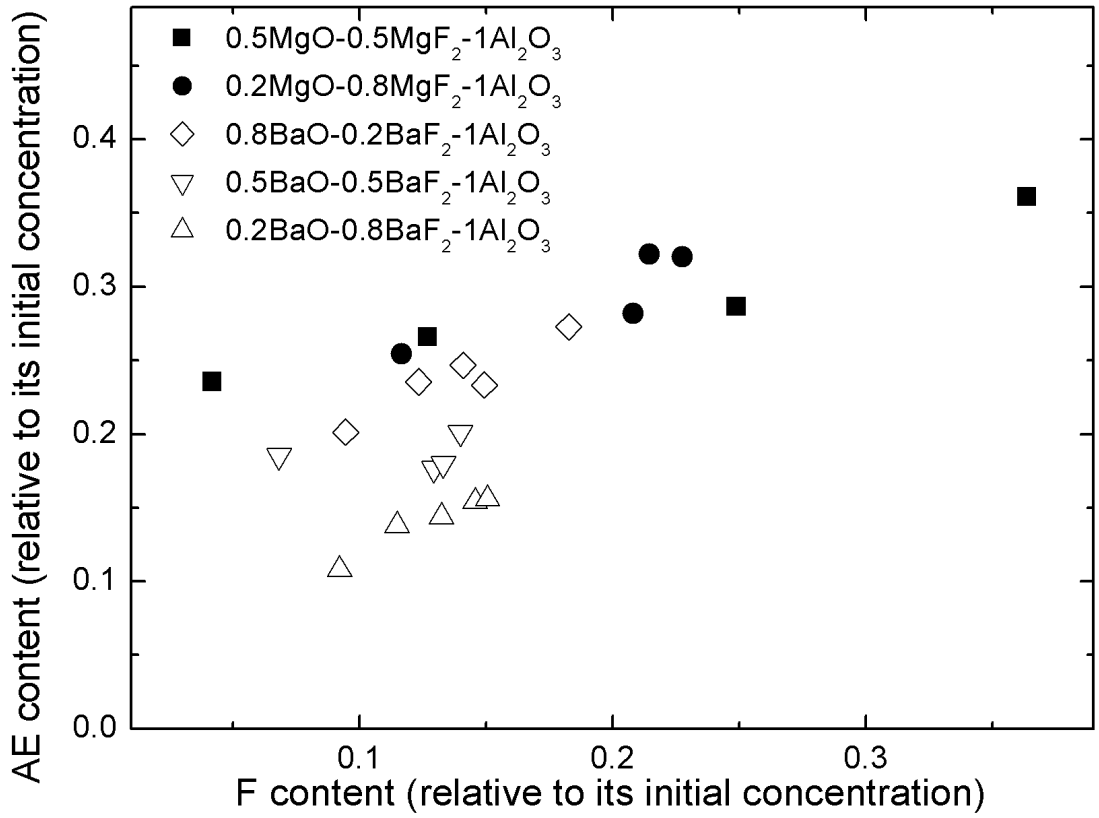

F vs. AE content (relative to their initial concentration) for a series of MgO-MgF_2-Al_2O_3 and BaO-BaF_2-Al_2O_3 initial precursor composition, with different AEO/AEF_2 initial ratio but with identical Al_2O_3 content.

Appendix V. 7. Positions, compositional analysis and optical basicity calculation of various oxyfluoride fibers

Elemental composition (At. %) and compound composition (mole %, assuming fluorine being attached to AE) for a series of BaF_2-BaO-Al_2O_3 and MgF_2-MgO-Al_2O_3 derived silicates optical fibers, along with the optical basicity calculated from compound composition.

Initial precursor composition	Position for each draw (in m)[a]	Elemental composition (in At. %)					Compound composition (mole %)				Optical Basicity
		[F]	[AE]	[Al]	[Si]	[O]	AEF_2	AEO	Al_2O_3	SiO_2	Λ
0.5MgO-0.5MgF_2-1Al_2O_3	1010	0.56	3.14	4.54	27.27	64.49	0.86	8.75	6.95	83.45	0.47577
0.5MgO-0.5MgF_2-1Al_2O_3	760	1.695	3.545	4.98	26.25	63.525	2.63	8.36	7.71	81.31	0.47142
0.5MgO-0.5MgF_2-1Al_2O_3	510	3.32	3.82	5.635	24.985	62.24	5.25	6.83	8.91	79.01	0.46446
0.5MgO-0.5MgF_2-1Al_2O_3	260	4.85	4.815	7.42	22.325	60.59	7.86	7.75	12.03	72.37	0.45695
0.2MgO-0.8MgF_2-1Al_2O_3	1000	2.395	3.26	5.64	25.665	63.045	3.77	6.50	8.88	80.85	0.46693
0.2MgO-0.8MgF_2-1Al_2O_3	750	4.27	3.615	6.375	24.185	61.555	6.89	4.78	10.29	78.05	0.45894

0.2MgO-0.8MgF_2-1Al_2O_3	500	4.67	4.105	7.715	22.61	60.9	7.64	5.79	12.62	73.96	0.4557
0.2MgO-0.8MgF_2-1Al_2O_3	388	4.4	4.13	8.175	22.295	60.99	7.21	6.33	13.40	73.07	0.45591
0.8BaO-0.2BaF_2-1Al_2O_3	1010	0.83	3.24	9.16	23.26	63.51	1.34	9.09	14.74	74.84	0.50284
0.8BaO-0.2BaF_2-1Al_2O_3	572.5	0.525	2.795	8.9	23.875	63.9	0.84	8.14	14.30	76.72	0.49846
0.8BaO-0.2BaF_2-1Al_2O_3	510	0.685	3.27	8.98	23.445	63.625	1.10	9.38	14.39	75.13	0.50409
0.8BaO-0.2BaF_2-1Al_2O_3	135	0.7825	3.4275	9.4675	22.9	63.425	1.26	9.78	15.24	73.73	0.50497
0.8BaO-0.2BaF_2-1Al_2O_3	0	1.015	3.79	11.455	20.925	62.82	1.67	10.78	18.81	68.74	0.5054
0.5BaO-0.5MgF_2-1Al_2O_3	750	0.91	2.47	9.135	23.775	63.72	1.48	6.54	14.82	77.16	0.4923
0.5BaO-0.5MgF_2-1Al_2O_3	500	1.725	2.355	11.345	21.735	62.84	2.90	5.01	19.06	73.03	0.48369
0.5BaO-0.5MgF_2-1Al_2O_3	250	1.865	2.68	9.875	22.7	62.885	3.08	5.76	16.29	74.87	0.49026
0.5BaO-0.5MgF_2-1Al_2O_3	18	1.775	2.395	8.025	24.465	63.35	2.87	4.88	13.00	79.25	0.4902

0.2MgO-0.8MgF_2-1Al_2O_3	1000	2.355	1.77	9.165	23.735	62.98	3.91	1.97	15.23	78.89	0.47768
0.2MgO-0.8MgF_2-1Al_2O_3	750	2.715	1.845	9.85	22.99	62.6	4.56	1.64	16.55	77.25	0.47606
0.2MgO-0.8MgF_2-1Al_2O_3	500	1.89	1.385	6.97	25.975	63.785	3.06	1.43	11.30	84.21	0.4784
0.2MgO-0.8MgF_2-1Al_2O_3	250	2.99	1.975	10.285	22.45	62.3	5.06	1.62	17.39	75.93	0.47595
0.2MgO-0.8MgF_2-1Al_2O_3	125	3.09	2	11.72	21.2	61.98	5.32	1.57	20.17	72.95	0.47319

[a]: Position (in m) is relative to the initial position of the draw (“0” would correspond to the beginning of the draw for each fiber).

Appendix V. 8. TGA of BaF_2-Al_2O_3 and BaF_2-Al_2O_3-SiO_2 systems

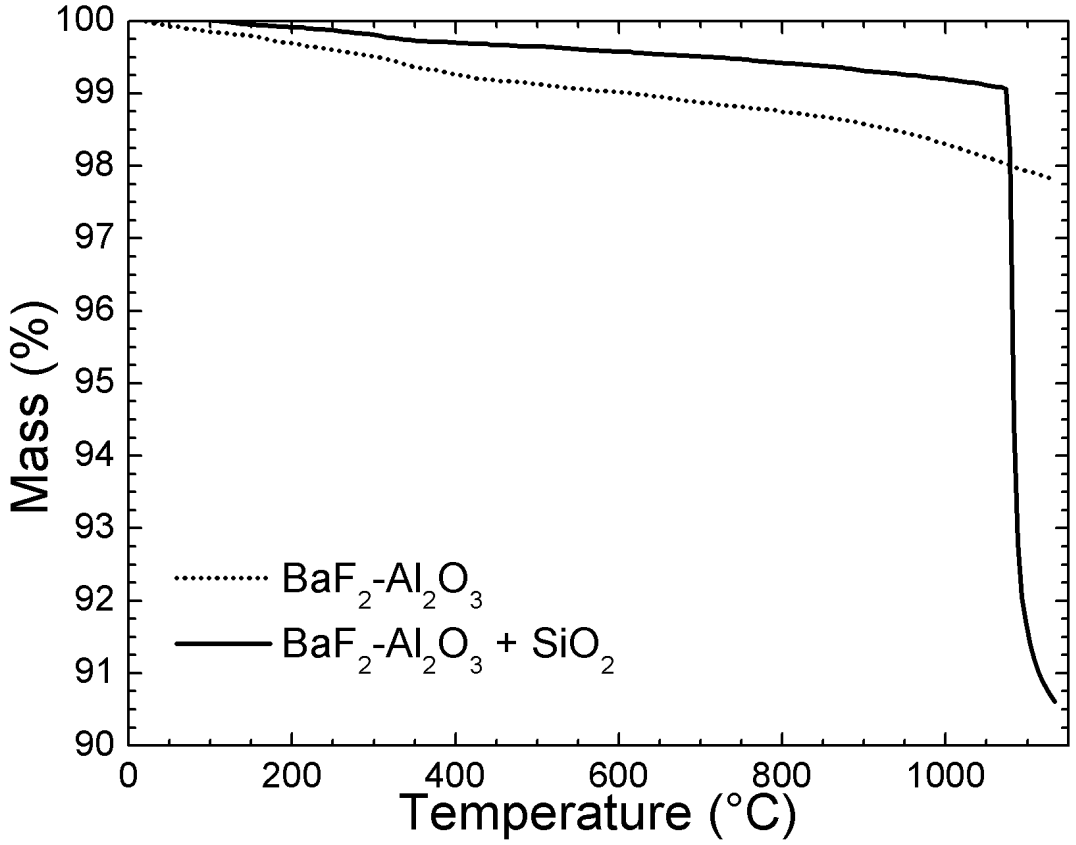

TGA experiment of two powder mixtures: $1BaF_2$-$1Al_2O_3$ and $0.5BaF_2$-$0.5Al_2O_3$-$1SiO_2$. The heating rate was 10 K/min. The behavior of BaF_2 containing powders is comparable to its SrF_2 analog, where there is an onset at about 1075 °C which gives rise to a sudden mass loss when SiO_2 is added to the system.

Appendix V. 9. XRD diffractograms of heat treated SrF_2-Al_2O_3-SiO_2 and SrF_2-SiO_2 pellets

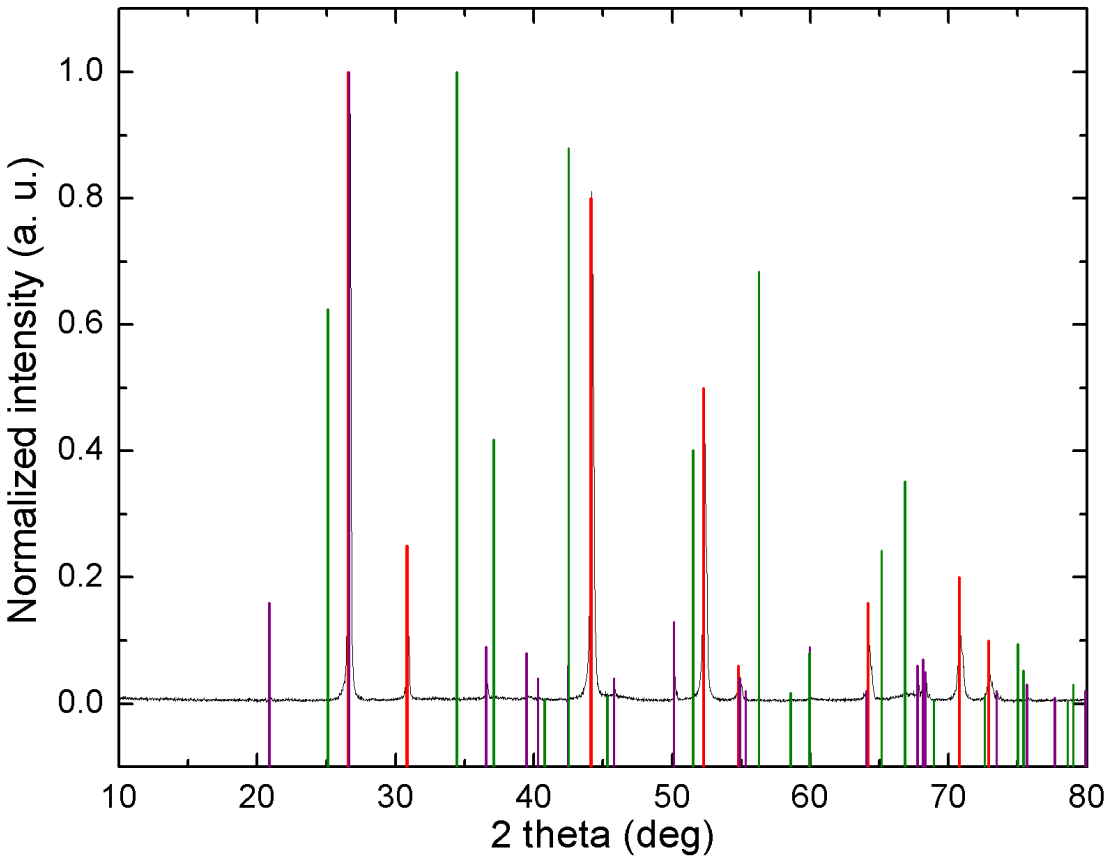

Peak attribution to XRD pattern for the "initial" pellet, that is the non-heat treated one. In red is SrF_2 (PDF card No. 00-006-0262), in purple is SiO_2 quartz, low (PDF Card No. 00-005-0490), and in green Al_2O_3 Corundum, syn (PCPDF 46-1212).

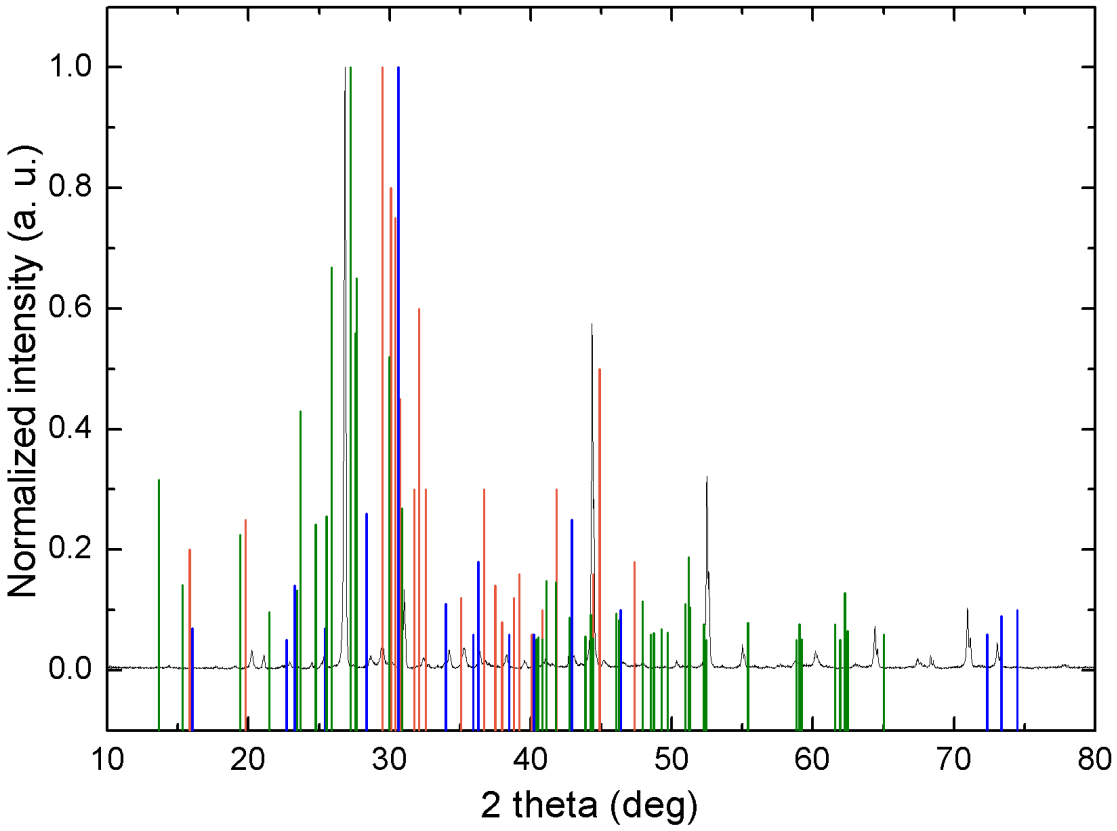

Peak attribution to XRD pattern for the heat-treated pellet for 1h at 1300 °C. In orange is $Sr_6Al_{18}Si_2O_{37}$ (PCPDF 10-0025), in blue is $Sr_2Al_2SiO_7$ (PDF Card No. 00-038-1333), and in green Al_2O_3 $SrAl_2Si_2O_8$ (PDF Card No. 01-070-7145). SrF_2, SiO_2 and Al_2O_3 are not represented on the graph. However, features of SrF_2 are still clearly present and some remaining SiO_2 and Al_2O_3 are also found.

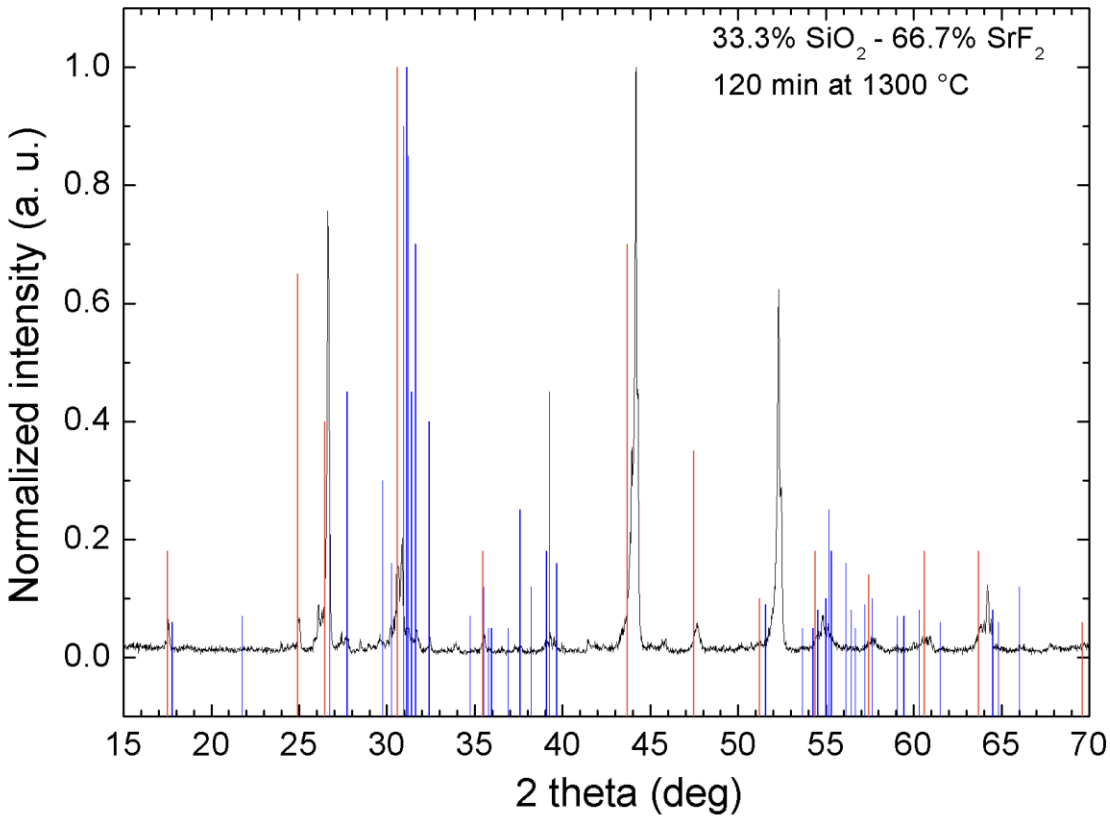

Peak attribution to XRD pattern for the heat-treated pellet for 2h at 1300 °C. In orange is $SrSiO_3$ (PDF card No. 00-006-0415) and in blue is β-Sr_2SiO_4 (PCPDF 38-0271).

V. J. References

[1] K. Schuster *et al.*, “Material and technology trends in fiber optics,” *Adv. Opt. Technol.*, vol. 3, no. 4, pp. 447–468, 2014.

[2] B. S. Morris and J. Ballato, “Molten-core fabrication of novel optical fibers,” *Am. Ceram. Soc. Bull.*, vol. 92, no. 4, pp. 24–29, 2013.

[3] P. Dragic, C. Kucera, J. Furtick, J. Guerrier, T. Hawkins, and J. Ballato, “Brillouin spectroscopy of a novel baria-doped silica glass optical fiber,” *Opt. Express*, vol. 21, no. 9, pp. 10924–10941, 2013.

[4] M. Cavillon *et al.*, “Brillouin Properties of a Novel Strontium Aluminosilicate Glass Optical Fiber,” vol. 34, no. 6, pp. 1435–1441, 2016.

[5] A. Mangognia *et al.*, “Spinel-derived single mode optical fiber,” *Opt. Mater. Express*, vol. 3, no. 4, p. 511, 2013.

[6] P. Dragic, T. Hawkins, P. Foy, S. Morris, and J. Ballato, “Sapphire-derived all-glass optical fibres,” *Nat. Photonics*, vol. 6, no. 9, pp. 629–635, 2012.

[7] M. N. Zervas and C. a. Codemard, “High Power Fiber Lasers: A Review,” *IEEE J. Sel. Top. Quantum Electron.*, vol. 20, no. 5, pp. 1–23, 2014.

[8] D. A. Coucheron *et al.*, “Laser recrystallization and inscription of compositional microstructures in crystalline SiGe-core fibres,” *Nat. Commun.*, vol. 7, p. 13265, 2016.

[9] M. Cavillon *et al.*, “Oxyfluoride core silica-based optical fiber with intrinsically low nonlinearities for high energy laser applications,” *J. Light. Technol.*, vol. 36,

no. 2, pp. 284–291, 2017.

[10] M. Persson, S. Seetharaman, and S. Seetharaman, “Kinetic Studies of Fluoride Evaporation from Slags,” *ISIJ Int.*, vol. 47, no. 12, pp. 1711–1717, 2007.

[11] N. N. Viswanathan, S. Fatemeh, D. Sichen, and S. Seetharaman, “Estimation of escape rate of volatile components from slags containing CaF_2 during viscosity measurement,” *steel Res.*, vol. 70, no. 2, pp. 53–58, 1999.

[12] I. Veksler, “Liquid Immiscibility and its role at the Magmatic Hydrothermal Transition: A Summary of Experimental Studies,” *Chemical Geology*, vol. 210, no. 1–4. pp. 7–31, 2004.

[13] V. McGahay and M. Tomozawa, “The origin of phase separation in silicate melts and glasses,” *J. Non. Cryst. Solids*, vol. 109, no. 1, pp. 27–34, 1989.

[14] J. Markis, K. Clemens, and M. Tomozawa, “Effect of Fluorine on the Phase Separation of Na_2O-SiO_2 Glasses,” *Communications of the American Ceramic Society*, vol. 64, no. 1. p. C-20, 1980.

[15] B. Hatta and M. Tomozawa, “Effect of Al_2O_3 on phase separation of SiO_2-Nd_2O_3 glasses,” *J. Non. Cryst. Solids*, vol. 354, no. 27, pp. 3184–3193, 2008.

[16] J. H. Park and D. J. Min, “Thermodynamics of fluoride vaporisation from slags containing CaF_2 at 1773 K,” *Steel Res. Int.*, vol. 75, no. 12, pp. 807–811, 2004.

[17] D. J. W. D. Kumar, R. G. Ward, “Effect of fluorides on silicates and phosphates,” *Discuss. Faraday Soc.*, vol. 32, pp. 147–154, 1961.

[18] N. P. Bansal and R. Doremus, *Handbook of Glass Properties*. Londond, England: Academic Press, 1986.

[19] F. Shahbazian, D. Sichen, K. C. Mills, and S. Seetharaman, “Experimental studies of viscosities of some CaO–CaF_2–SiO_2 slags,” *Ironmak. Steelmak.*, vol. 26, no. 3, pp. 193–199, 1999.

[20] J. A. Duffy and M. D. Ingram, “An interpretation of glass chemistry in terms of the optical basicity concept,” *J. Non. Cryst. Solids*, vol. 21, no. 3, pp. 373–410, 1976.

[21] R. Hill, D. Wood, and M. Thomas, “Trimethylsilylation analysis of the silicate structure of fluoro-alumino-silicate glasses and the structural role of fluorine,” *J. Mater. Sci.*, vol. 34, no. 8, pp. 1767–1774, 1999.

[22] J. A. Duffy, “Optical basicity of fluorides and mixed oxide-fluoride glasses and melts,” *Phys. Chem. Glas.*, vol. 52, no. 3, pp. 107–114, 2011.

[23] J. H. Park and D. J. Min, “Effect of fluorspar and alumina on the viscous flow of calcium silicate melts containing MgO,” *J. Non. Cryst. Solids*, vol. 337, no. 2, pp. 150–156, 2004.

[24] K. T. Semrau, “Emission of Fluorides From Industrial Processes—A Review,” *J. Air Pollut. Control Assoc.*, vol. 7, no. 2, pp. 92–108, 1957.

[25] F. Froehlich, C. Aichele, S. Grimm, and K. Schuster, “Fluorine incorporation into porous silica by gas phase doping with C_2F_6 in N_2,” *Opt. Mater. Express*, vol. 3, no. 11, p. 1839, 2013.

[26] A. Shukla, “Development of a Critically Evaluated Thermodynamic Database for the Systems Containing Alkaline-Earth Oxides,” Ecole Polytechnique de Montreal, Universite de Montreal, 2012.

[27] A. Mitchell, “Reactions of calcium silicates in solution in liquid calcium fluoride,”

Trans. Faraday Soc., vol. 63, pp. 1408–1417, 1967.

[28] I. Barin, *Thermochemical Data of Pure Substances*, Third Edit. VCH, 1995.

[29] M. Vermillac *et al.*, "Use of thulium-doped LaF_3 nanoparticles to lower the phonon energy of the thulium's environment in silica-based optical fibres," *Opt. Mater.*, vol. 68, pp. 24–28, 2017.

[30] P. R. Diamente, M. Raudsepp, and F. C. J. M. Van Veggel, "Dispersible Tm^{3+}-doped nanoparticles that exhibit strong 1.47 um photoluminescence," *Adv. Funct. Mater.*, vol. 17, no. 3, pp. 363–368, 2007.

[31] B. A. Shakhmatkin, N. M. Vedishcheva, and A. C. Wright, "Thermodynamic modelling of the structure of oxyhalide glasses," *J. Non. Cryst. Solids*, vol. 345–346, pp. 461–468, 2004.

[32] A. K. Swarnakar, A. Stamboulis, D. Holland, and O. Van Der Biest, "Improved prediction of young's modulus of fluorine-containing glasses using MAS-NMR structural data," *J. Am. Ceram. Soc.*, vol. 96, no. 4, pp. 1271–1277, 2013.

[33] R. G. Hill, A. Stamboulis, and R. V. Law, "Characterisation of fluorine containing glasses by ^{19}F, ^{27}Al, ^{29}Si and ^{31}P MAS-NMR spectroscopy," *J. Dent.*, vol. 34, no. 8, pp. 525–532, 2006.

[34] T. J. Kiczenski and J. F. Stebbins, "Fluorine sites in calcium and barium oxyfluorides: F-19 NMR on crystalline model compounds and glasses," *J. Non. Cryst. Solids*, vol. 306, no. 2, pp. 160–168, 2002.

[35] C. Dalou, C. Le Losq, B. O. Mysen, and G. D. Cody, "Solubility and solution mechanisms of chlorine and fluorine in aluminosilicate melts at high pressure and

high temperature," *Am. Mineral.*, vol. 100, no. 10, pp. 2272–2283, 2015.

[36] B. O. Mysen and D. Virgo, "Interaction between Fluorine and Silica in Quenched Melts on the Joins SiO_2 - AlF_3 and SiO_2 - NaF Determined by Raman Spectroscopy," *Phys. Chem. Miner.*, vol. 12, pp. 77–85, 1985.

[37] T. J. Kiczenski and J. F. Stebbins, "The effect of fictive temperature on the structural environment of fluorine in silicate and aluminosilicate glasses," *J. Am. Ceram. Soc.*, vol. 89, no. 1, pp. 57–64, 2006.

[38] P. F. McMillan, "Structural Studies of Silicate Glasses and Melts-Applications and Limitations of Raman Spectroscopy," *Am. Mineral.*, vol. 69, pp. 622–644, 1984.

[39] F. L. Galeener, "Raman and ESR studies of the thermal history of amorphous SiO_2," *J. Non. Cryst. Solids*, vol. 71, no. 1–3, pp. 373–386, 1985.

[40] A. K. Yadav and P. Singh, "A review of the structures of oxide glasses by Raman spectroscopy," *RSC Adv.*, vol. 5. p. 67583, 2015.

[41] J. D. Frantza and B. O. Mysen, "Raman spectra and structure of BaO-SiO_2, SrO-SiO_2 and CaO-SiO_2 melts to 1600°C," *Chem. Geol.*, vol. 121, no. 1994, pp. 155–176, 1995.

[42] P. F. Mcmillan, P. Mcmillan, B. Piriou, and A. Navrotsky, "A Raman spectroscopic study of glasses along the joins silica-calcium aluminate, silica-sodium aluminate, and silica-potassium aluminate," *Geochim. Cosmochim. Acta*, vol. 46, pp. 2021–2037, 1982.

[43] J. Ballato and P. Dragic, "Materials development for next generation optical fiber," *Materials (Basel).*, vol. 7, no. 6, pp. 4411–4430, 2014.

[44] P. D. Dragic and J. Ballato, “Characterisation of Raman gain spectra in Yb:YAG-derived optical fibres,” *Electron. Lett.*, vol. 49, no. 14, pp. 895–897, 2013.

[45] C. I. Merzbacher and W. B. White, “The structure of alkaline earth aluminosilicate glasses as determined by vibrational spectroscopy,” *J. Non. Cryst. Solids*, vol. 130, no. 1, pp. 18–34, 1991.

[46] D. R. Neuville, L. Cormier, and D. Massiot, “Al environment in tectosilicate and peraluminous glasses: A ^{27}Al MQ-MAS NMR, Raman, and XANES investigation,” *Geochim. Cosmochim. Acta*, vol. 68, no. 24, pp. 5071–5079, 2004.

[47] D. W. Matson, S. K. Sharma, and J. A. Philpotts, “The structure of high-silica alkali-silicate glasses. A Raman spectroscopic investigation,” *J. Non. Cryst. Solids*, vol. 58, no. 2–3, pp. 323–352, 1983.

[48] A. Quintas, “Etude de la structure et du comportement en cristallisation d’un verre nucléaire d’aluminoborosilicate de terre rare,” Chimie ParisTech, 2007.

[49] D. G. Mead and G. R. Wilkinson, “The temperature dependence of the Raman spectra of some alkaline earth crystals with the fluorite structure,” *J. Phys. C Solid State Phys.*, vol. 10, pp. 1063–1072, 1977.

[50] R. W. Luth, “Raman spectroscopic study of the solubility mechanisms of fluorine in glasses in the system calcium oxide-calcium fluoride-silica,” *Am. Mineral.*, vol. 73, no. 3–4. pp. 297–305, 1988.

[51] Y. Tsunawaki, N. Iwamoto, T. Hattori, and A. Mitsuishi, “Analysis of CaO-SiO_2 and CaO-SiO_2-CaF_2 glasses by Raman spectroscopy,” *J. non*, vol. 44, pp. 369–378, 1981.

[52] Y. N. P. Dumas, J. Corset, W. Carvalho, Y. Levy, “Fluorine doped vitreous silica analysis of fiber optic preforms by vibrational spectroscopy,” *J. Non. Cryst. Solids*, vol. 47, no. 2, pp. 239–242, 1982.

[53] M. Środa and Z. Olejniczak, “19F MAS-NMR studies of strontium oxyfluoride aluminosilicate glass,” *J. Mol. Struct.*, vol. 1001, no. 1–3, pp. 78–82, 2011.

[54] M. Środa and C. Paluszkiewicz, “The structural role of alkaline earth ions in oxyfluoride aluminosilicate glasses-Infrared spectroscopy study,” *Vib. Spectrosc.*, vol. 48, no. 2, pp. 246–250, 2008.

[55] J. E. Shelby and J. T. Kohli, “Rare-Earth Aluminosilicate Glasses,” *J. Am. Ceram. Soc.*, pp. 39–42, 1990.

[56] J. T. Kohli and J. E. Shelby, “Formation and properties of rare earth aluminosilicate glasses,” *Phys. Chem. Glas.*, vol. 32, no. 2, pp. 67–71, 1991.

[57] A. K. Varshneya, *Fundamentals of inorganic glasses*. Academic Press, 1993.

[58] D. S. Brauer, N. Karpukhina, R. V. Law, and R. G. Hill, “Structure of fluoride-containing bioactive glasses,” *J. Mater. Chem.*, vol. 19, p. 5629, 2009.

CHAPTER VI.

INVESTIGATION OF OPTICAL PROPERTIES IN OXYFLUORIDE GLASS OPTICAL FIBERS

VI. A. Introduction

The previous Chapter focused on understanding the kinetics and thermodynamics of fluoride-oxide systems, along with a structural and compositional analysis of the fabricated glass materials. The aim of this Chapter is to investigate the properties that drive optical nonlinearities in these oxyfluoride glass optical fiber systems, and comprehend the relationships between glass composition/structure and optical properties. This chapter provides insights into the role played by oxyfluoride materials in the reduction of optical nonlinearities.

Thus, this Chapter is organized as follow. Firstly, the methodology of fiber characterization is described in detail, and the reader is referred to this first section regarding the procedure used to measure or calculate each fiber property. The influence of fiber dopants on the aggregate property values of the fibers is determined with the help of additive models previously described in Chapters II and III.

Then, a series of fabricated strontium aluminosilicate and fluoro-aluminosilicate fibers are characterized and their principal waveguide parameters (e.g., refractive index profile, attenuation losses, modal index) are reported. Next, the principal properties that

drive optical nonlinearities, namely the linear and nonlinear refractive indices (n, n_2), the thermo-optic coefficient (dn/dT), the Brillouin gain and Raman gain coefficients (BGC, RGC), are successively investigated. The role of the core material dopants on these aforementioned properties is principally discussed as it is the main focus of this dissertation.

Additionally, because most of the fibers contain the active rare earth ion ytterbium (Yb), spectroscopic properties (e.g., lifetime, emission cross-section) are also studied with the goal to gain further insights on the performance of these oxyfluoride systems as fiber laser materials.

VI. B. Characterization of fiber properties

In this section, information regarding the techniques and methodologies to characterize fiber properties are detailed. If some levels of detail on the determination of acousto-optic properties have already be given in Chapter III, complementary information is provided below.

Linear refractive index

The refractive index profile (RIP) measurement for each fiber was performed by Interfiber Analysis, LLC (8 Manns Hill Crescent, Sharon, MA 02067, USA). The RIP is

measured at a wavelength of 950 nm transversely through the side of the fiber under test (FUT) using a spatially resolved Fourier transform interferometer [1]. It was previously shown that the refractive index dispersion over the wavelength range from 950 to 1550 nm is small [2], [3]. While these cited works specifically relate to dispersion in silica and lithium aluminosilicate fibers, there is no reason based on the glass chemistry, that the optical dispersion in alkaline earth aluminosilicate systems treated herein should be markedly different from alkali (Li_2O) aluminosilicate glasses [2]. Hence due to the enhanced spatial resolution of the measurement system at lower wavelengths, the measured RIPs at 950 nm are assumed to be identical to those in the 15XX nm region for the subsequent analysis.

Elemental composition analysis

Cross-section compositional profiling of the drawn fibers are performed by Energy Dispersive X-Ray (EDX) spectroscopy on a HITACHI-6600 Scanning Electron Microscope (SEM), with an acceleration voltage of 20 kV (at Advanced Materials Research Laboratory, , Anderson, SC). SEM micrographs were performed to characterize the shape and size of the core as well as to verify the absence of phase separation.

Raman spectroscopy

Spontaneous Raman spectra of the fiber core materials were obtained using a commercial Raman microscope (alpha300, WItech, with the help of Dr. Xiao's group at Advanced Materials Research Laboratory, Anderson, SC) in a backscattering geometry, utilizing a 532 nm pump source with a focused beam diameter of about 1 μm and a photon collection time of 120 s per datum. The Raman spectra are corrected similarly to that in [4], taking into consideration reflection loss and variation in the internal solid angle, along with dividing the Raman bandwidth by the Bose-Einstein correction factor. Raman gain coefficients, RGC, are measured relative to the one for SiO_2 (taken to be equal to 1) and correspond to the maximum intensity of the highest peak of the scattering bandwidth (situated around 440 cm^{-1}). Additionally, since the Raman gain coefficient, RGC, is determined relative to fused silica for each fiber, a data point in the fiber cladding is taken and serves as a reference value for pure fused silica.

Nonlinear refractive index

The nonlinear refractive index, n_2, is estimated via a simple self-phase modulation (SPM) measurement. In these experiments, high peak power pulses are propagated through the fiber to experience spectral broadening. The source used for this measurement was a passively mode-locked fiber laser emitting linearly polarized, 750 fs soliton pulses, centered at 1540 nm. The optical pulses were coupled into 4.8 m of the characterized fiber and the output spectra for different input powers were recorded using an optical spectrum analyzer (OSA). Experimentally, the coupling efficiency was optimized by monitoring the

output power and spectrum while adjusting the input polarization, to ensure propagation in the fundamental mode of the fiber. In order to obtain a value for n_2, the measured spectra were compared with numerical modelling using the standard nonlinear Schrödinger equation [5]. The measurements and modeling were realized by Dr. Antoine Runge and Dr. Anna Peacock (Optoelectronics Research Centre, University of Southampton, Highfield Campus, Hampshire, UK).

Attenuation losses

Fiber attenuation is measured using the standard cut-back technique, at a wavelength of 1534 nm. Typical cutback length is ~2-5 m. The measurements were performed by Dr. Peter Dragic (Department of Electrical and Computer Engineering, Micro and Nanotechnology Lab, University of Illinois, Urbana-Champaign, IL). Additionally, the following Brillouin spectroscopic, thermo-optic, and ytterbium spectroscopic measurement were also performed at University of Illinois.

Brillouin spectroscopy

A heterodyne approach, as shown in Fig. VI.1, was utilized to measuring the Brillouin gain spectrum (BGS) of the fiber.

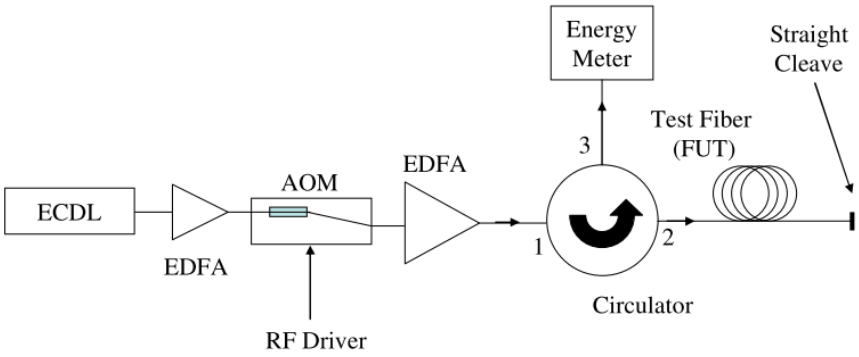

Figure VI.1. Experimental setup used for Brillouin spectroscopic measurements.

A pre-amplified narrow linewidth signal (~100 kHz linewidth at 1534 nm) is injected into the fiber under test (FUT) via an optical circulator. Light is scattered backward in at least three forms: Rayleigh scattered light, Fresnel reflected light from the splice point between the apparatus and FUT, and Brillouin backscattered light. The output end of the FUT was cleaved at an angle to prevent back reflections from the end-facet guiding backward through the FUT. The back-reflected signals then passed back through the optical circulator, were filtered and amplified in an erbium doped fiber amplifier (EDFA), and sent into a fast PiN detector. The resultant electrical signal produced by the PiN was analyzed utilizing an electrical spectrum analyzer (ESA). Signal levels from Rayleigh scattered light and Fresnel reflected light above, although small in magnitude, were sufficient to provide an adequate local oscillator (LO) signal and achieve a BGS measurement with good signal-to-noise ratio (SNR). It is important to note that the measurement system was constructed of SMF-28-like fibers and thus an apparatus signature (along with higher-order acoustic modes, HOAMs) appeared near 11 GHz in the measurements. To estimate BGC, the

relative Brillouin scattering strength (amplitude of the Brillouin back-scattered signal) from a known length of control fiber (whose BGC is known) is compared with that from the FUT, also of known length [6]. The mode field diameters (MFDs) are important for this measurement, and are therefore calculated from the RIPs. For further details regarding the apparatus, the reader is referred to [7], [8].

All losses associated with the measurement (splices, etc.) were also carefully characterized. A P_2O_5 doped silica control fiber was utilized for this measurement since i) it is very well mode-matched to the fundamental mode in the FUT and ii) its Brillouin frequency shift (BFS) lies far from that of both the FUT and apparatus fibers. The latter removes any uncertainty introduced via overlapping spectra. More details can be found in [6].

Thermo-optic coefficient (dn/dT)

The thermo-optic coefficient of the fibers are measured similarly as in [8], [9]. The apparatus utilized for the determination of dn/dT consists of a fiber ring laser, as illustrated in Fig. VI.2.

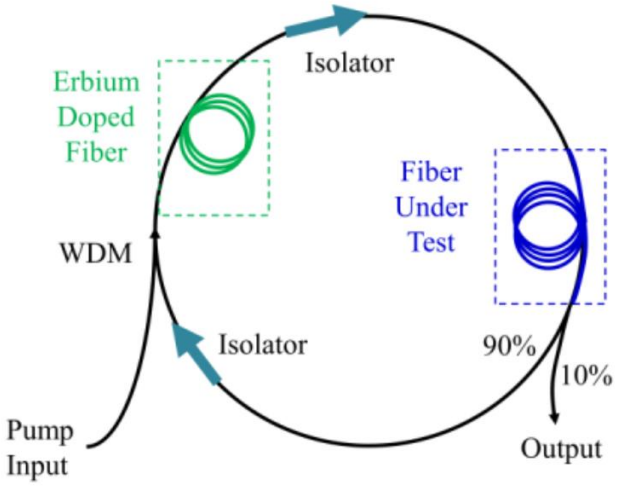

Figure VI.2. Ring laser apparatus used to measure the thermo-optic coefficient (dn/dT) of the various fibers investigated. Figure taken from [9].

First, the pump is injected into the cavity via a wavelength division multiplexer (WDM) and into a segment of erbium doped fiber (EDF), and two isolators ensure unidirectional laser operation. No care was taken to optimize the spectral characteristics of the laser. As will be discussed, the presence of a large number of cavity modes enhances the measurement sensitivity. The output signal is sent directly into a detector whose signal is interrogated using an electrical spectrum analyzer (ESA). The laser operates at a nominal wavelength of 1554 nm. The fiber under test (FUT, typically 4 – 6 m in length) forms part of the laser cavity and this fiber is coiled and held in a heated water bath in order to accurately control its temperature. The free spectral range (FSR) of the ring laser can be written generally as

$$FSR = c/(\sum_{i=1}^{M} d_i n_i), \tag{6.1}$$

where the subscript i simply refers to one of the M various different fibers, with length d and mode index n, associated with the different components (e.g. isolator, couplers, erbium doped fiber, etc.) encountered within the cavity. The FUT's temperature can be controlled and thus for it d → d(T) via the linear coefficient of thermal expansion (α), and n → n(T) via dn/dT. Because of the cavity modes beating on the detector, the FSR of the ring laser can be read directly from the ESA. Differentiating the FSR versus T gives the following expression

$$\frac{dFSR}{dT} = -\frac{c}{(nl+NL)^2}\left(n\alpha l_0 + l\frac{dn}{dT}\right), \qquad (6.2)$$

where NL is the refractive index-length product summed for all fiber segments whose temperatures are invariant (fiber comprising the WDM, coupler, EDF, etc.), n and l are the mode index and length of the FUT, respectively, α is the coefficient of thermal expansion of the core, l_0 is the room temperature length of the FUT, and l is the FUT length at the temperature T. Since the core is held rigidly in a much more voluminous pure silica cladding, the linear α_{core}, is taken to be that of silica (0.55×10^{-6} K^{-1}). Eqn. 6.2 represents the slope of the FSR as a function of temperature, FSR(T), and is therefore utilized to determine dn/dT.

The sensitivity of the measurements can be enhanced by performing measurements on cavity beating mode pairs that are separated by a large number of FSR, since the variation of FSR as a function of temperature (ΔFSR) will be greater, which consequently reduces uncertainties. The FSR=f(T) plot is then fit with Eqn. 6.2, where dn/dT is the fit

parameter. Measurements are repeated several times using different FUT lengths, coil diameters, and cavity mode pairs to reduce uncertainties. The error in the dn/dT measurement for the fiber is taken conservatively to be the magnitude of the largest departure from the mean value.

For disambiguation, in this section the mode index is referred as "n", and therefore dn/dT is the change of the mode index as a function of temperature. Later in this Chapter, the mode index will be referred as n_0 to differentiate from n (as in Δn), which corresponds to the measured refractive index.

Ytterbium spectroscopy

In order to measure fluorescence emission spectra, the FUT is spliced to a fiber laser and pumped at 976 nm. A fiber, used to collect the light, is brought very close to the side of the FUT with the help of a positioning mount. The fiber is connected to an ESA and the spectrum is registered. For fluorescence lifetime measurements, the same apparatus is used but the pump power is pulsed. The spectrum analyzer is set to monochromator mode where the output is filtered to pass Yb luminescence. Then the light goes to a sensitive receiver where the decay data is collected. To measure the absorption spectrum, a short segment of the FUT (typically ~1 mm) is spliced between two passive fibers, and a broadband light source (white light) passes through it. The spectrum is measured before and after it passes through the FUT, and is divided to give absorption. Because cladding

modes can be coupled into that short fiber segment, some ripples are typically visible in the absorption spectrum. The emission cross section is calculated using the Fuchtbauer-Ladenburg (F-L) formula [10], [11]

$$\sigma(\lambda) = \frac{1}{8\pi}\frac{\lambda^5}{\tau n^2 c}\frac{I(\lambda)}{\int I(\lambda)\lambda d\lambda}, \qquad (6.3)$$

where λ is the wavelength, τ is the fluorescence lifetime, n is the refractive index at the emission wavelength (λ), c is the velocity of light in the vacuum, I(λ) is the emission spectra intensity for a given wavelength, and the integral term corresponds to the total intensity of the emission bandwidth.

Material modeling Procedure

The governing equations that enable the modeling of material properties throughout this chapter have already been fully described in Chapters II and III, and, therefore, will not be further described. As already mentioned in Chapter III, it is important to note that measured values represent those arising from the optical mode and its interactions in the fiber. In cases where the refractive index difference between core and cladding (Δn) and core diameter conspire to produce an optical mode tightly confined at the core center, the measured properties are approximately those of the material in the center of the core. On the other hand, in cases where the mode field diameter (MFD) is comparable to the core radius, and the compositional profile is not uniform (fibers produced using the molten core method usually have graded profiles[12]), this approximation breaks down, and mode distribution must be taken into consideration. To do this, the core compositional profile is

typically approximated by a 4-layer step-like distribution, with each layer possessing unique composition and physical properties [13] that depend on physical environment such as temperature and strain. The optical mode characteristics are calculated from this approximate profile (as a function of temperature or strain), and the bulk constituents are ultimately utilized as fit parameters and determined. The same arguments also apply to the acoustic mode.

VI. C. Fabricated and characterized glass optical fibers

Table VI.1. Drawing temperatures and initial precursor compositions (molar ratio) of the fabricated fibers.

Fiber	Yb-SrAlSi	YbF-SrAlSi	Yb-SrAlSiF[a]	YbF-SrAlSiF[a]	SrAlSiF[b]	SrAlSi[b]
T_{draw} (°C)	2100	2000	2000	2000	2000	1925
Initial precursor[c] compositions (molar ratio)						
SrO	71.25	71.25	-	-	-	38.46
SrF_2	-	-	71.25	71.25	75	-
Yb_2O_3	5	-	5	-	-	-
YbF_3	-	5	-	5	-	-
Al_2O_3	23.75	23.75	23.75	23.75	25	61.54

[a]: For these fibers, 2 segments are characterized at different positions of the draw as they exhibit different elemental compositions and will be later distinguished as "A" and "B" (see Table VI.2).

[b]: These fibers were previously fabricated and characterized in [14] and [15], and are reported here for completeness.

[c]: Material precursor purities: SrO (99.9%), SrF_2 (99.99%), YbF_3 (99,99%), Al_2O_3 (99.997%), Yb_2O_3 (99.999%), SiO_2 glass cladding (Heraeus, Quality CFQ 099).

In Chapter V, a multitude of optical fibers were fabricated in order to study the oxyfluoride systems, and the role of fiber processing on them. As SrF_2-derived fibers were particularly emphasized, strontium-containing aluminosilicate and fluoro-aluminosilicate systems are chosen as preferential candidates to study their optical properties. It is worth recalling that for each drawn fiber, a powder packed precursor was inserted in a 3x30 mm fused silica capillary preform, and each draw was performed with a targeted draw speed of 28-30 m/min, and a cladding diameter of 125 µm. For more information regarding the sample preparation methodology and the molten core method, the reader is asked to refer to Chapter V, section V. B. The drawing temperatures and initial precursor compositions of the fibers investigated in this Chapter are reported in Table VI.1.

Most of the fabricated fibers studied herein are doped with Yb, introduced through YbF_3 or Yb_2O_3 material precursors, to enable ytterbium spectroscopic measurements. The different precursor compositions are chosen to allow the fabrication of optical fibers with a wide variety of core compositions (e.g., with varying fluorine concentration), this in order to better understand the role played by each individual dopant on the properties. Complementarily to the presented fibers in Table VI.1, other glass optical fiber segments were characterized in the following initial precursor compositions (in molar ratio): 5MgO-8Al_2O_3, 5CaO-8Al_2O_3, 5BaO-8Al_2O_3, 3CaF_2-1Al_2O_3, and BaF_2. If this chapter principally focuses on strontium fluoro-alumino-silicate glass core optical fibers, the properties of these aforementioned fibers are reported in Appendix VI.1.

The elemental compositions, in atomic percent (At. %) and at the core center, of the characterized fiber segments, along with some typical fiber parameters, are summarized in Table VI.2. The composition and refractive index profiles of the fiber cores are reported in Appendix VI.2, along with an SEM micrograph of this core. From Table VI.2, one should note the variety of fiber compositions, dimensions, and properties. Yb-SrAlSi fiber is found to have a higher Si content and a lower Sr and Al content compared to the other fibers, principally attributed to the higher temperature at which it has been drawn (2100 °C instead of 2000 °C or 1925 °C). SrAlSi fiber exhibits the highest Al content due to its higher Al_2O_3 initial content and its lower drawing temperature (1925 °C), which promotes higher dopant concentration.

The different fluorine concentration in the fiber cores arise from the nature of the precursor material composition (some of the them containing more fluorine, see Table VI.1), but it is also a strong function of the drawing conditions, as observed and described in Chapter V. Consequently, some segments, although from the same fiber, will present different doping concentration since they were collected at different positions of the draw (e.g., Yb-SrAlSiF A and B). Furthermore, the core diameter is a function of draw time and core composition. The reader is asked to refer to Chapter V for more details regarding the compositional evolution of dopants as a function of precursor nature and fiber draw conditions.

Table VI.2. Elemental composition at the core center of the fibers investigated, in addition to core and cladding diameters (ϕ_{core} and $\phi_{cladding}$), and some typical fiber parameters: mode index (n_0); mode area (A_{eff}); refractive index difference between core center and cladding (Δn); and attenuation coefficient (α).

Fiber	Elemental core composition (in At. %, at the core center)						Φ_{core} (μm)[a]	$\Phi_{cladding}$ (μm)[b]	n_0[c]	A_{eff}[c] (10^{-12} m^2)	Δn (10^{-3})[d]	α[e]
	F	O	Sr	Al	Yb	Si						
Yb-SrAlSi	0	65.73	1.78	1.76	0.32	30.42	5.8	125	1.46164	12.46	36.3	0.78
YbF-SrAlSi	0.33	64.48	3.76	3.90	0.40	27.14	10.6	125	1.49954	25.24	64.0	2.08
Yb-SrAlSiF A	2.35	63.45	3.35	2.70	0.50	27.65	9.2	125	1.48132	19.82	48.8	2.85
Yb-SrAlSiF B	4.64	61.6	4.08	3.09	0.62	25.97	13.0	125	1.48716	36.03	49.6	2.66
YbF-SrAlSiF A	4.42	61.91	3.81	2.98	0.28	26.60	11.2	125	1.47853	31.18	41.5	0.52
YbF-SrAlSiF B	5.26	61.32	3.92	2.93	0.28	26.29	22.0	185	1.47667	119.5	34.0	0.46
SrAlSiF[f]	2.72	63.51	2.98	2.11	0	28.68	8.0	125	1.4673	18.62	35.6	0.65
SrAlSi[f]	0	62.03	2.93	10.23	0	21.87	12.0	125	1.5109	-	74.8	2.68

[a]: Determined from RIP.

[b]: Determined from SEM micrographs.

[c]: Calculated at 1534 nm, for the fundamental mode, LP_0. A_{eff} is calculated using the standard model. The notation n_0, which corresponds to the refractive index of the fundamental mode (i.e., mode index) needs to be differentiated from n as in Δn, which is the measured refractive index of the core material (see [d]) as a function of core radial position.

[d]: Refractive index difference between fiber core center and silica cladding, where $n(SiO_2) = 1.444$. For Δn as a function of radial core position of the fibers in Table VI.2, see Appendix VI.2.

[e]: Attenuation coefficient, in dB/m, at 1534 nm.

[f]: These fibers were previously fabricated and characterized in [14] and [15], and are reported here for completeness.

Also shown in the previous chapter was that F preferentially bound to Sr as is SrF_2. If it cannot be excluded that each system may have F bound to different cations, e.g., with Si, Al, or Yb, the modeling of the fiber properties, assuming a oxyfluoride core system in

the SrF_2-SrO-Yb_2O_3-Al_2O_3-SiO_2 composition, will be considered. It should be noticed that Yb is assumed to be found as Yb_2O_3 only, although in some cases the initial precursor material was YbF_3. If this assumption is made for sake of simplicity when it comes to modeling, the initial amount of Yb is much smaller than Sr, therefore the remaining amount of YbF_3 compound in the glass, if any, is expected to be small. Additionally, in LaF_3-SrO containing oxyfluoride melts, the formation of Sr-F bonds was detected [16], [17]. Because bonding nature of Yb should not be markedly different from La, considering "SrF_2" as the only fluoride glass compound is a reasonable assumption. In Table VI.3 are summarized the fiber compositions, at the core center, considering this assumption. It is worth noting that for the fiber segments considered herein, some exhibit compositions where SrO > SrF_2, whereas others show the opposite trend (SrF_2 > SrO). As will be seen later, a varying SrO to SrF_2 ratio helps to better understand the effect of F on the aggregate glass optical properties.

The refractive index difference between core and cladding (Δn), reported in Table VI.2, are discussed in greater details in the following section, VI. D., when it comes to study the role of the dopants on the linear refractive index in these oxyfluoride systems. The mode areas (A_{eff}, using standard Petermann II method), also reported in Table VI.2, are found ~2-3.5 smaller than the core area, $\pi\times(\phi_{core}/2)^2$. Therefore, the optical power transported by the fundamental mode LP_0 is principally confined at the core center for the fibers considered. Moreover, if the reduction of attenuation losses has not been the principal focus of this dissertation, it is recognized that it is necessary to develop fibers

with lower background losses (<dB/m) for better practicality. Subsequently, some first analysis on the origins of the phenomena that mainly contribute to the fiber attenuation coefficients of the presently characterized fibers is presented in the following chapter (Chapter VII), and paths to significantly mitigate them are identified.

Table VI.3. Fiber core composition, in mole %, at the core center, assuming all the fluorine to be bound with Sr as in SrF_2.

Fiber	SrF_2	SrO	Al_2O_3	Yb_2O_3	SiO_2
Yb-SrAlSi	0.00	5.35	2.65	0.48	91.52
YbF-SrAlSi	0.50	10.88	5.90	0.61	82.12
Yb-SrAlSiF A	3.60	6.67	4.14	0.77	84.82
Yb-SrAlSiF B	7.27	5.52	4.84	0.97	81.40
YbF-SrAlSiF A	6.90	4.99	4.65	0.44	83.02
YbF-SrAlSiF B	8.27	4.05	4.60	0.44	82.63
SrAlSiF	4.16	4.95	3.22	0.00	87.67

VI. D. The linear refractive index

In this section, the goal is to understand the materials contribution to the linear refractive index (n) of the developed glass optical fibers. The refractive index profile (RIP) of each Yb-doped fiber considered herein (and SrAlSiF fiber segment) is reported in Appendix VI.2. The refractive index difference, Δn, between the core center and the glass cladding (fused silica, taken as 1.444 at 15XX nm) is reported in Table VI.2. SrO, Al_2O_3, and Yb_2O_3 increase the refractive index relative to SiO_2 [15], [18], when F decreases it

[19], [20]. Therefore, in the context of this work, where a reduced Δn is of interest, the contribution of fluorine to the fiber core refractive index is of particular interest. In order to determine its effect, n is calculated for each fiber at the core center using data from EDX, but considering there is no F in the glass composition. The refractive index of such "all-oxide" mixture, that is, considering the core solely composed of oxide compounds (SrO, Yb_2O_3, Al_2O_3, and SiO_2), can be calculated using the additive model previously described in Chapter II. Because the fluorine is known to reduce the refractive index, this calculated index, again excluding F from the composition, if found to be higher than the one measured from RIP. Hence, the difference between the calculated index and the measured index is attributed to be due to fluorine. This index difference (Δn_{diff}), as a function of fluorine concentration, is reported in Fig. VI.3.It is worth mentioning that, for Yb-SrAlSi fiber, the difference between calculated and measured indices shall be null, since this fiber does not contain any fluorine. However, the calculated index was found lower than the measured one by ~8.0×10^{-3}. This small difference can be explained as follow. During EDX microprobe analysis, the interaction volume of the electron beam with the glass core material is larger than each targeted area (a data point). Accordingly, the microprobe picks up x-rays from the surrounding materials, essentially silica richer regions for silicate graded index fibers, and therefore higher silica concentrations are typically found for each data point. Because of this "additional" SiO_2 content detected, the calculated refractive index based on EDX composition is found lower compared to the measured one. Consequently, 8.0×10^{-3} was added to each calculated index as a correction factor. This correction factor is applied to all the fiber segments. Subsequently, the compositions from Table VI.3 are

re-calculated appropriately and reported in Table VI.4. These corrected values are used throughout this chapter, as they are more representative of the fiber core compositions.

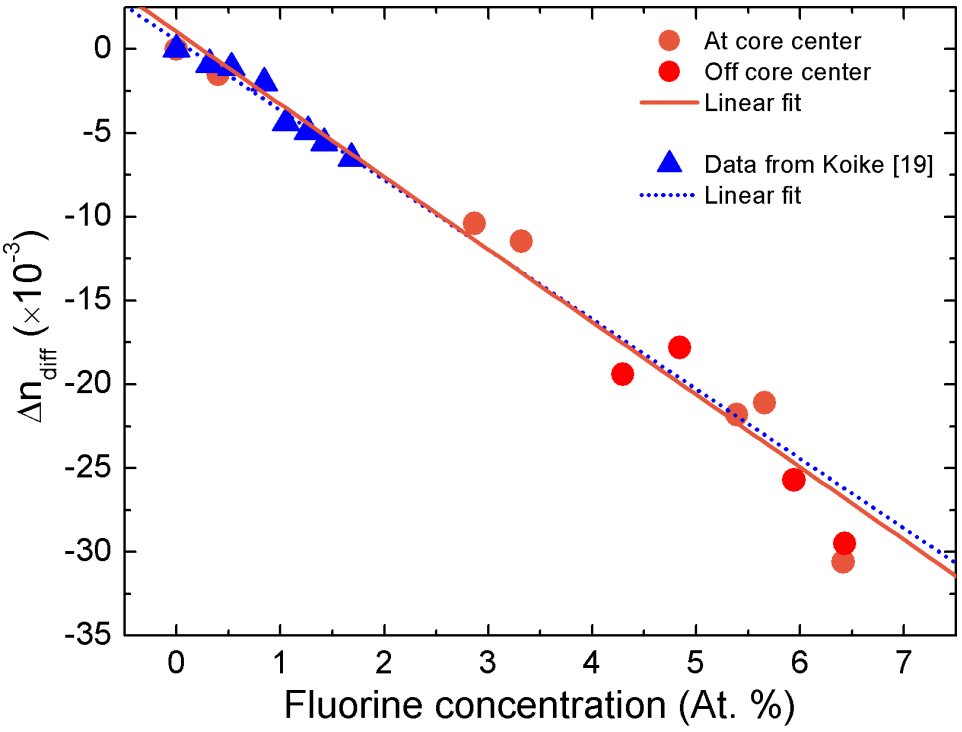

Figure VI.3. Linear refractive index difference, Δn_{diff}, between the measured index (from RIP) and the calculated index assuming no fluorine, that is, for an "all-oxide system", as a function of fluorine concentration (in At. %). The index mismatch is attributed to the effect of fluorine. In orange: Data point at the core center for each Yb-doped fiber and SrAlSiF fiber from Table VI.2. In red: Extra data point taken at different core positions for Yb-SrAlSiF B (3.95 µm and 5.92 µm off core center) YbF-SrAlSiF A (4.12 µm off core center) and B (3.95 µm and 7.90 µm off core center) fiber segments, in order to increase the number of data points. In blue: Data taken from Koike [19] in F-doped silica glasses for comparison.

In Fig. VI.3, it is shown that the reduction of the refractive index is nearly a linear function of the F content, at least in the range of composition investigated. By fitting the data linearly, the effect of fluorine in the presently studied fibers results in a reduction of the refractive index by ~-4.3×10^{-3} per At. % of F. The data from [19] for F-doped silica glasses reported in Fig. VI.3 give rise to a somewhat equivalent $\Delta n_{diff}=f([F])$ trend, where a linear fit gives a reduction of n of ~-4.2×10^{-3} per At. % of F, which is only ~3.7 % less than what is found here. Interestingly, as F is conjectured to be bound preferentially with Sr in the considered oxyfluoride fibers, it exhibits a similar decrease of the refractive index compared to F-doped silica glasses, where Si-F bonds should be predominant. It is noteworthy that YbF-SrAlSiF B segment, which contains the highest F concentration of the oxyfluoride fibers characterized, shows a Δn reduction of -30.6×10^{-3} relative to its "all-oxide" (i.e., assuming no fluorine) counterpart. In other words, the oxyfluoride fiber present a ~×2 lower Δn than its oxide analog.

From the assumption that F is exclusively bound to Sr as in SrF_2, the refractive index of amorphous SrF_2 (a-SrF_2) can be determined. It is assumed here that the addition of SrF_2 follows the same additivity principles that enunciated in Chapter II. To appropriately model the refractive index of SrF_2, its molar mass (g/mol) and its density must be known. The molar mass was taken as 125.62 g/mole and the density as 3980 kg/m^3, as in [21] for thin films, which exhibit lower density than their crystal analog (4240 kg/m^3 [22]). This is consistent with findings in [6], [15] where a-BaO, a-SrO and fused silica all

exhibit lower density than their crystalline phases. If this value of density is taken somewhat arbitrarily, it is shown in the following paragraph that taking different values for density (crystalline value, 4240 kg/m^3, and low density thin films, 2580 kg/m^3 as in [21]) has very little impact on the final calculated value of the refractive index.

Table VI.4. Calculated fiber core compositions (At the core center) when the correction factor (to match calculated vs. measured index is applied).

Fiber	SrF_2	SrO	Yb_2O_3	Al_2O_3	SiO_2
Yb-SrAlSi	0.00	6.41	3.17	0.58	89.84
YbF-SrAlSi	0.59	12.77	6.93	0.71	79.01
Yb-SrAlSiF A	4.26	7.88	4.89	0.91	82.07
Yb-SrAlSiF B	8.52	6.47	5.68	1.14	78.20
YbF-SrAlSiF A	8.11	5.87	5.47	0.51	80.03
YbF-SrAlSiF B	9.71	4.76	5.41	0.52	79.59
SrAlSiF	4.94	5.88	3.83	0.00	85.35

The modeling is performed on 10 different compositions and assuming a Yb_2O_3-SrF_2-SrO-Al_2O_3-SiO_2 compound mixture. The refractive index values for n(a-SrF_2) are then averaged. The reader is asked to refer to Appendix VI.3 for an example of the code used for one composition to calculate n(a- SrF_2) using the additive model expressed in Chapter II. The averaged refractive index for a-SrF_2 is calculated to be 1.4820 ± 15 % at 1534 nm. The refractive index of SrF_2 in thin films at 15XX nm from [21] is 1.479, which is very close to the calculated value using the additive model. Using a density of 4240 kg/m^3 or 2580 kg/m^3 gives an averaged n value of 1.4807 and 1.4812, respectively.

Consequently, a value of 1.48 for a-SrF_2 will be used. The estimated value of n for a-SrF_2 reinforces the validity of considering SrF_2 as a glass compound. In [23], the refractive index of crystalline SrF_2 (c-SrF_2), at 15XX nm, is found to be 1.4308, which is somewhat smaller (~4.5 %) than what is found here, and within the margin of errors of n(a-SrF_2). However, one possible explanation of a higher refractive index for a-SrF_2 relative to c-SrF_2 could be due to its more dissociated state. Interestingly, the signature of Sr-F bonding observed by Raman spectroscopy (Chapter V) suggests that the Sr-F distance is slightly higher than for c-SrF_2, as the characteristic Raman peak is slightly shifted to lower frequencies. Consequently, this would result in an increase in electronic polarizability, which can be traduced by an increase of n.

The evolution of n in a binary SrF_2-SiO_2 system can thus be computed using Eqn. 2.3 from Chapter II and is reported in Fig. VI.4, along with other systems of interest: SrO-SiO_2, GeO_2-SiO_2, B_2O_3-SiO_2, Al_2O_3-SiO_2, and P_2O_5-SiO_2. Glass stability issues that can arise from such binary compositions are purposely left out here. From this figure, the beneficial effect of starting with a fluoride precursor (SrF_2) relative to its oxide counter-part (SrO) is explicitly shown. If SrO is found to drastically increase the refractive index (n=1.81) relative to silica, SrF_2 only slightly participates to an increase of n (as n=1.48 << 1.81). Therefore, SrF_2 is a promising candidate as it enables an introduction of large concentration of this material without increasing the refractive index too significantly. This is of specific interest when single mode or few moded fibers are mandatory. However,

starting with SrF_2 also results in the formation of SrO as it reacts with SiO_2, and a SrO-SrF_2 mixture should be expected.

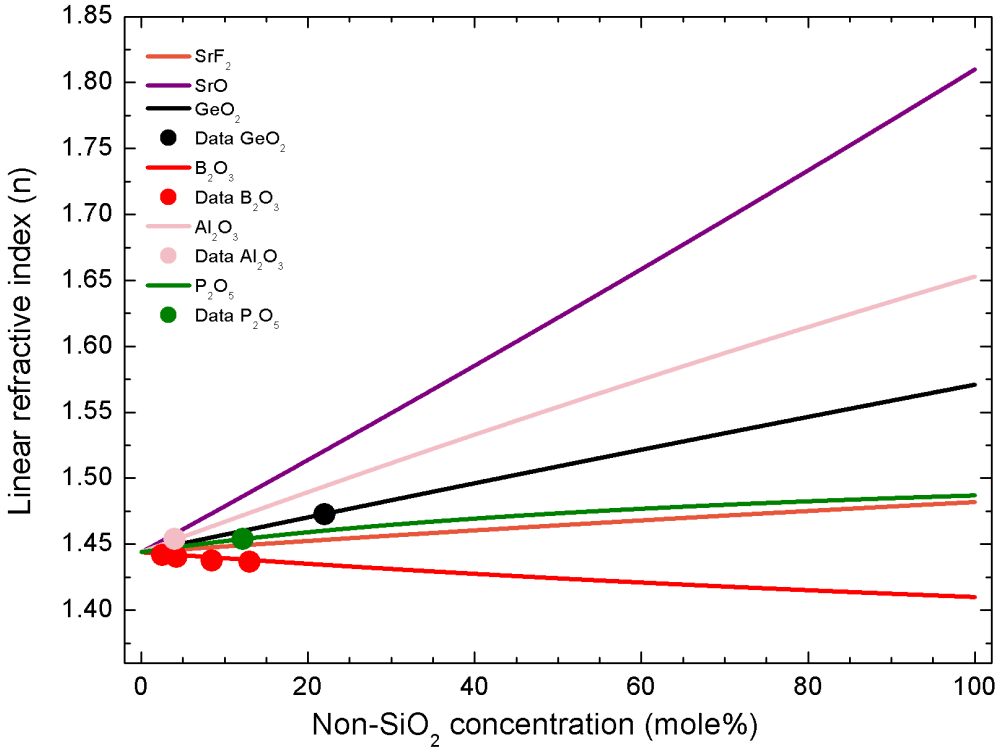

Figure VI.4. Computed linear refractive index for binary silicate systems as a function of non-SiO_2 concentration (in mole %). Note the beneficial effect of adding SrF_2 relative to its oxide analog, SrO, in order to prevent further increase of n relative to SiO_2. The overlaid data point are measured refractive index for the canonical dopants GeO_2, B_2O_3, Al_2O_3, and P_2O_5, taken from [9], [24], at $\lambda \sim 1$ µm.

VI. E. The nonlinear refractive index (n_2)

Measurements to determine the nonlinear refractive index, n_2, for SrAlSiF fiber segment were performed and the output spectra resulting from high power pulse propagation within the fiber are shown in Fig. VI.5, obtained for four different input powers (orange).

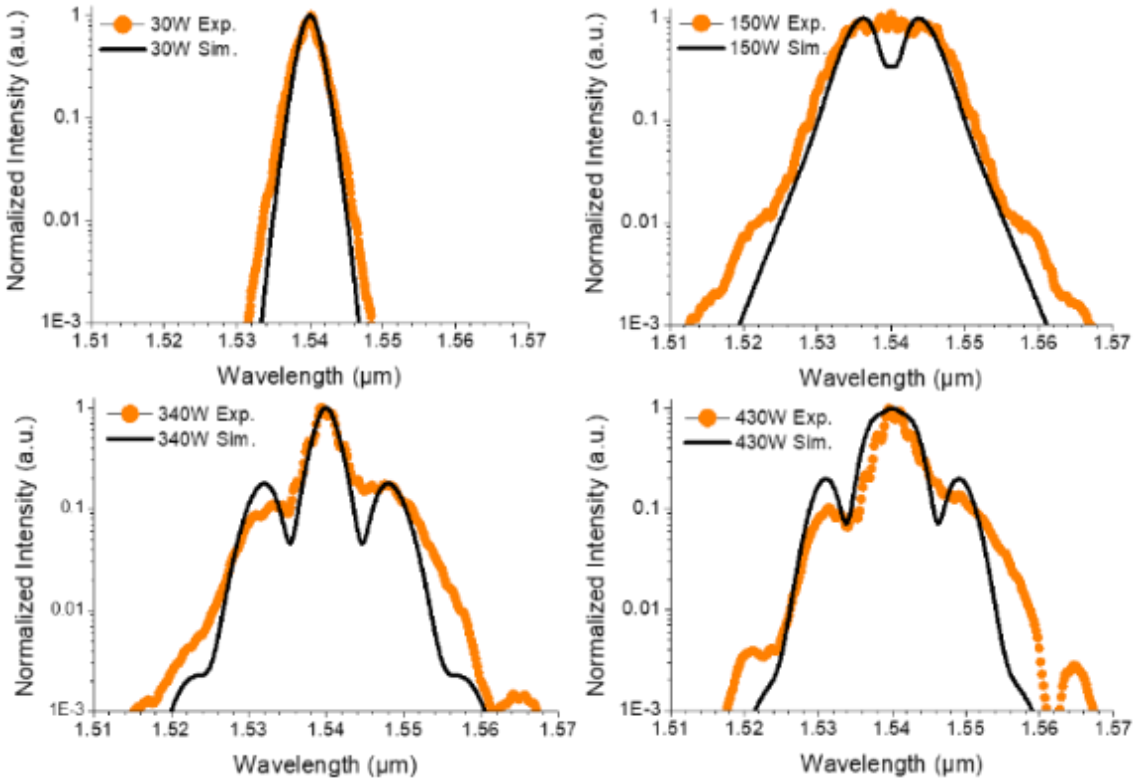

Figure VI.5. Experimental (orange dots) and simulated (black line) self-phase modulation (SPM) spectra for four different input pulse peak powers; 4.8 m of the SrAlSiF fiber were used for these measurements [14].

These results clearly display the effects of nonlinear spectral broadening due to self-phase modulation (SPM). Comparing these with the results of the numerical model (black), n_2 is estimated to be ~3×10^{-20} ± 10 % m^2/W. Although this value is similar to what is typically reported for fused silica [25], it is worth recalling that the linear refractive index of the SrAlSiF fiber core is comparatively higher (1.4796 vs. 1.444). In this core composition, assuming F is attached to Sr, the fiber is composed of an admixture of SrF_2, SrO, Al_2O_3, and SiO_2. If SrO and Al_2O_3 are found to increase n_2 relative to SiO_2 [26], [27], SrF_2 decreases it [25], [28]. Hence, a competing effect between SrF_2 and SrO + Al_2O_3 is expected, and n_2 is anticipated to be "reduced" for an oxyfluoride system versus an oxide system (i.e., with or without fluorides). It is worth mentioning that a higher n value typically results in a higher n_2 value [29], and therefore a further addition of F will have a beneficial effect in reducing the magnitude of n_2, and, consequently, wave-mixing phenomena. However, this argument is not always true. As an example, phosphate glasses exhibit higher or similar values of n than silicate glasses, but with reduced n_2 [30], [25]. This effect is attributed to the more covalent bonding nature of phosphate glasses relative to silicate glasses [30].

Some further efforts in modeling n_2 for strontium oxide, following a similar method than in [27], is provided below. This section is destined to give more insights on the role of fiber dopants on n_2. If n_2 for amorphous SrO (a-SrO) can be estimated with reasonable accuracy, further modeling to predict n_2 for amorphous SrF_2 (a-SrF_2) would introduce to much uncertainties, and is discussed later.

The determination of n_2 for a given material, using the empirical relationship from *Boling, Glass and Owyoung* [31], previously described in Chapter III, Eqns. 3.3 and 3.4, necessitate the knowledge of the refractive index dispersion of that material, that is, $n \rightarrow n(\lambda)$. For crystalline strontium oxide (c-SrO), $n(\lambda)$ is directly taken from [32]. The data are thus fit with a 3-oscillators Sellmeier model in the following form:

$$n^2 = 1 + \sum_{i=1}^{3} \frac{A_i \lambda^2}{\lambda^2 - l_i^2}. \quad (6.4)$$

The coefficients A_i and l_i^2 are determined from the fit and are reported in Table VI.5. In order to obtain the Sellmeier coefficients for amorphous strontium oxide (a-SrO), the refractive index for a-SrO at different wavelengths is taken from [33]. Using the additive model, n(a-SrO) is calculated at each wavelength (486, 535, 589, and 656 nm) and for the 5 different compositions (SrO-SiO_2, in mole %: 33.2-66.8, 36.7-63.3, 46.5-53.5, 49.9-50.1, 54.1-45.9) given in Table 7 from [33]. The calculation necessitates the knowledge of the refractive index for fused SiO_2 at each wavelength, which was calculated with the help of the Sellmeier coefficients provided in [34]. The calculated n(a-SrO) for the 5 given compositions, at each wavelength, are then averaged out, to give one n(SrO) per wavelength (4 data points total). Thus, a Sellmeier fit is performed on the data, using a

2-oscillators Sellmeier model owing the only 4 n(λ) data points. The Sellmeier coefficients for (a-SrO) are reported in Table VI.5.

Table VI.5. Sellmeier coefficients for a 3-oscillators and 2-oscillators Sellmeier model for crystalline and amorphous strontium oxides, respectively.

Material	A_1	l_1^2(nm^2)	A_2	l_2^2(nm^2)	A_3	l_3^2(nm^2)
c-SrO	0.5582	50400	0.6028	9552	1.196	9106
a-SrO	0.5009	29600	1.762	6113	-	-

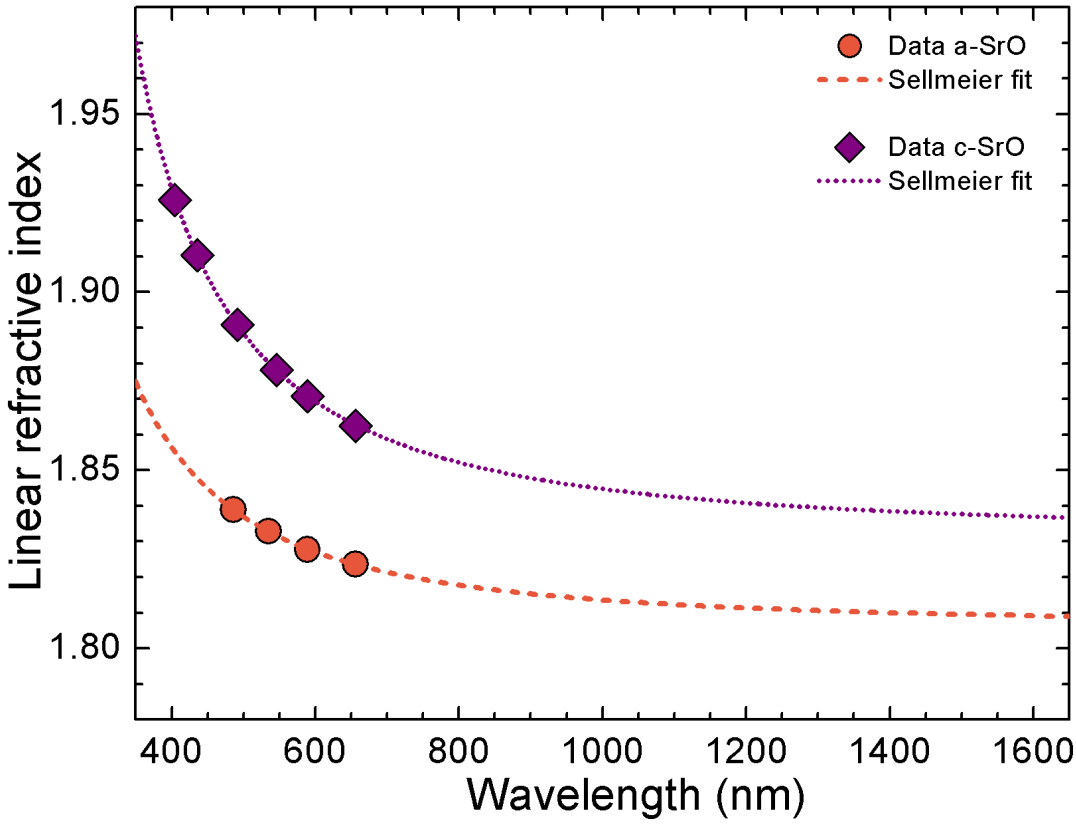

Figure VI.6. Sellmeier model fits for crystalline strontium oxide (c-SrO) and amorphous strontium oxide (a-SrO), using data from [32], [33].

The data, along with their Sellmeier fits, are displayed in Fig. VI.6. Note that n(a-SrO)~1.81 in the 15XX nm region, which is consistent with [15]. Using the Sellmeier coefficients determined above, n_2 can be calculated from Eqn. 39 in [35]. The equation takes the following form (and has been previously described in Chapter III):

$$n_2(10^{-13}\ \text{esu}) = 391\frac{(n_d-1)}{v_d^{5/4}}, \qquad (6.5)$$

If the results are given in esu, it is possible to convert back to m^2/W by using the relationship (Eqn. 5b in Chapter III):

$$n_2\left(\frac{m^2}{W}\right) = \frac{40\pi}{c_0}\left(\frac{n_2(esu)}{n}\right). \qquad (6.6)$$

The n_2 values for c-SrO and a-SrO are reported in Table VI.6. The close agreement between the calculated n_2(c-SrO) using the present method and its measured value from [26] should be noted. Additionally, n_2(a-SrO) was found to be ~5.12×10^{-20} m^2/W, which is ~55 % lower than that of its crystalline value. This value if found higher than the one of fused SiO_2 (~$2.73 \pm 0.27 \times10^{-20}$ m^2/W [25]) but also Al_2O_3 (~4.77×10^{-20} m^2/W [27]). Consequently, amorphous SrO and Al_2O_3 principally contribute to an increase of n_2, but also n. The uncertainties that arise from n_2 measurements (± 10 %) and calculations (estimated to be of the same range) do not permit further modeling of n_2(a-SrF_2). However, n_2 (c-SrF_2) has been reported to be ~$1.76 \pm 0.29 \times10^{-20}$ m^2/W at 1064 nm [25], which is ~35 % lower than fused silica, and suggests that a-SrF_2 contributes to a reduction of n_2 relative to silica.

Table VI.6. Linear refractive index (n) at different wavelength for crystalline and amorphous strontium oxide (c-SrO and a-SrO), Abbe number (v), and nonlinear refractive index (n_2) calculated from Eqn. 6.5.

Material	n^a	$n_C{}^a$	$n_D{}^a$	$n_F{}^a$	v^a	n_2 ($\times 10^{-13}$ esu)[b]	n_2 (literature)
c-SrO	1.837	1.863	1.871	1.892	53.98	4.92	5.07 [26]
a-SrO	1.809	1.823	1.828	1.839	29.66	2.21	-

[a]: n: at 1550 nm; n_C: at 656.27 nm; n_D: at 587.56 nm; n_F: at 486.13 nm.

[b]: $v=(n_D-1)/(n_F-n_C)$

[c]: Using Eqn. 6.6: At 1550 nm, n_2(a-SrO)=5.12×10^{-20} m^2/W and n_2(c-SrO)= 11.2×10^{-20} m^2/W.

In this section, insights on the role of each fiber dopant on the nonlinear refractive index of the aggregate glass was discussed. It was shown that the presence of SrF_2 would help in decreasing n_2. If herein the role of SrF_2 is of principal interest, it is worth mentioning that other glass constituents can be utilized to reduce n_2. In the alkaline earth fluoride family, n_2(MgF_2, CaF_2, and SrF_2) are lower than n_2(SiO_2) by ~65 %, ~30 %, and ~35 %, respectively; however, n_2(BaF_2) is found ~5 % stronger [25], [31]. Alkali fluorides such as NaF or LiF also exhibit reduced n_2 values [25], [28]. In oxide-based glasses, phosphates and borates can lead to glasses with intrinsically n_2 values as well [25], [29].

VI. F. The thermo-optic coefficient (dn/dT)

As described in the previous chapters, thermo-optic coefficient (dn/dT) is the material property that can be the most easily tuned and reduced in order to mitigate transverse mode instability (TMI). The measured thermo-optic coefficients (dn/dT) of the fibers are reported in Table VI.7. Because of the relatively high numerical aperture (NA) of the fabricated fibers, most of the optical power is confined at the core center. Hence, the material composition experienced by the optical mode as it propagates down the fiber can be approximated to be the composition at the core center. dn/dT for both YbF-SrAlSi and YbF-SrAlSiF B fiber segments could not be measured appropriately, due to their flat refractive index profile at the core center which prevent good coupling between the light source and the fundamental mode.

A reduced dn/dT for the characterized fibers, relative to silica, is found for both fluorine containing (Yb-SrAlSiF A and B, YbF-SrAlSiF A, and SrAlSiF) and non-containing (Yb-SrAlSi and SrAlSi) fibers. From previous work on SrO-Al_2O_3-SiO_2 system [15], it was shown that addition of SrO negatively contributes to fiber dn/dT as $dn/dT(a\text{-}SrO)=-12.4\times10^{-6}\ K^{-1}$, while Al_2O_3 slightly increases it with $dn/dT(a\text{-}Al_2O_3)=10.5\times10^{-6}\ K^{-1}$. Nevertheless, fibers exhibiting the lowest dn/dT values (Yb-SrAlSiF B and YbF-SrAlSiF A) contain the highest fluorine concentration.

Fig. VI.7a shows the evolution of dn/dT as a function of fluorine content for the four Yb-doped oxyfluoride fibers characterized. dn/dT of Yb-SrAlSi fiber, which contains no F, is also added as a reference point. The data exhibit a linear relationship between dn/dT and F concentration in the compositional region investigated. Interestingly, the multicomponent nature of the core materials seems to only play a secondary role in the reduction of dn/dT, as it is a strong function of F content. This can be explained with SrO concentration for the investigated fibers being somewhat similar, when SrF_2 concentration differs greatly. Moreover, Al_2O_3 has a dn/dT very close to SiO_2 and consequently is not expected to play any major role on the glass dn/dT.

Table VI.7. Thermo-optic coefficient (dn/dT) measured for the fibers investigated here.

Fiber	SrF_2	SrO	Al_2O_3	Yb_2O_3	SiO_2	dn/dT (10^{-6} K^{-1})	dn/dT (in dB, relative to SiO_2)
Yb-SrAlSi	0.00	6.41	3.17	0.58	89.84	7.96 ± 2%	-1.16
YbF-SrAlSi	0.59	12.77	6.93	0.71	79.01	-	-
Yb-SrAlSiF A	4.26	7.88	4.89	0.91	82.07	6.30 ± 6%	-2.18
Yb-SrAlSiF B	8.52	6.47	5.68	1.14	78.20	4.93 ± 3%	-3.24
YbF-SrAlSiF A	8.11	5.87	5.47	0.51	80.03	5.14 ± 3%	-3.06
YbF-SrAlSiF B	9.71	4.76	5.41	0.52	79.59	-	-
SrAlSiF	4.94	5.88	3.83	0.00	85.35	6.3 ± 5%	-2.18
SrAlSi	0.00	9.79	17.10	0.00	73.11	8.4 ± 5%	-0.93
SiO_2	-	-	-	-	100	10.4 [15]	-

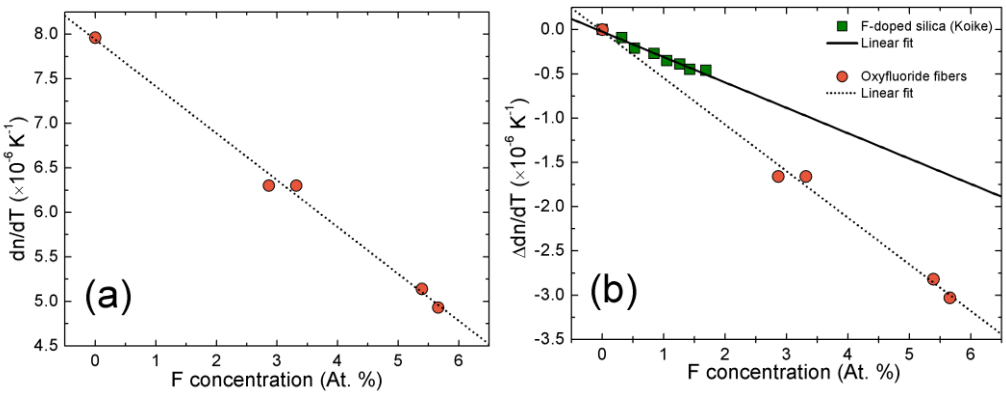

Figure VI.7. a) Thermo-optic coefficient (dn/dT) for the Yb-doped strontium fluoro-aluminosilicate and Yb-SrAlSi fibers as a function of fluorine concentration (in At. %). b) Variation of dn/dT as a function of fluorine concentration for the oxyfluoride fibers studied here and F-doped silica glasses from [19].

In Fig. VI.7b, the variation of dn/dT (Δdn/dT) as a function of F concentration is presented for the oxyfluoride systems investigated, and is compared to F-doped silica glasses from [19]. The evolution of dn/dT as a function of F content is found to greatly differ between oxyfluoride and silica glasses. If in F-doped silica glasses F is bound to Si, in the materials investigated herein F is found to principally bound to Sr, and, consequently, the reduction of dn/dT is different. This observation is different from the contribution of F on the refractive index, where its effect was found to be almost equal between oxyfluoride glasses and F-doped silica glasses.

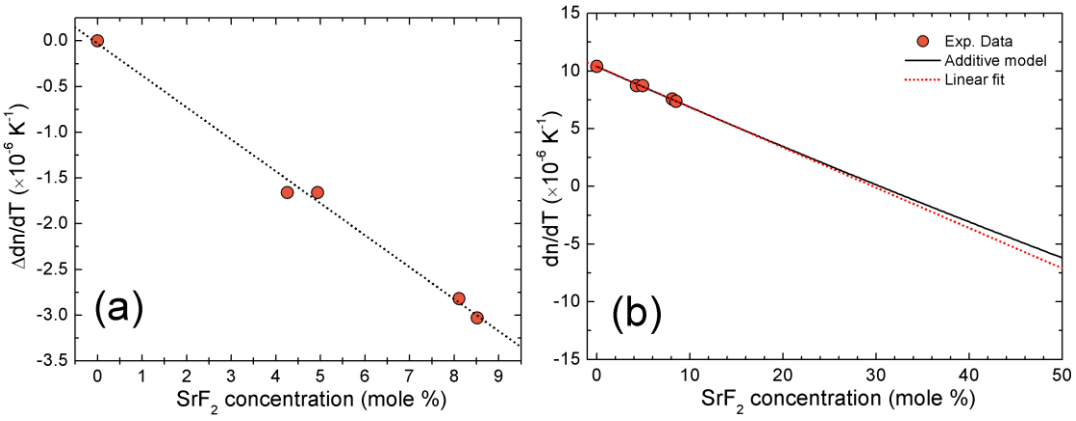

Figure VI.8. a) Variation of the thermo-optic coefficient (Δdn/dT) as a function SrF_2 concentration (mole %). b) Calculated thermo-optic coefficient in a hypothetical binary SiO_2-SrF_2 system. The solid line is a fit using the additive model, with dn/dT (SrF_2) being the fit parameter. The red dot line is a linear fit to the data.

Furthermore, one can express the variation of dn/dT as a function of the mole % of SrF_2 introduced in the fiber core, as in Fig. VI.8a. Then, using the additive model described in Chapter II, dn/dT for a hypothetical binary SiO_2-SrF_2 system can be calculated, with dn/dT(SrF_2) being the fit parameter (and values for SiO_2 are assumed). The results are displayed in Fig. VI.8b and dn/dT(a-SrF_2) is found to be ~-20.54×10^{-6} K^{-1}. Using a linear extrapolation to the data in Fig. VI.8b instead gives dn/dT(a-SrF_2) ~-24.56×10^{-6} K^{-1}. Uncertainties are estimated to be ± 10 %.

Value of dn/dT for crystalline SrF_2 (c-SrF_2) is found to be ~-12.5×10^{-6} K^{-1} [23], which is largely negative but about 45 % lower in magnitude than the value estimated for a-SrF_2. In addition, dn/dT(a-SrF_2) is also more negative than dn/dT(a-SrO). This difference

can be understood by discussing Prod'homme model [36] on the thermo-optic coefficient. The variation of the refractive index upon heating, derived from the Lorentz-Lorenz relation, takes the following form [36]:

$$\frac{dn}{dT} = \frac{(n^2-1)(n^2+2)}{6n}(\varphi - \beta), \qquad (6.7)$$

where n is the linear refractive index, φ is a polarization coefficient and β is the volumetric coefficient of thermal expansion. In Eqn. 6.7, φ and β both contribute to a change of n upon heating (i.e., dn/dT). An increase in polarizability (φ), resulting from the electrons becoming more loosely bound to their nucleus, increase n (assuming electronic polarizability is the principal contributor to this effect). On the other hand, when β is large, the number of dipoles per unit volume is decreased when the material expands upon heating, which results in a decrease of n. Thermal expansion coefficient of SrF_2 is ~18×10^{-6} K^{-1} [37], when SrO is ~17.6×10^{-6} K^{-1} (Chapter II, Fig. VI.4). However, fluorine has a lower polarizability than oxygen, and, therefore, the ϕ is expected to be lower for SrF_2 relative to SrO. This difference in polarizability would result in a more negative dn/dT. Consequently, the addition of SrF_2 as a material precursor greatly contributes to the reduction of dn/dT in optical glasses. As an example, YbF-SrAlSiF A fiber segment has ~3 dB reduction in dn/dT relative to conventional silica fibers.

The Raman gain coefficient (RGC)

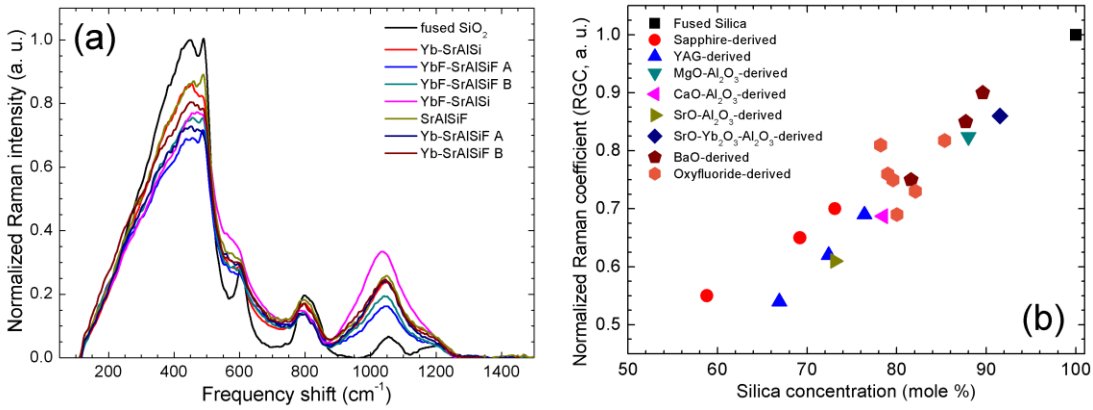

Figure VI.9. a) Corrected and normalized spontaneous Raman spectra for Yb-doped fibers (along with the SrAlSiF segment). b) Relative Raman gain coefficient (RGC) for various silicate, aluminosilicate, and oxyfluoride fiber core materials as a function of silica concentration (in mole %). Data for Sapphire-derived [38], BaO-derived [38], $SrO\text{-}Al_2O_3$-derived [14],and YAG-derived [39] are taken in the literature. $MgO\text{-}Al_2O_3$-, $CaO\text{-}Al_2O_3$-derived systems are here for completeness (characterized in Appendix VI.1), and Yb_2O_3- $SrO\text{-}Al_2O_3$-derived and oxyfluoride-derived fibers are the systems characterized herein.

The normalized spontaneous Raman spectra for the Yb-doped fibers, along with the SrAlSiF fiber segment, are reported in Fig. VI.9a. The Raman features for these aluminosilicate fibers have been discussed in great details in Chapter V. The Raman gain coefficients (RGC) for the various fibers are measured as being the intensity of the highest peak of the Raman scattering bandwidth, this relative to fused silica. Therefore, for fused

SiO_2 (taken in the cladding), the Raman gain coefficient is equal to unity (highest peak centered around 440 cm^{-1}). As can be seen from Fig. VI.9a, the multicomponent nature of the glass composition investigated tends to reduce the main silica peak. Consequently, the magnitude of RGC is principally a function of SiO_2 content in the core materials. Thus, RGC as a function of SiO_2, for a series of glass fiber core compositions which includes silicates, aluminosilicates and oxyfluorides, is reported in Fig. VI.9b. More information regarding the systems investigated can be found in the caption. As it can be observed from Fig. VI.9b, RGC for the oxyfluoride fibers follow the trend of aluminosilicate or silicate systems, as they are mainly composed of oxides (fluorine being only a minor component). In the limit of very large incorporation of dopants into the silica matrix (and therefore, lower silica content), one may expect that peaks other than the one at ~440 cm^{-1} will begin to dominate the Raman scattering cross section intensity, likely in the high energy region characteristic of NBOs formation. This may then ultimately be a limiting factor for further reduction of RGC. Moreover, glass formation and fabrication of systems with low silica content can become more challenging.

VI. G. The Brillouin gain coefficient (BGC)

Table VI.8. Brillouin properties of the investigated fibers: Brillouin Frequency (ν_B), Brillouin spectral width ($\Delta\nu_B$), longitudinal acoustic velocity (V_a) and, Brillouin gain coefficient (BGC).

Fiber	SrF_2	SrO	Al_2O_3	Yb_2O_3	SiO_2	ν_B (GHz)	$\Delta\nu_B$ (MHz)[b]	V_a (m/s)	BGC (10^{-11} m/W)	BGC (dB) relative to SiO_2
Yb-SrAlSi	0.00	6.41	3.17	0.58	89.84	10.905	52.9	5722	0.49 ± 5%	-6.9
YbF-SrAlSi	0.59	12.77	6.93	0.71	79.01	10.945	70.9	5598	0.29 ± 8%	-9.2
Yb-SrAlSiF A	4.26	7.88	4.89	0.91	82.07	10.755	50.5	5569	0.47 ± 5%	-7.1
Yb-SrAlSiF B	8.52	6.47	5.68	1.14	78.20	10.617	47.5	5476	0.45 ± 5%	-7.3
YbF-SrAlSiF A	8.11	5.87	5.47	0.51	80.03	10.677	52.4	5539	0.39 ± 4%	-7.9
YbF-SrAlSiF B[a]	9.71	4.76	5.41	0.52	79.59	-	-	-	-	-
SrAlSiF	4.94	5.88	3.83	0.00	85.35	10.975	52.0	5621	0.56 ± 5%	-6.3
SrAlSi	0.00	9.79	17.10	0.00	73.11	11.975	123	6079	0.11	-13.4
SiO_2	-	-	-	-	100	11.239	17	5970	2.4	-

[a]: The Brillouin properties of this fiber could not be measured correctly due to the short length of the test fiber.

[b]: At 11 GHz.

Characteristic Brillouin properties, i.e., Brillouin frequency (ν_B), Brillouin spectral width ($\Delta\nu_B$), longitudinal acoustic velocity (V_a) and, Brillouin gain coefficient (BGC), for the fibers characterized above, are reported in Table VI.8. First, all the fibers present a reduced BGC, ranging between 75 % to 95 % decrease in the Brillouin strength relative to silica. These results confirm the success of a materials route toward the fabrication of low BGC core materials, previously described in Chapters I, II and III, and IV. Second, some insights can be gained regarding the role that each core constituent plays on the reduction

of BGC. In order to ease the discussion regarding material contribution to BGC, Equation 6.8 provides the expression it takes in optical fiber form:

$$BGC\ \left(\frac{\mathrm{m}}{\mathrm{W}}\right) = \frac{2\pi \mathrm{n}^7 \mathrm{p}_{12}^2}{\mathrm{c}\lambda_0^2 \rho \mathrm{V_a} \Delta \upsilon_\mathrm{B}}. \qquad (6.8)$$

Table VI.9 reports the acousto-optic properties of amorphous SiO_2, Al_2O_3, SrO, and Yb_2O_3. Moreover, the properties for crystalline SrF_2 (c-SrF_2) are provided to facilitate a discussion on the effect of a fluoride precursor on the Brillouin properties of the fabricated glass fiber cores. From Eqn. 6.8, it can be seen that a decrease of n and p_{12}, coupled with an increase of ρ, V_a, and $\Delta\nu_B$ would result in a reduced BGC. Because each fiber has a different composition, BGC will vary as each constituent that composes the core glass presents different properties. For instance, in Yb-SrAlSi fiber, SrO, Al_2O_3 and Yb_2O_3 increase $\Delta\nu_B$ relative to silica. However, again relative to silica, both SrO and Yb_2O_3 are found to decrease V_a when Al_2O_3 significantly increases it. Regarding p_{12}, all the dopants in this fiber segment would contribute in a reduction of its magnitude since their p_{12} values are lower than p_{12} (SiO_2). It is worth noting that SrAlSi fiber has a large $\Delta\nu_B$. This significantly larger value compared to the other fibers is due to the acoustically anti-guiding nature of this fiber. It results from its high Al_2O_3 concentration which increases V_a (fiber mode) to a point where V_a (fiber mode) > V_a (SiO_2 cladding) [15]. This effect is also observed for MgAlSi, CaAlSi, and CaAlSiF A and B fiber segments, reported in Appendix VI.1. For the Yb-doped and SrAlSiF fibers, both SrO and SrF_2 are expected to contribute to the reduction of V_a. Therefore, the fibers are acoustically guiding.

Table VI.9. Summary of acousto-optic properties for amorphous glass compounds (SiO_2, Al_2O_3, SrO, and Yb_2O_3) determined using additive models described in Chapter III. Properties for crystalline SrF_2 (c-SrF_2) are also reported.

Value	SiO_2[a]	Al_2O_3[b]	SrO[c]	Yb_2O_3	c-SrF_2
Index (at 1534 nm)	1.444	1.653	1.810 ± 1.1%	1.881	1.438[d] [25]
Molar mass (g/mol)	60.08	101.96	103.62	394.106	125.62
Density ρ (kg/m^3)	2200	3350	4015 ± 1.0%	8102	4280 [40]
V_a(m/s)	5970	9790	3785 ± 1.6%	4110	5175[f] [40]
$\Delta\nu_B$ (MHz at 11 GHz)	17.0	274	187 ± 11%	1375	-
dn/dT (10^{-6} K^{-1})	10.4	10.5	-12.4 ± 68%	-	-12.5 [23]
p_{11}	+0.098	-0.237 ± 0.020	-0.296 ± 0.113	-0.275	+0.080[e] [22]
p_{12}	+0.226	-0.027 ± 0.012	-0.245 ± 0.034	-0.123	+0.269[e] [22]
Poisson Ratio	0.16	0.25	0.231 [41]	0.28	0.29 [22]

[a]: Data from [42], [7], [8], [13] for silica were utilized in the analysis here. Determination of the Pockels' coefficients near 15XX nm for silica can be found in [42]. The Pockels' values are somewhat lower here than in the visible wavelength range [22], [43], [44] due to dispersion in these parameters [45]–[48].

[b]: Data from [42], [49], [50] for alumina was utilized in the analysis here.

[c]: Data from [15].

[d]: At 1064 nm.

[e]: At 633 nm.

[f]: At room temperature, averaged over [100], [110], and [111] crystallographic plan orientations.

Now, if the contributions of the oxide glass compounds have been characterized and investigated (Table VI.9, but also Chapter III, Table III.1), an attempt to characterize the effect of SrF_2 as an amorphous glass constituent is made. As Brillouin spectroscopy involves the interaction between acoustic and optical modes, a 4-layer approximation, described in Chapter III, Section B.1, is utilized. The fiber segments chosen for this

analysis are Yb-SrAlSiF A and B. A 4-layer approximation is first made with the help of refractive index profile (RIP), and the compositional (from EDX) profile is overlaid on the RIP. Then, both profiles are interpolated to determine the composition and refractive index. For each given layer, the modeled property values of amorphous SrF_2 (a-SrF_2) at each modeled layer can be determined and are reported in Table VI.10.

Table VI.10. Summary of the calculated properties using a 4-layer approximation for Yb-SrAlSiF A and B fiber segments.

Yb-SrAlSiF A									
Layer	SrF_2	SrO	Al_2O_3	Yb_2O_3	SiO_2	n(SrF_2)	V_a (SrF_2) (m/s)	$\Delta\nu_B$ (SrF_2) (MHz)	p_{12}
1	4.09	7.88	4.79	0.89	82.35	1.507	2960	<0	+0.245[a,b]
2	3.92	7.88	4.53	0.86	82.81	1.477	3052	<0	+0.285[a,b]
3	3.53	6.88	4.08	0.76	84.75	1.504	3006	<0	
4	3.13	5.05	3.57	0.64	87.61	1.492	3095	<0	
Average	-	-	-	-	-	1.49	3028	<0	+0.265
Yb-SrAlSiF B									
Layer	SrF_2	SrO	Al_2O_3	Yb_2O_3	SiO_2	n(SrF_2)	V_a (SrF_2) (m/s)	$\Delta\nu_B$ (SrF_2) (MHz)	p_{12}
1	8.52	6.26	5.68	1.11	78.43	1.51	3280	<0	+0.095[a,b]
2	8.12	6.05	5.48	1.05	79.3	1.50	3292	<0	+0.065[a,b]
3	7.70	5.56	5.07	1.03	80.64	1.49	3357	<0	
4	6.50	5.07	4.50	0.79	83.14	1.48	3381	<0	
Average	-	-	-	-	-	1.495	3328	<0	+0.080

[a]: Acoustic wave is confined to the first two layers.

[b]: $\Delta\nu_B(SrF_2)$ was set to -212 MHz (negative) to make the spectral width match that which was measured. However, by changing $\Delta\nu_B(Yb_2O_3)$, one can find more reasonable (i.e., positive) $\Delta\nu_B(SrF_2)$ values.

First, it should be noted that both n and V_a for a-SrF_2 are somewhat consistent throughout the layers, which may suggest at first that considering SrF_2 as a glass compound is a reasonable assumption. Using the 4-layer approximation, n(SrF_2) = 1.49 (Yb-SrAlSiF A) and 1.495 (Yb-SrAlSiF B), is found close to what was previously found in section VI. D., i.e., 1.48. The average acoustic velocity is calculated to be 3028 and 3328 m/s, which is ~35-40% lower that for its crystalline analog (Table VI.9). If this value seems low compare to its crystalline analog, amorphous BaO is found to also present lower V_a value (~33%) than its crystalline analog [6]. In order to retrieve $\Delta\nu_B$ for each layer, a negative $\Delta\nu_B$ value for SrF_2 is necessary, which is non-physical. However, it is possible that the fluorine modifies the local environment of other cations than Sr, such as Yb, and can subsequently modify $\Delta\nu_B$ for the other glass compounds. This can be a possibility as the Yb spectroscopic properties are very sensitive to the fluorine concentration (see next section), which suggests fluorine to be in the environment near to the rare earth ion, Yb. Finally, the transverse photoelastic coefficient p_{12} of amorphous SrF_2 is calculated to be ~0.265 and ~0.080 for segments A and B, respectively. Interestingly, the former value is found to be nearly the same as the crystalline value (0.269, Table VI.9) for segment A. However, it is much lower for segment B, and suggests that the fluorine may modify the glass in such a way that the additive models used herein breaks down. Overall, further investigation of a-SrF_2 properties should be carried out, as the additive models used herein only permit a qualitative understanding of its influence on the aggregate glass properties. Nevertheless, if SrF_2 participates to the reduction of n, n_2, and TOC, the modeled values reported in Table VI.10 suggest that it does not participate to the reduction of BGC as its

oxide analog SrO would do, primarily due to its positive p_{12} coefficient, as well as its low acoustic velocity. Therefore, a glass core that contains both SrO and SrF_2 as glass compounds is critical in order to mitigate all nonlinearities concomitantly.

The 4-layer approximation of the core fibers was also used to determine the $dn/dT(SrF_2)$. This calculation differs from section VI.F above, where the assumption that the fundamental mode (FM) is tightly confined at the core center was made, suggesting dn/dT to be the value corresponding to the glass composition at the fiber core center. Using the 4-layer approximation, the spreading of the FM over the effective area (i.e., at and away from the core center) is considered. Performing the calculation gives a $dn/dT(SrF_2) \sim -52\times10^{-6}\ K^{-1}$ and $\sim -38\times10^{-6}\ K^{-1}$ for both Yb-SrAlSiF A and B, respectively. These values are 2 to 2.5 times higher than what was found in Section VI.F ($-20.5\times10^{-6}\ K^{-1}$). This difference is expected as the whole optical mode is considered, which comprises more silica due to silica-richer layers away from the core center, hence less SrF_2, resulting in an increase of the magnitude of $dn/dT(SrF_2)$ using the additive model. The magnitude of dn/dT still remains very large, and only a qualitative understanding, given in Section VI.F., can be provided regarding the contribution of SrF_2 on dn/dT.

VI. H. Ytterbium spectroscopy of oxyfluoride fibers

Although not directly related in the characterization of parameters that drive optical nonlinearities, the importance in studying the spectroscopic properties of the fibers is many fold. First, it enables a better understanding of the local environment of the Yb ions, which, in turn, leads to a better comprehension of the optical properties to structure/composition relationships. In addition, Yb-doped fibers lasers are of interest due to their simple electronic level structure, their low quantum defect (necessary when it comes to heat management and to prevent thermal nonlinearities such as TMI), and the availability of pump diodes at the operating wavelength bandwidth [51]. Consequently, characterization of properties that dictate fiber laser performance such as emission cross section or fluorescence lifetime [52] is valuable.

Thus, this section focuses on the study of some spectroscopic properties of Yb ion $^2F_{5/2}$ and $^2F_{7/2}$ transition electronic states. The fluorescence lifetimes (τ), average emission wavelengths (λ_{av}), emission cross sections (σ_{em}) are reported in Table VI.11, along with the core center fiber compositions to help the reader in comparing compositions vs. spectroscopic properties. Spectroscopic properties of a commercial aluminosilicate fiber (LIEKKI® Yb1200-4/125) is also reported for comparison.

The normalized emission spectra of the fabricated fibers are reported in Fig. VI.10a. For fibers with high fluorine concentrations, the secondary peak of the emission bandwidth

is shifted to lower wavelengths and its magnitude is increased relative to the zero-line peak. This behavior is similar to [53], [54] and is attributed to the so-called nephelauxetic effect, where the fluorinated glass modifies the local environment of the active ion, resulting in a shift to lower wavelength (blue shift).

Table VI.11. Fiber compositions at the core center (in mole %), fluorescence lifetimes (τ, in µs), average emission wavelengths (λ_{av}, in nm), emission cross section (σ_{em}, in $\times 10^{-20}$ cm^2) calculated from Eqn. 6.3.

Fiber	SrF_2	SrO	Al_2O_3	Yb_2O_3	SiO_2	τ[a]	λ_{av}[b]	σ_{em}[c]
Yb-SrAlSi	0.00	6.41	3.17	0.58	89.84	1060	1004.9	2.45
YbF-SrAlSi	0.59	12.77	6.93	0.71	79.01	968	1003.6	2.55
Yb-SrAlSiF A	4.26	7.88	4.89	0.91	82.07	1239	1001.6	1.91
Yb-SrAlSiF B	8.52	6.47	5.68	1.14	78.20	850	1000.0	2.44
YbF-SrAlSiF A	8.11	5.87	5.47	0.51	80.03	1270	999.19	1.73
YbF-SrAlSiF B	9.71	4.76	5.41	0.52	79.59	1270	1000.8	1.59
LIEKKI® fiber[d]						743	1006.6	2.53

[a]: The fluorescence lifetimes are calculated for a decrease of 1 of the log (I), with "I" describing the fluorescence intensity. Spectra of Log(I)=f(time) for the Yb-doped fibers are reported in Appendix VI.4.

[b]: Defined as $\lambda_{av} = \int \lambda \times I(\lambda) \times d\lambda \; / \; \int I(\lambda) \times d\lambda$.

[c]: σ_{em} calculated using the Fuchtbauer-Ladenburg (F-L) formula (Eqn. 6.3). Emission cross section spectra (in cm^2) are reported in Appendix VI.4.

[d]: Typical Yb-doped aluminosilicate optical fiber (LIEKKI® Yb1200-4/125).

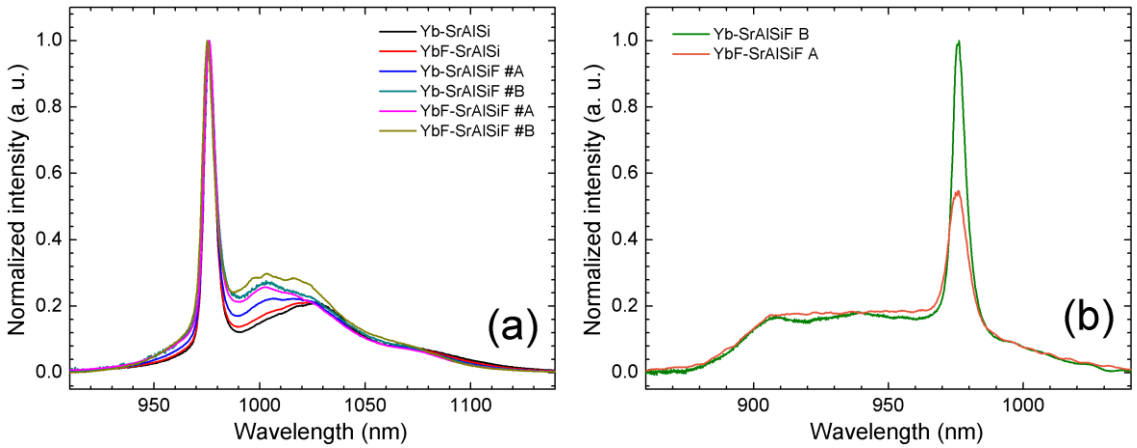

Figure VI.10. Normalized emission spectra for Yb-doped fibers. b) Normalized absorption spectra for two fibers (Yb-SrAlSiF B and YbF-SrAlSiF A).

The Yb^{3+} doping, through introduction of Yb_2O_3 or YbF_3 in a similar precursor system matrix, say $SrO\text{-}Al_2O_3$ (black vs. red curve in Fig. VI.10a), gives rise to a small, but significant, shift to lower wavelength. A similar trend is observed when Yb_2O_3 is again substituted by YbF_3 in an $SrF_2\text{-}Al_2O_3$ initial precursor mixture (blue vs. pink in Fig. VI.10a). This clearly suggests some nearest-neighbor fluorine ions in the local environment of Yb^{3+}. Additionally, the less resolved stark splitting and the significant inhomogeneous broadening suggests formation of highly disordered glasses, in part explained by the multicomponent nature of these fiber core materials.

In Fig. VI.10b, the absorption bandwidths of two fibers (Yb-SrAlSiF B and Yb-SrAlSiF A) are reported. The absorption spectra exhibit a very wide and flat bandwidth, which resembles to borate or phosphate glasses [53], and again suggests Yb ions to have multiple local environments. Furthermore, the line strength of the YbF-SrAlSiF A fiber segment is

reduced compared to the Yb-SrAlSiF B segment. Interestingly, the two compositions have somewhat similar SrF_2 concentration, but the starting precursor for YbF-SrAlSiF A segment is YbF_3, when it is Yb_2O_3 for the Yb-SrAlSiF B. The line strength of fluoride glasses being smaller than silicate glasses [53], it is likely that some F remains attached to Yb during fiber drawing when YbF_3 is a starting precursor. Moreover, the absorption peak is slightly more shifted to lower wavelength for YbF-SrAlSiF A fiber, which is understood as a more fluorinated environment of the Yb ions and consequently consistent with the argument formulated above.

For completeness, a comparison of the emission spectra between Yb-SrAlSi fiber and two Yb-doped aluminosilicate fibers is given in Appendix VI.4. The non-containing fluorine fiber (Yb-SrAlSi) has a less resolved stark splitting that typical aluminosilicate fibers. The asymmetry of the secondary peak is attributed to the effect of strontium since alumina is found to modify the magnitude of the 1025 nm peak relative to the zero-line peak, but does not give rise to a noticeable frequency shift. Because the emission bandwidth is affected by strontium, it is likely that Sr ions are in the proximity of Yb ions. Interestingly, F is found to also modify the local environment of Yb ions and thus some Sr-F bonds to be in their first coordination shells. It also explains the drastic change of spectroscopic properties with the addition of only few percent of fluorine. This is consistent with the observation in strontium oxyfluoride glasses [16] where F is found to be principally distributed around Sr and the rare earth (Lanthanum in the study).

The average emission wavelength (λ_{av}) and the emission cross section (σ_{em}) as a function of SrF_2 concentration are reported in Fig. VI.11 (a and b). The fluorescence lifetime as a function of SrF_2 and Yb_2O_3 content are displayed in Fig. VI.11 (c and d).

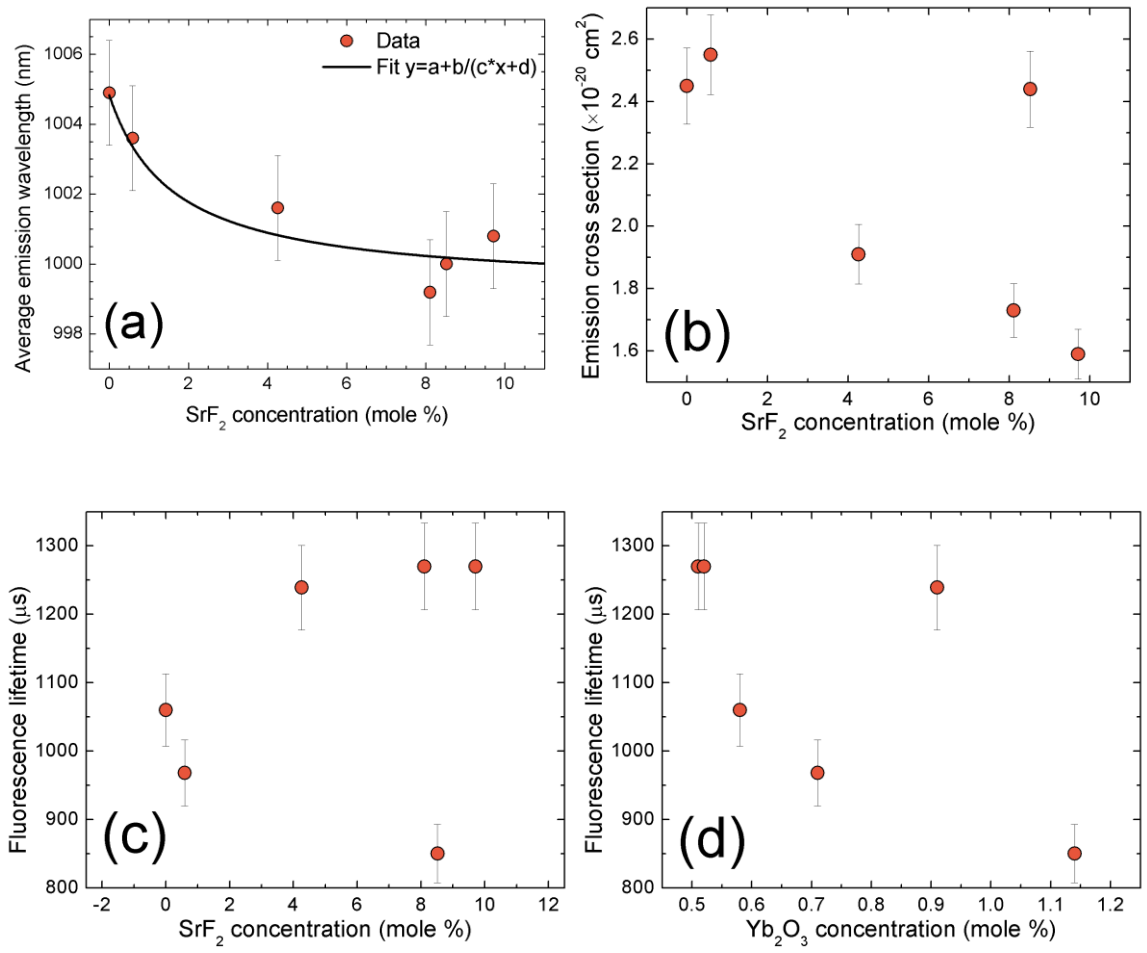

Figure VI.11. a) Average emission wavelength (nm) and b) Emission cross section ($\times 10^{-20}$ cm^2) as a function of SrF_2 concentration (mole %). c) and d) are the fluorescence lifetime (in µs) as a function of SrF_2 and Yb_2O_3 concentration (in mole %), respectively. The outlier data points in (b), (c), and (d) are discussed in the text.

From Fig. VI.11, on can observe that the average emission wavelength, emission cross section and lifetime are strong function of the glass material composition. The reduction of λ_{av} as a function of SrF_2, already described as originating from the nephelauxetic effect, is clearly visible from Fig. VI.11a. Interestingly, if only few mole percent of SrF_2 seem to have a strong effect in reducing λ_{av}, the frequency shift becomes less pronounced with further addition of SrF_2 as it reaches a horizontal asymptote. This blue shift can potentially be beneficial for reducing the Quantum Defect laser operation, as λ_{input} to λ_{output} difference can be reduced. The λ_{av} for the fibers investigated herein is typically lower than commercial aluminosilicate systems (see LIEKKI® fiber, Table VI.11). In Fig. VI.11b, if the fibers exhibit a reduced σ_{em} when fluorine concentration increases, as typical when going from oxide to fluoride systems [53], [55], [56], one fiber (Yb-SrAlSiF B) significantly deviates from this trend. This arises from lifetime quenching due to its high Yb concentration, similarly to what is observed in [57]. Because σ_{em} and τ are inversely proportional to each other (Eqn. 6.3), a sudden decrease of τ is concomitant to a higher calculated cross section, as observed in Fig. VI.11b for this fiber. The fluorescence lifetime (τ) is found to increase with higher SrF_2 content (Fig. VI.11c), excepted for Yb-SrAlSiF B fiber segment. This fiber deviates from the trend due to lifetime quenching effect as described above. The lifetime tends to plateau at higher SrF_2 concentration, which resembles the asymptotic behavior observed in Fig. VI.11a. Interestingly, it suggests that for SrF_2 concentration > 5 mole %, both λ_{av} and τ values plateau. In Fig. VI.11d, the lifetime as a function of Yb_2O_3 concentration is also reported. When Yb_2O_3 content is increased, excepted for Yb-SrAlSiF A segment, which has a

substantially high lifetime granting its high Yb_2O_3 content, the lifetime decreases. This is characteristic of lifetime quenching. Consequently, two principal contributions to the lifetime are identified, i) an increase of fluoride as a core material leads to longer fluorescence lifetime and ii) an increase of Yb concentration, in contrast, reduces it.

Table VI.12. Fluorescence lifetime (τ, in µs), averaged emission wavelength (λ_{av}, in nm), averaged emission cross section ($\sigma_{em,av}$, in $\times 10^{-20}$ cm^2), and cross section-lifetime product ($\sigma_{em,av} \times \tau$, in $\times 10^{-20}$ cm^2.ms).

Fiber	τ	λ_{av}	$\sigma_{em,av}$[a]	$\sigma_{em,av} \times \tau$
Yb-SrAlSi	1060	1004.9	1.089	1.15
YbF-SrAlSi	968	1003.6	1.204	1.17
Yb-SrAlSiF A	1239	1001.6	0.901	1.12
Yb-SrAlSiF B	850	1000.0	0.835	0.71
YbF-SrAlSiF A	1270	999.19	0.845	1.07
YbF-SrAlSiF B	1270	1000.8	0.767	0.97
LIEKKI® fiber	743	1006.6	1.056	0.78

[a]: defined as $\sigma_{em,av} = \int \sigma \times I(\sigma) \times d\sigma \; / \; \int I(\sigma) \times d\sigma$.

The product $\sigma \times \tau$ is a good figure of merit to provide insights on fiber laser performance [10], [52], especially in this context where glass composition vs. optical properties are of interest (both lifetime and cross section are material dependent). To calculate this factor, the averaged emission cross section ($\sigma_{em,av}$) is taken instead of the emission cross section of the highest peak of the emission bandwidth, and is reported in Table VI.12. One should not that, excepted for Yb-SrAlSiF B fiber segment, which exhibits strong lifetime quenching, all the fibers present a higher figure of merit than the

conventional aluminosilicate fiber. However, no direct correlation between $\sigma_{em,av}$ and SrF_2 concentration was found. Then, in addition from having reduced optical nonlinearities, the investigated fibers exhibit promising spectroscopic properties. Furthermore, the addition of fluorine in silicate systems enables potential tailoring of the emission cross section and fluorescence lifetime.

VI. I. Conclusion

The optical properties of alkaline earth oxyfluoride fibers have been discussed. The study of a variety of Yb-doped strontium oxyfluoride fibers has enabled a better comprehension of the role that each dopant plays on the parameters/properties that drive optical nonlinearities.

It was found that the introduction of SrF_2 into the core glass optical fiber causes a reduction of the refractive index (n), and subsequently a reduction of the nonlinear refractive index (n_2), relative to its oxide analog (i.e., SrO). Moreover, the possibility to reduce core-cladding index difference (Δn) can be crucial when the development of fibers with low NA is mandatory. For instance, YbF-SrAlSiF B fiber segment was found to have a Δn that is ×2 lower than if the same core material was considered, but without fluorine (i.e., containing only SrO instead of an admixture of SrO and SrF_2).

The thermo-optic coefficient (dn/dT) was found to be reduced by ~50 % in high fluorine content fibers, and was explained by the large negative dn/dT exhibited by the fluoride precursor. The Raman gain coefficient (RGC) reduction in the developed fibers was found to be principally driven by the silica concentration in the fiber core, somewhat indistinctly from the precursor composition. Reduction of the Brillouin gain coefficient (BGC), ranging between 75 to 95 % depending on the fibers, was ascribed to the role played by the alkaline earth oxide (AEO) and alumina (Al_2O_3) into the silica matrix.

Finally, investigation of the spectroscopic properties of the Yb-doped fibers revealed the influence of fluorine on the lifetime and emission cross section of the fibers. Interestingly, the shift to lower wavelengths of the average emission wavelength is characteristic of the more ionic character of the oxyfluoride fibers relative to typical aluminosilicate systems. The hybrid character of these oxyfluoride fibers (fluoride-like properties in silica-based core) could enable spectroscopic property tunability.

This chapter clearly shows the potential in the development of oxyfluoride core glass optical fibers for continuing power scaling, as they are materials solution in reducing optical nonlinearities. However, several challenges remain to make these fibers practicable, and these are discussed in the following chapter.

Appendix VI. 1. Properties of alkaline earth aluminosilicates, fluoro-aluminosilicates, and fluoro-silicates

Properties of alkaline earth aluminosilicate optical fibers.

Fiber properties	**MgAlSi[e]**	**CaAlSi[e]**	**SrAlSi[e]**	**BaAlSi[e]**
T_{draw} (°C)	**2100**	**1950**	**1925**	**1950**
Optical Wavelength (nm), Brillouin Scattering Measurements	1534	1534	1534	1534
Δn^a ($\times 10^{-3}$)	34.7	62.8	74.8	29.1
Mode Index, n_m (1534 nm); room temp. and zero strain[b]	1.4649	1.4979	1.5109	1.4503
Mode Field Diameter (μm)	4.80	5.47	6.10	4.82
Attenuation Coefficient (dB/m) at 1534 nm[f]	1.02	1.93	2.68	3.64
ν (GHz)	12.199	12.435	11.975	11.275
V (m/s) (acoustic mode value)	6387	6367	6079	5963
$[Al_2O_3]^{a,d}$ mole%	7.8	12.8	17.1	3.1
$[AEO]^{a,d}$ mole%	4.2	7.4	9.8	1.8
Thermal Coefficient (MHz/K)	+0.637	+0.067	-0.064	+0.838
TOC (10^{-6} K^{-1})	10.9	10.9	8.4	10.6
Strain Coefficient (GHz/ε)	45.8	32.2	24.4	49.1
εOC (unitless)	0.142	0.128	0.102	0.159
Δν (MHz)	148	138	123	38
$\Delta\nu_{intrinsic}$ (MHz)[c]	76.8	97.5	87.2	38
ρ (kg/m^3)[a,b]	2315	2385	2585	2290
BGC (10^{-11} m/W)	0.07	0.12	0.11	1.05
BGC (in dB, relative to SMF-28™)	-15.35	-13.01	-13.39	-3.6
RGC (relative to SiO_2)	0.82	0.69	0.61	-

[a]: Value at the core center.

[b]: Calculated from the additive model.

[c]: Waveguide attenuation coefficient contribution is calculated.

[d]: Calculated from EDX.

[e]: MgAlSi, CaAlSi, SrAlSi, and BaAlSi have initial precursor composition (molar ratio) of 5AEO-8Al_2O_3. SrAlSi fiber from [15] is reported here for comparison with its AEO-Al_2O_3-derived optical fiber analogs.

[f]: Precursor material purities: Al_2O_3 (99.997%), MgO (99.998%), CaO(99.998%), SrO(99.9%), BaO(99.99%).

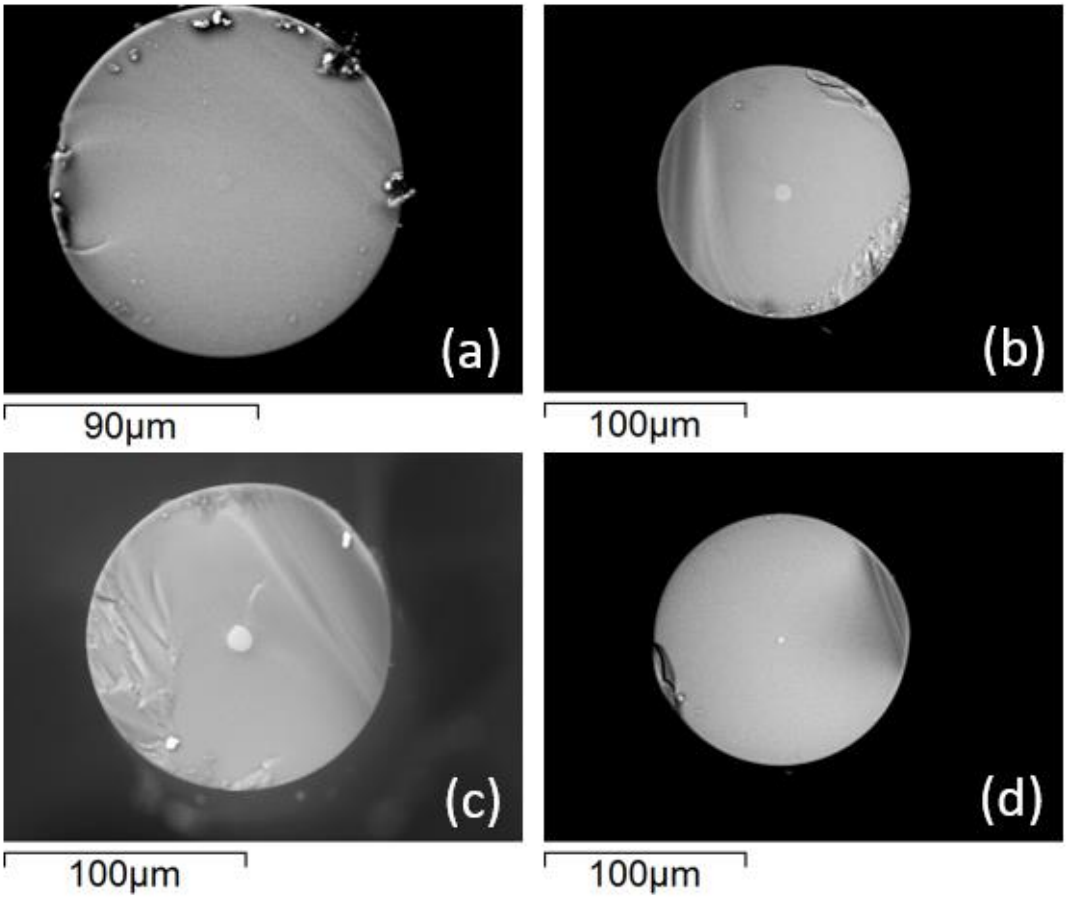

SEM micrographs of MgAlSi (a), CaAlSi (b), SrAlSi (c), and BaAlSi (d) optical fiber segments.

Properties of alkaline earth fluoro-aluminosilicate and fluoro-silicate fibers.

Fiber properties	**CaAlSi-F A**	**CaAlSiF B**	**BaF**
T_{draw} (°C)	**2000**	**2000**	**2000**
Optical Wavelength (nm), Brillouin Scattering Measurements	1534	1534	1534
Δn^a ($\times 10^{-3}$)	34.974	34.866	16.90
Mode Index, n_m (1534 nm); room temp. and zero strain[b]	1.4703	1.4660	1.4500
Mode Field Diameter (μm)	5.685	4.849	6.105
Attenuation Coefficient (dB/m) at 1534 nm[g]	0.42	0.46	1.19
ν (GHz)	11.494	11.481	10.659
V (m/s) (acoustic mode value)	5996	6007	5638
$[Al_2O_3]^{a,d}$ mole%	4.68	3.66	-
$[AEO]^{a,d}$ mole%	4.11	5.38	2.32
$[AEF_2]^{a,d}$ mole%	8.86	4.87	1.12
Thermal Coefficient (MHz/K)	0.528	0.527	0.973
TOC (10^{-6} K^{-1})	6.0	5.9	8.0
Strain Coefficient (GHz/ε)	32.5	35.2	42.7
Δν (MHz)	50.0	56.0	34.0
$\Delta\nu_{intrinsic}$ (MHz)[c]	37.9	35.1	34.0
BGC (10^{-11} m/W)[f]	0.67	0.72	0.80
BGC (in dB, relative to SMF-28™)	-5.54	-5.23	-4.77

[a]: Value at the core center.

[b]: Calculated from the additive model.

[c]: Waveguide attenuation coefficient contribution is calculated.

[d]: Calculated from EDX.

[e]: MgAlSi, CaAlSi, SrAlSi, and BaAlSi have initial precursor composition (molar ratio) of $5AEO\text{-}8Al_2O_3$. SrAlSi fiber from [15] is reported here for comparison with its $AEO\text{-}Al_2O_3$-derived optical fiber analogs.

[f]: BaF fiber BGC material is probably not reliable due to a higher order acoustic mode hiding beneath the instrument peak, and therefore BGC value is likely to be slightly higher. For CaAlSiF A and B segments, there is excitation of higher order optical modes. Once this happens, estimates of BGC are no longer fully reliable. The calculation above assumes that the Brillouin spectrum accounts for all the optical power (no loss of higher order optical modes when going back into the measurement system).

[g]: Precursor material purities: Al_2O_3 (99.997%), BaF_2 (99.998%), CaF_2 (99.99%).

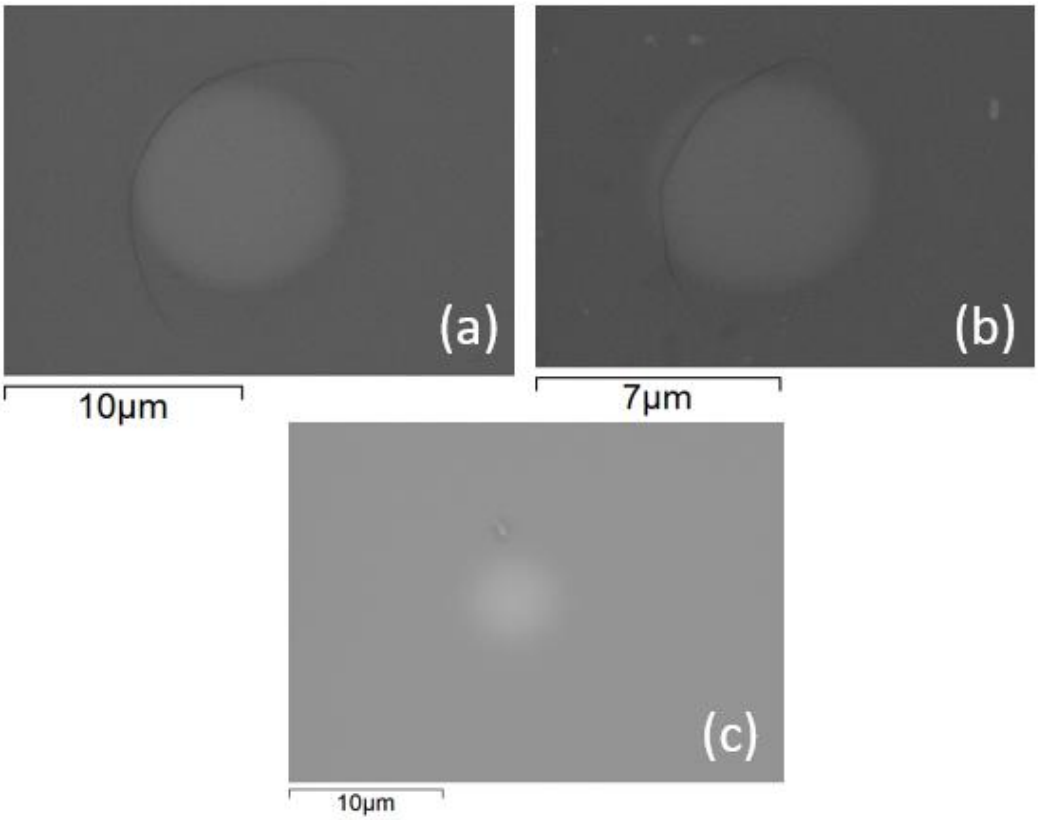

SEM micrographs of CaAlSiF A (a), CaAlSiF B (b), and BaF (c) fiber cores.

Appendix VI. 2. Composition and Refractive index profiles, and SEM micrograph of fiber cores

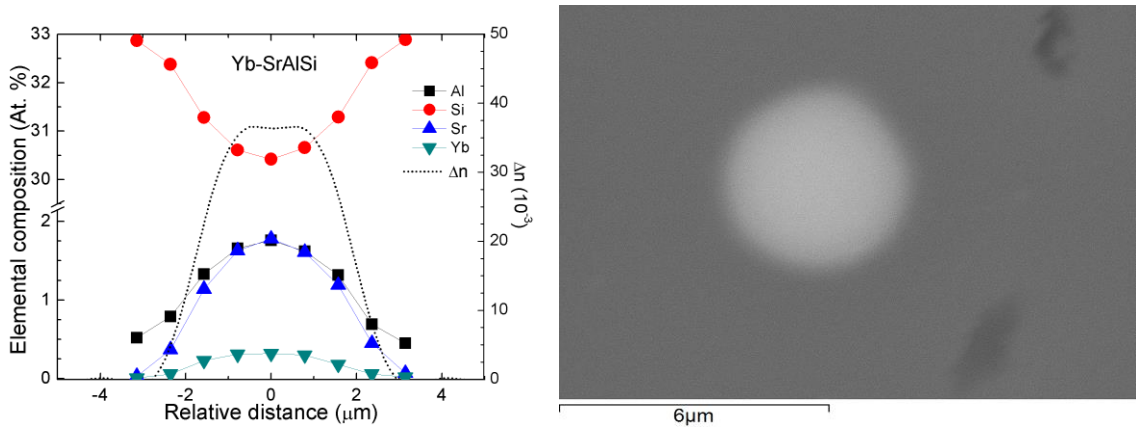

Elemental composition and refractive index radial profiles, along with SEM micrograph of the Yb-SrAlSi fiber segment. Not shown for reasons of clarity is the oxygen concentration, %O. However, %O (At. %) = 100 – [%F + %Sr + %Al + %Si].

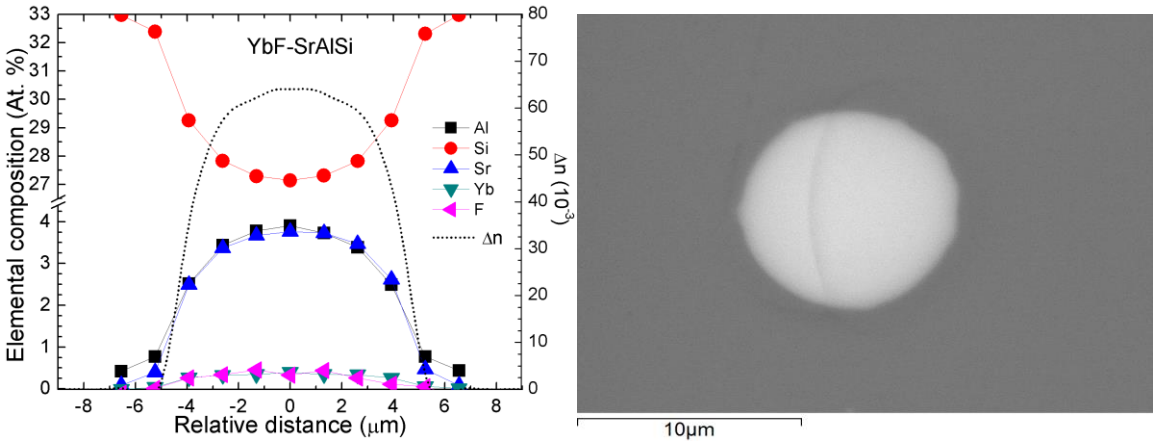

Elemental composition and refractive index radial profiles, along with SEM micrograph of the YbF-SrAlSi fiber segment. Not shown for reasons of clarity is the oxygen concentration, %O. However, %O (At. %) = 100 – [%F + %Sr + %Al + %Si].

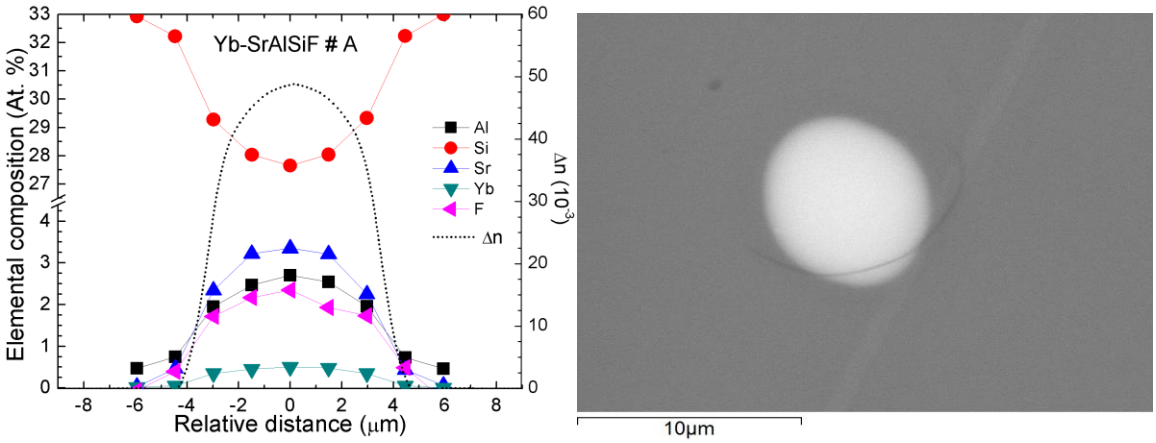

Elemental composition and refractive index radial profiles, along with SEM micrograph of the Yb-SrAlSiF A fiber segment.

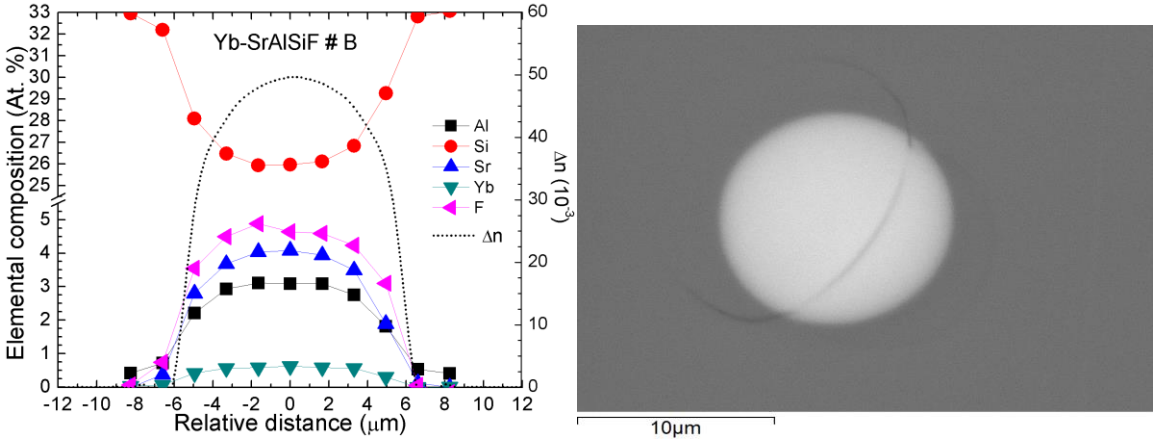

Elemental composition and refractive index radial profiles, along with SEM micrograph of the Yb-SrAlSiF B fiber segment.

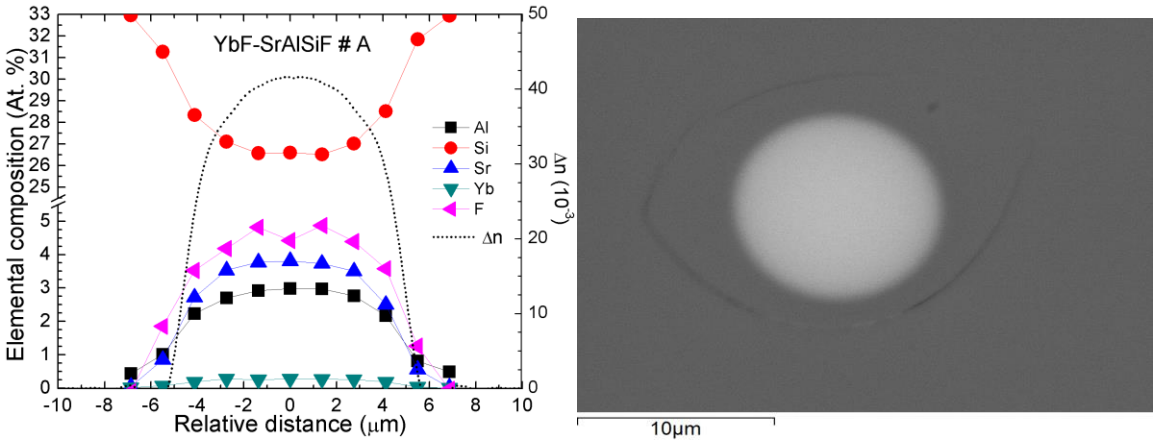

Elemental composition and refractive index radial profiles, along with SEM micrograph of the YbF-SrAlSiF A fiber segment. Not shown for reasons of clarity is the oxygen concentration, %O. However, %O (At. %) = 100 – [%F + %Sr + %Al + %Si].

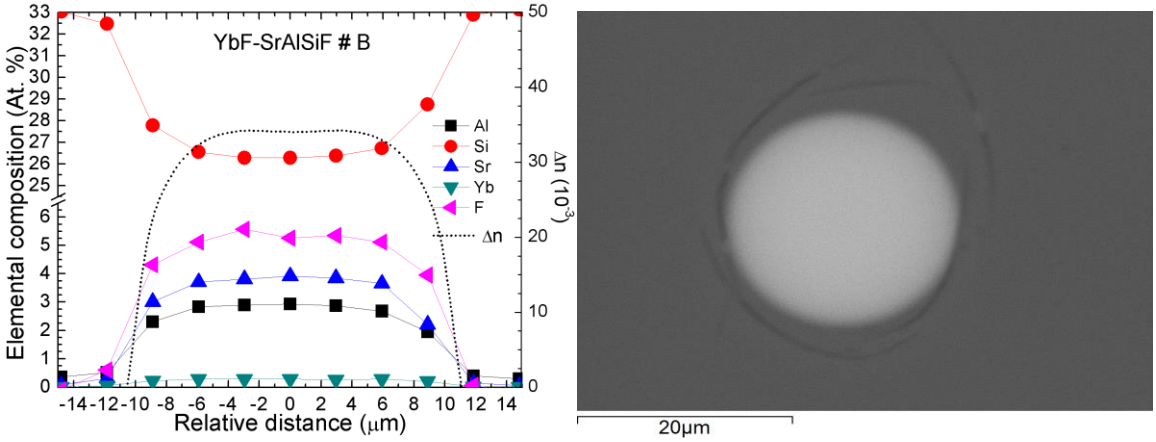

Elemental composition and refractive index radial profiles, along with SEM micrograph of the YbF-SrAlSiF B fiber segment. Not shown for reasons of clarity is the oxygen concentration, %O. However, %O (At. %) = 100 – [%F + %Sr + %Al + %Si].

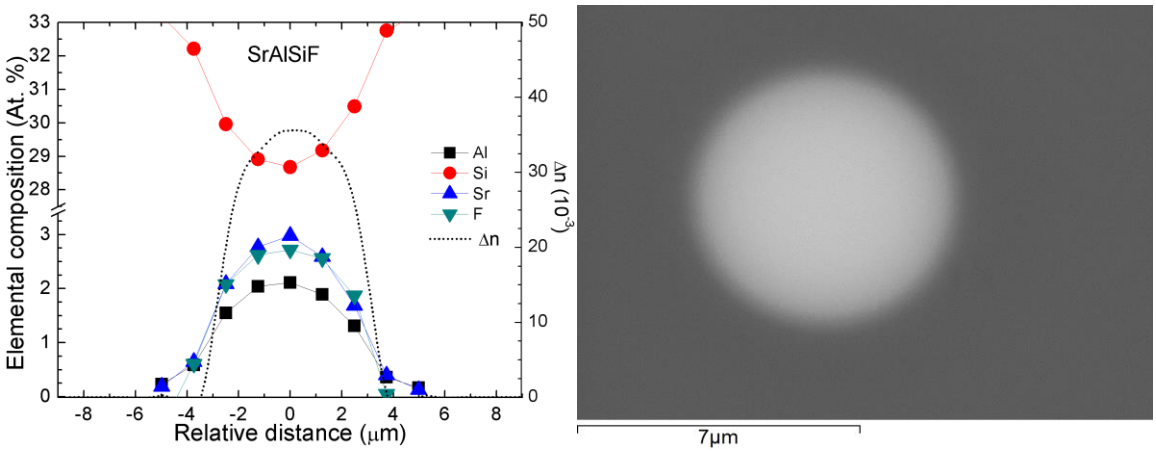

Elemental composition and refractive index radial profiles, along with SEM micrograph of the SrAlSiF fiber segment. Not shown for reasons of clarity is the oxygen concentration, %O. However, %O (At. %) = 100 – [%F + %Sr + %Al + %Si].

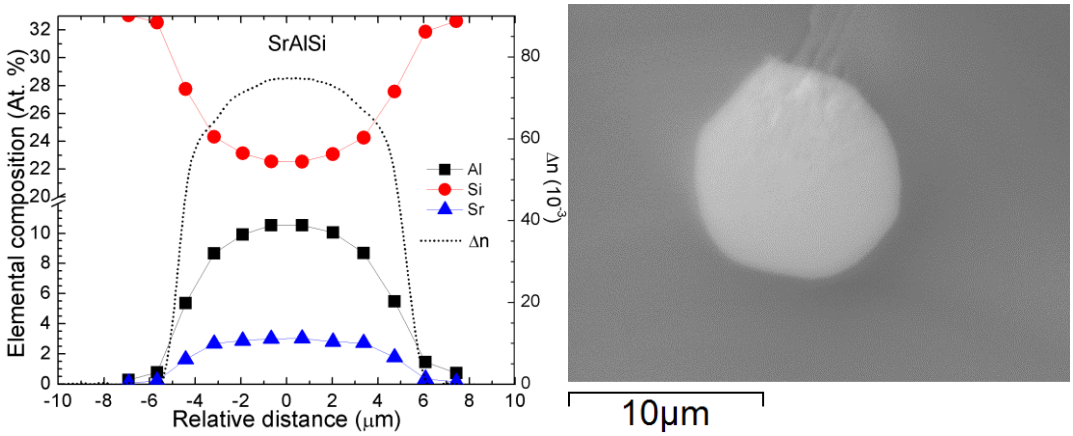

Elemental composition and refractive index radial profiles, along with SEM micrograph of the SrAlSi fiber segment. Not shown for reasons of clarity is the oxygen concentration, %O. However, %O (At. %) = 100 – [%F + %Sr + %Al + %Si].

Appendix VI. 3. Matlab code used to compute n(SrF_2)

```
clear all; close all;
%%%%%%%%%%%%% calculation of n(SrF2) %%%%%%%%%%
MS=60.08; rhoS=2200; nS=1.444; %SiO2
MA=101.96; rhoA=3350; nA=1.653; %Al2O3
MSr=103.62; rhoSr=4015; nSr=1.81; %SrO
MY=394.08; rhoY=8102; nY=1.881; %Yb2O3
MSrF2=125.62; rhoSrF2=4240; %rhoSrF2=2580; %rhoSrF2=3980; %SrF2

n=1.444+41.5*10^-3; %refractive index
srf2=8.11; %mole percent of SrF2
sr=5.87; %mole percent of SrO
y=0.51; %mole percent of Yb2O3
a=5.47; %mole percent of Al2O3
s=100-srf2-sr-y-a; %mole percent of SiO2

syms nSrF2

volS=(s*MS/rhoS)/(s*MS/rhoS+a*MA/rhoA+sr*MSr/rhoSr+y*MY/rhoY+srf2*MSrF2/rhoSr
F2);
volA=(a*MA/rhoA)/(s*MS/rhoS+a*MA/rhoA+sr*MSr/rhoSr+y*MY/rhoY+srf2*MSrF2/rhoSr
F2);
volSr=(sr*MSr/rhoSr)/(s*MS/rhoS+a*MA/rhoA+sr*MSr/rhoSr+y*MY/rhoY+srf2*MSrF2/r
hoSrF2);
volY=(y*MY/rhoY)/(s*MS/rhoS+a*MA/rhoA+sr*MSr/rhoSr+y*MY/rhoY+srf2*MSrF2/rhoSr
F2);
volSrF2=(srf2*MSrF2/rhoSrF2)/(s*MS/rhoS+a*MA/rhoA+sr*MSr/rhoSr+y*MY/rhoY+srf2
*MSrF2/rhoSrF2);
v=volS+volA+volSr+volY+volSrF2;

S=vpasolve(n==volS*nS+volA*nA+volSr*nSr+volY*nY+volSrF2*nSrF2, nSrF2)
```

Code (Matlab) to calculate n(a-SrF_2): As an example, entering fiber composition at the core center for fiber segment YbF-SrAlSiF A and assuming a density of 4240 kg/m^3 gives an estimated index for a-SrF_2 of 1.5015.

Appendix VI. 4. Spectroscopic properties of oxyfluoride glasses

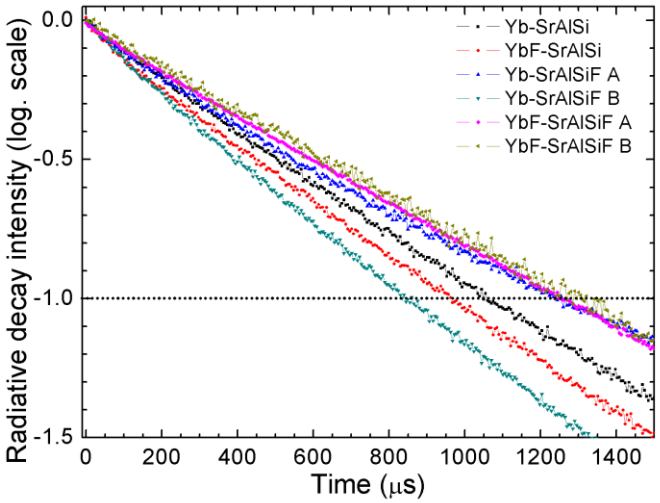

Radiative lifetime for Yb-doped glass optical fibers (see Table VI.2 for compositional details)

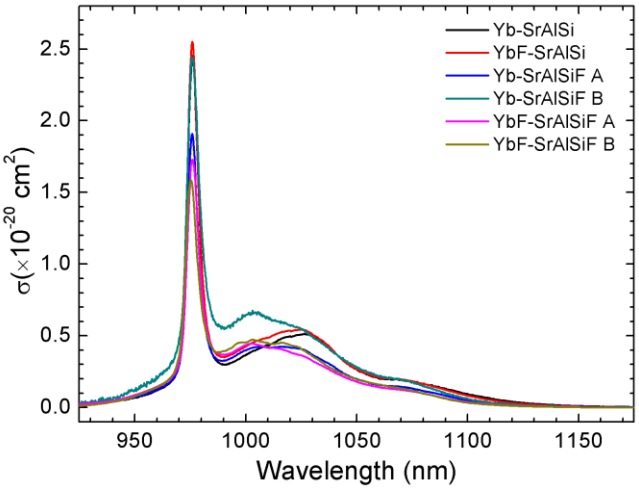

Emission cross section (σ) for Yb-doped fiber segments.

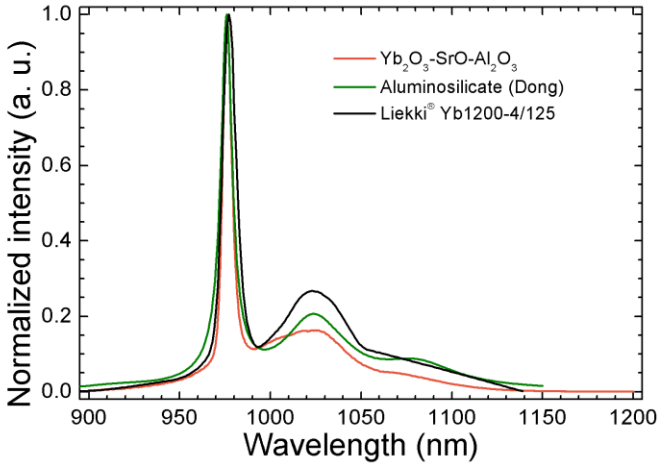

Normalized emission spectra in aluminosilicates fibers vs. strontium aluminosilicate system (Dong [58] **and Yb-doped LIEKKI® fiber).**

VI. K. References

[1] A. D. Yablon, “Multi-wavelength optical fiber refractive index profiling by spatially resolved fourier transform spectroscopy,” *J. Light. Technol.*, vol. 28, no. 4, pp. 360–364, 2010.

[2] P. D. Dragic *et al.*, “Single- and few-moded lithium aluminosilicate optical fiber for athermal Brillouin strain sensing.,” *Opt. Lett.*, vol. 40, no. 21, pp. 5030–3, 2015.

[3] A. D. Yablon and J. Jasapara, “Hyperspectral optical fiber refractive index measurement spanning 2.5 octaves,” *Proc. SPIE*, vol. 8601, p. 86011V–86011V–6, 2013.

[4] M. D. O’Donnell *et al.*, “Raman gain of selected tellurite glasses for IR fibre lasers calculated from spontaneous scattering spectra,” *Opt. Mater.*, vol. 30, no. 6, pp. 946–951, 2008.

[5] G. P. Agrawal, *Nonlinear Fiber Optics*, 2nd ed. Academic Press, 1995.

[6] P. Dragic, C. Kucera, J. Furtick, J. Guerrier, T. Hawkins, and J. Ballato, “Brillouin spectroscopy of a novel baria-doped silica glass optical fiber,” *Opt. Express*, vol. 21, no. 9, pp. 10924–10941, 2013.

[7] P. D. Dragic, “The Acoustic Velocity of Ge-Doped Silica Fibers: A Comparison of Two Models,” *Int. J. Appl. Glas. Sci.*, vol. 1, no. 3, pp. 330–337, 2010.

[8] P. Law, A. Croteau, and P. D. Dragic, “Acoustic coefficients of P_2O_5-doped silica fiber : the strain-optic and strain-acoustic coefficients,” *Opt. Mater. Express*, vol.

1, no. 4, pp. 686–699, 2011.

[9] P. Dragic, M. Cavillon, and J. Ballato, “On the thermo-optic coefficient of P_2O_5 in SiO_2,” *Opt. Mater. Express*, vol. 7, no. 10, pp. 3654–3661, 2017.

[10] J. Dong, M. Bass, Y. Mao, P. Deng, and F. Gan, “Dependence of the Yb^{3+} emission cross section and lifetime on temperature and concentration in yttrium aluminum garnet,” *J. Opt. Soc. Am. B*, vol. 20, no. 9, p. 1975, 2003.

[11] M. J. Weber, D. C. Ziegler, and C. A. Angell, “Tailoring stimulated emission cross sections of Nd^{3+} laser glass: Observation of large cross sections for $BiCl_3$ glasses,” *J. Appl. Phys.*, vol. 53, no. 6, pp. 4344–4350, 1982.

[12] J. Ballato *et al.*, “On the fabrication of all-glass optical fibers from crystals,” *J. Appl. Phys.*, vol. 105, no. 5, 2009.

[13] P. Law, Y. Liu, A. Croteau, and P. D. Dragic, “Acoustic coefficients of P_2O_5-doped silica fiber: acoustic velocity, acoustic attenuation, and thermo-acoustic coefficient,” *Opt. Mater. Express*, vol. 1, no. 4, p. 686, 2011.

[14] M. Cavillon *et al.*, “Oxyfluoride core silica-based optical fiber with intrinsically low nonlinearities for high energy laser applications,” *J. Light. Technol.*, no. 99, 2017.

[15] M. Cavillon *et al.*, “Brillouin Properties of a Novel Strontium Aluminosilicate Glass Optical Fiber,” vol. 34, no. 6, pp. 1435–1441, 2016.

[16] M. Środa and Z. Olejniczak, “19F MAS-NMR studies of strontium oxyfluoride aluminosilicate glass,” *J. Mol. Struct.*, vol. 1001, no. 1–3, pp. 78–82, 2011.

[17] M. Środa and C. Paluszkiewicz, “The structural role of alkaline earth ions in

oxyfluoride aluminosilicate glasses-Infrared spectroscopy study," *Vib. Spectrosc.*, vol. 48, no. 2, pp. 246–250, 2008.

[18] P. D. Dragic, J. Ballato, S. Morris, and T. Hawkins, "The Brillouin gain coefficient of Yb-doped aluminosilicate glass optical fibers," *Opt. Mater. (Amst).*, vol. 35, no. 9, pp. 1627–1632, 2013.

[19] A. Koike and N. Sugimoto, "Temperature dependences of optical path length in fluorine-doped silica glass and bismuthate glass," vol. 6116, no. 3, pp. 1–8, 2006.

[20] J. W. Fleming and D. L. Wood, "Refractive index dispersion and related properties in fluorine doped silica.," *Appl. Opt.*, vol. 22, p. 3102, 1983.

[21] L. R. M. Marcos *et al.*, "Optical constants of SrF_2 thin films in the 25-780-eV spectral range," *J. Appl. Phys.*, vol. 113, no. 14, 2013.

[22] M. J. Weber, *Handbook of optical materials*. CRC Press, 2003.

[23] A. Feldman, D. Horowitz, R. M. Waxler, and M. J. Dodge, "Optical Materials Characterization Final Technical Report February 1, 1978 - September 30, 1978," Washington D. C., 1978.

[24] H. M. Presby and I. P. Kaminow, "Binary silica optical fibers: refractive index and profile dispersion measurements," *Appl. Opt.*, vol. 15, no. 12, pp. 3029–3036, 1976.

[25] M. Weber, D. Milam, and W. Smith, "Nonlinear refractive index of glasses and crystals," *Opt. Eng.*, vol. 17, no. 5, pp. 463–469, 1978.

[26] R. Adair, L. L. Chase, and S. A. Payne, "Nonlinear refractive index of optical crystals," *Phys. Rev. B*, vol. 39, no. 5, pp. 3337–3350, 1989.

[27] P. Dragic, M. Cavillon, and J. Ballato, “The linear and nonlinear refractive index of amorphous Al_2O_3 deduced from aluminosilicate optical fibers,” *Submitt. to Int. J. Appl. Glas. Sci.*, 2017.

[28] D. Milam, M. J. Weber, and A. J. Glass, “Nonlinear refractive index of fluoride crystals,” *Appl. Phys. Lett.*, vol. 31, no. 12, pp. 822–825, 1977.

[29] V. Dimitrov and S. Sakka, “Linear and nonlinear optical properties of simple oxides. II,” *J. Appl. Phys.*, vol. 79, no. 3, p. 1741, 1996.

[30] R. Adair, L. L. Chase, and S. a. Payne, “Nonlinear refractive-index measurements of glasses using three-wave frequency mixing,” *J. Opt. Soc. Am. B*, vol. 4, no. 6, p. 875, 1987.

[31] N. Boling, A. J. Glass, and A. Owyoung, “Empirical Relationships for Predicting Nonlinear Refractive Index Changes in Optical Solids,” *IEEE J. Quantum Electron.*, vol. 14, no. 8, p. 608, 1978.

[32] G. E. Pynchonf and E. F. Sieckmann, “Refractive Index of Strontium Oxide,” pp. 595–597, 1966.

[33] P. Eskola, “The silicates of strontium and barium,” *American Journal of Science*, vol. 4, no. 23. pp. 331–375, 1922.

[34] I. H. Malitson, “Interspecimen Comparison of the Refractive Index of Fused Silica,” *J. Opt. Soc. Am.*, vol. 55, no. 10, p. 1205, 1965.

[35] N. Boling, A. Glass, and A. Owyoung, “Empirical relationships for predicting nonlinear refractive index change in optical solids,” *IEEE J. Quantum Electron.*, vol. 14, no. 8, pp. 601–608, 1978.

[36] L. Prod'homme, "A new approach to the thermal change in the refractive index of glasses," *Phys. Chem. Glas.*, vol. 1, no. 4, pp. 119–122, 1960.

[37] R. B. Roberts and G. K. White, "Thermal expansion of fluorites at high temperatures," *J. Phys. C Solid State Phys.*, vol. 19, pp. 7167–7172, 2000.

[38] J. Ballato and P. Dragic, "Materials development for next generation optical fiber," *Materials (Basel).*, vol. 7, no. 6, pp. 4411–4430, 2014.

[39] P. D. Dragic and J. Ballato, "Characterisation of Raman gain spectra in Yb:YAG-derived optical fibres," *Electron. Lett.*, vol. 49, no. 14, pp. 895–897, 2013.

[40] K. C. Crouch, R. B. Rayment, and G. W. Marks, "Elastic Properties of Fluorides of Groups IA and IIA," *Final Rep. ZR 011 01 01 (NELC Z1), Nav. Undersea Warf. Center, DTIC Doc. # 848978*, 1968.

[41] B. Ghebouli, M. A. Ghebouli, M. Fatmi, and M. Benkerri, "First-principles calculations of structural, elastic, electronic and optical properties of XO (X=Ca, Sr and Ba) compounds under pressure effect," *Mater. Sci. Semicond. Process.*, vol. 13, no. 2, pp. 92–101, 2010.

[42] P. Dragic and J. Ballato, "Pockels' coefficients of alumina in aluminosilicate optical fiber," *J. Opt. Soc. Am.*, vol. 30, no. 2, pp. 244–250, 2013.

[43] T. Horiguchi, T. Kurashima, and M. Tateda, "Tensile Strain Dependence of Brillouin Frequency Shift in Silica Optical Fibers," *IEEE Photonics Technol. Lett.*, vol. 1, no. 5, pp. 107–108, 1989.

[44] A. D. Yablon *et al.*, "Refractive index perturbations in optical fibers resulting from frozen-in viscoelasticity," *Appl. Phys. Lett.*, vol. 84, no. 1, pp. 19–21, 2004.

[45] P.-C. Law and P. D. Dragic, “Wavelength dependence of the Brillouin spectral width of boron doped germanosilicate optical fibers.,” *Opt. Express*, vol. 18, no. 18, pp. 18852–65, 2010.

[46] A. Bertholds and R. Dandliker, “Determination of the individual strain optic coeficients in single-mode optical fibers,” *J. Light. Technol.*, vol. 6, no. 1, pp. 17–20, 1988.

[47] A. J. Barlow and D. N. Payne, “The Stress-Optic Effect in Optical Fibers,” *Quantum Electronics*, no. 5. pp. 834–839, 1983.

[48] N. Kashima, T. Kawashima, and S. Miyauchi, “Wavelength dependence of stress-induced time of flight variations in graded-index multimode fibers,” *Optical Fiber Technology*, vol. 25. pp. 7–12, 2015.

[49] P. Dragic, T. Hawkins, P. Foy, S. Morris, and J. Ballato, “Sapphire-derived all-glass optical fibres,” *Nat. Photonics*, vol. 6, no. 9, pp. 629–635, 2012.

[50] P. Dragic *et al.*, “Mass density and the Brillouin spectroscopy of aluminosilicate optical fibers,” *Opt. Mater. Express*, vol. 2, no. 11, p. 1641, 2012.

[51] M. N. Zervas and C. A. Codemard, “High Power Fiber Lasers: A Review,” *IEEE J. Sel. Top. Quantum Electron.*, vol. 20, no. 5, pp. 1–23, 2014.

[52] A. S. Pinheiro *et al.*, “Laser performace parameters of Yb^{3+} doped UV-transparent phosphate glasses,” *Chem. Phys. Lett.*, vol. 592, pp. 164–169, 2014.

[53] M. Weber, J. Lynch, D. Blackburn, and D. Cronin, “Dependence of the stimulated emission cross section of Yb^{3+} on host glass composition,” *Quantum Electron. IEEE J.*, vol. 19, no. 10, pp. 1600–1608, 1983.

[54] Z. Lin, H. Zeng, Y. Yang, X. Liang, G. Chen, and L. Sun, “The effect of fluorine anions on the luminescent properties of Eu-Doped oxyfluoride aluminosilicate,” *J. Am. Ceram. Soc.*, vol. 93, no. 10, pp. 3095–3098, 2010.

[55] L. D. DeLoach, S. A. Payne, L. L. Chase, L. K. Smith, W. L. Kway, and W. F. Krupke, “Evaluation of Absorption and Emission Properties of Yb^{3+} Doped Crystals for Laser Applications,” *IEEE J. Quantum Electron.*, vol. 29, no. 4, pp. 1179–1191, 1993.

[56] J. L. Doualan, P. Camy, A. Benayad, M. Von Edlinger, V. Ménard, and R. Moncorgé, “Spectroscopic and laser properties of Yb^{3+} doped CaF_2 , SrF_2 and BaF_2 laser crystals,” in *Advanced Solid State Laser*, 2008.

[57] R. Paschotta, J. Nilsson, P. R. Barber, J. E. Caplen, A. C. Tropper, and D. C. Hanna, “lifetime quentching in Yb-doped fibers,” *Opt. Commun.*, vol. 136, pp. 375–378, 1997.

[58] S. Suzuki, H. a McKay, X. Peng, L. Fu, and L. Dong, “Highly ytterbium-doped silica fibers with low photo-darkening.,” *Opt. Express*, vol. 17, no. 12, pp. 9924–9932, 2009.

CHAPTER VII.

PRESENT CHALLENGES AND FUTURE PERSPECTIVES IN THE DEVELOPMENT OF OXYFLUORIDE GLASS OPTICAL FIBERS

VII. A. Introduction

In the previous chapters, oxyfluoride fibers using the molten core method have been successfully fabricated and characterized. These fibers have shown property values that drive reductions in optical nonlinearities. However, further remaining challenges have been identified as necessary to be overcome in order to develop fibers for practical use.

At first, attenuation losses of the fabricated fibers are measured to be between approximately 0.4 to 3.7 dB/m at 1534 nm. The fibers do not necessarily need to exhibit the low loss levels achieved by telecom optical fibers as the fiber length needed for high power applications are typically in the tens of meters range. However, lower attenuation losses would greatly improve heat management or lasing efficiency. Origins of these losses are discussed and solutions to further reduce them proposed.

Additionally, developing fibers with a higher dopant concentration in the glass silicate core is beneficial to further mitigate optical nonlinearities through the material approach adopted in this dissertation, but also to enable the study of properties in not yet explored glass fiber core compositions. As the molten core method is an adequate fiber

fabrication process to fabricate such unconventional compositions, a way in developing those highly doped core is proposed, which consists in starting with denser precursor materials. Challenges that arise from the fabrication of highly doped silicate cores, e.g., the necessity to reduce crack formation at the fiber core/cladding interface, are also discussed.

Finally, the potential in combining alkaline earth fluorides (AEF_2) as starting materials using the molten core technique to enable greater fiber property tunability is addressed.

VII. B. Origins of losses in the fabricated fibers and approaches to mitigate them

The attenuation losses in the fibers investigated throughout this dissertation (in the dB/m range) are substantially higher than typical losses found for telecommunication applications (<0.2 dB/km). As the typical fiber lengths required for high energy laser applications do not generally exceed tens of meters [1], ultra-low losses are not as critical as for long haul telecom applications. However, heat-induced effects can lead to the deterioration of the optical system considered (e.g., thermal fracture, melting of the core [2]). Therefore, fibers with reduced attenuation losses are necessity to render the fabricated fibers more practical.

Here some insights in to the origins of the attenuation losses are given, and solutions to reduce them proposed. In Chapter I, scattering phenomena (e.g., “classical” Rayleigh,

Brillouin, Raman) that contribute to fiber loss have been described. In addition to these scattering phenomena, ultraviolet (UV) and infrared (IR) absorption losses also participate to the total fiber loss. Finally, waveguide imperfections, and presence of impurities (e.g., OH hydroxyl group or transition metals) also lead to further attenuation of the light propagating inside the fiber core [3–5].

Table VII.1. Attenuation coefficient (α, in dB/m, at 1534 nm) and averaged material precursor purity for aluminosilicate fibers investigated in Chapters V and VI.

Fiber	α (dB/m, at 1534 nm)	Averaged material precursor purity[a]
Yb-SrAlSi	0.78	99.92799
YbF-SrAlSi	2.08	99.92754
Yb-SrAlSiF A	2.85	99.99211
Yb-SrAlSiF B	2.66	99.99211
YbF-SrAlSiF A	0.52	99.99166
YbF-SrAlSiF B	0.46	99.99166
SrAlSiF	0.65	99.99175
SrAlSi	2.68	99.95969
CaAlSiF A	0.42	99.99175
CaAlSiF B	0.46	99.99175
BaF	1.19	99.99800
MgAlSi	1.02	99.99738
CaAlSi	1.93	99.99738
BaAlSi	3.64	99.99431

[a]: Precursor purities: SrO (99.9%), SrF_2 (99.99%), Yb_2O_3 (99.999%), YbF_3 (99,99%), Al_2O_3 (99.997%), CaO (99.998%), MgO (99.998%), BaO (99.99%), BaF_2 (99.998%), SiO_2 glass cladding (Heraeus, CFQ 099). Starting material precursors and ratios can be found in Chapter VI, Table VI.1, and Appendix VI.1).

In Table VII.1 are summarized the attenuation coefficients for some fiber segments characterized in this dissertation, along with the averaged (from molar ratios) purity of the starting precursor materials. Remarkably, the attenuation coefficients measured herein are in the same order of magnitude of what is reported in [6–11], and this for very different systems, comprising SiO_2, Al_2O_3, La_2O_3, Y_2O_3, BaO, SrO, MgO.

Then, the attenuation coefficients are plotted as a function of the averaged purity of the precursor materials in Fig. VII.1. Interestingly, no direct correlation between higher purity of the starting precursors and attenuation losses is found. This can be best seen when comparing Yb-SrAlSiF fiber segments A and B vs. YbF-SrAlSiF segments A and B. Both fibers contain the same precursor materials, with the exception that the former fiber contains Yb_2O_3 (99.999 % purity) and the second fiber contains YbF_3 (99.99 % purity). However, the starting precursor composition with the highest purity materials exhibit losses that are about 2 dB higher than that of the other fiber. In addition, Yb-SrAlSi fiber, which has SrO as a principal initial precursor material (75%), exhibits losses of only 0.78 dB/m, even when SrO purity is of 99.9%. If no direct trend between the precursor materials purity and attenuation losses is explicitly observable, one should be aware that many variables come into play which may hinder any precursor purity to attenuation coefficient correlation. For instance, the nature of the impurities influences fiber loss differently; as an example, each transition metal exhibits a different absorption cross section [4]. From the same reference, it is shown that at 15XX nm, 1 ppb (wt.%) of Cr or Co can contribute to 0.5 to 1 dB/km in the attenuation losses. Then, taking a powder such as SrF_2, which exhibits

a purity of 99.99%, present impurities in the order of 100 ppm, or 10^5 ppb. If 1 ppm (wt.%) of Cr is present as an impurity, it would account to ~0.8dB/m, which is very consequent. This example is here simply to pinpoint the critical influence the transition element impurities (and therefore material purity) on attenuation losses.

Furthermore, possible environmental contamination of some precursor mixtures during sample preparation could play a significant role, as suggested in [11], and especially when considering the impact of OH contamination [5]. Characteristic OH absorption peak is clearly observable for one baria-derived fiber [6] and YAG-derived fibers [8], both fabricated using the molten core method. It is worth mentioning than in [8,9], attenuation coefficients in the 0.1-0.3 dB/m range were achieved, and, consequently, starting with high purity precursor materials still remains essential in developing low loss fibers.

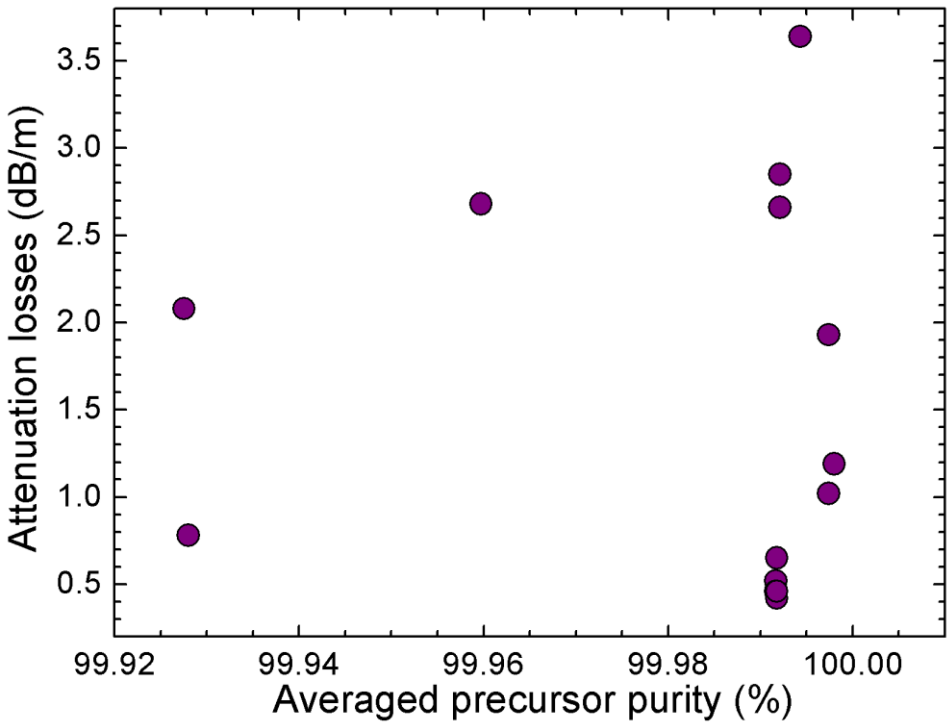

Figure VII.1. Attenuation losses (in dB/m) as a function of the averaged purity of the starting precursor materials (calculated from molar ratios) for the fiber segments listed in Table VII.1.

A second contribution to waveguide loss can arise from linear scattering (e.g., Rayleigh, Mie), due to the tendency of the alkaline earth silicate systems investigated herein to phase separate [12], which can result in some inhomogeneities in the glass core. It should be mentioned that no phase separation for the characterized fibers (Table VII.1) was detected by scanning electron microscopy (SEM) imaging. In order to observe if any nanoscale phase separation is present in these fibers that could not be easily detected with SEM, three fiber segments (Yb-SrAlSi, Yb-SrAlSiF A, and, YbF-SrAlSiF A) were investigated by transmission electron microscopy (TEM). These fiber segments were

chosen as they exhibit different attenuation coefficients but are of similar compositional nature. Each glass fiber core was core drilled using a Focused Ion and Electron Beam System (FIB-SEM HITACHI NB5000) and thinned down to ~100 nm thin layer. Then, each core slice was mounted on a TEM sample grid and analyzed with the help of a STEM HITACHI HD2000. The TEM micrographs at the core center and at the core clad interface of these fibers are summarized in Figs. VII.2, VII.3, and VII.4.

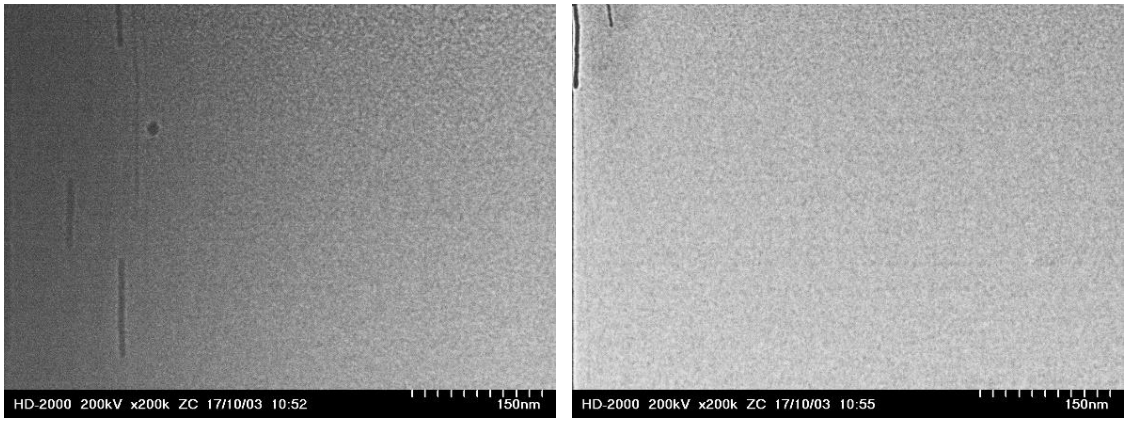

Figure VII.2. TEM micrographs at the core-cladding interface (left) and at the core center (right) for fiber Yb-SrAlSi (α=0.78 dB/m).

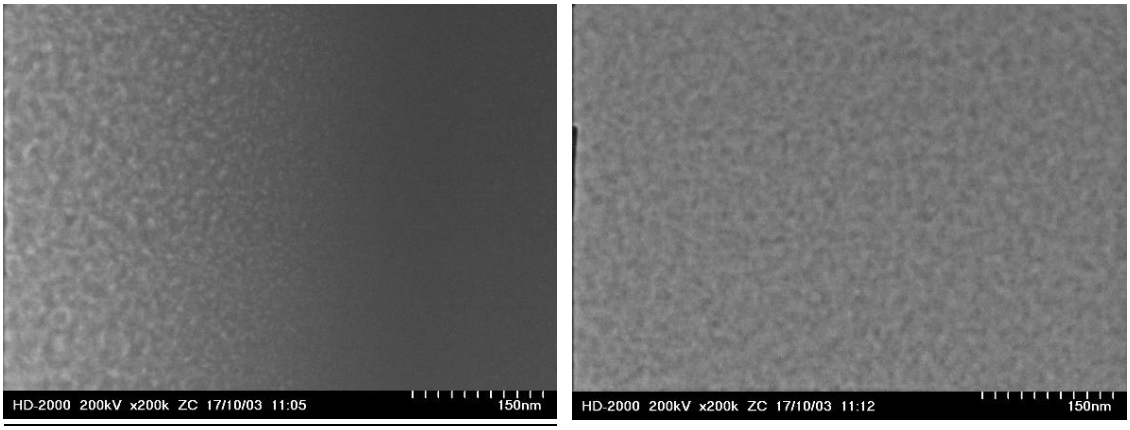

Figure VII.3. TEM micrographs at the core-cladding interface (left) and at the core center (right) for fiber YbF-SrAlSiF A (α=0.52 dB/m).

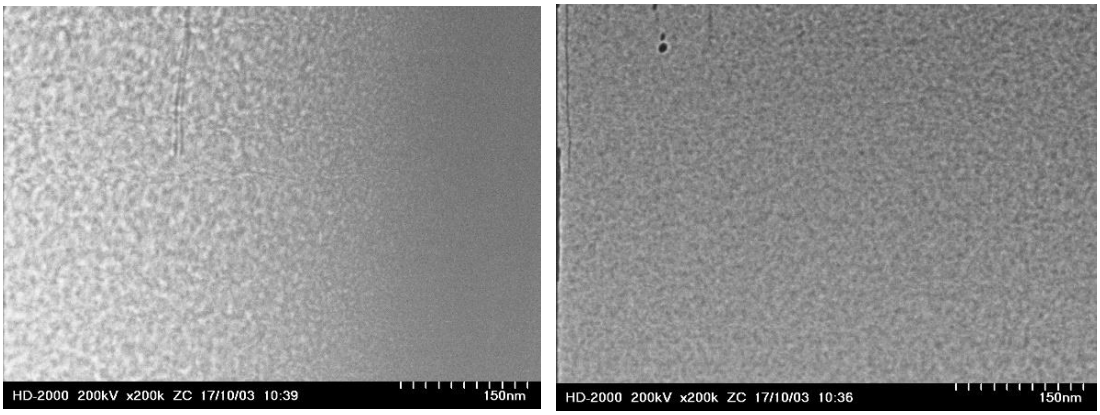

Figure VII.4. TEM micrographs at the core-cladding interface (left) and at the core center (right) for fiber Yb-SrAlSiF A (α=2.85 dB/m).

From TEM analysis, phase separation is clearly observed, especially at the core/cladding interface, but it differs from one fiber to another (note that on Figs. VII.2, VII.3, and VII.4, the magnification for the 6 micrographs is identical). These features are somewhat similar to findings in [11]. Interestingly, in the same paper, the authors pinpoint the preferential scattering of higher order modes at the core/clad interface, where the phase separation is enhanced and principally contributes to the attenuation coefficient. Yb-SrAlSiF A fiber segment (Fig. VII.4), which exhibits the most pronounced phase separation, also presents the highest attenuation losses (2.85 dB/m). The inhomogeneities are on the order of ~10-20 µm, but are not always well resolved at the core center, suggesting spinodal phase separation [13]. On the other hand, at the core/cladding interface, the phase separation is more resolved, characteristic of binodal phase separation. More on the phase separation morphology difference, which arises from the varying glass composition within the core, is discussed later. For completeness, Yb-SrAlSi fiber segment

(Fig. VII.2) exhibits much smaller inhomogeneities, whereas YbF-SrAlSiF A one (Fig. VII.3) shows larger but less coarse and pronounced phase separated regions compared to Yb-SrAlSiF A segment. The phase separated regions are < ×75 smaller in size than the 1534 nm wavelength used for attenuation measurements, and can typically result in Rayleigh scattering.

An attempt to quantify the amount of Rayleigh scattering that contributes to the attenuation coefficient in the Yb-SrAlSiF A fiber segment (Fig. VII.4) is performed. This segment is preferred as the phase separation is more distinct. Two models, reported in [14,15], are utilized to estimate the light attenuation due to Rayleigh scattering. The principal assumptions are that the scattering centers (i.e., the particles) are spherical and of equal refractive index. The matrix is silica (n=1.444 at 1.534 μm), and the particles have a refractive index of 1.444 + Δn, where Δn is the difference of the refractive index between the core and the cladding in that fiber. This assumption appears reasonable as most of the power would be focused at the core center. However, it should be noted that most of the inhomogeneities (considered here as particles) are not clearly resolved and not always spherical. Therefore, this succession of assumptions would certainly result in quite large uncertainties. Nevertheless, the attenuation coefficient as a function of particle size diameter is calculated using the two different models, and the results are display in Fig. VII.5. For completeness, the code utilized to perform the calculations is reported in Appendix VII.1.

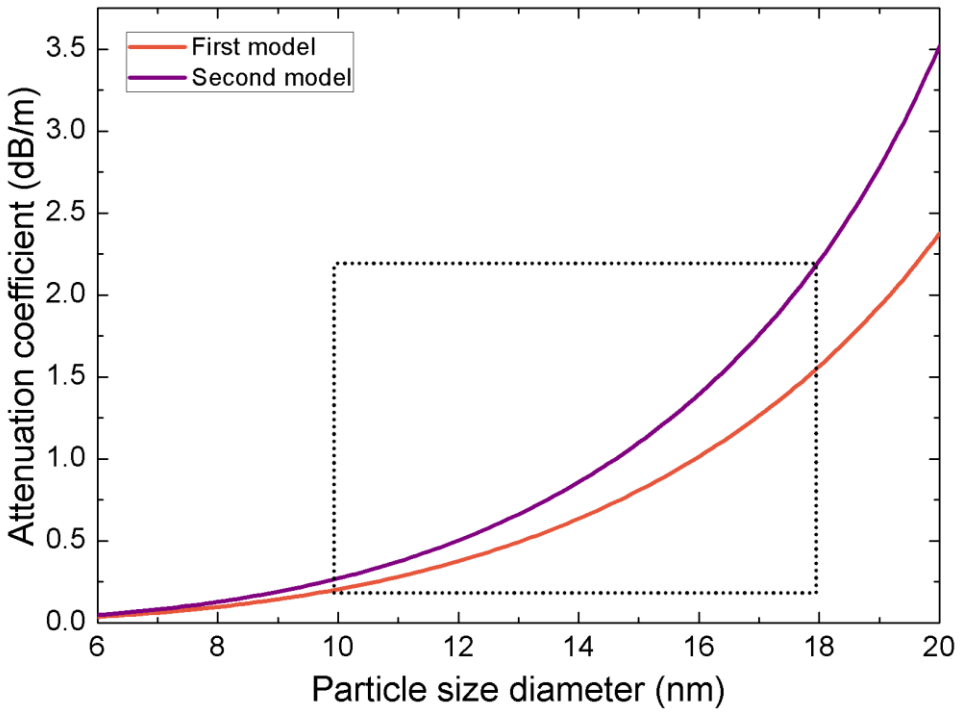

Figure VII.5. Estimation of attenuation coefficient (in dB/m) due to Rayleigh scattering as a function the particle size diameter (in nm), for Yb-SrAlSiF A fiber segment. The first model is taken from [15], and the second model from [14]. Parameters used for this estimation (other than the particle size diameter, which is varying), are given in the text and in Appendix VII.1, where the code is reported. The box is here to provide upper and lower boundaries of the estimated particle sizes, and, consequently, of the attenuation coefficient.

If both models give slightly different results, it should first be noted that for the particle size estimated based on Fig. VII.4 (here between 10 – 18 nm). The attenuation coefficient is calculated as between 0.25 – 2.25 dB/m, when the measured attenuation coefficient for this segment is 2.85 dB/m. The estimated contribution of Rayleigh scattering

to the attenuation coefficient for this fiber is in the same order of magnitude (dB/m) than the measured value and, accordingly, is believed to be one of the major contribution to total loss. However, even the upper attenuation coefficient limit (2.25 dB/m, from model 1, and 1.5 dB/m from model 2) is lower than the measured value of 2.85 dB/m. This suggests that Rayleigh scattering is not the only contributor to losses, and, as discussed previously, light absorption by impurities also plays an important role. It is worth mentioning that in Fig. VII.4, the morphology of the phase separation at the core center and at the core/cladding interface is quite different (in shape and size). To better observe the features, micrographs from Fig. VII.4 were colored in Black and White, then contrast was modified. These results are reported in Fig. VII.6.

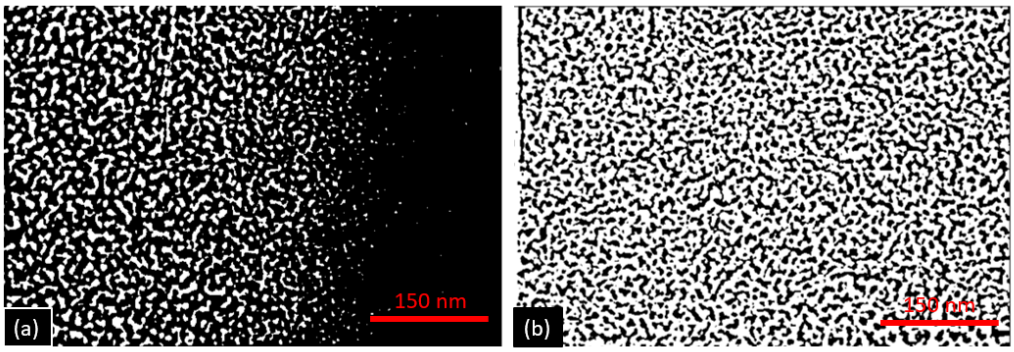

Figure 7.VII.6. TEM micrographs showing phase separation at the core-cladding interface (a) and at the core center (b) for Yb-SrAlSiF A fiber segment (Fig. VII.4). In white are the high index phase separated regions, and in black the silica matrix. The difference in morphology between the core center (spinodal) and the core/cladding interface (binodal) is clearly identifiable.

Higher index phase separated regions are shown in white, and the silica matrix in black. As mentioned previously, the change in morphology of the phase separated regions is clearly visible: at the core center, the phase separation is spinodal, when at the core/cladding interface it is principally binodal.

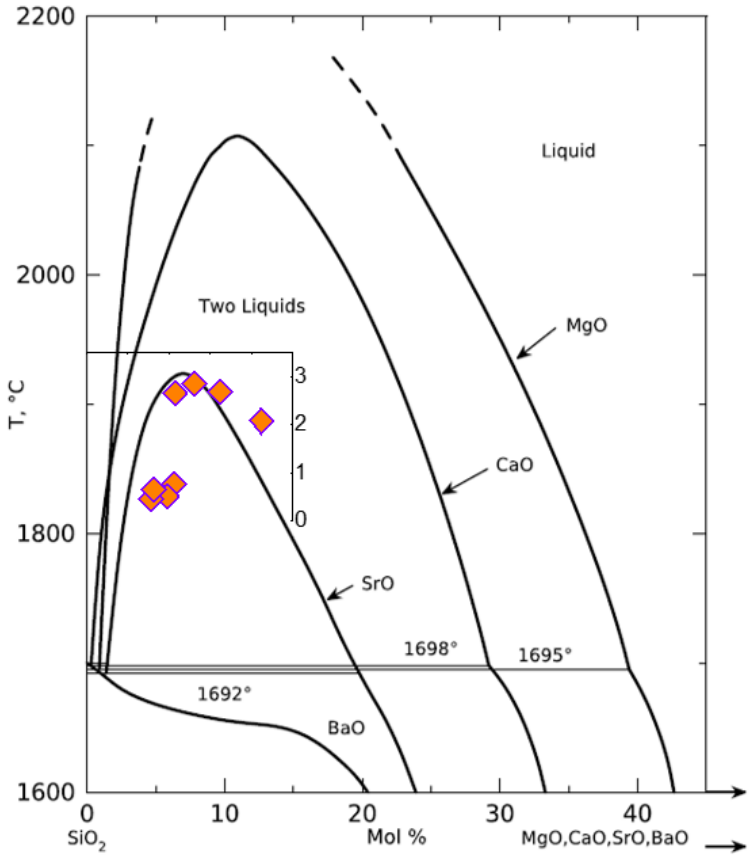

Figure VII.7. Liquid-liquid immiscibility region in binary alkaline earth silicate systems, taken from [16]. Overlapped on this graph are the attenuation losses (Y-axis, in dB/m) for the strontium containing fibers reported in Table VII.1 as a function of SrO concentration (X axis, in mole %). The SrO concentration of each investigated system can be found in Chapter VI.

Interestingly, the attenuation losses for the present fibers seem to follow the immiscibility dome of the SrO-SiO_2 system. Yb-SrAlSiF A fiber segment is composed of ~6.7 mole % of SrO, which corresponds to the maximum of the LLIR in a SrO-SiO_2 binary system. Furthermore, this fiber exhibits a spinodal phase separation at the core center (Fig. VII.6b), which comforts the relation that exists between LLIR and loss attenuation. As the composition moves away from the center of the LLIR, as it is the case in this fiber as one approaches the core/cladding interface (higher SiO_2 content), the phase separation is expected to become more binodal, as visible from Fig. VII.6a.

This observation again suggests that the inhomogeneities observed under TEM are in part responsible to the losses measured in the fibers. For completeness, the drawing temperature for these fibers is 2000 °C (excepted for SrAlSi, which is 1925 °C). In the limit case of an infinitely fast quenching rate (i.e., with the core material being instantaneously "frozen in" during quenching, and where the fictive temperature T_f =2000 °C), the core should in principle be free of phase separation as the molten material, in thermal equilibrium, is found above its LLIR. However, as already seen with the help of IR spectroscopy (Chapter III), the fictive temperature of the fabricated fibers is substantially lower than the fiber drawing temperature, which is consistent with the appearance of some phase separation (as a result of a lower T_f).

For completeness, the addition of Al_2O_3 in a multicomponent glass system is expected to play an important role on the presence (and absence) of phase separation [17–

19]. Also, the graded-index profiles of the fibers give rise to a gradient of glass composition across the fiber core region, from the high doping content at the core center to the fused silica cladding at the core/cladding interface. Hence, this radial evolution of glass compositions, which result in different glass morphologies as observed in Figs. VII.2, VII.3, and VII.4, adds some complexity to pinpoint the relationship between phase separation morphology and losses.

Below are some proposed paths to develop optical fibers similar to the ones studied herein but with further reduced fiber attenuation:

- Starting with higher purity materials should lead to further loss reduction. As an example, commercial single crystal YAG rods were used in [8] as the material precuror and the drawn fiber (silica preform) exhibited attenuation losses in the 100-200 dB/km range.

- By increasing the drawing temperature, one can expect to move away from the LLIR and therefore, upon quenching, do not promote phase separation due to a resulting lower T_f. Additionally, increasing the fiber drawing speed should in principle increase the quenching rate, which may result in a higher T_f of the core material.

- A further addition of Al_2O_3 would reduce the immiscibility critical temperature [17] and consequently promote more homegeneous glasses.

- An introduction of several AEO and/or AEF_2 species would favor a more disordered structure by mean of a resulting multicomponent glass system. Among the AEO-AEF_2 materials, barium silicate systems exhibit reduced immiscibility with respect to the other alkaline earth (Sr, Ca, Mg) systems.

VII. C. Route to fabricate optical fibers with higher dopant concentrations

Further development of highly doped optical fibers can enable supplementary reduction of parameters that lead to parasitic optical nonlinearities. For instance, higher strontium concentration in the oxyfluoride fibers developed could potentially result in a complete eradication of Brillouin scattering. In a similar system, a fiber exhibiting a null dn/dT value can be, in principle, fabricated. If the focus of this dissertation is to understand the role of dopants on optical nonlinearities, some insights on how to further increase dopant concentration of the silicate core are provided. In Chapter V, it was concluded that a high alumina containing precursor mixture drawn at a low temperature (low here refers to 1925 °C, which is the low limit to draw 3x30 mm silica preform) typically results in higher dopant concentrations.

Most of the oxyfluoride fibers studied herein were fabricated with powder packed precursor materials. The route proposed here is the possibility of increasing dopant concentration by drawing fibers with denser starting materials. In [20], a sapphire-derived optical fiber was fabricated using the molten core method, starting from a single-crystalline sapphire rod precursor. This dense material, drawn into a fiber (inside a silica capillary preform) at 2100 °C, led to Al_2O_3 concentration up to ~55 mole %. Despite this high drawing temperature, the high Al_2O_3 content post draw suggests that drawing denser precursor materials (i.e., sleeved rod > pressed pellets > powder packed) results in higher concentration of that material in the silicate fiber core. It is worth mentioning that each material precursor is expected to react differently with the silica cladding, and corrosion/dissolution/diffusion rates in the various systems considered are expected to be different.

Nevertheless, to illustrate the benefit of starting with denser materials to achieve higher dopant concentration, a mixture of $64.4SrO\text{-}35.6Al_2O_3$ (molar ratio) powder was ground and sintered at 1600 °C for 24 hours inside a Platinum crucible. This concentration was chosen as at this composition, the strontium aluminate system forms a phase with a melting temperature of ~1670 °C [21]. The sintered material was then shaped into a 2.5x15 mm rod and sleeved inside a 3.2x15 mm silica capillary preform. The fiber was drawn at 1925 °C with a targeted cladding diameter of 350 µm to avoid fiber breaking during the draw. The fabricated strontium aluminate precursor material is presented in Fig. VII.8a. A SEM micrograph of a characterized drawn fiber segment is also displayed in Fig. VII.8b, and its radial composition profile is reported in Fig. VII.8c.

Firstly, it is interesting to note that the fiber core is not perfectly round, as was the initial shape of the precursor rod, which was manually polished. Secondly, energy dispersive x-ray (EDX) analysis revealed a concentration of 22.3 mole % SrO – 12.7 mole % Al_2O_3 – 65 mole % SiO_2 at the core center. This concentration is sensitively higher than what was previously found when starting with powder packed or pressed pellet precursors. For example, SrAlSi fiber, presented in Chapter VI, was fabricated using a 5SrO-8Al_2O_3 precursor molar ratio, and pressed pellets of that composition were inserted inside a silica capillary preform; the fiber was also drawn at 1925 °C. This fiber exhibits ~73 mole % of SiO_2 at the core center, for 65 mole % for the fiber fabricated here. Using the additive model, the Brillouin gain coefficient for this fiber segment is estimated to be ~18 dB lower than conventional silica fibers, whereas dn/dT of the core material would be ~2.7 dB lower than silica.

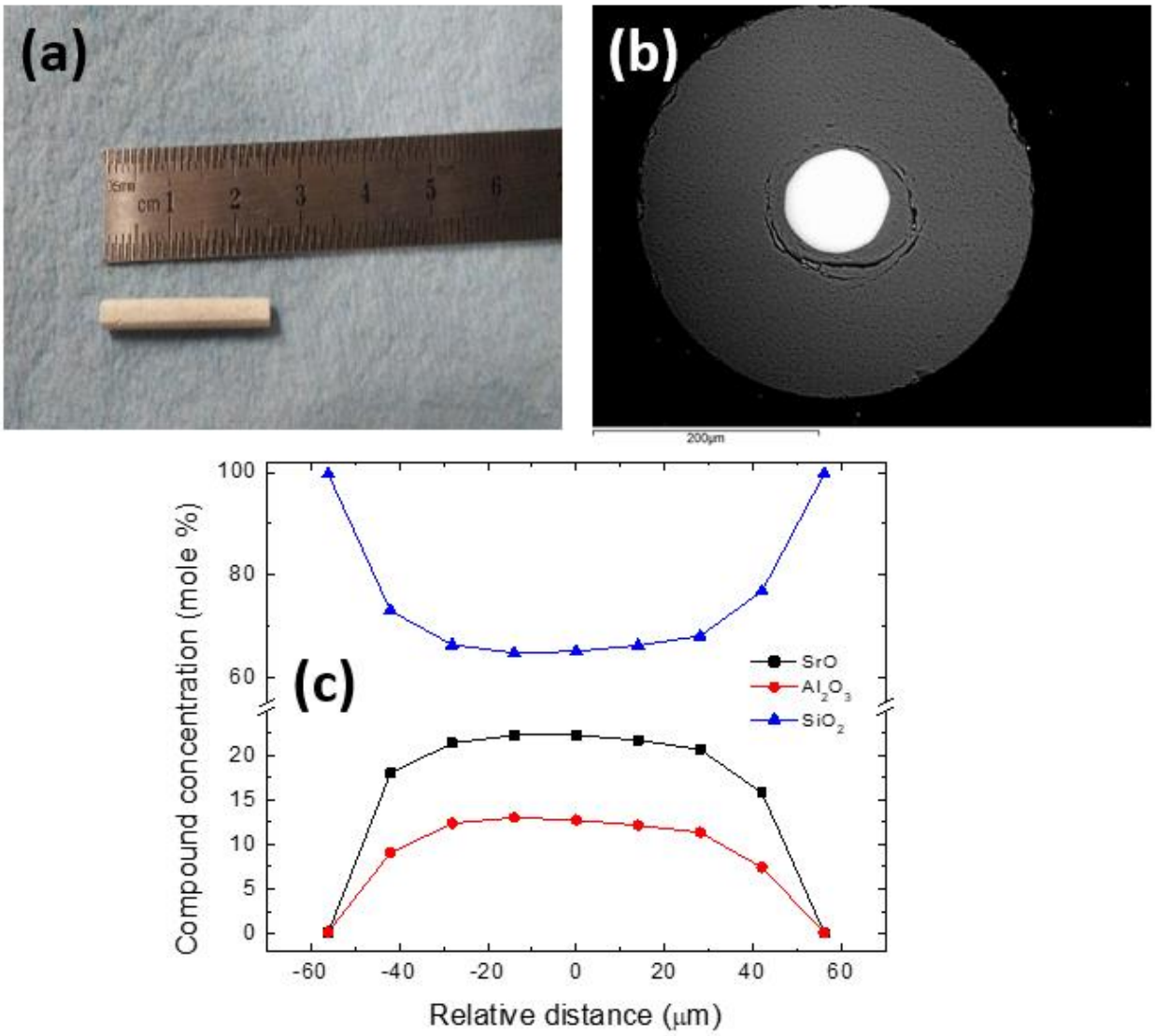

Figure VII.8. a) Strontium aluminate sintered rod utilized as a precursor material. b) SEM micrograph of a characteristic segment of the strontium aluminosilicate fiber drawn at 1925 °C in a 3.2x15 mm silica capillary preform, with a targeted cladding diameter of 300 μm. c) Compositional analysis of the core materials as a function of the core radial distance.

However, the fabricated rod density was calculated to be only ~1800 kg/m^3, which is more than 2× lower than the theoretical density for strontium aluminates (e.g., $SrAl_2O_4$, than is $1SrO\text{-}1Al_2O_3$, has a density of ~3560 kg/m^3). This low density is due to the sintering of a coarse and loose powder, which prevented further densification. More efforts in developing higher density materials are therefore encouraged in order to achieve optical fibers with continuously higher dopant concentrations. This can be easily achieved by sintering precursors with a higher green body density.

It should be considered than the development of highly doped silicate cores is also limited by another important challenge: the coefficient of thermal expansion (CTE) mismatch that exists between the core and the cladding (fused silica) materials. This can be very well seen in Fig. VIIb, where cracks appear around the core/cladding interface, induced by the high stress concentration in this region due to the CTE mismatch. Indeed, the fused silica cladding exhibit a linear CTE of only ~0.55×10^{-6} K^{-1}, when CTEs of the materials that compose the core, such as SrO and Al_2O_3, are much higher (respectively ~×30 and ~×17 times higher than silica [22], Chapter II).

Cracks are found to preferentially propagate along the core/cladding interface as illustrated in Fig. VII.9a, leading to poor mechanical strength and ultimately fiber breaking. In addition to cracks, inclusions of air bubbles inside the fiber core can be found, as shown in Fig. VII.9b, which is manifestly detrimental for light transmission.

One way to overcome CTE mismatch is to use glass claddings with higher CTE, to match the one of the core material and therefore minimize CTE difference between core and cladding. As an example, glass cladding materials in the Silica – Alumina – Lanthana (SAL) system can be implemented [23,24]. In addition to reducing CTE mismatch, such high index cladding glass materials would ease the development of single mode fibers by reducing the refractive index difference between core and cladding. This is specifically interesting when dopants such as the AEO family or Al_2O_3, which significantly increase the refractive index relative to silica, are utilized.

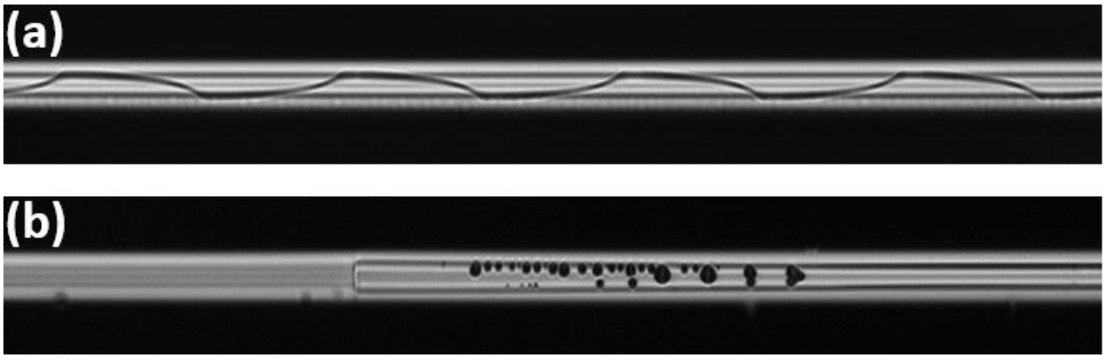

Figure VII.9. a) Optical microscope picture of crack propagation at the core/cladding interface for a strontium aluminosilicate fiber, in the $1SrF_2$-$1Al_2O_3$ initial precursor molar ratio composition, and drawn at 1925 °C in a 3x30 mm silica capillary preform. b) Optical microscope picture of inclusions (air bubbles) observed during fiber splicing for the same fiber but at a different position of the spool.

VII. D. Investigation of mixed AEF_2-derived systems

The previous chapters principally focus on the fabrication and characterization of SrF_2-derived glass optical fibers. However, and as it was discussed in Chapter IV, a multitude of glass systems can be considered, depending on the desired final fiber properties. Therefore, the possibility of developing optical fibers with combined alkaline earth fluorides as initial precursor materials is of interest, as it offers greater tunability of optical properties. As an example, a CaF_2-SrF_2-derived aluminosilicate fiber was developed (Fig. VII. 10) using similar drawing parameters than the Yb-doped fibers presented in Chapter VI. Substituing SrF_2 with CaF_2 (but also MgF_2) is typically expected to reduce the linear and nonlinear refractive indices relative to a SrF_2-derived fiber [25–27]. This can be a preferential option when single mode operation is mendatory. Additionally, the multicomponent nature of the glass can lead to a more disordered glass system, which, in turn, would further reduce Raman scattering. However, if a multicomponent system is expected to favor glass formation and promote more disordered (i.e., homogeneous) glasses , one could also argue that calcium silicates exhibit a more pronounced immiscibility region with respect to strontium of barium silicates (Fig. VII.2), and, consequently, promote liquid-liquid immiscibility.

This example illustrates the potential in combining alkaline earth fluorides as starting precursor materials using the molten core method. It is worth mentioning that all BaF_2, SrF_2, CaF_2, and, MgF_2 can be drawn into fibers at ~2000 °C, and therefore can be

used in any combination needed to achieve the desired property by virtue of similar thermal properties. Additionally, if the properties of SrF_2 have been identified, future work would consist in a better comprehension of the role that BaF_2, CaF_2, and MgF_2 play on the fiber properties. It is expected to benefit fiber designers in the development of optical fibers with targeted properties.

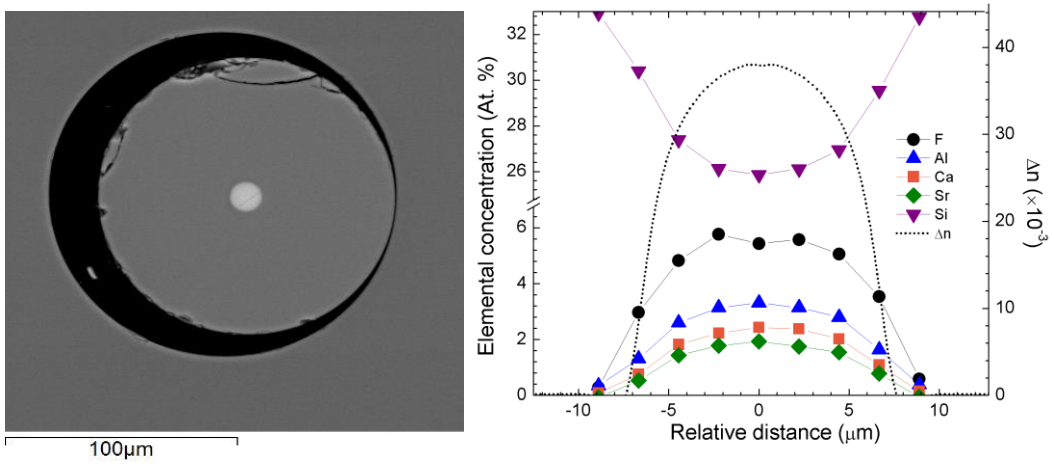

Figure VII.10. SEM micrograph (left) of a calcium-strontium-fluoro-aluminosilicate glass optical fiber segment in the $0.375CaF_2$-$0.375SrF_2$-$0.25Al_2O_3$ initial precursor composition, drawn at 2000 °C in a 3x30 mm silica capillary preform, along with its elemental composition and refractive index radial profiles (right).

VII. E. Conclusion

In this chapter, the origins of attenuation losses are herein discussed. It is speculated that both impurities and nanoscale phase separation, detected with the help of TEM, contribute to losses through both absorption of impurities and Rayleigh scattering. Proposed solutions to mitigate losses are i) to start with high purity materials, ii) to favor multicomponent glasses, iii) to start with higher concentration of Al_2O_3 and iv) to increase fiber drawing temperature.

It is also presented that starting with more compact precursor materials helps in increasing the final dopant concentration of the fiber core. However, high concentration of dopants generally results in cracks at the core/cladding interface, attributed to CTE mismatch between core and cladding. This issue can be overcome by substituting silica cladding with other glass claddings (e.g., in the SAL glass composition) that exhibit higher CTE to match the one of the core.

Finally, it is pointed out that fibers investigated in this dissertation are with a single AEF_2 precursor material. However, mixing several AEF_2 initial precursor materials can lead to further tailoring of optical properties. More efforts in understanding the oxyfluoride glass optical fibers investigated throughout this dissertation are expected to beget materials solution in the realm of continuing power scaling in optical systems.

VII. F. Appendices

Appendix VII. 1. Matlab code used to calculate Rayleigh scattering

```
clear all; close all;
%%%%% parameters %%%%%
i=1;
for d=0.005:0.0001:0.02 % particle diameter (um)

deltad=0.001;    % spacing between particles, um
lembda= 1.534; % wavelength (um)
n1= 1.444; %    matrix index
n2= 1.444+0.0488; % particle index
deltan= n2-n1; %index difference
N=  (1/(d+deltad))^3; % spheres per micron (um-3)
V=  (4*pi*(d/2)^3)/3;   %volume sphere (um3)
phi=N*V; %particle volume ratio

%%%% model 1 %%%%
T1=(32*pi^4*(d/2)^3*(n1*deltan)^2*N*V)/(3*lembda^4)*10^6;
attenuation1(i)=-10*log10(1-T1);% attenuation losses

%%%% model 2 %%%%
T2=(1-exp(-32*pi^4*(d/2)^3*phi*(n1/lembda)^4*((n2^2-
n1^2)/(n2^2+2*n1^2))^2))*10^6;
attenuation2(i)=-10*log10(1-T2);% attenuation losses

D(i)=d;

i=i+1;

end
```

VII. G. References

[1] M. N. Zervas and C. A. Codemard, “High Power Fiber Lasers: A Review,” *IEEE J. Sel. Top. Quantum Electron.*, vol. 20, no. 5, pp. 1–23, 2014.

[2] J. W. Dawson *et al.*, “Analysis of the scalability of diffraction-limited fiber lasers and amplifiers to high average power.,” *Opt. Express*, vol. 16, no. 17, pp. 13240–13266, 2008.

[3] W. Zhi, R. Guobin, L. Shuqin, and J. Shuisheng, “Loss properties due to Rayleigh scattering in different types of fiber.,” *Optics express*, vol. 11, no. 1. pp. 39–47, 2003.

[4] P. C. Schultz, “Optical Absorption of the Transition Elements in Vitreous Silica,” *J. Am. Ceram. Soc.*, vol. 57, no. 7, pp. 309–313, 1974.

[5] O. Humbach, H. Fabian, U. Grzesik, U. Haken, and W. Heitmann, “Analysis of OH absorption bands in synthetic silica,” *J. Non. Cryst. Solids*, vol. 203, pp. 19–26, 1996.

[6] P. Dragic, C. Kucera, J. Furtick, J. Guerrier, T. Hawkins, and J. Ballato, “Brillouin spectroscopy of a novel baria-doped silica glass optical fiber,” *Opt. Express*, vol. 21, no. 9, pp. 10924–10941, 2013.

[7] M. Cavillon *et al.*, “Brillouin Properties of a Novel Strontium Aluminosilicate Glass Optical Fiber,” vol. 34, no. 6, pp. 1435–1441, 2016.

[8] J. Ballato *et al.*, “On the fabrication of all-glass optical fibers from crystals,” *J. Appl. Phys.*, vol. 105, no. 53110, pp. 1–9, 2009.

[9] A. Mangognia *et al.*, “Spinel-derived single mode optical fiber,” *Opt. Mater. Express*, vol. 3, no. 4, p. 511, 2013.

[10] S. H. Z. Heng, J. L. I. Iang, C. Y. U. Hunlei, Q. I. Z. Hou, D. Anping, and C. Hen, “Preparation and characterizations of Nd : YAG ceramic derived silica fibers drawn by post- feeding molten core approach,” *Opt. Express*, vol. 24, no. 21, pp. 24248–24254, 2016.

[11] M. J. Dejneka *et al.*, “La_2O_3–Al_2O_3–SiO_2 Glasses for High-Power, Yb^{3+}-Doped, 980-nm Fiber Lasers,” vol. 106, pp. 1100–1106, 2002.

[12] V. McGahay and M. Tomozawa, “The origin of phase separation in silicate melts and glasses,” *J. Non. Cryst. Solids*, vol. 109, no. 1, pp. 27–34, 1989.

[13] A. K. Varshneya, *Fundamentals of inorganic glasses*. Academic Press, 1993.

[14] B. Guo, J. Tang, B. Cai, and Y. Zhu, “Highly efficient terahertz wave filter for high-power laser beam separation,” *Appl. Phys. Lett.*, vol. 105, no. 22, 2014.

[15] M. J. Dejneka, “The luminescence and structure of novel transparent oxyfluoride glass-ceramics,” *J. Non. Cryst. Solids*, vol. 239, no. 1–3, pp. 149–155, 1998.

[16] Y. I. Ol’shanskii, “Equilibrium of two immiscible liquids in silicate systems of alkaline earth metals,” *Dokl. Akad. Nauk SSSR*, vol. 76, no. 1, pp. 93–96, 1951.

[17] B. Hatta and M. Tomozawa, “Effect of Al_2O_3 on phase separation of SiO_2-Nd_2O_3 glasses,” *J. Non. Cryst. Solids*, vol. 354, no. 27, pp. 3184–3193, 2008.

[18] M. Tomozawa and R. A. Obara, “Effect of Minor Third Components on Metastable Immiscibility Boundaries of Binary Glasses,” *J. Am. Ceram. Soc.*, vol. 56, no. 7, pp. 378–381, 1973.

[19] J. Ballato and P. Dragic, “On the Clustering of Rare Earth Dopants in Fiber Lasers,” *J. Dir. Energy,* vol. 6, pp. 175–181, 2017.

[20] P. Dragic, T. Hawkins, P. Foy, S. Morris, and J. Ballato, “Sapphire-derived all-glass optical fibres,” *Nat. Photonics,* vol. 6, no. 9, pp. 629–635, 2012.

[21] A. Shukla, “Development of a Critically Evaluated Thermodynamic Database for the Systems Containing Alkaline-Earth Oxides,” Ecole Polytechnique de Montreal, Universite de Montreal, 2012.

[22] M. Cavillon, J. Ballato, and P. D. Dragic, “Additivity of the coefficient of thermal expansion in silicate optical fibers,” *Opt. Lett.,* vol. 42, no. 18, pp. 3650–3653, 2017.

[23] D. Litzkendorf *et al.*, “Study of Lanthanum Aluminum Silicate Glasses for Passive and Active Optical Fibers,” *Int. J. Appl. Glas. Sci.,* vol. 3, no. 4, pp. 321–331, 2012.

[24] K. Schuster *et al.*, “Material and technology trends in fiber optics,” *Adv. Opt. Technol.,* vol. 3, no. 4, pp. 447–468, 2014.

[25] D. Milam, M. J. Weber, and A. J. Glass, “Nonlinear refractive index of fluoride crystals,” *Appl. Phys. Lett.,* vol. 31, no. 12, pp. 822–825, 1977.

[26] M. Weber, D. Milam, and W. Smith, “Nonlinear refractive index of glasses and crystals,” *Opt. Eng.,* vol. 17, no. 5, pp. 463–469, 1978.

[27] R. Adair, L. L. Chase, and S. a. Payne, “Nonlinear refractive-index measurements of glasses using three-wave frequency mixing,” *J. Opt. Soc. Am. B,* vol. 4, no. 6, p. 875, 1987.